

**DEVELOPMENT OF HYBRID METAL OXIDE-BASED PEROVSKITE
FUNCTIONAL MATERIALS FOR CATALYTIC DEGRADATION OF ENDOCRINE
DISRUPTIVE CHEMICALS (EDCs) FROM INDUSTRIAL AQUATIC WASTE**

Thesis Submitted for the Award of the Degree of

DOCTOR OF PHILOSOPHY

in

Chemistry

By

Saima Jan

Registration Number: 12109622

Supervised By

Prof. Ajit Kumar Sharma

Professor

Department of Chemistry, Lovely Professional University



L OVELY
P ROFESSIONAL
U NIVERSITY

Transforming Education Transforming India

**LOVELY PROFESSIONAL UNIVERSITY, PUNJAB
2025**

**Dedicated
To
My Parents
(Haji Bashir Ahmad Ahanger & Jana Bano)
&
Siblings**

(Riyaz Ahmad, Gowhar Jan & Mehreen Jan)

For their inspiration, kindness, continuous support, and prayers day and night

DECLARATION

I, hereby declared that the presented work in the thesis entitled “**Development of hybrid metal oxide-based perovskite functional materials for catalytic degradation of endocrine disruptive chemicals (EDCs) from industrial aquatic waste**” in fulfilment of degree of **Doctor of Philosophy (Ph.D.)** is outcome of research work carried out by me under the supervision of Dr. Ajit Kumar Sharma, working as Professor, in the Department of Chemistry, School of Chemical engineering and physical sciences of Lovely Professional University, Punjab, India. In keeping with the general practice of reporting scientific observations, due acknowledgements have been made whenever work described here has been based on findings of another investigator. This work has not been submitted in part or in full to any other University or Institute for the award of any degree.

(Signature of Scholar)

Name of the scholar: Saima Jan

Registration No.: 12109622

Department/school: Department of Chemistry

School of Chemical Engineering and Physical Sciences

Lovely Professional University,

Punjab, India

CERTIFICATE

This is to certify that the work reported in the Ph.D. thesis entitled “**Development of hybrid metal oxide-based perovskite functional materials for catalytic degradation of endocrine disruptive chemicals (EDCs) from industrial aquatic waste**” submitted in fulfillment of the requirement for the award of degree of **Doctor of Philosophy (Ph.D.)** in the Department of Chemistry, School of Chemical Engineering and Physical Sciences, is a research work carried out by **Saima Jan, (12109622)**, is bonafide record of his/her original work carried out under my supervision and that no part of thesis has been submitted for any other degree, diploma or equivalent course.

(Signature of Supervisor)

Name of supervisor: Dr Ajit Kumar Sharma

Designation: Professor

Department/school: Department of Chemistry

University: Lovely Professional University

ABSTRACT

Endocrine-disrupting chemicals (EDCs) have become a significant environmental concern, prompting extensive research and interest within the scientific community. Endocrine-disrupting chemicals (EDCs) present a considerable threat to the enduring viability of both human and wildlife populations. Even at minimal concentrations, these compounds can disrupt endocrine system function, resulting in persistent and severe biological effects, including an elevated prevalence of hormone-related cancers, developmental anomalies, and reproductive dysfunction. Therefore, the effective treatment of wastewater containing endocrine-disrupting chemicals (EDCs) is crucial. Conventional wastewater treatment methods often fail to eliminate EDCs, as they primarily facilitate phase transfer rather than full degradation. Additionally, the transformation of these compounds during treatment can lead to the formation of intermediate byproducts that exhibit higher toxicity than the original contaminants. Consequently, an optimal treatment approach should be non-selective, ensuring rapid and complete mineralization of EDCs to prevent secondary pollution.

Semiconductors capture light energy and form electron-hole pairs for redox processes, making them popular photocatalysts. After absorbing high-energy light, electrons migrate from the valence band to the conduction band and generate holes. The charge carriers migrate to the surface of the semiconductor, interacting with adsorbed substances, which facilitates oxidation and reduction processes. This property improves the efficiency of semiconductor photocatalysts for a range of environmental applications, such as the degradation of organic pollutants, water splitting, and air purification. Materials like titanium dioxide (TiO_2) and zinc oxide (ZnO) are extensively researched due to their stability, non-toxicity, and strong photocatalytic performance under UV or visible light exposure.

For eliminating contaminants from wastewater, photocatalytic degradation is one of the most interesting, affordable, and environmentally friendly methods. Here, we utilize an efficient sol-gel and microwave method for producing CuS , CdS , MoS_2 , $\text{Cs}_3\text{Bi}_2\text{Br}_9$, and doped MoS_2/CdS , $\text{CdS}/\text{Cs}_3\text{Bi}_2\text{Br}_9$, and $\text{MoS}_2/\text{Cs}_3\text{Bi}_2\text{Br}_9$ nanomaterials. Several methods, including UV-visible, XRD, Energy Dispersive X-ray Analysis (EDX), and Field Emission Scanning Microscopy (FE-SEM), FTIR, will be used to optimize the materials. FE-SEM measurements validated the morphology of the produced nanocomposites.

The efficiency of catalytic degradation is evaluated using representative endocrine-disrupting chemicals (EDCs), such as 2-chlorophenol, ciprofloxacin, paracetamol, and ibuprofen, under optimized reaction conditions. Key parameters, including pH, temperature, catalyst dosage, and reaction time, are systematically analyzed to determine their impact on the degradation process.

The outcomes of the present study advance the development of sustainable, cost-effective, and high-efficiency catalytic systems for industrial wastewater treatment. The halide-based perovskite materials synthesized in this research demonstrate substantial potential for practical environmental remediation, aiding in the reduction of the ecological impact of hazardous industrial effluents.

ACKNOWLEDGEMENT

“The real spirit of achieving a goal is through the way of excellence and Discipline”

First of all, I would like to express my gratitude to Almighty **Allah**, whose presence gives me the power, possibilities, and desire to work for achievement and guides me in the greatest and brightest path.

My profound appreciation goes out to my esteemed supervisor, **Dr. Ajit Kumar Sharma**, for all of his invaluable advice and unwavering support. They have consistently encouraged me when challenges have arisen, given me total freedom to share my ideas, and offered helpful tips to enhance my scientific methodology. In addition to teaching me research techniques, they taught me many life lessons. Their passionate dedication and excitement for their work were inspiring and productive, and they will always motivate me to pursue similar goals in the future. They helped to shape the most significant aspect of my research career, for which I will always be grateful. Their efficient and significant contributions at every stage were essential to the completion of this task.

I am sincerely thankful to **Lovely Professional University (LPU)** for providing me with the opportunity, resources, and supportive environment to carry out this work successfully. The university's commitment to excellence in education and research has inspired me to strive for high academic standards.

I would like to express my sincere gratitude to the Head of School, **Dr. Kailash Chandra Juglan**, for providing constant guidance, encouragement, and support throughout this work. I am also deeply thankful to the Head of Department, **Dr. Harmanjit Singh Dosanjh**, for their valuable advice, motivation, and for creating a positive learning environment that greatly contributed to the successful completion of this project. Their leadership and inspiration have been instrumental in shaping my understanding and growth.

I would especially like to thank Aadil Ahmad Bhat of the Chinese University of Hongkong Shenzhen, Guangdong, Owais Hassan Wani and Shah Jahan Ul Islam of Kashmir University, and NIT Srinagar, Jammu and Kashmir, and Manoj Verma of Lovely Professional University for their helpful assistance in characterization studies. I am appreciative of my friends, **M D Shaquib Jahangir, Asma Masood, Zahid Ahmad Lone, Dr. Humira Assad, Dr. Mir Bilal, Zahid Ahmad Thoker, Shah Muzamil, Shahid Ahmad Shah, Souheen Lone, Insha Muzaffar,**

Sadaf Bashir, Sham Sun Nisa, Toyyiba Parihar, Irshad Ahmad Bhat, Dr. Mehnaz Ayoub, Dr. Irtiqa Ashraf Mir, Adfar Rashid, for their assistance and collaboration when required.

I extend my deepest gratitude to my parents for their lifelong guidance, love, and support. Their selfless sacrifices and inspiring philosophy have been instrumental in shaping my values and accomplishing my academic goals. Additionally, I am grateful to my **siblings Hilala Firdous, Rehana Bashir, Gulzar Ahmad Ahanger, Mohd Ishfaq Ahanger, Mahira Jan, Hareem Siddiqui, Mohammad Hammad Dar, and Fariha Gulzar** for their unwavering affection, generous assistance, and collaborative spirit, which have significantly contributed to my personal growth. Finally, I acknowledge Allah Subhanahu wa ta'ala's divine guidance and blessings, which have granted me the strength and perseverance to overcome challenges and achieve success.

Great thanks to all my well-wishers

Saima Jan

List of Content

S. No.	Title	Page No.
1	Chapter 1: (INTRODUCTION)	21-42
1.1	Crisis and scenario	21-24
1.2	Endocrine-disrupting chemicals	25-27
1.3	Classification of Endocrine Disrupting Chemicals	27-29
1.4	Source of endocrine-disrupting chemicals	30-32
1.5	Effect of endocrine-disrupting chemicals	33-36
1.6	Mechanism of Action of Endocrine Disrupting Chemicals	37-40
2	Chapter 2: (REVIEW OF LITERATURE)	43-102
2.1	Overview of Endocrine-disrupting chemicals	43-44
2.2	Endocrine-disrupting chemicals consumption and production	45-46
2.3	Removal methods for EDCs from wastewater	47-51
2.4	Role of Nanomaterials and nanotechnology for the remediation of endocrine-disrupting chemicals	52-53
2.5	Photocatalysis	54
2.6	Advanced oxidation process	55-66
2.7	Mechanism of Photocatalysis	67-69
2.8	Applications of photocatalyst	70-71
2.9	Semiconductor as a photocatalyst	72-79
2.10	Modifications of Semiconductor Materials	80-84
2.11	Methods used for the preparation of nanoparticles	85-89
2.12	Photocatalytic remediation of organic pollutants	90-100
2.13	Research gap and Objectives of the present Thesis	101-102
3	Chapter 3: (MATERIALS AND METHODS)	103-119
3.1	Materials	104
3.2	Preparation of Catalyst	105-109
3.3	Catalyst Characterization Analysis	110-118
3.4	Photocatalytic degradation activity test	119
	Chapters 4, 5, 6, and 7: (RESULTS AND DISCUSSION)	120-201

4	Synthesis and characterization studies of CuS nanoparticles synthesised via the wet chemical coprecipitation method and their photo-degradation of 2-chlorophenol.	
4.1	Introduction	121-123
4.2	Results and Discussion	
4.2.1	Characteristics studies	124-128
4.2.2	Photocatalytic degradation of 2-CP	129-137
4.2.3	Batch absorption experiment	138
4.2.4	Schematic mechanism of CuS for 2-CP degradation	139
5	Photocatalytic Degradation of Ciprofloxacin Using Microwave-Assisted CdS/Cs ₃ Bi ₂ Br ₉ Nanocomposite in Industrial Aquatic Waste	
5.1	Introduction	140-143
5.2	Results and Discussion	
5.2.1	Characteristics studies	144-152
5.2.2	Photocatalytic degradation of Ciprofloxacin (CIP)	153-162
5.2.3	Elucidating the Photocatalytic Degradation Pathway of Ciprofloxacin	163-166
6	MoS ₂ /CdS Nanocomposites for Enhanced Visible Light Photocatalytic Degradation of Paracetamol in Synthetic Pharmaceutical Wastewater	
6.1	Introduction	167-169
6.2	Result and Discussion	
6.2.1	Characterization studies	170-174
6.2.2	Photocatalytic Degradation of Paracetamol	175-180
6.2.3	Mechanism for photocatalytic degradation of Paracetamol	181-182
7	Photocatalytic Removal of Ibuprofen from Wastewater using Novel MoS ₂ @Cs ₃ Bi ₂ Br ₉ Nanocomposites	
7.1	Introduction	183-185
7.2	Result and Discussion	
7.2.1	Characterization studies	186-195
7.2.2	Photocatalytic Degradation of Ibuprofen	196-200
7.2.3	Mechanism for photocatalytic degradation of Ibuprofen	201
8	CHAPTER 8: (SUMMARY OF WORK AND FUTURE SCOPE)	202-208
	CONCLUSION	203-207

	REFERENCES	209-254
	List of Publications	255-260
	Conferences Attend	261

List of Tables

S. No.	Table No.	Title	Page No.
1.	1.1	The adverse effects of popular pharmaceuticals are presents in wastewater.	23
2.	1.2	The harmful effects of prevalent EDCs on human health.	25
3.	2.1	Comparing the methods used in wastewater and water systems for the removal and treatment of endocrine disruptors.	50
4.	2.2	Basic semiconductor photocatalysts and their band positions (water at pH 1).	73
5.	2.3	Photocatalytic degradation of various Endocrine Disrupting Chemicals by Semiconductors Heterojunctions.	100
6.	4.1	Photocatalytic degradation of organic pollutants by using CuS and hybrid materials for treatment of wastewater.	130
7.	4.2	Pseudo first-order rate constant for 2-CP.	132
8.	5.1	FWHM, crystallite Size, and Lattice strain for CdS (S.G), CdS (M.W), Cs ₃ Bi ₂ Br ₉ , and (1, 5, and 10%) CdS/Cs ₃ Bi ₂ Br ₉ nanocomposite.	147
9.	5.2	The electronic transition band gap energies and VB and CB potential positions of the utilized samples were determined.	150
10.	5.3	Efficiency Comparison of Photocatalysts for Ciprofloxacin Degradation.	154
11.	5.4	Apparent First-Order Rate Constant for Ciprofloxacin Photodegradation.	156
12.	6.1	Research chart for Paracetamol showing photocatalytic degradation efficiency.	176
13.	6.2	Rate constants of Pseudo-first order for catalytic elimination of Paracetamol using CdS, MoS ₂ , and 1:1M MoS ₂ /CdS.	177
14.	7.1	FWHM, crystallite Size and Lattice strain for MoS ₂ , Cs ₃ Bi ₂ Br ₉ and (1, 5 1nd 10%) MoS ₂ @Cs ₃ Bi ₂ Br ₉ nanocomposite	190
15.	7.2	Ibuprofen Photodegradation Estimated First-Order Rate Constant	198

List of Figures

S. No.	Figure No.	Title	Page No.
1	1.1	Different sources of endocrine-disrupting chemicals	32
2	1.2	Illustration of the primary endocrine glands that Endocrine Disrupting Chemicals target	33
3	1.3	Endocrine Disrupting Chemicals exposure in humans and its molecular effects.	38
4	1.4	Endocrine Disrupting Chemicals mechanism of action	39
5	2.1	Various techniques used for the degradation of endocrine-disrupting chemicals	47
6	2.2	Representatives of the advanced oxidation process (AOP)	55
7	2.3	Illustration of the process by which Fenton-like nanoparticles break down organic compounds. The reactive free radicals that break down harmful contaminants are produced by the $\text{Fe}^{2+}/\text{Fe}^{3+}$ redox pair	57
8	2.4	The overall process of photocatalysis. Toxic organics completely degrade due to the hydroxyl radicals and superoxide anions generated by electron-hole pairs.	63
9	2.5	Illustration of an indirect sonolysis concept. After going through several cycles of growth and collapse, the bubbles create powerful breaking forces at very high pressures and temperatures, which cause the sonolysis of water molecules and the production of reactive radicals.	66
10	2.6	The mechanism through which a semiconductor is excited at the bandgap	69
11	2.7	Bandgap values of different semiconductors	73
12	2.8	States localized above the valence band, Semiconductor with reduced E_g , Localized conditions below the conduction band, color centers created in E_g , and surface modification	79

13	2.9	Codoping effect	82
14	2.10	Schematic illustration of co-precipitation methods	85
15	2.11	Diagram representing the several steps of the Sol-Gel process	87
16	2.12	Schematic diagram of the hydrothermal method showing the synthesis of nanomaterials	88
17	2.13	Diagram for the microwave-irradiation technique	90
18	3.1	Schematic representation of FTIR spectroscopy	110
19	3.2	X-ray Diffraction technique	112
20	3.3	Bragg's law and Geometrical drawing of crystal planes	112
21	3.4	Illustration of the SEM instrument	114
22	3.5	Principle of scanning electron microscopy (SEM)	115
23	3.6	Schematic illustration of a UV-Vis spectrophotometer	116
24	3.7	Energy level diagrams	117
25	3.8	Thermogravimetric analysis (TGA) graphic illustrations	118
26	4.1	FTIR of CuS nanoparticle	124
27	4.2	XRD of CuS nanoparticles synthesized by wet chemical co-precipitation and Sol-Gel method	125
28	4.3	TGA/DSC of CuS nanoparticle (wet chemical co-precipitation method)	126
29	4.4	Tauc plot of CuS nanoparticle (wet chemical co-precipitation method)	127
30	4.5	FESEM of CuS nanoparticle wet chemical co-precipitation and Sol-Gel method	128
31	4.6	EDX of CuS nanoparticle (wet chemical co-precipitation method)	128
32	4.7	Effect of pH on degradation of 2-CP, Conc. of 2-CP; 100 mg/L, reaction volume; 30 mL, catalyst dose; 10 mg, irradiating time; 2 h, pH; 6, Temperature; 30°C	130
33	4.8	Effect of reaction time, Conc. of 2-CP; 100 mg/L, reaction volume; 30 mL, catalyst dose; 10 mg, irradiating time; 2 h, pH; 6, Temperature; 30°C	133

34	4.9	Pseudo i st - order kinetics. Conc. of 2-CP; 100 mg/L, reaction volume; 30 mL, catalyst dose; 10 mg, irradiating time; 2 h, pH; 6, Temperature; 30°C	133
35	4.10	Effect of catalyst dosage, Conc. of 2-CP; 100 mg/L, reaction volume; 30 mL, irradiating time; 2 h, pH; 6, Temperature; 30°C	134
36	4.11	Effect of H ₂ O ₂ , Conc. of 2-CP; 100 mg/L, reaction volume; 30 mL, catalyst dose; 10 mg, irradiating time; 2 h, pH; 6, Temperature; 30°C	136
37	4.12	Regeneration of CuS (WCP) photo-catalyst (reaction condition: 2-CP concentration of 100 mg/L, catalyst dose; 10 mg, volume; 30 mL, H ₂ O ₂ ; 0.01%, pH; 6.0, Temperature; 30° C).	137
38	4.13	Effect of catalyst dosage, Conc. of 2-CP; 100 mg/L, volume; 30 mL, time; 2 h, pH; 6, Temperature; 30°C	138
39	4.14	Schematic mechanism of CuS (WCP) for 2-CP degradation	139
40	5.1	FTIR of CdS (S.G). CdS (M.W), Cs ₃ Bi ₂ Br ₉ , and their various composites	144
41	5.2	XRD graphs of CdS (S.G), CdS (M.W), Cs ₃ Bi ₂ Br ₉ , and their various composites.	146
42	5.3	SEM/Mapping/EDX graphs of CdS (A1, A2, A3), Cs ₃ Bi ₂ Br ₉ (B1, B2, B3) and 5% CdS/ Cs ₃ Bi ₂ Br ₉ composites (C1, C2, C3)	148
43	5.4	Tauc plot of CdS, Cs ₃ Bi ₂ Br ₉ and 5%CdS/Cs ₃ Bi ₂ Br ₉ for n=2	151
44	5.5	Zeta potential of (a) CdS, (b) Cs ₃ Bi ₂ Br ₉ , and (c) 5%CdS/Cs ₃ Bi ₂ Br ₉	152
45	5.6	Effect of pH on Ciprofloxacin. Conc. of CIP; 100m/L, Reaction volume; 30mL, Catalyst dose; 10mg, irradiation time; 3h, pH; 8, Temperature; 30°	155
46	5.7	Effect of time. Conc. of CIP; 100m/L, Reaction volume; 30mL, Catalyst dose; 10mg, irradiation time; 3h, pH; 8, Temperature; 30°	157
47	5.8	Rate of CIP photocatalytic degradation reaction. Conc. of CIP; 100m/L, Reaction volume; 30mL, Catalyst dose; 10mg, irradiation time; 3h, pH; 8, Temperature; 30°	157
48	5.9	Effect of H ₂ O ₂ . Conc. of CIP; 100m/L, Reaction volume; 30mL, Catalyst dose; 10mg, irradiation time; 3h, pH; 8, Temperature; 30°	158

49	5.10	Effect of catalytic dosage. Conc. of CIP; 100m/L, Reaction volume; 30mL, Catalyst dose; 10mg, irradiation time; 3h, pH; 8, Temperature; 30°	159
50	5.11	Effect of Temperature on degradation of CIP by (a) CdS, (b) Cs ₃ Bi ₂ Br ₉ , (c)5% CdS/Cs ₃ Bi ₂ Br ₉ . Conc. of CIP; 100m/L, Reaction volume; 30mL, Catalyst dose; 10mg, irradiation time; 2.5h, pH; 8	160
51	5.12	Effect of initial concentration on degradation of CIP by (a) CdS, (b) Cs ₃ Bi ₂ Br ₉ , (c)5% CdS/Cs ₃ Bi ₂ Br ₉ . Conc. of CIP; 100m/L, Reaction volume; 30mL, Catalyst dose; 10mg, irradiation time; 2.5h, pH; 8 Temperature; 30	161
52	5.13	Hinshelwood model for degradation of CIP by (a) CdS, (b) Cs ₃ Bi ₂ Br ₉ , (c)5% CdS Cs ₃ Bi ₂ Br ₉ . Conc. of CIP; 100m/L, Reaction volume; 30mL, Catalyst dose; 10mg, irradiation time; 2.5h, pH; 8	162
53	5.14	The regeneration rate of 5%CdS/Cs ₃ Bi ₂ Br ₉ . Conc. of CIP; 100m/L, Reaction volume; 30mL, Catalyst dose; 10mg, irradiation time; 3h, pH; 8, Temperature; 30	163
54	5.15	A proposed mechanism for Ciprofloxacin degradation	165
55	6.1	XRD pattern of (a) MoS ₂ , (b) CdS, (c) 1:1M MoS ₂ /CdS, (d) 1:2M MoS ₂ /CdS and (e) 2:1M MoS ₂ /CdS	170
56	6.2	FTIR of (a) MoS ₂ , (b) CdS and (c) MoS ₂ /CdS nanocomposites	171
57	6.3	SEM/EDX of (a) pure MoS ₂ , (b) pure CdS and (c)1:1M MoS ₂ /CdS nanocomposite	172
58	6.4	Optical band gap of (a) MoS ₂ , (b) CdS and (c) 1:1M MoS ₂ /CdS nanocomposite	174
59	6.5	Effect of pH on paracetamol (PCM) degradation under visible light irradiation	176
60	6.6	kinetic studies of paracetamol (PCM) degradation under visible light irradiation	178
61	6.7	Photodegradation reaction rate of PCM. Conc. of PCM; 10mg/L, Reaction volume; 30mL, catalyst dose; 10mg, irradiation time; 3.5h, pH; 4, Temperature; 30°C	179

62	6.8	Effect of H ₂ O ₂ for paracetamol (PCM) degradation under visible light irradiation.	180
63	6.9	Effect of Photocatalyst concentration for paracetamol (PCM) degradation under visible light irradiation	181
64	6.10	Mechanism of photocatalytic degradation process for Paracetamol (PCM) by MoS ₂ , CdS, and 1:1M MoS ₂ /CdS under visible light irradiation	182
65	7.1	FTIR spectra of MoS ₂ (SG), MoS ₂ (MW), Cs ₃ Bi ₂ Br ₉ and their various composites	187
66	7.2	XRD graphs of MoS ₂ (SG), MoS ₂ (MW), Cs ₃ Bi ₂ Br ₉ and their various composites	188
67	7.3	SEM and EDX graphs of MoS ₂ , Cs ₃ Bi ₂ Br ₉ and 5% MoS ₂ @Cs ₃ Bi ₂ Br ₉ nanocomposite	191
68	7.4	Elemental mapping of MoS ₂ , Cs ₃ Bi ₂ Br ₉ and 5% MoS ₂ @Cs ₃ Bi ₂ Br ₉ nanocomposites	192
69	7.5	UV visible spectra of Cs ₃ Bi ₂ Br ₉ , MoS ₂ and 5% MoS ₂ @Cs ₃ Bi ₂ Br ₉ nanocomposite	193
70	7.6	Optical band gap of MoS ₂ , Cs ₃ Bi ₂ Br ₉ and 5%MoS ₂ @Cs ₃ Bi ₂ Br ₉ nanocomposite	195
71	7.7	Effect of pH on Ibuprofen. Conc. of IBF; 100mg/L, Reaction volume; 30mL, Catalyst dose; 10 mg, irradiation time; 3h, pH; 6, Temperature; 30° C.	196
72	7.8	Effect of time. Conc. of IBF; 100mg/L, Reaction volume; 30mL, Catalyst dose; 10mg, irradiation time; 3h, pH; 6, Temperature; 30° C	197
73	7.9	Rate of IBF photocatalytic degradation reaction. Conc. of IBF; 100mg/L, Reaction volume; 30mL, Catalyst dose; 10mg, irradiation time; 3h, pH; 6, Temperature; 30° C	198
74	7.10	Effect of H ₂ O ₂ . Conc. of IBF; 100mg/L, Reaction volume; 30mL, Catalyst dose; 10mg, irradiation time; 3h, pH; 6, Temperature; 30° C	199

75	7.11	Effect of catalytic dosage. Conc. of IBF; 100 mg/L, Reaction volume; 30mL, Catalyst dose; 10mg, irradiation time; 3h, pH; 6, Temperature; 30° C	200
76	7.12	A proposed mechanism for IBF degradation	201

List of Abbreviations

ARs	Androgen receptors
AOPs	Advanced oxidation processes
AOS	Average oxidation state
ATTTs	Advanced tertiary treatments
AGD	Anogenital distance
BPA	Bisphenol A
CECs	Contaminants of emergent concern
CTs	Chlorotriazine
COD	Chemical oxygen demand
CIP	Ciprofloxacin
CWAO	Catalytic wet air oxidation
COS	Carbon oxidation state
DMF	N, N-dimethylformamide
DMSO ₄	Dimethyl sulfoxide
DDT	Dichlorodiphenyltrichloroethane
DEHP	Di(2-ethylhexyl) phthalate
DES	Diethylstilbestrol
Dtpa	Diethylenetriamine pentaacetic acid
EDCs	Endocrine-disrupting chemicals
EDS	Energy dispersive spectra
E _g	Bandgap energy
E1	Estrone
ERs	Estrogen receptors
FTIR	Fourier Transform - Infrared Spectroscopy
GC-MS	Gas chromatography-mass spectrometry
hAR	Human androgen receptor
HA	Humic acid
IR	Insulin receptors
LED	Light-emitting diodes
MCMs	Multicatalytic materials

NP	Nonylphenol
NHCs	N-doped hydrochars
NZVI	Nano-zero valent iron
NPES	Nonylphenol ethoxylates
OP	Octylphenol
OCPs	Organochlorine pesticides
OCs	Organochlorines
OCs	Organic contaminants
PBDE	Polybrominated diphenyl ether
PPCPs	Pharmaceuticals and personal care products
PMS	Peroxymonosulfate
PCBs	Polychlorinated biphenyls
PC	Polycarbonate
PFAS	Poly- and perfluoroalkyl compounds
PFOA	Perfluorooctanoic acid
PCM	Paracetamol
RhB	Rhodamine B
RBC	Rotating biological contactor
SEM	Scanning electron microscopy
TCS	Triclosan
TRs	Thyroid receptors
TGA	Thermogravimetric analysis
UPW	Ultrapure water
VOC	Volatile organic compounds
WAO	Wet Air Oxidation

CHAPTER 1

INTRODUCTION

1.1 CRISIS AND SCENARIO:

Throughout history, water has been the most important natural resource for the development of humanity and one of the most fundamental prerequisites for the existence of all living forms. It is also an issue of discussion worldwide. Having constant access to safe and clean water is one of the biggest issues facing the current world. There is a big problem for the globe to provide a uniform universal volume of water since there aren't enough sources. There is no denying the importance of having potable, high-quality drinking water; without it, the safety of people's health would be affected [Zubair et al., 2020]. The degradation of effluents carrying newly discovered micro-pollutants that are known to remain in diverse water sources is one of the many human activities endangering clean and safe water. The sustainability of human health, agriculture, industry, and the financial system heavily depends on water [Dhote et al., 2012].

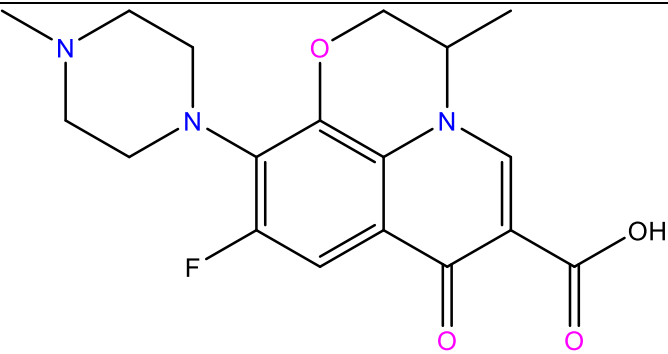
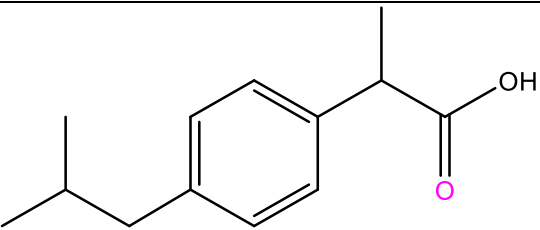
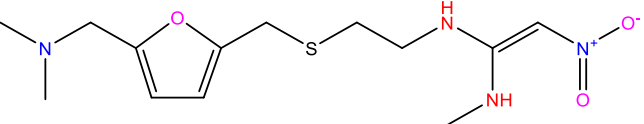
According to recent peer-reviewed studies, the water crisis in India is due to a fast-growing population, irresponsible groundwater extraction, climate change, and ineffective water management [Rakkasagi et al., 2025; Singh and Kumar, 2021]. India has merely 4% of global freshwater resources despite having 17.81% of the global population, which results in the high shortage of freshwater in the region and the situation of the so-called Day Zero in cities [Katoch, 2024; Rakkasagi et al., 2025]. It is confirmed by satellite data that the groundwater of northwest India is being depleted at an alarming rate of approximately 4 cm per year, particularly in the states with high rates of agricultural production such as Punjab and Rajasthan, where more than 60 -75 percent of blocks are already critically overdrawn [Panda, 2011; Rakkasagi et al., 202]. The climate variability, unpredictable monsoons, and pollution are other factors that worsen the crisis and put food security, citizens' health, and social stability at risk [Singh and Kumar, 2021; Halder and Chattopadhyay, 2024].

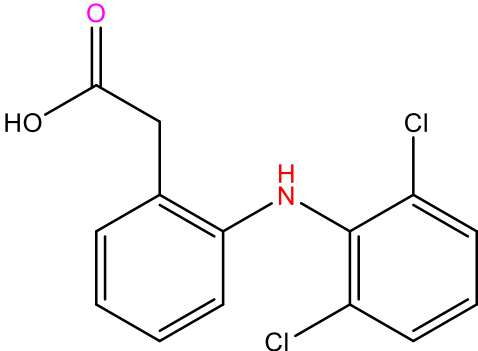
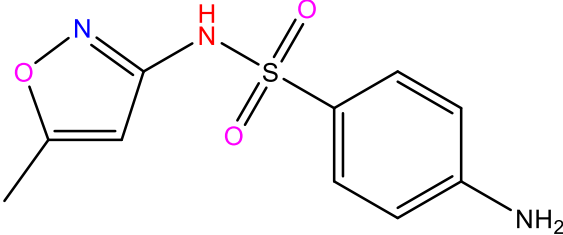
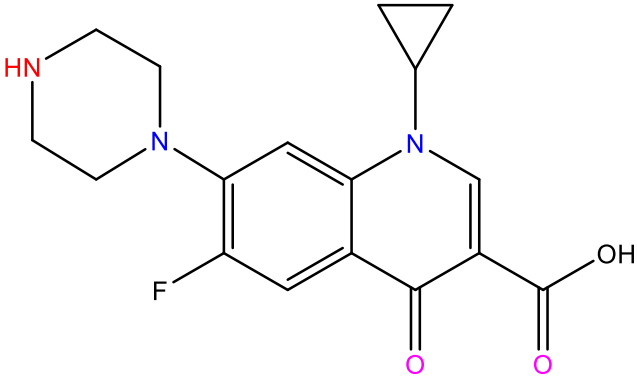
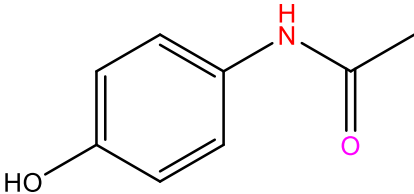
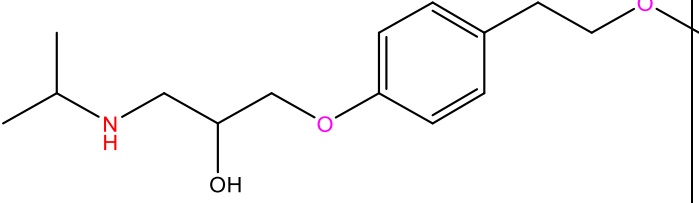
The availability of water per capita has already dropped far below the water-stressed level, and it is expected to keep falling as population grows [Rakkasagi et al. 2025; Singh and Kumar, 2021]. Research has shown that the water withdrawals in India are already beyond the sustainable levels in most aquifers and that the depletion of groundwater may jeopardize the future agricultural production and livelihoods [Katoch, 2024; Panda, 2011]. There is an urgent necessity in establishing robust, fair, and sustainable water governance, with the addition of the enhancement of infrastructure, policy, and resource management [Halder and Chattopadhyay, 2024; Rakkasagi et al., 2025].

However, several causes, including urbanization, industry, and population increase, are severely affecting hydrological resources [UNESCO 2015]. The current state of water shortage is being made worse by the eutrophication of rivers and lakes, dead zones in water bodies, biomagnification of harmful substances, and the continued use of pesticides and other chemicals [Du et al., 2018]. In addition, obstacles to reaching objectives are caused by the carelessness with which wastewater is recycled and by the lack of government regulations or the non-application of those that do exist. The environment, economics, society, and human health and hygiene are all impacted by the scarcity of clean water [Yang et al., 2017]. The WHO said in 2017 that 785 million people still do not have access to clean drinking water, with 144 million of them mostly dependent on surface water. An estimated 8 million people die each year from diarrhoea contracted from tainted drinking water. Additionally, reports indicated that by the end of 2025, the majority of the world will be inherent in "water-stressed" areas [Anderson et al., 2004]. Water pollution can originate from a multitude of sources, including industrial wastes, household, agricultural, and health-related effluents. These sources typically include paints, dyes, oil spills from ships, mining, industrial runoff and metallurgical leaches, pharmaceutical wastes, pesticides, cosmetic wastes, fertilizers, and other materials that contaminate water and make it unfit for human consumption. The whole situation is badly impacted by the continuous increase in trash created by anthropogenic activities and their subsequent discharge into the environment. The development of analytical methods for identifying these substances, even in minute quantities, aids in the elimination of contaminants from water bodies. Pharmaceuticals, Endocrine disruptor chemicals (EDCs), and personal care products (PPCPs) represent an important class of pollutants at low concentrations. In the past, the elimination of medicinal wastes was restricted to avoid unintentional exposure of animals or children. As a result, medications were being disposed of in public trash or washed into sewage systems. Additionally, as a result of the misuse of popular antimicrobial agents like quinolones, the medication and its metabolites are finding their way into all kinds of soils, water bodies, debris, and drainage systems at dangerous levels [Hirsch et al., 1998]. The signs of these pollutants' slow release into the environment started to appear. Numerous pathways for environmental infiltration have been investigated, including the flushing of bodily wastes, the discarding of expired goods, the leaching of chemicals from landfills, the use of agricultural wastes, and chemical runoff. Hignite and Azarnoff examined the findings of numerous metabolites of drugs in sewage treatment facilities (influent and effluent systems), including salicylic acid. Since then, several studies have been conducted on the existence of medicinal products and their byproducts in water, as indicated by the references. Since then,

extremely sensitive analytical methods (ppb and ppt levels) have been developed for the quantitative measurement and identification of pharmaceutical compounds existing in organisms and the environment, eliminating these wastes from the earth. Daughton and Ternes first used the name "PPCPs" to describe this class of compounds, which are found in everyday items, including cosmetics and pharmaceuticals. Among the substances that are classified as PPCPs are butyl acetate, diethanolamine, triclosan, musk xylene, musk ketone, carbamazepine, acetaminophen, and acetylsalicylic acid, among others. Chemicals, whether indirectly or directly, have evolved into an essential component of the goods we consume daily and are, as a result, contributing to the environment in several ways. The removal of environmentally persistent pharmaceutical pollutants (EPPPs) cannot be achieved entirely by wastewater treatment technologies. They may also find their way into aquatic systems through wastewater treatment plant effluent. **Table 1.1** is a list of some of the popular medications that have been discovered in wastewater, along with information on how they affect human health.

Table 1.1: Adverse effects of popular pharmaceuticals present in wastewater.

Pharmaceuticals in wastewater	Adverse effect on humans	Structure of pharmaceuticals
Ofloxacin	Headache, nausea, sleeplessness, and neurological illnesses	
Ibuprofen	Drowsiness, hypertension, and myocardial infarction	
Ranitidine	Lightheadedness, sleeplessness, tremors, irregular heartbeat, and liver failure	

Diclofenac	Headache, feeling dizzy, and fatigue	
Sulfamethoxazole	Anorexia, rashes on the skin, nausea, and vomiting	
Ciprofloxacin	Headache, tremors, tendinitis, and long-term carcinogenicity	
Acetaminophen	Adverse effects on the liver, bronchitis	
Metoprolol	Arrhythmias, hypotension, and bradycardia	

1.2 ENDOCRINE DISRUPTING CHEMICALS (EDCs):

On the other hand, endocrine-disrupting chemicals (EDCs) are a family of substances that mimic hormonal functions and inhibit the normal operation of the endocrine system (Hormone fabrication and management) [Daughton et al., 1999]. These disruptions may result in birth defects, cancerous tumour, developmental disorders such as learning disabilities in children, cognitive child development, severe attention deficit disorder, problems with brain development, deformities in body parts like limbs, cancer (breast, cervical, prostate, thyroid, etc.), problems with human sexual development such as de-feminization of female gonads or de-masculinization of male gonads, etc. Environmental degradation products (EDCs) have entered the ecosystem from natural, man-made, or both sources [Lucaccioni et al., 2020]. The majority of them are pharmaceutical goods, which include dichlorodiphenyltrichloroethane (DDT), polychlorinated biphenyls (PCBs), dioxins and their derivatives, and a few additional insecticides, Di(2-ethylhexyl) phthalate, plasticizers (BisphenolA) and phytoestrogens (derived from plants) [Saggiaro et al., 2019]. In current times, studies have been conducted to examine the cytotoxicity resulting from the photodegradation by-products of 17 β -estradiol, 17 α ethynilestradiol, and Bisphenol A; instances of the suppression of estrogenic activity in cellular cultures have been reported. Metal cans, soaps, detergents, plastic bottles, food items, fire retardants, cosmetics, pesticides, and toys are just a few of the materials that are constantly being introduced into the environment. According to recent studies, there may be a significant risk associated with EDCs throughout the prenatal and early postnatal stages of organ and neural system development (NIEHS) [Dodson et al., 2012]. A summary of several prevalent EDCs and their negative effects may be observed in **Table 1.2**.

Table 1.2: The harmful effects of prevalent EDCs on human health

Origin	Class	Chemical example	Effect
Industry washings and surfactants	Alkylphenols	Nonylphenol	influences pregnancy by mimicking female hormones
Incineration, Leaches	Polychlorinated Compounds	2,3,7,8-Tetrachlorodibenzodioxin	Central nervous system damage, diabetes, effects on the

			immune system, Thyroid disorders
Atmospheric transport /Agricultural runoff	Organochlorine pesticide	DDT, 1,2,3,4,10,10 hexachloro- 1,1,4a,5,8,8a-Hexahydro 1,4:5,8- dimethanonaphthalene	Hepatocarcinogenicity and Neurotoxicity
Industrial effluent	Phthalates	Dibutyl phthalate, Diethyl phthalate	Increases Quantity of damaged DNA in sperm motility, reduces male fertility
Agricultural chemicals	Insecticides	Fipronil	Thyroid Tumors
Municipal effluents	Natural Hormones (Produced naturally by animals)	Estradiol	Ovarian cancer, endometrial cancer, and Breast cancer
via sewage networks and household garbage	Cosmetics, personal products	Methylparaben	interferes with hormone function, raises the risk of reproductive damage, and breast cancer
Pulp mill effluents	Phytoestrogens (found in plant material)	Genistine	Tiredness, rashes, anaphylaxis, itching, and Nausea
Plasticizers in plastic products	Plastics (Bisphenol A)	4,4'-(propane-2,2-diyl) diphenol	Infertility

Contraceptive pills (added through municipal wastes or industrial effluents from the pharmaceutical industry)	Synthetic steroids	Estrone	Abnormal sexual development in teenagers and the functioning of the prostate
---	--------------------	---------	--

1.3 CLASSIFICATION OF ENDOCRINE DISRUPTING CHEMICALS:

Due to the toxic and environmental persistence, triclosan (TCS), nonylphenol (NP), and Bisphenol A (BPA) are three EDCs from the environment that have drawn the most attention. This section provides an overview of these developing contaminants' uses in daily life as well as their harmful impacts on the environment and biological systems. Furthermore, a brief discussion of estrone (E1), a natural oestrogen, is also included.

Bisphenol (A)

Bisphenol A is used in the creation of polycarbonate plastic and epoxy resin, as well as in a variety of packaging for food and beverage materials, dental sealants, and infant bottles [Staples et al., 1998]. Strong endocrine disruptors like BPA can lead to the development of cancer. Despite the knowledge that BPA is dangerous, it is nonetheless frequently utilized. As a result, from 2009 to 2012, the worldwide consumption of BPA increased by 5.5% annually. According to reports, there are three major ways for a person to be exposed to BPA in the environment: by eating, by breathing, and by coming into contact with their skin. Additionally, research has demonstrated that BPA can harm aquatic creatures even in situations with BPA concentrations below 1 mg/L. Due to the possibility that BPA might progressively be released through routine use of infant bottles, children are the major target of public concern over BPA [Flint et al., 2012]. Currently, multiple countries have laws that restrict the usage of Bisphenol A. For instance, China has outlawed the manufacture of infant bottles containing Bisphenol A. In 2008, Canada prohibited the use of polycarbonate plastics in infant bottles that contained BPA. Furthermore, papers limiting the use of BPA have been released by the US, Malaysia, and the EU [Birkett et al., 2002].

Nonylphenol (NP)

Nonylphenol serves as both the primary raw material and end product for the manufacture of NP ethoxylates. Surfactants, including Nonylphenol and its ethoxylates, including NP1EO, are

often utilized in commercial, home, and industrial applications. Personal care items, detergents, pesticides, and goods frequently used in industry, such as defoamers, lubricants, paints, and emulsifiers, are just a few of the everyday items that contain nonylphenol endocrine disruptors. Additionally, NP works in the processing of metal and textiles [Brooke et al., 2005]. Due to their extensive usage, endocrine disruptors such as nonylphenol have entered the environment in increased amounts, increasing human interaction with them. Additionally, the tendency for these compounds to build up has sparked increased worry. According to the UN Environmental Protection Agency, NP is one of 27 essential regulated persistent hazardous pollutants. Environmental NP concentrations are now defined in various nations. The U.S. has taken measures to safeguard aquatic life. According to the EPA's Ambient Water Quality Criteria for NP, freshwater settings must have an acute exposure value of $28\mu\text{g/L}$ and a chronic exposure value of $6.6\mu\text{g/L}$. Furthermore, in seawater, the value of chronic revelation is $1.7\mu\text{g/L}$, while the severe measure is around $7.0\mu\text{g/L}$ [Waltman et al., 2006].

Triclosan

Along with the renowned endocrine-disrupting chemicals, triclosan is a broad-spectrum antibacterial agent, which is typically included in household products, including toothpaste, face cleansers, and soap [D'Ascenzo et al., 2003]. TCS is likewise employed as a preservative. TCS has been discovered to have a possible estrogenic effect and a minimal teratogenic effect. When a TCS-containing product leaks from a drain pipe, the sewage system collects it and transports it to a sewage disposal facility. Afterward, the untreated TCS eventually reaches the aquatic environment and may endanger the life there.

Estrone

In both humans and animals, estrone (E1), a kind of natural oestrogen, is present. The oestrogen activity in wastewater settings is thought to be significantly influenced by E1. In addition, estriol and estradiol are two more naturally occurring oestrogens, with estradiol being the most efficient. The distribution of EDCs in the environment is similar to that of natural oestrogens like E1 and E2, as well as synthetic endocrine disruptors like the ones indicated above (BPA, NP, and TCS). These contaminants have been found in soil, marine water samples, groundwater, surface water, and other ecosystems throughout various countries. According to several investigations, municipal sewage treatment plant (MSTP) effluents and water both contain EDCs [Tan et al., 2007].

2-Chlorophenol (2-CP) is a chlorinated phenol, which is widely used in the industrial sector, in the production of pesticides, and preservation of wood. It is recalcitrant in the environment and has been observed in industrial effluents and groundwater exhibiting toxicity and endocrine-disrupting properties on aquatic life as a result of its structural homology to natural hormones [Diamanti-Kandarakis et al., 2009; Azimi et al., 2022].

One of the most common antibiotic agents, ciprofloxacin (CIP), is a fluoroquinolone and is an emerging pollutant present in wastewater and surface water because of the high rate of its use in medicine and agriculture. It is persistent and not fully eliminated even after wastewater treatment, resulting in residual effects on the environment, affecting microbial communities and possibly endocrine system disruption in aquatic life [Azimi et al., 2022; Li et al., 2023].

The commonly identified pharmaceutical in surface and groundwater is paracetamol (PCM), which is released through excretion by humans and inadequate disposal processes. Even though PCM and its metabolites are not considered a classical endocrine disruptor, they have been shown to exhibit endocrine-related toxicity in laboratory studies, rendering them a significant contaminant of emerging importance in ecotoxicological studies [Agarwal, n.d.; Yusuf et al., 2023].

Ibuprofen is a widely consumed non-steroidal anti-inflammatory drug (NSAID). Although partially metabolized in humans, significant amounts are excreted unchanged. Its persistence in surface and ground waters has been linked to ecotoxic effects, including altered fish physiology and endocrine disruption [Kezzim et al., 2017].

Domestic researchers have ruled out four contaminants whose management in China's urban sewage treatment facilities should be prioritized, three of which are NP, BPA, and E1 in order of the risk to the environment index and oestrogen equivalent. Undoubtedly, in recent years, there has been an increasing attention on endocrine disruptors and natural estrogens with potent endocrine disruption capabilities. However, it is now difficult to analyze and manage every EDC due to the large number of organisms that exist in the environment. The removal effectiveness of current sewage treatment procedures and the current status of EDCs in real sewage should be considered when determining the priority of management.

1.4 SOURCE OF ENDOCRINE DISRUPTING CHEMICALS:

The primary ways that these artificial or natural compounds are exposed to people and animals are through open runoff or wastewater discharges from home and commercial wastewater treatment facilities, hospital and animal waste, leaching at disposal sites, and agro-industrial

effluents, which directly contaminate ground and surface water bodies with EDCs (**Figure 1.1**). The most commonly recorded EDCs in drinking, underground, and wastewater sources are phenolic environmental estrogens (EDEs), which have been linked to detrimental health effects in humans. Examples of these EDCs include OP (octylphenol), BPA, NP (nonylphenol), DES (diethylstilbestrol), and their equivalent ethoxylates [Thacharodi et al., 2023].

Common Sources of EDCs

Drinking Water

Arsenic, perchlorate, and atrazine are three contaminants that can affect drinking water quality and cause endocrine system disruption. One effective way to guard against EDC exposure is to use a high-quality water filtration system in the shower or bath as well as at the tap. Surface water (rivers and lakes) and groundwater are frequently polluted with Endocrine-disrupting chemicals (EDCs) due to septic tanks and treated wastewater, industrial waste, agriculture, oil spills, household items, and airborne fallout. The majority of waste treatment facilities release EDCs into surface water because they do not filter these compounds out of effluent.

Personal Care Products

Endocrine disruptors, such as phthalates, are frequently found in cosmetics, conditioners, shampoos, moisturizers, and other personal care products (PCP). A class of chemicals known as phthalates is responsible for the more feminine traits seen in the males of many species. Phthalates cause genital malformations, testicular cancer, reduced sperm counts, and infertility by interfering with the endocrine systems of wildlife, such as deer, otters, whales, and polar bears. Some toothpaste brands contain triclosan, another chemical that disrupts hormones. Avoiding EDC exposures can be achieved by switching to natural and/or handmade personal care products.

Canned Foods

Despite being proven to be an endocrine disruptor, Bisphenol-A (BPA) is still used by 78 canned food brands, according to an analysis of 252 products. BPA has been connected to several health issues, mostly affecting fetuses, young children, and pregnant women, but also affecting adults. In North America, almost 75% of cans are coated with BPA, so if you eat canned food, you are probably exposed to a lot of BPA. Since BPS, a chemical that is identical to BPA, is frequently used to coat cans, even those labelled as BPA-free are not safe. It is best to purchase goods in glass jars and bottles as opposed to plastic or cans.

Kitchen Products

EDCs can also come from non-stick cookware and plastic containers, which are ubiquitous in many kitchens. The plastic containers may include BPA or other hormone-disrupting substances that can seep into food, particularly when heated. In addition to being hazardous and extremely persistent in the environment, poly- and perfluoroalkyl compounds (PFAS), which are used to provide nonstick, stain-resistant, and water-repellent surfaces, are also harmful to human health. Perfluorooctanoic acid (PFOA) is released by heated non-stick cookware and has been connected to infertility, thyroid disorders, and issues with development and reproduction. Cookware made of ceramic and enameled cast iron is a healthier option because it is long-lasting, simple to clean (even the most stubbornly cooked-on food can be removed with a warm water soak), and entirely inert, meaning it won't emit EDCs.

Conventionally Grown Produce

Endocrine-disrupting chemicals may be applied to vegetables and fruits that are conventionally farmed with herbicides, pesticides, and industrial effluent. Reduce your exposure to EDCs by purchasing and consuming as many organic vegetables and free-range, organic meats as you can.

High-Mercury Fish

Fish that have excessive mercury and other heavy metal contamination pose a threat since these metals may affect the balance of hormones in the body. The most hazardous species include swordfish, shark, marlin, monarch mackerel, and tilefish, although dangerously high levels of mercury and heavy metal contamination have also been identified in tuna. Furthermore, farmed fish dubbed the "CAFOS of the sea" tend to contain more pollutants and should be avoided. Little fish, including anchovies, herring, and sardines, are often higher in omega-3 fats and lower in pollutants when it comes to seafood.

CAFO Meat, Poultry, and Dairy Products

Antibiotics, hormonal substances, and other industrial chemicals are frequently present in animals maintained in concentrated animal feeding operations (CAFOs), which may cause endocrine disruption. Seek out animal products that are produced on small, local farms using organic farming practices, free-range practices, and with no possible EDCs.

Cleaning Products

Potential EDCs can be found in commercial cleaning products used to clean windows, floors, ovens, and toilets. For example, nonylphenol ethoxylates (NPEs), a ubiquitous chemical in all-purpose cleansers and laundry detergents, are known to be a strong endocrine disrupter

that can cause fish to morph into females. NPEs are banned in Europe. Using various mixtures of baking soda, vinegar, coconut oil, and essential oils to make cleaning solutions is surprisingly simple [Ashraf et al., 2019].



Figure 1.1 Different sources of endocrine-disrupting chemicals

1.5 EFFECT OF ENDOCRINE DISRUPTING CHEMICALS:

The principal concern regarding endocrine disruptors lies in the disturbances they may induce in humans or animals by modifying hormonal levels within the body, attributable to their mechanisms of accumulation in both biological tissues and the surrounding environment [Heindel et al., 2015].

1.5.1. EFFECT ON HUMANS:

Endocrine disruptors target several human organs and associated glands, including the pancreas, thymus, adrenal gland, thyroid, parathyroid, hypothalamus, and gonads (testes and ovaries), as **Figure 1.2** reveals.

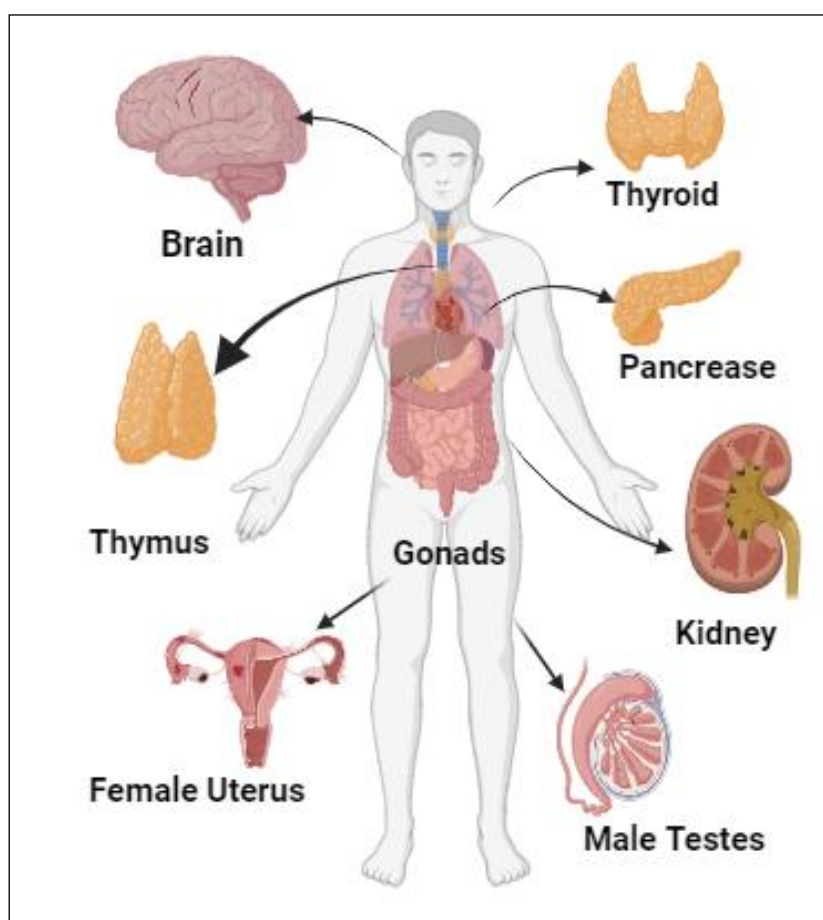


Figure 1.2: Illustration of the primary endocrine glands that Endocrine Disrupting Chemicals target

Even in humans, EDCs have antiandrogenic properties. Additionally, as demonstrated by both in vivo and in vitro tests, they resemble estrogenic activity [Montano et al., 2020]. The reproductive system can serve as a sentinel organ for environmental stressors, as demonstrated by the increased attention being paid to it. Compared to blood, human semen is a valuable source of early indicators for determining the influence of the environment on human health, as confirmed by the most current research and epidemiological data [Montano et al., 2016].

Using very sensitive transactivation experiments using Chinese hamster ovary cells, pesticides were evaluated for their ability to bind to the human androgen receptor (hAR). Out of the 200 pesticides studied, the results revealed that 66 of them had antiandrogenic action. Numerous studies have been conducted in the literature that provide evidence of the hazardous effects of endocrine-disrupting chemicals on the endocrine system as well as their intricate regulatory

mechanisms [Quesada et al., 2002]. Organochlorine pesticides have been used for many years all over the globe. It is well known that they are capable of bioaccumulation in the atmosphere, notably in the food chain, when they eventually make their way into the human body. As a result, they are frequently found in population screenings and are linked to several disorders [Kojima et al., 2004]. Indeed, the 1993–1997 Agricultural Health Study found a cross-sectional connection between OCP use and the risk of hyperthyroidism and hypothyroidism in female partners (n = 16,529) in North Carolina and Iowa, United States of America. Breast milk residues of various OCPs, including hexachlorocyclohexanes, were shown to be substantially correlated with intake of cow milk and beef, as well as menstrual features, in Taiwan. Additionally, a connection was found between β - and γ -hexachlorocyclohexanes and the reproductive disorders that plague Taiwanese women, suggesting that dietary practices may have an impact on exposure to these EDCs [Martyniuk et al., 2020]. Significant correlations were found between thyroid dysfunctions like hyperthyroidism and hypothyroidism, and the usage of the fungicides benomyl, OCPs chlordane, and herbicides paraquat and maneb/mancozeb. These findings point to a possible synergistic interaction between fungicides and organochlorines in the pathogenesis of thyroid disorders in women. Numerous epidemiological studies have examined the potential link between exposure to the herbicide glyphosate (which is widely used) and elevated risk of unfavourable birth defects and reproductive outcomes in the offspring. These studies have demonstrated that women who are exposed to glyphosate are more likely to experience spontaneous abortions and a reduction in fecundability. Additionally, this revelation throughout pregnancy is linked to higher testosterone levels in the female, longer anogenital distances in both sexes, and an array of abnormalities in the reproductive and developmental parameters of the offspring, including fetal skeletal retardation [Goldner et al., 2010]. Some EDCs, including phthalates, have been linked to reproductive harm in both animals and humans. A large number of these compounds are anti-androgenic, and they can lead to male reproductive issues like infertility. Due to their greater susceptibility to exposure, even throughout prenatal life, they are more harmful to little children. In Mexican male newborns, there was a statistically significant and adverse correlation found between exposure to Phthalates (including monobutyl, monobenzyl phthalates, and monoethyl) and anogenital distance, penis breadth, and length [Muñoz et al., 2021]. When it comes to human health, Bisphenol A poses several risks, particularly for women. Even at extremely low doses, Bisphenol A can serve as a reproductive toxic substance and disrupt fertility due to its estrogenic action, binding to α - and β -estrogen receptors. Recent research [Bustamante-Montes et al. 2008] has confirmed the presence of Bisphenol A in all

infertile women diagnosed with polycystic ovarian syndrome. Furthermore, recent studies [Calaf et al., 2021] indicate that endocrine disruptors also impact the balance of energy metabolism. These substances can negatively affect adipose tissue by increasing the size and number of fat cells and altering their endocrine regulation and adipocytokine production. This can lead to disruptions in hunger and satiety regulation and a decrease in the basal metabolic rate. Early life exposure to these substances, known as "obesogens," heightens the risk of these harmful health effects as well as a tendency to acquire weight even when food and exercise are balanced appropriately [Street et al., 2018]. The diencephalic system serves as a representative target for hormone-disrupting substances. EDCs may imitate the effects of neurotransmitters in addition to their association with endocrine receptors, which might change how the central nervous system functions normally. Furthermore, some EDCs have an impact on the pathophysiology of diabetes, such as Bisphenol A, polychlorinated biphenyls, phthalates, and organochlorine pesticides. Variations in exposure to these compounds may also be a factor in racial/ethnic and economic inequalities [Gore et al., 2010]. Multiple studies have revealed an association between exposure to endocrine disruptors and various conditions such as attention-deficit hyperactivity disorder, communication problems, intellectual impairment, global developmental delay, autism spectrum disorder, etc. Specifically, it is indicated that a number of EDCs, including Bisphenol A, hexachlorobenzene, and polybrominated diphenyl ethers, provide a significant risk for the development of neurodevelopmental disorders [Sargis et al., 2019]. In addition, early development exposure to endocrine-disrupting substances generated from plastic (such as dibutyl phthalate, Bisphenols, and bis (2-ethylhexyl) phthalate) may modify the development of the embryo and placenta, thereby affecting the result of a pregnancy [Basak et al., 2020]. Indeed, exposure to EDCs during early development, that is, when hormones are regulated by cell modifications to generate tissues and organs, can have far more harmful consequences. Lower dosages of EDCs than those needed for effects in adults during a tissue's developmental programming may cause alterations in tissue development that may not be noticeable at birth but may manifest later in life. Long-term research is still required to fully understand the impact of these detrimental effects on postnatal health and fetal development. Regulatory toxicology generally considers EDC concentrations to be dangerous, although aquatic environments often contain lower quantities of these substances. However, low concentrations of these specific compounds may be harmful. These factors suggest that, to more fully assess the consequences for human health, studies on the effects of prolonged exposure to low concentrations of EDCs should be conducted.

1.5.2. EFFECT ON ANIMALS:

EDCs are thought to be responsible for several wildlife issues, including the sex changes in shellfish and fish, the decrease of some species (such as the potential rise in sterility in American alligators), and other issues [Hayes et al., 2011]. Indeed, several pesticides (including chlorogenic, thiocarbamates, imidazoles, triazines, and triazoles) have been shown to have an antiandrogenic effect. This is evidenced by the alterations in observations of sexual characteristics in aquatic animals at a macroscopic level, especially those exposed to fungicides and herbicides: demasculinization in fish and rats, frogs' manufacture of hermaphroditism and estrogens, and various progressive abnormalities in alligators of male gonads [Grilo et al., 2017]. For instance, research on *Daphnia Magna* has demonstrated that endosulfan sulfate interferes with the juvenile hormone activity (which controls the gender ratio) and ecdysteroidal system (which controls processes like embryonic development and molting) of crustaceans [Guillette Jr et al., 1994; Palma et al., 2009]. Numerous studies have demonstrated that EDCs, even at extremely small doses (parts per trillion and ppb), can have negative effects on animals, including gene repression and activation [Vom Saal et al., 2016]. Bosveld reported on how organohalogens impact hormone metabolism, reproductive outcomes, and steroid concentrations in fish-eating birds. Research has shown that exposure to PCBs and PBDEs can lead to thyroid abnormalities and reproductive failure in various animals, including seals, fish, whales, and others [Lemaire et al., 2004]. According to certain studies conducted on the brains of zebra fish, diethylhexyl phthalate, especially at very low concentrations (0.02 mg/L), may cause an adverse modulation of appetite stimuli in the organism. This was additionally confirmed through real-time quantitative reverse transcription PCR analysis of key molecules associated with appetite regulation. Furthermore, estrogenic feedback can be changed by pesticides like dichlorodiphenyltrichloroethane (DDT) because they block receptors, preventing hormone action and their function [Combarnous et al., 2017]. Pesticide interactions with wildlife's hormonal (endocrine) systems have frequently resulted in reduced fertility and a slow reduction in the population of several species. It influences the endocrine system in various ways, such as causing feminization and demasculinization of male vertebrate gonads, affecting the neurohormones released from the eyestalk of the crab *Neohelice granulata* that regulate ovarian development, and inducing long-term histofunctional alterations in the thyroid gland of the crocodilian species *Caiman latirostris* during embryonic growth [Galoppo et al., 2020]. Various animals have exhibited signs of endocrine disruption from pesticides and their metabolites, like dialkyl phosphates [Yang et al., 2019]. Hormonal imbalances affecting homeostasis were observed in the hypothalamus-pituitary-thyroid axis in zebrafish, the

hypothalamus-pituitary-gonad axis in rats, and the hypothalamus-pituitary-adrenal axis in rats. [Wu et al., 2018]. The aforementioned effects have been documented in animals (such as rats) that are either utilized as human models or are likely to be visible to EDCs. The majority of them have something to do with sexual dysfunctions that may be detrimental to the survival of animal species.

1.6 MECHANISM OF ACTION OF ENDOCRINE DISRUPTIVE CHEMICALS:

Endocrine-disrupting chemicals have the potential to directly or indirectly affect the endocrine system. To disrupt the hormonal balance, estrogen receptors (ERs), androgen receptors (ARs), progesterone receptors, retinoid receptors, insulin receptors (IR), thyroid receptors (TRs) are among the nuclear hormone receptors that EDCs directly act as an antagonist on [Diamanti-Kandarakis et al., 2009]. The binding of EDCs on hormone receptors resulted in either activation or inhibition of the downstream biological route in target cells (**Figure 1.3**). EDCs have the potential to negatively impact endogenous hormone control through the binding or stimulation of hormone receptors, modification of hormone concentrations, or alteration of the turnover of hormone-binding receptors. EDCs have nine different ways of acting on the endocrine system (**Figure 1.4**).

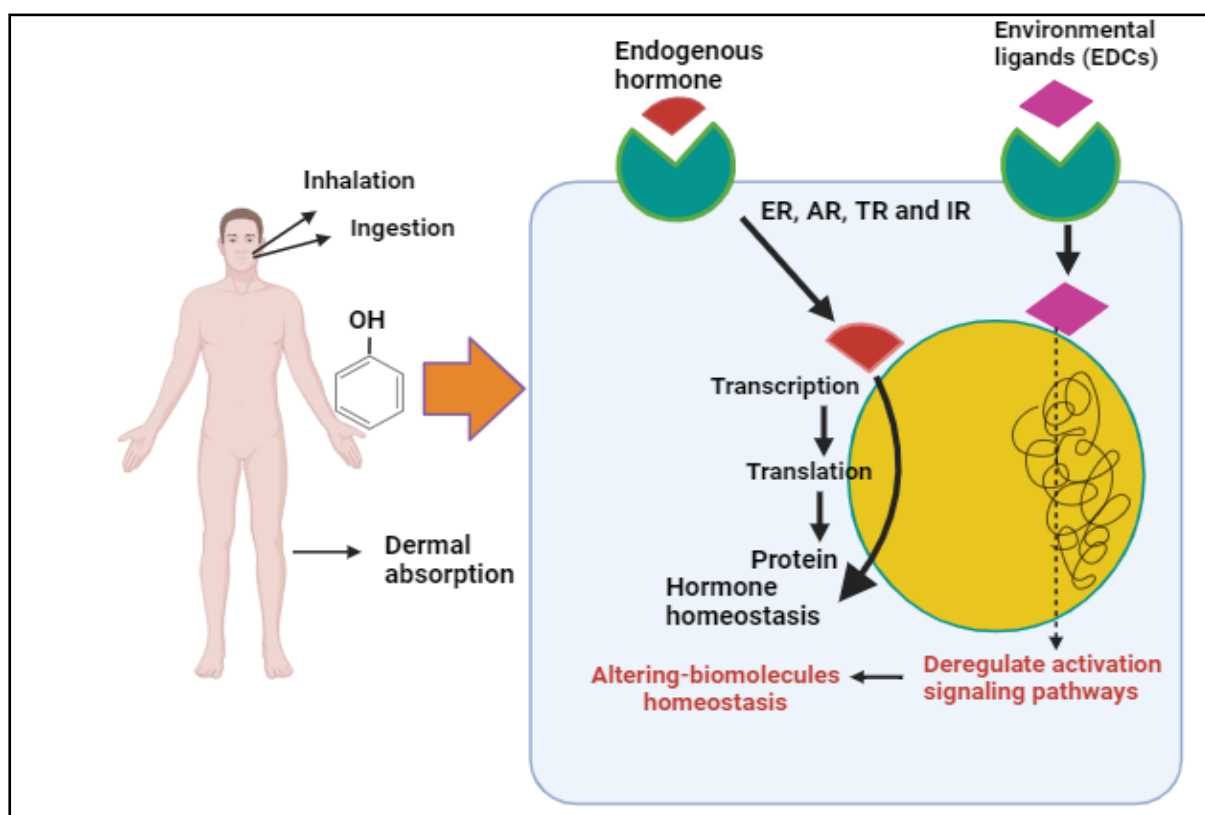


Figure 1.3 Endocrine Disrupting Chemicals exposure in humans and its molecular effects

Negative impacts on human health could result from EDCs activating or binding hormone receptors inappropriately. During the developing stage, some of the aforementioned endocrine-disrupting chemicals incorrectly stimulate the estrogen receptor, leading to infertility in both sexes [Golub et al. 2004]. Dichlorodiphenyltrichloroethane (DDT) binds to estrogen receptors alpha ($ER\alpha$) and beta ($ER\beta$), affecting their transcriptional activation and cell proliferation. DDT also enhances the synthesis of cAMP by binding to GPCRs and the receptors for the hormone that stimulates growth [Mazur et al., 2015]. EDCs suppress or block the natural hormone by acting as receptor antagonists. Additionally, DDT prevents androgen from binding to the androgen receptor (AR), which further stops humans from experiencing androgen-dependent AR transactivation. The number of receptors and the way hormones behaved in specific circumstances dictated the concentrations of each hormone. Endocrine-disrupting chemicals (EDCs) influence the expression, degradation, and internalization of hormone receptors. Di (2-ethylhexyl) phthalate inhibited the expression of the aldosterone receptor. Conversely, the production of testosterone was positively modulated by the aldosterone receptor [Wadzinski et al., 2014].

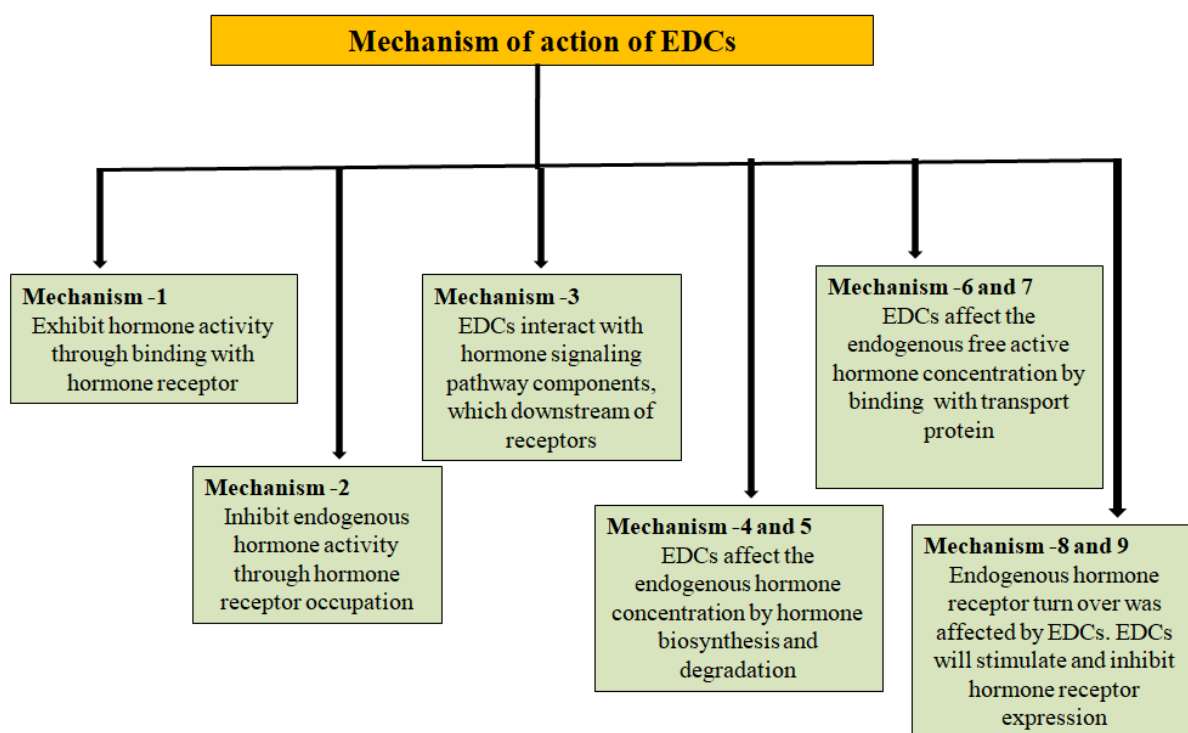


Figure 1.4 Mechanisms of action of endocrine-disrupting chemicals

Hormone binding to a receptor and target cell characteristics specific to a particular tissue set off an intracellular reaction. EDCs have the ability to modify the transmission of signals via intracellular and membrane hormone receptors. Nuclear steroid hormone receptors and cell surface membrane receptors are the two types of receptors that fall under these categories. Hormones alter the epigenetic process, which affects differentiation and development [Gore et al., 2015]. The EDCs inhibited these cascade activities. Pesticides like methoxychlor also enhanced the expression of important essential enzymes.

It is the nature of hormones (steroid hormones) to passively travel through membranes; they include progestogens, estrogens, androgens, and adrenal steroids. EDCs interfered with these hormones' ability to travel. BPA at a modest dose inhibited the entry of calcium into pancreatic β -cells. According to the composition of the hormones, the transport protein (serum protein) usually carries the hormones [Walker et al., 2016; Zhang et al., 2016]. They have the option of binding with or without the conjugative protein. In these situations, the hormones are dislodged from their transport protein by EDCs, resulting in hormones that are not as effective in the target tissue [Zhou et al., 2013].

Furthermore, proteases break down hormones, rendering them inactive. EDC also influenced this mechanism, resulting in different amounts of hormones depending on how well hormones were cleared or degraded. Hormones maintained tissue shape through cellular differentiation and proliferation. The EDCs changed the stable cell counts in endocrine organs by either encouraging or disturbing cell numbers. Well-known EDCs, polychlorinated biphenyls (PCBs), have the potential to disrupt thyroid hormone communication and result in aberrant endocrine organ morphology [Bansal et al., 2008; Sangeetha et al., 2021].

Major objectives of the present Thesis

In this thesis, semiconductor-based nanocomposite materials are synthesized by the sol-gel and Microwave method for photocatalytic degradation of endocrine-disrupting chemicals. This thesis focuses on the synthesis and characterization analysis of semiconductor–perovskite-based nanocomposite materials such as CuS, CdS, MoS₂, Cs₃Bi₂Br₉, CdS/Cs₃Bi₂Br₉, MoS₂/Cs₃Bi₂Br₉, and MoS₂/CdS for the degradation of various endocrine-disrupting chemicals. This thesis is divided into 5 chapters, which are as follows:

Chapter –1 Introduction:

The introduction of EDCs and their effects on the environment and humans are covered in this unit. Additionally, sources, classification, and mechanisms of endocrine-disrupting chemicals are also discussed.

Chapter 2 Review of literature:

This chapter offers a comprehensive overview and an understandable explanation of the elimination of EDCs from effluent through photocatalysis. In addition, the best procedures are also explained in this chapter. This chapter concluded with a more thorough explanation of the goal and scope of the present research topic.

Chapter 3 Materials and Methods:

This unit focuses on material, methods, and techniques. It also explains materials, analysis, and instruments for the synthesis of a photocatalyst.

Chapters – 4, 5, 6, and 7 Results and Discussion: results and discussion are focused in this chapter. CuS, CdS, MoS₂, Cs₃Bi₂Br₉ nanoparticles and their composites were synthesized by Sol-Gel and Microwave methods. As prepared pure and novel composites were confirmed and analyzed by FTIR, XRD, UV-Vis, and FE-SEM/EDX. Pure nanoparticles show less degradation efficiency as compared to nanocomposites in the visible region.

Chapter 8 Conclusions:

This chapter summarizes the results and draws attention to the key conclusions covered in the previous chapters.

CHAPTER 2

REVIEW OF LITERATURE

EDCs are hazardous environmental pollutants that can significantly impact human health by interfering with the endocrine system, even at relatively low exposure levels. Researchers have looked into using catalysts based on nanomaterials to effectively absorb pollutants, absorb visible light, produce and consume electrons and holes, and prevent their recombination in order to achieve improved performance. Several nanocomposites were used for the degradation of different Endocrine Disrupting Chemicals.

2.1. An overview of Endocrine Disruptive Chemicals

Numerous contaminants of emergent concern (CECs) have been released into the environment worldwide as a result of human activity. This category includes many chemicals found in the water cycle that was not earlier known to exist, and thus not currently under agency regulation, and frequently manifests at extremely low percentage levels [Patel et al., 2020; Richardson et al., 2018; Guarino et al., 2020; Ricciardi et al., 2021]. Contaminants of emerging concern (CECs) encompass a wide range of organic and inorganic compounds that can impact both human health and ecosystems. This group includes industrial chemicals, natural toxins, endocrine-disrupting substances, disinfection byproducts, brominated flame retardants (BFRs) [Fiorentino et al., 2017], as well as lifestyle-related compounds such as caffeine, artificial sweeteners, pharmaceuticals, pesticides, and PPCPs [Bilal et al., 2019; Kasonga et al., 2021; Proto et al., 2014; Pironti et al., 2020].

Among them are xenobiotics known as endocrine-disruptive compounds (EDCs) sometimes known as Endocrine Disrupting Chemicals or basically endocrine disruptors. They are mostly found in produced items such as plastic containers, toothpaste, cleanses, children's toys, polyvinyl chloride pipes, and cosmetics [Flint et al., 2012]. By binding endocrine receptors to body, these substances can inhibit, activate or modify the body's natural processes of synthesizing and degrading hormones. These processes happen through a variety of methods, which can cause an aberrant or "false" absence of hormone indicators that can either boost or decrease normal endocrine activity [Zoeller et al., 2012]. Colborn coined the term endocrine disruptor in 1991 [Sharma et al., 2009]. It was later defined as an exogenous substance or mixture that alters functions of the endocrine system and consequently causes adverse health effects in an intact organism, or its progeny, or (sub) populations by the WHO in 2002 and 2012 and UNEP (United Nations Environment Programme). An endocrine disruptor chemical

is an external substance that can potentially cause endocrine disruption in an organism or its offspring. [Colborn et al., 1993].

The endocrine disruptors that are most often researched include polychlorinated biphenyls, pesticides, phthalates, Bisphenols, and both natural and synthetic hormones [Yilmaz et al., 2020]. These compounds can be detected in water using chemical analytical techniques such as gas chromatography, high-performance liquid chromatography with mass spectroscopy, and biological techniques like biosensors. They are typically found in the environment in the range of nanograms to micrograms per litre (ng/L and µg/L) [Caliman et al., 2009; Tijani et al., 2016]. Herbicides like glyphosate and chlorotriazine (CTs), as well as organophosphorus and organochlorine pesticides (OCPs), are frequently used pesticides that function as EDCs. Atrazine, a widely used herbicide, has been detected in surface and subsurface water globally, along with other banned endocrine-disrupting chemicals (EDCs) [Groger et al., 2020]. The use of synthetic pesticides in agriculture harms the environment, human health, and resources, despite boosting food production. Bisphenol A, found in plastics and hygiene products, is a common EDC that mimics estrogen and is used in women's health products and to accelerate the growth of livestock [Yang et al., 2020; Wan et al., 2021].

The World Health Organization emphasized in 2013 that control measures for human and environmental exposure to these substances are necessary since exposure to them poses a risk to both humans and wildlife [Bergman et al., 2013].

Not all chemicals are classified as EDC, according to the jurisdictions. Therefore, evaluating a chemical's inherent danger is a crucial step in calculating exposures to compounds with EDC characteristics. To verify the available proof of its identity, regulatory bodies employ a variety of techniques. Researchers have identified key criteria, including latency from exposure age at exposure, the significance of mixtures, epigenetic and untraditional response dynamics, and transgenerational impacts, to better understand the effects of endocrine-disrupting chemicals (EDCs). Furthermore, endocrinologists have proposed that these EDCs have very high lipid solubility and low water solubility, which causes them to bioaccumulate in adipose tissue [Mukherjee et al., 2021].

2.2. EDCs consumption and production:

The growing global population is driving up demand for fresh water. In the modern world, it is considered a luxury to use water just once. Sustainable reuse from non-traditional sources, such as municipal wastewater, is both technically and financially possible [Basile et al., 2011].

Both humans and the aquatic ecosystem are negatively impacted by the manufactured contamination of the water. Every year, a large number of innovative and expensive pharmaceutical treatments are introduced onto the market for both the prevention and treatment of illnesses or other bodily dysfunctions in people and other animals, especially farm animals, as a result of the world's population growth and medical advancements. Due to the high demand for various medications for both human and animal usage, the pharmaceutical industry is expanding quickly. As per Grand View Research (2020), the pharmaceutical manufacturing industry had a global value of around USD 324.42 billion in 2019. Pharmaceutical drug factory effluents have been shown to have high levels of pharmaceuticals, which vary from 90 to 31,000lg/L [Larsson et al., 2007]. In Putrajaya, Malaysia, pharmaceuticals with concentrations ranging from 0.14 to 0.32ng/L have been found in tap water. Controlling the discharge of various medications into the environment from all of these sources needs further focus [Praveena et al., 2021].

India's economy has expanded rapidly in recent years, with a total GDP of US\$3.12 trillion in the year 2021–2022, but at a significant environmental cost. Numerous environmental and social issues, such as increasing depletion of natural resources, greenhouse gas emissions, and an increase in the amount of several manufactured chemical substances in the water resources and atmosphere, have been brought on by India's rapid economic transition, rapid industrialization (especially of the country's chemical industry), and urbanization. Over the past twenty years, India's yearly cost of damage from pollution and natural calamities has increased from \$14 to \$80 billion, or about 6% of GDP. Despite only taking into account a small portion of EDCs and related health effects, estimates of the burden and disease cost of EDCs in the US and the EU reached up to \$340 million and €163 million, respectively. For India, no comparable computations have been performed. Nonetheless, incomplete information on EDC concentrations in Indian environmental and human samples indicates that the pressure from these pollutants is comparable to that in the US and Europe. Furthermore, India is expected to be particularly vulnerable to the severe social and health effects of EDCs due to the country's high rate of poverty, hunger, illiteracy, poor living circumstances, and restricted access to healthcare for a sizable portion of the population [Sharma et al., 2023].

Data on priority EDCs (such as lindane, polychlorinated biphenyls (PCBs), dichlorodiphenyltrichloroethane (DDT), etc. revealed higher amounts in the Indian environment and people when compared to other countries, particularly growing economies like China [Sharma et al., 2014]. According to a recent global investigation conducted by WHO

and UNEP, Indian women and newborns are among the highest exposed to some EDCs (namely, DDT) in breast milk [Bornman et al., 2017]. In another investigation, phenolic EDCs such as Bisphenol-A (BPA), triclosan, and parabens were found in quantities similar to those found in populations from industrialized nations like Spain and Japan, with a focus on pregnant mothers and their offspring from Southern India [Dutta et al., 2015; Xue et al., 2015].

India is home to around 18% of the world's population and has a fast-evolving socioeconomic environment. Industrially processed food and intensive food production systems are gradually replacing traditional agricultural and traditionally prepared food. In India, there is a dearth of comprehensive data on human exposure to major EDCs and environmental pollution. The POP-related findings that are now available have continuously shown excessive contamination levels in Indian environmental matrices and human populations. Only a small number of researchers have yet have identify EDC concentrations in Indian food baskets, providing a groundbreaking but incomplete picture of dietary exposure. There have never been any systematic evaluations of the health effects and exposure to numerous important EDCs (such as PBDEs) in India. There have never been any systematic evaluations of the health effects and exposure to numerous important EDCs (such as PBDEs) in India [Sharma et al., 2021].

While a lot of study is done in India on the dispersion of pesticide residues in various environmental matrices, less focus is placed on how these residues are distributed in aquatic environments. No comprehensive research was conducted to investigate the dispersion of pesticide residues in the aquatic ecosystem, despite Vasai's significance, as shown by the previously published work [Singare et al., 2016]. As of now, it is difficult to pinpoint the precise causes of EDC exposure because they are diverse and differ greatly globally. However, as certain EDCs were outlawed decades ago and others more recently, the situation varies greatly throughout nations. As a result, individuals such as migrants offer an approach for studying exposure start and/or cessation based on initial and novel environments [Mukherjee et al., 2021]. Nonetheless, scientists are debating whether or not drinking water kept in plastic containers poses a risk. Scientists are paying attention to the problem of effluents contaminating the water in these containers. Research has indicated that water from plastic bottles contains several pollutants, including antimony, Bisphenol A, and phthalates.

In Kerala, boiling water before using it and transferring it to bottles before it cools down entirely are common practices. As a result, lukewarm water may be filled in plastic bottles. The

issue of effluents from plastic water bottles that are used to transport hot water has not yet been investigated [Geetha et al., 2021].

2.3. Removal methods for EDCs from wastewater

The main advantage of wastewater and current water treatment methods is the decrease in the concentration of endocrine disruptors. These technologies include chemical coagulation, activated sludge, adsorption, precipitation, membrane, and flocculation processes as depicted in **Figure 2.1**. To minimize the health risks of these substances, even at low concentrations (below the LoAEL), sophisticated procedures must remove them completely from waterways. A variety of procedures can be used as treatment technologies to achieve different removal efficiencies because of the endocrine disruptors' varied physicochemical qualities. For the elimination of EDCs, phthalates, parabens, alkyl phenols, pharmaceuticals, primarily Bisphenol A, natural and synthetic estrogens, a variety of techniques, including adsorption, membrane filtration, biosorption, biodegradation, and advanced oxidation, have been researched as viable methods of treatment [Okonkwo et al., 2007; Artham et al., 2012; Vieira et al., 2020].

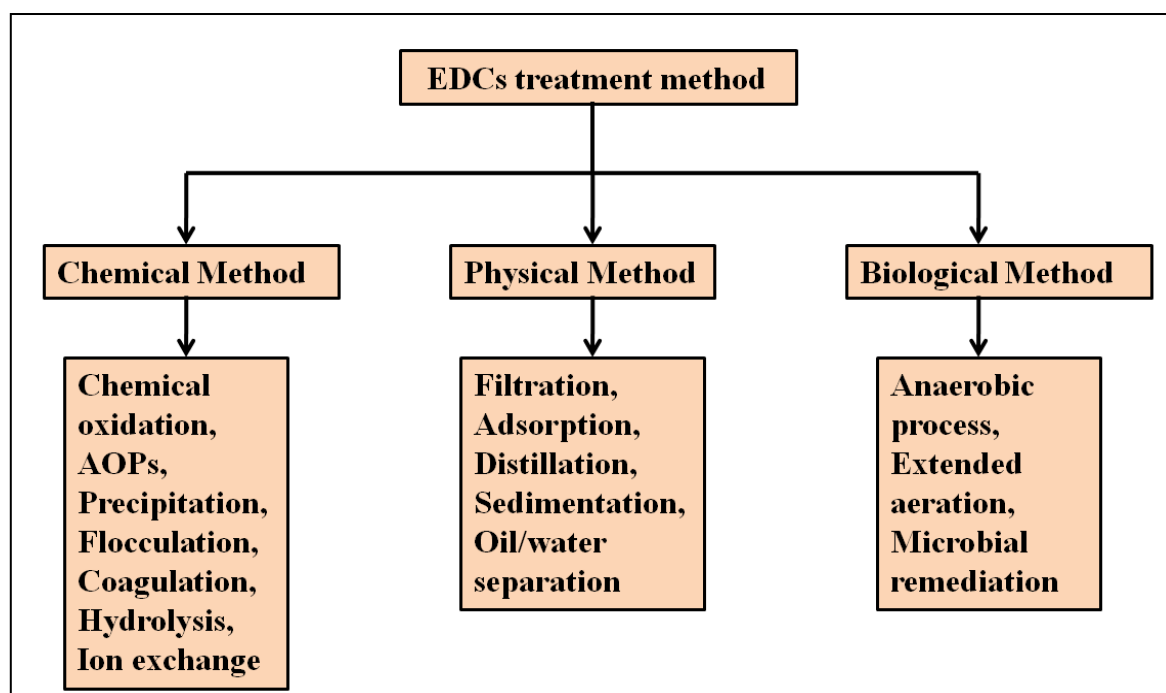


Figure 2.1 Various techniques used for the degradation of endocrine-disrupting chemicals

Adsorption is a commonly used method for removing EDCs from water due to its high efficiency, low operating costs, and minimal byproduct formation. To enhance the sustainability of this process, various compounds like carbon nanotubes have been studied

[Djebri et al., 2017], clays [Goyal et al., 2016], zeolites [Zhang et al., 2013], Biochars, bioadsorbents, metal-organic frameworks [Maia et al., 2019], graphene oxide [de Souza et al., 2018], and industrial waste have been investigated as novel non-conventional adsorbents, serving as a cost-effective alternative to activated carbon. Since bioadsorbents are plentiful, they can be viewed as cost-effective and environmentally friendly substitutes for carbon-based adsorbents, which are often utilized in this context. Although the biosorption technique is simple to use, affordable, requires little energy, and produces safe byproducts, it has been widely employed in the treatment of industrial wastewater and drinking water [Coelho et al., 2020]. Biosorbents, which are often more selective than traditional adsorbents, are most commonly used and include fungus, bacteria, yeast, algae, wood, chitosan, agricultural wastes, and biopolymers. A sulfonated derivative of coffee waste (CW-SO₃H) has been proposed as an effective biosorbent for removing BPA from water [Sahu et al., 2019]. CW-SO₃H has a biosorption capacity of 270 mg/g for BPA, which is five times higher than activated carbon. Additionally, activated carbon derived from residual bean biomass has shown promise in sequestering ibuprofen from water, with a maximum adsorptive capacity of 50.00 mg/g at pH 4.75 and 50°C [Crini et al., 2019].

However, membrane filtering techniques (ultrafiltration, microfiltration, reverse osmosis, and nanofiltration) use the unique physicochemical properties of the material from which the membrane is produced to effectively reject a broad range of endocrine disruptors [Ahsan et al. 2018]. A combination of ultrafiltration with advanced technologies such as ozonation, chlorination, and sophisticated oxidation processes can increase the effectiveness of ultrafiltration. Si et al. combined ultrafiltration and ozonation to eradicate up to 99% of EDCs (Bisphenol A, estriol, 17 β -estradiol, and 17 α -ethynylestradiol), compared to 46% and 70% removal rates with ozonation or ultrafiltration alone. Membrane bioreactors are commonly paired with reverse osmosis or nanofiltration to improve pollutant removal of substances like carbamazepine, Alkylphenols, and Bisphenol A [Rodriguez-Narvaez et al., 2017].

The removal of endocrine disruptors also commonly involves the use of biological processes (both anaerobic and aerobic), such as fungal bioreactors, anaerobic digester systems, and activated sludge treatment [Si et al., 2018]. These processes are especially useful when combined with other tertiary treatments to increase their efficacy. Different enzymatic processes, such as accumulation and adsorption, allow bacteria, fungi, and microalgae to digest EDCs more effectively in mixed populations than in individual microorganisms [Kamaz et al., 2019]. In this regard, nonylphenol (NP) may be eliminated from contaminated aquatic

environments by marine microalgae species such as *N. oculata*, *P. globosa*, *P. subcordiformis*, and *D. salina* via biodegradation, biotransformation, or biosorption, with removal efficiencies ranging from 43% to 91% [Schmidt et al., 2017; Hu et al., 2002]. White rot fungi produce extracellular ligninolytic enzymes that can effectively degrade endocrine-disrupting chemicals such as nonylphenol and Bisphenol A in wastewater. Removal efficiencies range from 60–100% for BPA and 65–90% for NP, depending on the specific fungus, incubation period, and initial pollutant concentration [Roccuzzo et al., 2021]. Due to their extremely active enzymatic systems, fungi had the greatest results when it came to biologically removing EDCs from water. In the literature, many investigations on advanced oxidation processes (AOPs)—ozonation, Fenton, UV/peroxide, and photocatalysis are established. Typically, these studies are combined to yield superior outcomes. For instance, the combination of ozone–UV is more effective than ozone alone at removing EDCs from water, such as Bisphenol A, 17 β -estradiol, and estriol. On the other hand, chlorine oxidant yields many byproducts without lowering the estrogenic impacts of EDCs. In addition to lowering toxicity from 73% to 30%, the Fenton procedure combined with biological treatment employing an up-flow anaerobic wastewater blanket reactor demonstrated a 99% initial EE2 elimination (1000 μ g/L of these chemicals were injected in the samples daily) [Grelska et al., 2020]. The use of EDC therapies depends on the different quantities and complexity of EDC chemicals; thus, proper and reliable methods for collecting, determining, extracting, quantifying, storing, and preserving must be followed [Varma et al., 2020]. The properties of each EDC pollutant may be taken into account while choosing the best removal strategy; in certain situations, separate treatment approaches are required for distinct EDC contaminants. In actuality, the membrane filtering procedure is a successful means of eliminating EDC without the need for further treatment. However, the membrane filtrations are not able to eliminate emerging contaminants as much as other EDC treatment techniques. However, there are green alternatives to employing waste items, thus even if the process necessitates the regeneration or disposal of the sorbent, adsorption may be a useful procedure with a broad range of dependability and low cost. Additionally, a range of 95% to 100% was demonstrated using the photo-Fenton technique for the removal of phenolic, PPCP, pesticide, and medicinal compounds [Kohantorabi et al., 2019; Hu et al., 2018]. However, these procedures were limited by the unsuitability of iron ion regeneration and the need to treat wastewater to fulfill discharge regulations for iron concentrations. Thus, the application of the treatment procedures from the degrading pathways and the byproducts created was impacted by the overall factor of limits and obstacles in endocrine-disrupting compounds treatment systems, such as hydrophilicity, solubility, polarity, and degradation.

Table 2.1 compares the most popular approaches for removing EDC from water, taking into account the types of EDC and the sources of the water. It also highlights the benefits and limitations of each treatment, offering a possible future for EDC treatment approaches in the treatment of wastewater and water systems.

Table 2.1: Comparing the methods used in wastewater and water systems for the removal and treatment of endocrine disruptors.

Strategies for Removal	EDC type/water source	Advantages	Constraints
Biological process	<ul style="list-style-type: none"> – Estrogenic compounds: EE2, E2, 17α-acetate, pentachlorophenol, 4tert-octylphenol, triclosan; – Water and wastewater: no hazardous chemicals 	<ul style="list-style-type: none"> -High biodegradation up to 90% —no byproducts —cheap prices 	<ul style="list-style-type: none"> - Efficiency linked to many enzymatic processes - Time spent incubating – Sample preparation as the starting pollutant concentration
Membrane filtration	<ul style="list-style-type: none"> -Wastewater -Rising chemicals, include triclosan, NP, E1, E2, EE2, BPA, PPCPs, and 17β-estradiol-17-acetate 	<ul style="list-style-type: none"> -Broad range of activities -Ultrafiltration techniques capable of eliminating a significant amount of all endocrine disruptors 	<ul style="list-style-type: none"> -Expensive –Byproduct of toxic waste –Concentrates (brine) are mostly released into surface water –Post treatments –Difficulties in treating and releasing the pollutants accumulated throughout the process
Adsorption	<ul style="list-style-type: none"> - Pesticides, naproxen, triclosan, ibuprofen, trimethoprim, 	<ul style="list-style-type: none"> - Excellent effectiveness – Minimal operating 	Regeneration or disposal of the sorbent

	acebutolol, ketoprofen, diltiazem, and diazepam are present in drinking water and wastewater.	and maintenance expenses – No waste products – Simple to use – Low energy use	– Utilizing unconventional adsorbents improves – Sufficient dose and contact duration impact the performance - Low propranolol and carbamazepine elimination
Advanced oxidation processes	– Water and wastewater – Antibiotics (including amoxicillin, ciprofloxacin, sulfamethazine, and sulfathiazole), nonylphenol decaethoxylate, carbamazepine, hormones, phenolic, pesticide, PPCPs, and pharmaceutical chemicals	Broad range of effectiveness Elimination of up to 80% of EDC chemicals – Enhanced level of sensitivity	Exorbitant expenses– Active substance regeneration– Water after treatment– Byproducts

We need to develop advanced, environmentally friendly technologies that can reduce or eliminate contaminants and provide clean alternatives. Alternatively, a long-term fix for the issue should exist.

2.4. Role of Nanomaterials and nanotechnology for remediation of Endocrine-disrupting chemicals

Water is a vital but limited resource, with only 1% of it usable by humans. Over 1.1 billion people lack access to clean drinking water due to factors like population growth and

environmental issues. Contaminants in fresh water supplies pose a major challenge. Conventional treatment methods need to be more effective in addressing new pollutants and meeting water quality standards. Current wastewater treatment methods have drawbacks such as high energy consumption and inadequate pollutant removal [Ferroudj et al., 2013].

Enhancing the amount and uniformity of water can be done more affordably and consistently with the use of nanotechnology. This technological area is anticipated to see an increase in industrial and commercial uses for lowering energy consumption and production costs, as well as improving quality and environmental controls. Successful uses of nanomaterials have been documented in several domains in the past, such as catalysis and medical research. Researchers have recently observed that nanomaterials are a superior method of treating wastewater because of their unique properties, which include large surface area, nanoscale, solid, mobility solution, highly reactive, strong mechanical properties, hydrophilicity, porosity characteristics, and dispersibility [Patil et al., 2016]. Several nanomaterials have been effectively used to remove hazardous bacteria and toxic elements, including Mo, Pb, and other inorganic and organic contaminants [Mohammad et al., 2019]. Due to their distinctive chemical and structural characteristics, nanoparticles have sped up research on the knowledge-based economy.

Significant technical advancements, such as the ability to arrange particles into distinct nano-shapes with sizes of less than 100 nanometers, are the source of all of this knowledge [Goh et al., 2016]. Since nanotechnology has the potential to be employed in a wide range of sectors, it is successful in wastewater treatment and a wide range of industrial processes. Due to the ability to regulate and modify materials at the nanoscale or dwarf size, this kind of technology presents a feasible option for improved wastewater treatment. Several studies have discovered that due to their special characteristics (such as their massive surface area) and distinctive properties (like reactivity, transferable atomicity, and low size-specific surface energy), nanocatalysts are effective at purifying alternative water sources. These characteristics may aid in the advancement of nanotechnology for the efficient removal of contaminants from drinking water and enhanced methods for treating wastewater [Jain et al., 2013].

Various government and commercial sector endeavors have been initiated to promote the worldwide advancement of nanotechnology development, with a focus on Japan, China, the United States, and Germany. Presently, a multitude of experts are doing diverse tests and

investigations about the application of nanotechnology in the purification of water and wastewater [Appelbaum et al., 2016].

Researchers are paying close attention to nano-catalysts, particularly those made of inorganic materials like metal oxides and semiconductors, for use in wastewater treatment. For the purpose of treating wastewater, a variety of nano-catalysts are used, including Fenton-based catalysts, photocatalysts, and electrocatalysts, which enhance the chemical oxidation of organic pollutants and have antibacterial properties [Anjum et al., 2019].

The photocatalytic reaction is an environmentally friendly method of treating waste that breaks down pollutants in water when it is exposed to light and the right catalyst. It is defined as the shift in the rate at which a chemical reaction is initiated under the appropriate ultraviolet, visible, and infrared light energy, depending on the catalyst's band [Khan et al., 2013]. This energy produces an electron-hole pair (e^-/h^+), which in turn produces highly reactive reducing and/or oxidizing radicals on the conduction and valence bands, respectively. These radicals react with organic or inorganic pollutants in contaminated water, degrading them through a secondary reaction. Because of their large band gap and visible region, semiconductor nanoparticles are a good catalyst for treating wastewater [Tahir et al., 2022].

2.5. Photocatalysis

In the 1970s, Fujishima discovered photocatalysis, which became known as the Honda-Fujishima Effect [Coronado et al., 2013]. They described the photolysis of water using a single crystal of titanium dioxide (TiO_2) exposed to UV light and subjected to a slight electrical bias using a platinum counter electrode. Their finding is a significant advancement in the study of photo-induced redox reactions on TiO_2 photocatalysts through solar energy conversion. Subsequently, there was a surge in interest in photocatalysis using semiconductors for the production of solar fuel as well as other photocatalytic reactions, including the degradation of organic contaminants [Chimmikuttanda et al., 2022].

Photocatalysis is a chemical reaction in which a material is activated by light to change the pace of a chemical reaction without the substance being involved. The use of a catalyst to change a chemical reaction while light is present is known as photocatalysis. As the catalyst is light-active, it is also referred to as a photocatalyst. This addresses the process of photosensitization, in which a chemical composition changes as a result of light being absorbed by the photosensitizer; however, it does not cover the process of electromagnetic radiation accelerating a heat reaction [Fujishima et al., 1972]. One of two methods exists for the

photocatalyst to quicken the photoreaction: it can interact with the reaction's byproducts or it can interact with the substrate in its excited or original state. Hazardous organic molecules can be mineralized into carbon dioxide, water, and basic mineral acids through photocatalytic reactions. Photocatalysis reactions can be classified into two categories: 1) Heterogeneous Photocatalysis and 2) Homogeneous Photocatalysis.

2.5.1. Heterogeneous photocatalysis

The last four decades have seen a remarkable expansion of the science of heterogeneous photocatalysis, with several advancements, particularly in the areas of energy and the environment. It is the photoreaction's acceleration when a photocatalyst is introduced. The catalyst and the reactants in a heterogeneous catalysis reaction are in distinct phases. Heterogeneous photocatalysis encompasses a wide range of reactions, such as the partial or complete oxidation of organic pollutants, dehydrogenation, and hydrogen transfer, Isotopic exchange of $^{18}\text{O}_2$ - $^{16}\text{O}_2$, deuterium-alkane, water purification, elimination of gaseous pollutants, metal deposition, and more [Linsebigler et al., 1995].

2.5.2. Homogeneous Photocatalysis

Homogeneous photocatalysis occurs when the photocatalysts and reactants are present in the same phase. Photo-Fenton systems (Fe^+ and $\text{Fe}^+/\text{H}_2\text{O}_2$) and Ozone are the two homogeneous photocatalysts that are most frequently utilized. Although it wasn't utilized extensively because of certain restrictions, this photodegradation technology was also one of the most popular in advanced oxidation processes. Though it wasn't utilized extensively because of certain restrictions, this photodegradation technology was also one of the most popular in advanced oxidation processes. Homogeneous photocatalysis employing the Photo-Fenton and ferrioxalate reagents was successful in breaking down and mineralizing imidacloprid, a systemic chloronicotinoid insecticide [He et al., 2021].

2.6. Advanced oxidation process

Advanced oxidation processes (AOPs) are an eco-friendly method of eliminating nearly all kinds of pollutants, including insecticides, dyes, pesticides, volatile organic compounds (VOCs), air and water pollutants, aromatics, petroleum-based materials, petroleum hydrocarbons, and chlorinated hydrocarbons. AOPs have a brief lifespan since they are reliant on the production of reactive oxygen species, such as hydroxyl radicals containing a single unpaired electron [Glaze et al., 1987]. This species may be manufactured from water utilizing energy sources like solar, electrical, or acoustic energy, or it can be made by simple chemicals

like ozone, H_2O_2 , or other molecules with or without the aid of a suitable catalyst. The only difference is in the method by which the hydroxyl radicals are created. As a result, they interact aggressively and quickly with a variety of chemical species that would be exceedingly challenging to break down otherwise. Since oxidation products, including carbon dioxide, water, and biodegradable organics, are produced by AOPs, they are relatively superior to other traditional techniques [Kurian et al., 2015]. AOPs involve the photocatalysis process, which is crucial to a photocatalyst's ability to capture sunlight. Subsequently, in the presence of various solar spectrum ranges, these photocatalysts have been successfully employed to address issues pertaining to environmental pollution and energy shortages.

Heavy metals like arsenic and chromium may be removed from municipal wastewater using AOPs. Pathogens and pharmaceutical residues can also be removed, and hazardous effluents from sources like hospitals and slaughterhouses can be treated using AOPs. Examples of industrial effluent treatment include agrochemical, distillery, paper and pulp, oilfield, textile, and metal-plating wastes [Wols et al., 2012]. AOPs may be divided into various groups according to the mechanism that produces the transient hydroxyl radical, as shown in **Figure 2.2**.

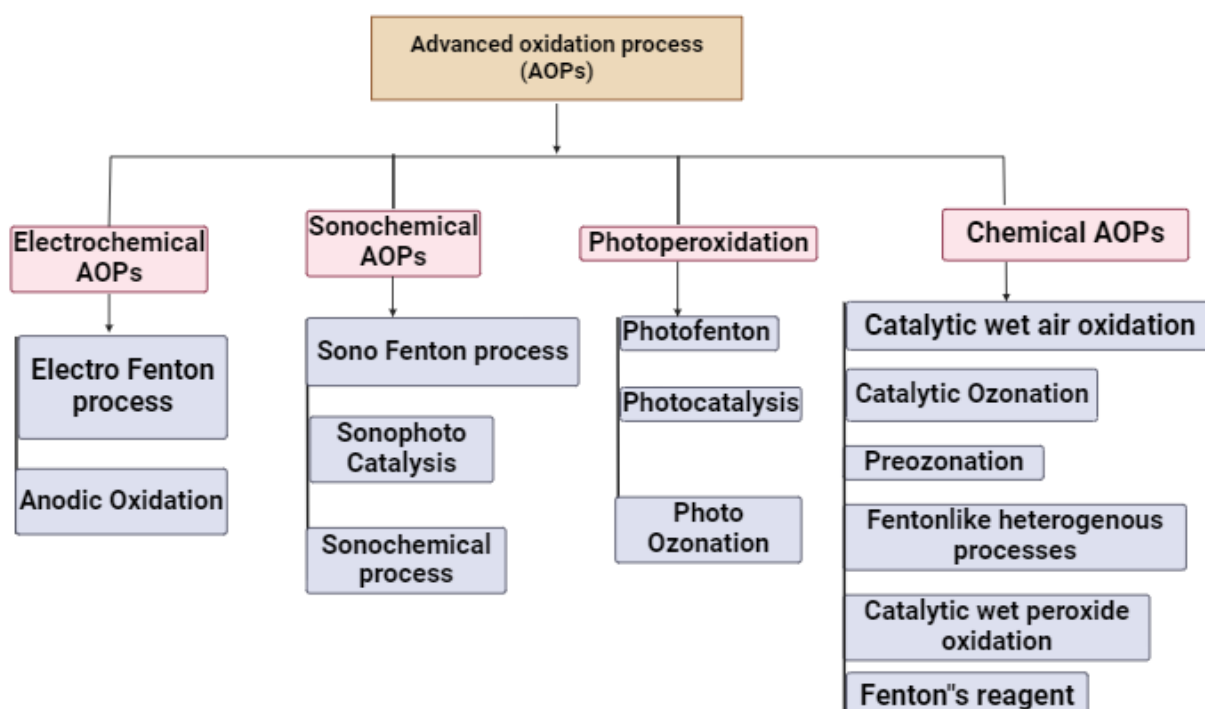


Figure 2.2 Representatives of advanced oxidation process (AOP)

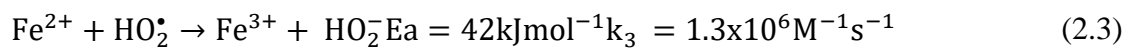
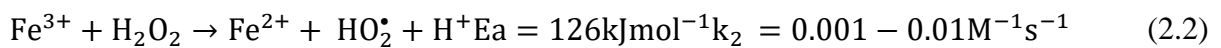
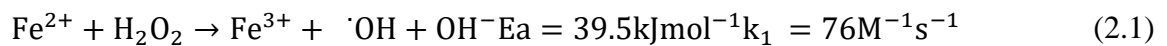
In AOPs, both homogeneous and heterogeneous catalysts have proven effective. Heterogeneous systems have several benefits over homogeneous ones. These advantages include the ability to tolerate harsh working conditions, the ease with which the catalyst may be separated for reuse from the treated water, and the absence of further treatment for the removal of dissolved metals [Nair et al., 2017]. Furthermore, the heterogeneous system works well throughout a wider pH range, which includes the typical pH range of 2 to 9 for natural water and wastewater. Catalysts that are stable, effective, and active are essential for decomposing contaminants in AOPs.

2.6.1. Advanced chemical oxidation processes

In chemical AOPs, the transient species are created using combinations of chemical reagents. The most common type of oxide is H₂O₂; however, ozone and air are also occasionally employed.

Fenton's reagent (Fe²⁺/H₂O₂)

An essential type of chemical AOPs is the Fenton technique, which uses a solution of a soluble iron (II) salt and H₂O₂, sometimes referred to as Fenton's reagent, to break down and eliminate contaminants. The technique was first developed by Fenton, who published groundbreaking research on the oxidation and destruction of tartaric acid using a combination of H₂O₂ and Fe²⁺ [Fenton et al. 1894]. **Equations 2.1 to 2.5** describe the chain mechanism and complex radical that governs the catalytic breakdown of hydrogen peroxide by iron salts [Nogueira et al., 2007].



It should be mentioned that while a specific H₂O₂ concentration promotes the highest rate of OH oxidizing species generation, an increase in H₂O₂ concentration over an ideal value leads to higher rates of reaction 2 and other parasite processes. For example, H₂O₂ and ·OH combine to generate HO₂·, which has a reduced oxidation potential and reduces the effectiveness of pollutant breakdown [Rodríguez et al., 2016]. Numerous pollutants have been thoroughly studied in the homogeneous Fenton process, including pesticides, organic compounds such as

chlorophenoxy herbicides, actual effluent water, etc. The Fenton method is advantageous for treating water and wastewater since it requires no energy input and operates in a straightforward, flexible manner. Its chemicals are also reasonably priced. The application of this technology for in situ environmental remediation is, however, limited by significant limitations such as acidification to pH 2-4 before treatment, neutralization following treatment, and deposit of ferric hydroxide sludge after treatment.

Heterogeneous Fenton process (Fenton-like reactions)

The homogeneous Fenton process has several apparent drawbacks, which have led to extensive research on heterogeneous solid catalysts for Fenton-like reactions across a broad pH range [Bae et al., 2016]. Under such conditions, H_2O_2 is converted to hydroxyl radicals by the Fe (III) species that is trapped inside the catalyst's pores or structure **Figure 2.3**. This technique stops iron ions from leaching into water and causing iron hydroxide to precipitate. Moreover, the process offers the benefits of sustained activity spanning several operations and simple spent catalyst recovery and separation. A variety of nanomaterials have been tried, with notable outcomes due to their high porosity and surface area, which enhance the OH radical generation. Recently, a family of heterogeneous Fenton reactions known as Fenton-like reactions employing nano-zero valent iron (NZVI) has been identified. As demonstrated in **Equation 2.6**, oxidation of NZVI offers an alternate method of generating Fenton reagent in situ.

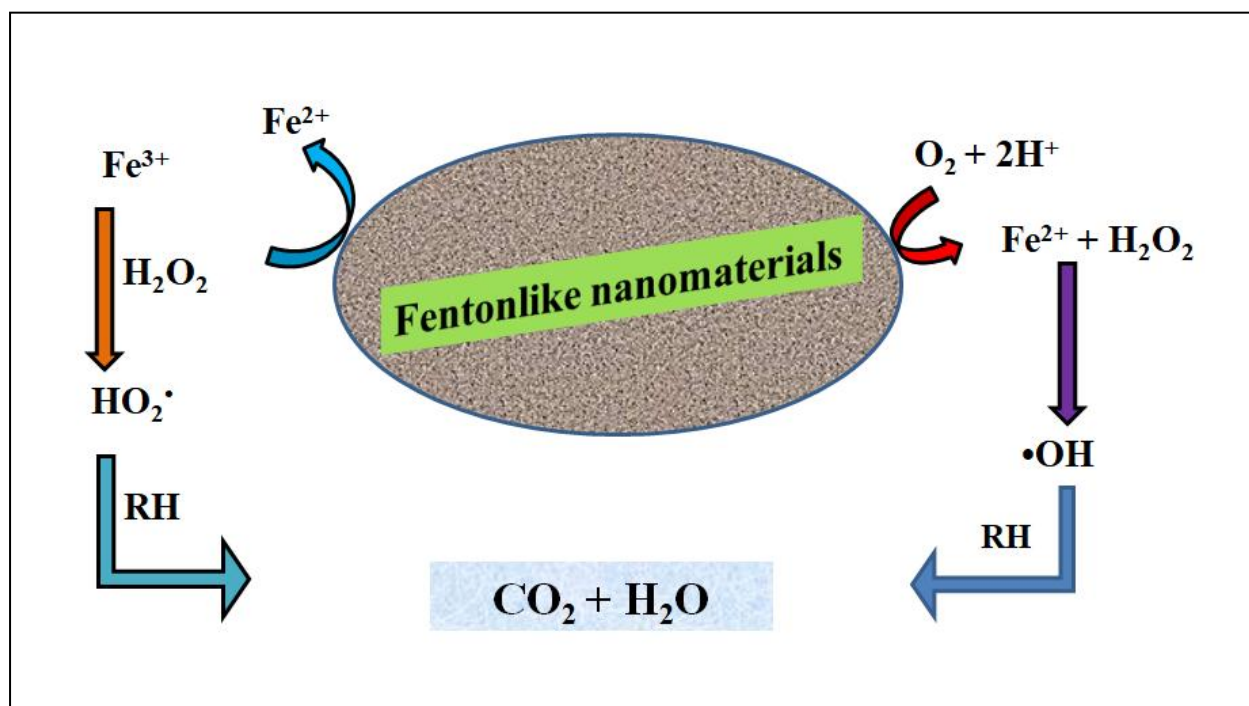
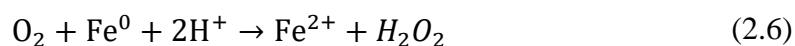


Figure 2.3 Illustration of the process by which Fenton-like nanomaterials break down organic compounds. The reactive free radicals that break down harmful contaminants are produced by the $\text{Fe}^{2+}/\text{Fe}^{3+}$ redox pair.



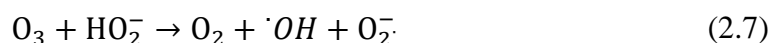
Materials such as clays, chitosan, and polygorskite composites are typically used to support NZVI. It has also been shown that several types of carbon, including activated carbon, doped graphene oxide, mesoporous carbon, and biochar, may serve as supports. When combined with metals like Cu or metal oxides like Ceria, NZVI nanoparticles function as effective catalysts for the breakdown of the targeted contaminants.

Catalytic wet peroxide oxidation ($\text{H}_2\text{O}_2/\text{catalyst}$)

To produce the transitory oxidant species from water, Fenton-like systems operate in a heterogeneous manner using the $\text{Fe}^{2+}/\text{Fe}^{3+}$ redox pair. Similarly, OH can be produced via standard Fenton-like routes from H_2O_2 when elements with different valences, like nickel, chromium, cobalt, cerium, gold, vanadium, copper, etc, are present. To release hydroxyl free radicals from H_2O_2 , a variety of iron-free nanomaterials have been employed as heterogeneous catalysts [Ribeiro et al., 2017]. There have also been new reports on catalysts based on carbon-containing materials, such as graphitic nanocomposites, carbon nanotubes, and magnetic carbon nanocomposites. These materials, despite their neutral pH, promote the production of hydroxyl radicals from hydrogen peroxide by means of many processes unique to the catalysts employed and their specific composition.

Perozonation ($\text{O}_3/\text{H}_2\text{O}_2$)

Equation (2.7) describes the rapid process that produces hydroxyl radicals when ozone (O_3) and H_2O_2 come together to form perozonation [Van Geluwe et al., 2009].

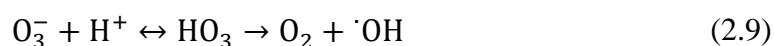


Potable waters can be disinfected using the perozonation technique because of its benefits, which include bactericidal activity and ease of use. At H_2O_2 to ozone ratios between 0.2 and 3.0, H_2O_2 is supplied as an aqueous solution. The poor solubility of ozone in water and its susceptibility to several parameters, such as pH, temperature, type of micropollutants, and side reactions, restricts the effectiveness of this approach. It has been shown recently that

nanoparticles operate as active catalysts during the peroxidation process. Perozonation has made use of inexpensive metal slags such as Cu-S, Fe-S, Cd-S, Zn-S, and Pb-S, iron slag, and zerovalent iron.

Catalytic ozonation (ozone/catalyst)

Ozone has a strong oxidation capacity, which makes it useful in water treatment technology. However, because it requires complex equipment and has high operating costs, its usage in wastewater is restricted. Additionally, ozone reacts selectively with organic contaminants. To increase ozonation's reactivity with various organic contaminants under kinder circumstances and lower costs, heterogeneous catalysts can be employed. Both homogeneous and heterogeneous processes are possible, depending on whether active metal species break down ozone or build a complex between the organic component and the catalyst. **Equations (2.8) and (2.9)** describe how O₃ and organics chemisorb onto the surface of the catalyst in a heterogeneous manner, starting a chain of redox reactions that create the active oxidizing species.



The type and surface characteristics of the catalyst, as well as the pH at which the process is operating, determine the process's efficiency. Numerous nanomaterials, including Fe₃O₄/multi-walled carbon nanotubes, Co₃O₄, NiFe₂O₄, Fe₃O₄, MgO, and Mn/γ-Al₂O₃, have been tried and tested as catalysts with differing degrees of effectiveness [Wang et al., 2016].

Wet Air Oxidation catalyst (O₂/catalyst)

To treat wastewater contaminated by non-biodegradable substances, Wet Air Oxidation uses molecular oxygen as an oxidizing agent. To fully degrade pollutants, the indirect technique of generating hydroxyl radicals, or active oxygen species, needs high pressure (20–200 bars) and temperature (473–593 K). This approach is frequently utilized to address effluents characterized by elevated organic content (COD between 10 and 100 g/L) that are not amenable to direct biological treatment. The procedure deconstructs intricate compounds into simpler, more manageable molecules before their discharge, as demonstrated in **Equations (2.10–2.12)**. Typically, with residence times of 15 to 120 minutes, the efficiency of COD removal ranges from 75% to 90%.



A major limitation of the WAO process is its inability to completely mineralize organic compounds, as certain low molecular weight oxygenated byproducts, such as methanol, acetaldehyde, and acetic and propionic acids, are impervious to further degradation into carbon dioxide. Additionally, the majority of organic nitrogen molecules are converted to ammonia, which is likewise stable under WAO working conditions. Since wastewaters need further treatment, usually in a traditional biological treatment facility, the wet air oxidation process is regarded as a pretreatment step. Several nanomaterials have been treated using catalytic wet air oxidation (CWAO), which aims to lower the operating temperature and pressure and, in turn, lower the treatment process's total cost. Examples include carbon-based catalysts, ruthenium, manganese, cobalt, and nickel, as well as Pt/TiO₂-CeO₂, Ru/nitrogen-doped carbon nanofibers, (Ce-Fe) O₂ mixed oxides, and Cu/clays [Lai et al., 2019].

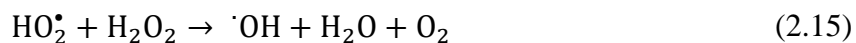
2.6.2. Photochemical advanced oxidation processes

Photochemical AOPs utilize light energy to generate transient reactive species. Compared to chemical AOPs, they are generally considered simpler, more cost-effective, environmentally friendly, and more efficient processes. They are also capable of disinfecting water. Therefore, strong oxidants like O₃ and H₂O₂, as well as catalysts like Fe³⁺ or TiO₂, have been linked to UV radiation. The degradation of pollutants can be achieved by three different reactions facilitated by these photochemical processes: photooxidation in the presence of H₂O₂, photodecomposition in the presence of O₃, and oxidation via photocatalysis.

Photo peroxidation (H₂O₂/UV)

At wavelengths between 200 and 300 nm, absorbed UV light has the ability to photolyze hydrogen peroxide [Chong et al., 2010]. **Equations 2.13-2.19** provide specifics on the sequence of events that result from the homolytic fission of the O-O bond of the H₂O₂ molecule, which produces OH radicals.

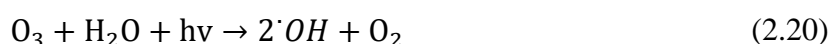




Since UV light may form the free radicals HO_2^\bullet and $\cdot\text{OH}$, the reaction rate is higher in alkaline media with a pH of more than 10. However, the UV area has a very low molar absorption coefficient for H_2O_2 ; therefore, high quantities of hydrogen peroxide are required for the effective destruction of target contaminants.

Photo ozonation (O_3/UV)

In aqueous solution, ozone exhibits a molar absorption coefficient of $3600 \text{ L mol}^{-1} \text{ cm}^{-1}$, enabling it to absorb UV radiation in the range of 200 to 360 nm, with a peak at 253.7 nm. At this wavelength, the ϵ_{max} of O_3 ($18.6 \text{ L mol}^{-1} \text{ cm}^{-1}$) is higher than that of H_2O_2 , indicating that ozone photolysis is a more efficient process compared to H_2O_2 photolysis. According to **Equations 2.20–2.23**, which outline a series of competitive steps, the photolysis of ozone in water generates OH radicals, potent oxidizing agents with higher reactivity [Ruppert et al., 1994].



Recently, heterogeneous catalysts for the photoozonation process have been tested using ZnO and TiO_2 nanoparticles, with intriguing outcomes. Further study may be done on the application of heterogeneous catalysts in the photo-ozonation process since these materials were proven to be effective catalysts in producing the oxidant species in the presence of photons.

Heterogeneous photocatalysis

In a photo-electrochemical solar cell, water may be divided into hydrogen and oxygen using titanium dioxide (TiO_2), a photo-excited semiconductor, as shown by Fujishima and Honda in 1972. Since then, several modifications to this method have been put forth, which have resulted in the creation of a new AOP technology based on semiconductor photocatalysis for a variety of energy and environmental applications [Fujishima et al., 1972].

A valence band electron is driven to the conduction band when a semiconductor is exposed to light with an ultraviolet band-gap energy ($h\nu > E_g$), creating a photogenerated hole (h^+) in the valence band. When pollution is photocatalytically degraded in wet circumstances, e^-/h^+ couples can migrate to the semiconductor's surface and engage in redox processes involving hydroxyl radical ($\cdot\text{OH}$), h^+ , and superoxide ion radical (O_2^\cdot) (**Figure 2.4**). As an oxidant whose capacity is dictated by the oxidation conditions and catalyst employed, photogenerated h^+ is also thought to be capable of directly destroying organic contaminants. In order to achieve optimal efficiency, it is essential to have specialized scavengers present to decrease the charge recombination rates, since the photo-induced electrons may readily recombine with h^+ in the absence of electron or hole scavengers. **Equations 2.24 to 2.29** use TiO_2 as the model photocatalyst and provide the sequence of subsequent reactions.

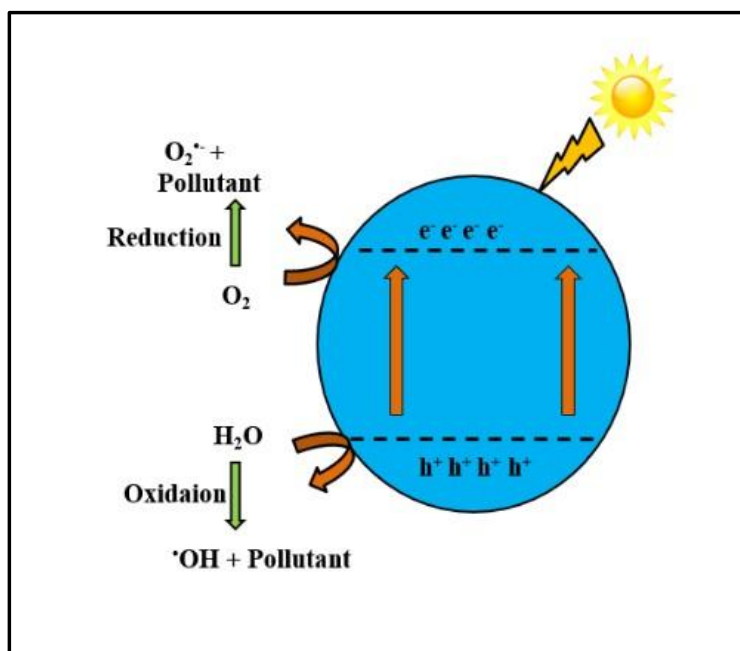
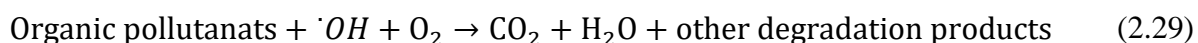
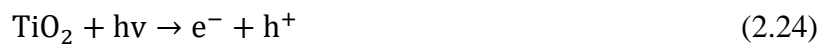


Figure 2.4 The overall process of photocatalysis. Toxic organics completely degrade due to the hydroxyl radicals and superoxide anions generated by electron-hole pairs

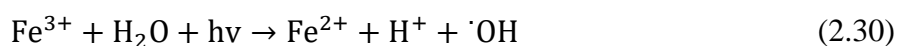


In the case of photodegradation processes, titania-based photocatalysis has moved into the nanoscale realm. Additionally, titanium nanoparticles have been employed in conjunction with other substances as graphene oxide, carbon nanotubes, zeolites, magnetic nanoparticles, UVLED, Au–TiO₂/SiO₂, mp-MXene/TiO_{2-x} nanodots, etc.

Apart from titania-based semiconductors, a wide range of semiconductors have been studied for photocatalytic destruction of contaminants. These materials show a titania-like process wherein holes and electrons develop first, and then free radicals are produced. The second most extensively researched photocatalyst is zinc oxide, which has been used in combination with other nanomaterials, including FeNi₃@SiO₂@ZnO, ZnO/CdSe, and ZnO/graphene oxide/nanocellulose, as well as for the photoassisted destruction of target pollutants. Additional semiconductors that are often utilized are g-C₃N₄/Bi₂O₂CO₃/CoFe₂O₄, ZnS, Ag@Mn_xO_y, SnO₂, MnCo₂O₄, NiO, bismuth oxychloride, and CdS nanoparticles.

Photo-Fenton/Fenton-like systems

Equation 2.30 shows how the photo-assisted Fenton reaction, which was covered in section 2.6.1, may be used to increase the production of OH radicals by catalyzing the reduction of Fe³⁺ to Fe²⁺ [Arana et al., 2001].



The pace at which contaminants are destroyed is greatly influenced by the UV radiation's wavelength and intensity. Despite having a comparatively better efficiency than the conventional Fenton process, the photo Fenton approach has certain intrinsic disadvantages, such as sedimentation after treatment, reduced pH, and the need to collect wasted homogeneous catalyst, among other things. Heterogeneous Fenton systems incorporating a variety of nanomaterials have been developed. Various iron-containing nanomaterials, including Fe/ZSM-5 zeolite, Fe/Ferric hydroxide, iron oxide, NZVI, Fe₂O₃/kaolin, FeO (OH)/reduced graphene oxide, LaFeO₃, and Fe-supported bentonite, have been employed as photo-Fenton catalysts. A growing number of reports have been made on ferrite-based nanostructures, including nickel ferrite; SnMgNd substituted M-hexaferrite, MoS₂/MnFe₂O₄, graphite carbon covering hollow CuFe₂O₄, and DNSA@chitosan@ MnFe₂O₄. Various heterogeneous photo Fentonlike systems have been experimented with varied degrees of success using Fentonlike catalysts such as pillared clays, Mg/Ce ferrite perovskites, Ag/AgCl/ferrihydrite, and Bi₂WO₆.

Microwave assisted advanced oxidation processes

owing to its benefits such as a shorter reaction time and a high degrading efficiency and the advancement of scale-up microwave reactors, microwave-induced oxidation (MW-induced oxidation) has drawn interest as an Advanced Oxidation Process in recent years.

Since microwave energy can be hotspot produced to manufacture more radicals and can be selectively absorbed by a catalyst, microwave irradiation may significantly improve pollutant degradation. Furthermore, the non-thermal impact of the MW raises the rotational and vibrational energy levels of the pollutant molecules, boosting their activity [Verma et al., 2018]. The problem, therefore, is in creating appropriate materials for microwave absorption when radiation interaction such as polarization or hot spots causes heating and non-heating effects, resulting in the production of reactive oxygen species and/or electron-hole pairs. The surface area of the catalyst is a key factor in determining catalytic activity in microwave-assisted AOPs since H_2O_2 is mostly activated there. Consequently, a great deal of nanoparticles has been created recently to enhance catalytic performance. Examples of these are MnO_2 , $\text{CeO}_2/\text{Co}_3\text{O}_4$, $\text{Cu}/\text{Cu}_2\text{O}/\text{CuO}$, $\text{Mn}_2\text{O}_3/\text{AC}$, $\text{LaFe}_{0.5}\text{M}_{0.5}\text{O}_3$ -carbon aerogel, $\text{Bi}_2\text{O}_2\text{CO}_3$, NiFe_2O_4 /natural mineral, Fe_3O_4 , and CuO_x/GAC .

Sonochemical advanced oxidation processes

Wastewater can be purified using ultrasound waves by a physical (direct) method or a chemical (indirect) method. High frequencies of sound are produced by the chemical process, which involves the homolytic fission of oxygen and water molecules to produce $\cdot\text{O}$, $\cdot\text{HO}_2$, and $\cdot\text{OH}$ radicals. The physical mechanism is the production of expanding and contracting bubbles that generate powerful breaking forces at pressures of around 2000 atmos and temperatures of approximately 5000°C (**Figure 2.5**). As demonstrated by **Equations 2.31 and 2.32**, sonolysis of water molecules results in the production of reactive radicals that can react with organic chemical species existing in the aqueous media or destroy organic contaminants via pyrolysis.



Figure 2.5 Illustration of an indirect sonolysis concept. After going through several cycles of growth and collapse, the bubbles create powerful breaking forces at very high pressures and temperatures, which cause the sonolysis of water molecules and the production of reactive radicals.

Due to the enhanced production of OH radicals, the combination of ultrasonic irradiation and Fenton (sono Fenton process) and photocatalysis and ultrasonic irradiation (sonophotocatalysis) has a noticeable impact on the degradation ratio of organic contaminants. It has been found that sonophotocatalysis improves the ratio of hazardous chemical material breakdown. Target pollutants' Fenton degradation and photodegradation have been demonstrated to benefit from the combined action of ultrasound and other treatments [Reddy et al., 2016].

2.7. Mechanism of photocatalysis

UV light generates a redox environment in the aqueous solution and activates a semiconductor photocatalyst in the photocatalytic process. In addition to their electronic structure, which is made up of an empty conduction band and a filled valence band, semiconductors serve as sensitizers for light-induced redox reactions [Hoffman et al., 1995]. The term bandgap refers to the energy difference between the conduction band and the valence band. For a semiconductor photocatalyst to generate excited-state conduction band electrons and positive holes in the valence band, it absorbs photons with energies that are equal to or exceed its bandgap or threshold energy (E_g), thereby promoting electrons from the valence band to the conduction band. To use these charge carriers for redox processes involving adsorbed species, it is necessary to efficiently avoid their recombination. The charge carriers may follow distinct routes to dissipate the input energy as heat. They may recombine non-radiatively or radiatively, or they may become trapped in shallow or deep traps (ST or DT). Ultimately, they have the ability to react with electron acceptors or donors that are deposited on the photocatalyst's surfaces. Indeed, Serpone et al. have demonstrated that trapped holes and electrons are the source of every photoredox reaction that takes place at the surface of a particle [Serpone et al., 2006].

Semiconductors absorb light with energy equal to or greater than the bandgap energy (E_g), which results in the promotion of an electron from the valence to the conduction band. This results in the development of an electronic vacancy or hole (h^+) at the valence band edge. It is also possible to identify this hole as a chemical substance. This hole may lead to further initiate chemical reactions, interfacial electron transfer, or facilitate the diffusion of surface-bound OH^- ions into the bulk solvent or adsorbate. Typically, the hole is in the valence band edge, and the photogenerated electron is in the conduction band edge. If the energies of the electron and the hole are not equal, electron-hole recombination may not be sufficient to deactivate the catalyst. Semiconductors, in contrast to metals, do not have a continuous chain of interband states to

promote electron-hole pair recombination [Saravanan et al., 2017]. This guarantees a lifetime of electron-hole pairs that is long enough for these species to engage in interfacial electron transfer. Accordingly, photoexcitation typically results in the creation of an electron-hole pair that is positioned at the valence band and conduction band boundaries, respectively, **Equation 2.33**.



The electron-hole pairs that were photogenerated in the semiconductor's aerated solution in contact with organic compounds start a sequence of redox processes that are described below.

- i) Hydroxyl radicals are produced when photogenerated holes oxidize hydroxyl ions and adsorbed water molecules, **Equations 2.34 and 2.35**.

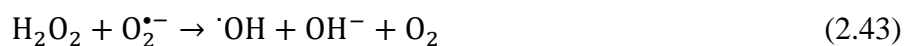


- ii) **Equation 2.36** describes the reduction of oxygen that is dissolved by photogenerated electrons, which results in superoxide anion radicals. These radicals then trigger a sequence of redox processes, which yield H_2O_2 , **Equations 2.37 to 2.41**.



- iii) Hydroxyl radicals are produced by gradually degrading the photogenerated H_2O_2 **Equations 2.42 to 2.44**.





- iv) The holes take part in the oxidation reactions directly.
- v) Generation and involvement in the oxidation of singlet oxygen species.

These $\text{O}_2^{\bullet-}$, and $\cdot\text{OH}$, are essential participants in the degradation of the contaminants. A schematic illustration of the several activities that take place on a photocatalyst's illuminated surface may be found in **Figure 2.6**.

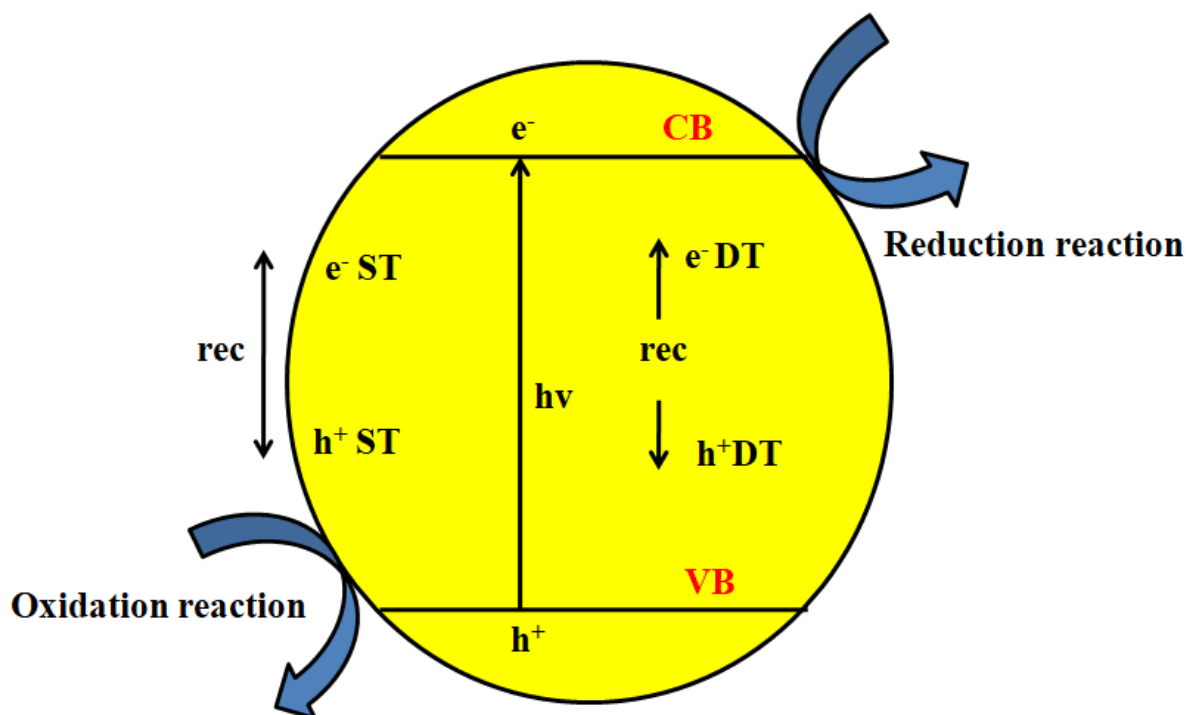


Figure 2.6 The mechanism through which a semiconductor is excited at the bandgap

Given that the adsorbate possesses a redox potential conducive to a thermodynamically favourable reaction, a photogenerated hole that arrives at the semiconductor's surface may engage in interfacial electron transfer with an adsorbed substrate (**Equations 2.45 and 2.46**).



Furthermore, it is possible to diminish an adsorption acceptor by removing an electron from the surface, and it is also possible to oxidize an electron donor that has been adsorbed by transferring an electron to a hole that has been produced by a photon on the surface. An anion radical, $A^{\bullet-}$, is produced by electron trapping, while a cation radical, $D^{\bullet+}$, is produced by hole trapping. Such radical ions are involved in various processes. They may participate in bulk solution chemical processes by diffusing off the semiconductor surface, or they could react chemically with the adsorbates and even themselves. To disperse the excitation energy by a method that does not involve radioactivity, they might also recombine through the process of reverse electron transfer [Ajmal et al., 2014].

2.8.Applications of photocatalyst

Numerous fields have seen the application of photocatalysts. This section presents a few prototype chemical changes that have drawn a lot of interest, in line with our core objective of exposing materials-related features of photocatalysts. These include processes like water purification, CO₂ reduction, and N₂ reduction that are thermodynamically uphill.

2.8.1. Water purification

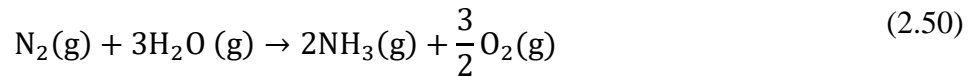
The global challenge of clean water scarcity and demand stemming from prolonged droughts, population expansion, and fast industrialization has grown. In response to this increasing need, several solutions and feasible methods have been used to provide more sustainable water supplies. Some short-term solutions include storing rainwater for use in everyday tasks and expanding catchment areas to accommodate stormwater runoff. It can be difficult for governments and the water industry to find sustainable water supplies in some dry regions with plenty of sunshine, little precipitation, and prolonged drought. Millions of people each year pass away from serious waterborne illnesses, and an estimated 4 billion people worldwide lack access to clean, sterilized water supplies [Malato et al., 2009]. These statistics are anticipated to rise shortly as a result of the overwhelming release of pollutants and micropollutants into the natural water cycle, which is causing growing water pollution. To prevent the limitation of clean water from getting worse, it would be ideal to treat wastewater using cutting-edge, inexpensive, and highly effective water treatment technology [Bradley et al., 2002].

2.8.2. N₂ reduction

N₂ reduction, occurring at a pace of more than 150 million tons per year, is an artificial reaction that is extremely significant to contemporary society [Pattabathula et al. 2016]. According to some estimates, it contributes considerably to CO₂ emissions and makes up around 3–6% of the world's total electric energy usage. Technically speaking, the majority of the reaction is conducted via the Haber-Bosch method ($\text{N}_2 + 3\text{H}_2 \rightarrow 2\text{NH}_3$), which requires high pressures (20–40 MPa), high reaction temperatures (400–600 °C), and a significant amount of H₂ that is produced by methane stream reforming. As a result, the process faces difficulties such as quick catalyst deactivation and low efficiencies. In theory, photocatalytic processes might potentially tackle these problems by utilizing photocatalysts to activate N₂ by photoexcitation. In fact, Schrauzer and Guth claimed groundbreaking work as early as 1977 [Schrauzer et al. 2002]. N₂ reduction has key processes with CO₂ reduction and water splitting. **Equations 2.47 and 2.48** demonstrate how photogenerated electrons decrease Nitrogen to create Ammonia (0.057 V vs NHE) and how H₂O is oxidized by photogenerated holes (1.23 V vs NHE).



The overall reaction ($E \sim 1.17\text{V}$) may be written as (2.49)



2.8.3. CO₂ reduction

In general, there are three steps participated in the photocatalytic CO₂ reduction method of semiconductors: 1) Under light irradiation, electron–hole pairs occur, with the electrons moving to the conduction band and remaining holes in valence band after the semiconductors absorb input photons with energy greater than or equal to the bandgap energy (E_g). 2) Charge recombination occurs concurrently with the movement of charge carriers and spatial separation toward the surface of photocatalysts. 3) The holes and electrons produced by photogenerated processes interact with the CO₂ and H₂O reaction agents that are adsorbed on the catalysts' surface to initiate the redox reactions. The reduction of CO₂ molecules adsorbed on semiconductor surfaces to carbonaceous fuels (such as acetaldehyde, methane, and carbon monoxide) and the oxidation of water or electron donors constitute the third stage. The total activity and reusability of the photocatalytic CO₂ conversion reaction depend on the other two

processes: desorption of final reaction products and the absorption and activation of CO₂ molecules.

On the other hand, thermodynamics and kinetics present a combined challenge for photocatalytic CO₂ reduction. At 750 kJ mol⁻¹, CO₂ is substantial bond energy of a stable linear molecule. In order to establish the C-H link and form hydrocarbon molecules, breaking the C=O bond requires a suitable light-responsive semiconductor, which can be obtained thermodynamically through photocatalytic CO₂ reduction [Wang et al., 2021].

2.9. Semiconductor as a photocatalyst

Semiconductors, such as ZnO, Fe₂O₃, TiO₂, CdS, SnO₂, ZrO₂, ZnS, and WO₃, have electronic structures that are filled in the valence band and unoccupied in the conduction band, which makes them potential sensitizers for light-induced redox reactions [Wang et al., 2014]. A semiconductor's lower edge of the conduction band can be thought of as a measure of the photoexcited electrons' reduction strength, while the higher edge of the valence band represents the holes' oxidation strength. Band energies of several semiconductors are shown in Figure 2.7 in relation to the electrochemical potentials of hydrogen and oxygen [Maruska et al., 1978]. **Table 2.2** shows the determined band energy, valence band position, and Conduction band position of semiconductors (at pH = 1).

For the formation of an electron-hole pair, a photon must have an energy greater than the band gap energy. Recombination releases the stored energy in an instant of nanoseconds when appropriate scavengers are not present [Meng et al., 2002]. Recombination is inhibited, and further redox reactions are possible if an appropriate scavenger is accessible to capture the hole or electron. In contrast to the conduction band electrons, which are effective reductants (+0.5 to - 1.5V vs NHE), the valence band holes, depending on the pH and Semiconductor, can be powerful oxidants against the usual hydrogen electrode (+1.0 to + 3.5V). A large number of organic degradation processes made use of the holes' oxidizing activity, in either a direct or indirect way [Wang et al., 2018]. In bulk semiconductor electrodes, band bending results in the availability of only one species, either the electron or the hole, for the reaction. On the other hand, both species are present on the surface of extremely tiny suspensions of semiconductor particles. As a result, there are potential oxidative and reductive routes.

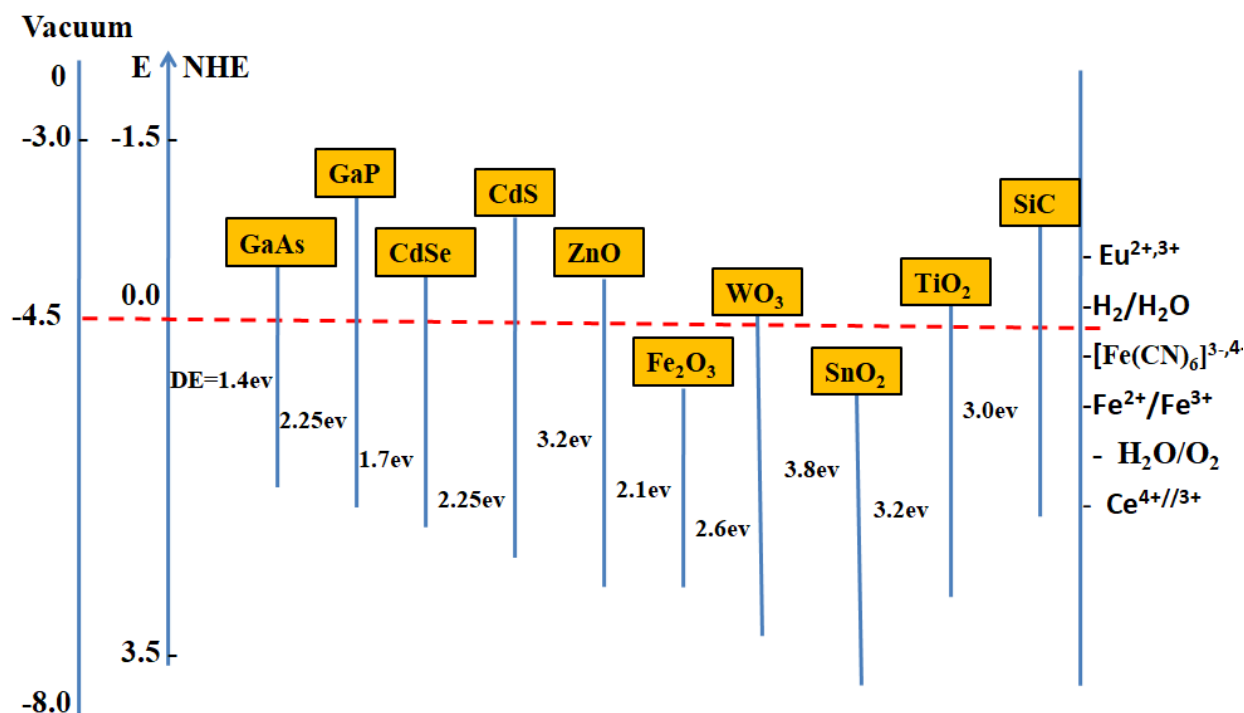


Figure 2.7 Bandgap values of different semiconductors

If the recombine of electron-hole pairs is as much repressed as feasible, photocatalysis can produce chemical products. One way to achieve this is by capturing either a photogenerated hole or an electron, or both. According to a literature review, organic molecules can go through their first oxidation either directly via the valence band hole before becoming trapped inside or on the surface of the particle, or indirectly via a surface-bound hydroxyl radical, which is a hole at the surface of the particle that is trapped [Swift et al., 2019].

Table 2.2: Basic semiconductor photocatalysts and their band positions (water at pH 1).

Semiconductor material	Valence band (V vs NHE \pm 0.1 V)	Conduction band (V vs NHE \pm 0.1 V)	Eg (eV)	Bandgap wavelength (nm)
GaAs	+ 2.2	-1.0	3.0-3.2	413-380
GaP	+ 1.0	-0.4	3.9	318
CdSe	+ 1.6	-0.1	2.8	440
CdS	+ 2.1	-0.4	3.7	336

WO ₃	+ 3.0	+ 0.2	2.8	343
ZnS	+ 1.4	-2.3	2.5	497
ZnO	+ 3.0	-0.2	1.7	730
SnO ₂	+ 4.1	+ 0.3	1.4	887
TiO ₂	+ 3.1	-0.1	2.3	540

There are various intriguing characteristics of particulate semiconductor photocatalysts. For a semiconductor particle loaded with metal, each photocatalyst serves as a photochemical or a micro photoelectrode diode. They are beneficial for surface reactions due to their huge surface area. They have unique photophysical characteristics that are influenced by the quantum size effect. Their affordability and simplicity of production render them appealing for various real-world uses [Vaya et al., 2020]. Despite TiO₂ having low catalytic activity for electron transfer reactions, its substantial bandgap energy (> 3.0 eV) makes it an effective photocatalyst. It was found that large bandgap semiconductors outperformed low bandgap materials as photocatalysts. These ideas have numerous uses in the fields of pollution control and environmental chemistry. Photocatalytic water splitting for hydrogen production and photocatalytic degradation of pollutants in wastewater are two areas that have attracted a lot of attention [Navidpour et al., 2023].

The choice of copper sulfide (CuS), cadmium sulfide (CdS), and molybdenum disulfide (MoS₂) in this study was based on their clearly established photocatalytic properties and their performance in destroying the environmental pollutants in the presence of visible light. CuS has been appreciated due to its chemical stability, low toxicity, and optical qualities that assist in the production of reactive species that are essential in the dismantling of the organic contaminants. A narrow band gap semiconductor, CdS, is a material that seriously absorbs the visible spectrum; thus, it is a good photocatalyst, although its performance is limited by fast electron-hole recombination. MoS₂ is a two-dimensional material and characterized by high surface area and active site catalytic sites, which make it more stable and active as a photocatalyst. As heterostructures, e.g., MoS₂/CdS, CdS/Cs₃Bi₂Br₉, and MoS₂/Cs₃Bi₂Br, these materials can show synergistic effects, which inhibit charge recombination and add more active sites, resulting in a much higher pollutant degradation rate. The optical and catalytic complementary properties of CuS, CdS, and MoS₂, therefore, offer a strong platform of high-

performance photocatalytic environmental remediation in the presence of visible or sunlight. A combination of this kind was made to effectively increase degradation rates and capitalize on the advantageous properties of each constituent in sustainable pollutant removals (Sudhaik et al., 2022; Liu et al., 2020; Ullah et al., 2023; Tran et al., 2024).

2.9.1. Role of CdS as photocatalyst

Cadmium sulfide has attracted much attention because it is a good semiconductor photocatalyst under visible light, with a low direct bandgap of 2.4 eV [Li et al., 2015]. The majority of photocatalytic processes are best suited for it because of its ideal band locations, which are VB at 1.8 eV and CB at -0.5 eV with regard to NHE. It has a powerful reduction power and a broad range of light absorption. However, the quick charge recombination rate is one of its limitations. As a result, a lot of research is being done to improve the transfer charge rate and retard the charge recombination rate. Additionally, photocorrosion is an issue for CdS, which severely limits its use in photocatalysis. It is an irreversible process whereby the holes readily oxidize the sulphide ions, forming solid sulfur as a result [Zhao et al., 2016].



Therefore, it is necessary to prevent hole aggregation on the surface and delay the charge recombination rate to effectively use CdS as a semiconductor photocatalyst. It may be possible to get over these constraints by recombining CdS with oxidation (TiO_2 , ZnO , BiOI , etc.) or reduction (C_3N_4 or Co_9S_8) photocatalysts to generate a Z-scheme photocatalyst. When CdS and the reduction photocatalyst are combined, the electrons in CdS's CB interact with the holes in the reduction photocatalyst's valence band, preserving both the holes and the electrons of the reduction photocatalyst. However, the drawback is that CdS holes can still encourage the material to corrode itself. Consequently, the prepared photocatalyst's stability is affected.

Cadmium sulfide-based heterojunction photocatalysts

The majority of metal sulfides function as reduction photocatalysts because of their negative CB locations. Therefore, CdS photocorrosion might be greatly reduced by combining it with oxidation photocatalysts, which would maintain both the holes of the oxidation photocatalyst and the electrons of CdS. Meng et al. synthesized CdS/InVO_4 using a microwave-assisted hydrothermal technique and examined how RhB dye degraded in samples of water. When 40% InVO_4 and CdS were added, almost 93% of the 10 ppm RhB solution could be broken down in 40 minutes of exposure to visible light (400 nm cutoff filters on a 250 W Xe lamp). Under

comparable circumstances, the photocatalytic effectiveness of CdS/InVO₄ is five times better than that of pristine CdS and InVO₄ [Meng et al., 2017].

The hydrothermal synthesis of cadmium sulphide (CdS), which produced well-crystalline nanoparticles, was employed as a photocatalyst to degrade the fluoroquinolone antibiotic ofloxacin in the presence of visible light. After 80 minutes, about 80% conversion was attained, mostly due to the action of $\cdot\text{OH}$. The tetracycline antibiotic's susceptibility to degradation was examined in CdS nanoparticles produced under microwave irradiation and electrophoretically coated on aluminium plates under simulated daylight irradiation. The deterioration was caused by $\text{O}_2^{\cdot-}$ and $\cdot\text{OH}$ radicals. Additionally, complicated CdS-based heterostructures have been researched. Yang and colleagues produced CdS/MOF-derived porous carbon (MPC) composites by pyrolyzing zeolitic imidazolate framework (ZIF-8) and then growing CdS photocatalyst in visible light. The structure, in comparison to bare CdS, exhibits much superior photocatalytic activity for the decomposition of cephalexin antibiotics by reducing both bulk and surface recombination, as reported by the scientists. Hydrothermal synthesis was used to produce octahedral CdS/SnIn₄S₈ nano-heterojunctions at various CdS to SnIn₄S₈ molar ratios. Compared to both CdS and SnIn₄S₈, the heterojunction with the ideal ratio (0.5:1) demonstrated significantly better visible-light photocatalytic activity. This is most likely because the photogenerated charges were separated and transferred more effectively. With outstanding reusability, this photocatalyst could successfully mineralize actual pharmaceutical effluent [Mishra et al., 2023].

Recently, Ag/CdS/Pr-TiO₂ nanoparticles were able to degrade a 32ppm dye solution by 98%. The scientists proposed that a higher quantity of hydroxide ions was adsorbed on the TiO₂ surface to counteract the charge distribution brought about by the addition of Pr³⁺ ions, which is why the photocatalytic effectiveness increased. Moreover, the surface imperfections on CdS led to a delayed rate of charge recombination, improving the produced composite's photocatalytic performance. Gadore et al. presented a one-pot synthesis method for the production of CdS/CeO₂ nanocomposite. After 60 minutes of exposure to direct sunlight, the produced photocatalyst was able to eliminate 190 parts per million of RB dye [Gadore et al., 2023].

2.9.2. Role of MoS₂ as photocatalyst

For applications including energy production and environmental cleanup, MoS₂ has been demonstrated to be the perfect catalyst [Gadore et al. 2021]. There are two phases of monolayer

MoS₂: semiconducting 2H MoS₂ and metallic 1T MoS₂. The most stable phase of MoS₂ that occurs naturally is 2H. MoS₂ is able to absorb photons in the visible spectrum due to its tiny bandgap, which is between 0.9 and 1.9 eV. It is extensively utilized in dye-sensitized gas sensors, solar cells, supercapacitors, and photocatalysis. Nevertheless, MoS₂'s narrow bandgap energy limits the photogenerated holes and electrons' ability to interact quickly, thereby reducing its photocatalytic activity. Consequently, it is recommended to make changes such as doping and producing nanocomposite materials that incorporate additional semiconductors in order to postpone charge recombination and enhance light-harvesting capabilities.

Heterojunction Molybdenum sulphide-based photocatalysts

Although pure MoS₂ typically has a greater charge recombination rate, which retards its photocatalytic activity, modifying the prepared samples' morphology and size may be able to increase the activity. With a bandgap of roughly 2.15 eV, MoS₂/rGO is suited for the decomposition of organic contaminants found in wastewater. When compared to pure MoS₂ nanoparticles, MoS₂/rGO produced using a hydrothermal approach demonstrated a higher surface area and enhanced photocatalytic efficiency. After exposure to visible light for 30 minutes, the produced nanocomposite had a maximum degradation efficiency of 72% for a 10 ppm RhB solution, whereas virgin MoS₂ only demonstrated 24% degradation under the same conditions [Zhang et al., 2016].

A simple in-situ hydrothermal technique was used to create a MoS₂/CoTiO₃ nanorod heterostructure with a flower-like appearance. The synthesized MoS₂/CoTiO₃ heterostructures demonstrated photocatalytic performance under solar radiation for the CIP and BPA degradation, with the degradation procedure proceeding according to pseudo-first order kinetics. Nevertheless, among all the catalysts that were constructed, the 5-MS/CTO heterostructure demonstrated the highest photocatalytic performance, outperforming pure MoS₂ by 15.66 (BPA) and 22.32 (CIP) and pure CoTiO₃ by 26.85 (BPA) and 39.97 (CIP). The reduced electron-hole recombination rate in heterostructures and accelerated charge carrier separation across the interface are attributed to the intimate high contact between MoS₂ micro-flowers and CoTiO₃ nanorods, which further improves photocatalytic activity [Dadigala et al., 2021].

The successful fabrication of an efficient photocatalyst, C₃N₄/MoS₂ – PANI, was employed to degrade BPA. The gC₃N₄/MoS₂ – PANI nanocomposite demonstrated photocatalytic rate of degradation that were 1.5 times higher than those of the gC₃N₄/MoS₂ sample in the

context of Bisphenol A photodegradation. The improved degradation efficiency of $gC_3N_4/MoS_2 - PANI$ can be attributed to PANI's conductive properties, as well as its enhanced surface characteristics and structural morphology [Ahmad et al., 2020].

2.9.3. Perovskite as photocatalyst

The mineral perovskite was named for the Russian mineralogist Lev Perovskite when it was first found in the Ural Mountains in 1839. The first reports of organic-inorganic hybrid perovskite materials date back to 1978, according to Weber et al. The chemical structure of metal halide perovskites is ABX_3 , with the A-site typically being a monovalent inorganic cation like Rb^+ , Cs^+ or an organic cation like Formamidinium (FA^+ , $CH_5N_2^+$). Generally, the B-site is occupied by a divalent metal cation, including Bi^{3+} , Sn^{2+} , Ge^{2+} , Pb^{2+} , among others. Ions of the halide type, such as Br^- , Cl^- , I^- etc, inhabit the X site in most. Due to their favourable properties, such as high optical absorption coefficients, tunable emission wavelengths, elevated charge carrier mobility, extended carrier diffusion lengths, structural simplicity, facile synthesis methods, and mechanical flexibility, these materials are extensively utilized in diverse optoelectronic applications, including light-emitting diodes (LEDs), photovoltaic devices, photocatalytic systems, and photodetectors. Historically, research on perovskite materials has predominantly centered on their electrical transport behavior, magnetic properties and structural phase transitions [Zhou et al., 2022].

Heterojunction perovskite-based photocatalysts

Perovskite nanocrystals in the Gamma phase of Cesium Lead tribromide nanocrystals have the potential to degrade photocatalytically and exhibit long-term stability. In order to enhance the photocatalytic degradation efficiency toward various dye pollutants, suppress the recombination of photogenerated electron-hole pairs, and mitigate the toxicity concerns associated with gamma $CsPbBr_3$ nanocrystals, Zhang et al. developed gamma $CsPbBr_3$ NCs/poly (methyl methacrylate) electrospun nanofibrous membranes (ENMs) via electrospinning technology. The developed γ - $CsPbBr_3$ NCs/PMMA ENMs exhibit a high surface to volume proportion and a multitude of functional assemblies on the ENM surface, making them advantageous for putting gamma $CsPbBr_3$ nanocrystals on PMMA ENM surfaces. The findings suggest that high photocatalytic degradation efficiencies of 83.89%, 98.43%, and 99.18% for MV, MG, and MB dyes, respectively, might be revealed by γ - $CsPbBr_3$ NCs/PMMA ENMs [Zhang et al., 2020].

According to Jing et al. LaFeO₃/GO composite was effectively developed and utilized as a targeted and effective catalyst to activate PS for the breakdown of BPA in wastewater from food. It is possible to eliminate almost 97% of BPA in 0.25% of food wastewater, even with the highly complicated background of food wastewaters [Jing et al., 2021].

2.10. Modifications of Semiconductor Materials

A semiconductor's performance can be improved in four fundamental ways, which are as follows (**Figure 2.8**):

- By a confined state that forms slightly higher than the valence band.
- Incorporating low band gap semiconductors.
- By forming a confined state directly beneath the conduction band
- Through band gap development to establish the color center.
- Via adaptation of the surface.

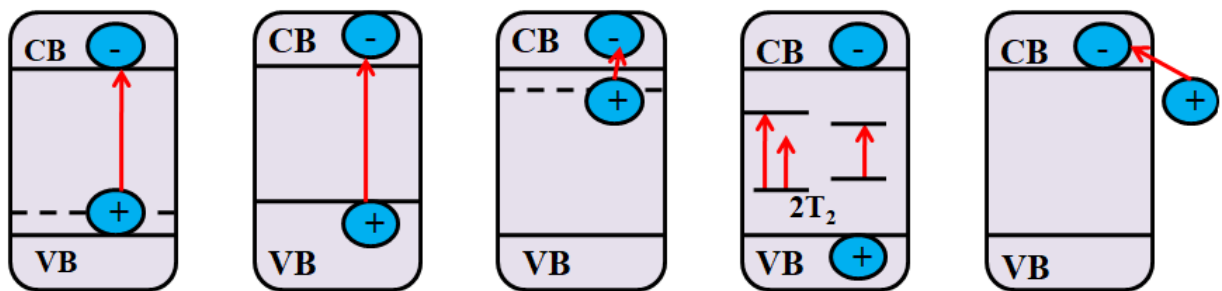


Figure 2.8 Introduction of localized states above the valence band; narrowing of the band gap in the semiconductor; formation of localized states below the conduction band; generation of color centers within the band gap; and surface alteration

As a result, the following methods are used in adaptations:

- Metal and nonmetal doping
- Codoping using different combinations of materials for the donor and acceptor.
- Substitution
- Coupling photocatalysts
- Miscellaneous

Photocatalysts with wide band gaps have a high rate of recombination for hole-electron and are colorless. The substance's light-harvesting period, the lifetime of hole- electron pairs, and the

quantity of reactive sites on the semiconductor all affect photocatalytic activity [Johar et al., 2015].

Doping

Doping is one type of photocatalyst modification that involves introducing impurity into a semiconductor that is otherwise clean in order to decrease the E_g among the conduction and valence band. Semiconductors can be doped with both metallic and non-metallic elements, each type of dopant imparting distinct modifications to the crystal lattice and influencing the material's structural and electronic properties. Metal and non-metal doping enhances the photo-responsiveness of photocatalysts to the visible light spectrum by introducing impurity states (new energy levels) situated between the valence and conduction bands, that facilitate improved charge carrier excitation under lower-energy photons. With the introduction of these new levels, the band gap narrows and excited electrons move from the impurity state into the conduction band. A hole or an electron is introduced into the photocatalytic semiconductor during doping, regarded as a band gap engineering component. Non-metals like P, N, F, S, Si, Cl, I, Se, Br, and so on form new bands above the valence band, while metal dopants like Cr, Co, W, Zn, Cu, Mo, Mn, Ni, Fe, and so on form new bands below the conduction band. It facilitates better electron trapping, which assists in avoiding recombination. Consequently, there is an increment in the activity of photocatalytic substances. The surface area, morphology, electrical, magnetic, and photocatalytic activity of photocatalytic semiconductors are all enhanced by metal dopants [Patil et al., 2013].

There are three distinct mechanisms by which non-metals can interact with oxide photocatalysts. Firstly, the non-metal dopant can directly interact with the photocatalyst oxide, leading to the creation of oxygen vacancy states. For example, carbon doping in TiO_2 has been shown to induce the formation of Ti^{3+} species, which introduces mid-gap states between the valence and conduction bands, thereby modifying the band structure and enhancing visible light absorption. The second possibility is that the dopant might stand in for oxygen at that location. Finally, the incorporation of doping material at oxygen-deficient sites or within oxygen-substoichiometry regions can stabilize these defects and act as a barrier to reoxidation, thereby enhancing the structural stability and photocatalytic durability of the material [Rehman et al., 2009]. In the TiO_2 -terminated surface, lower radius types like Nitrogen, Fluorine, or Carbon substitute the oxygen atom, while bigger radius types such as Chlorine, Bromine, Phosphorus, and Sulphur displace the oxygen in the SrO-terminated surface, as demonstrated by Guo et al. 2015. When photocatalyst oxides and non-metal dopants have similar energies,

the bandgap of the material (catalyst) constricts, and it becomes more efficient at absorbing light in the visible spectrum. The structural, morphological, optical, and electrical characteristics of a semiconductor are also changed by the band gap engineering method, which has an impact on the redox potential, surface area, charge-carrier mobility, and light absorption. According to Le et al., introducing acceptor and donor species has a direct influence on the electronic structure of the photocatalyst, which in turn changes its reactivity. Doping results in a decrease of the bandgap of the photocatalyst, meaning that the dispersion of the photocatalyst's conduction and valence and exhibits a beneficial effect. The absorption spectra edge redshift is the outcome of such alteration. A decrease in bandgap or the inclusion of an intraband gap state as a result of doping results in this form of bathochromic shift, which allows for the extraction of additional photons from visible light. The following factors contribute to the improved performance of dopants added to photocatalysts.

- Electron-hole recombination is prevented.
- Offers a larger surface area.
- Might trigger a sample's pore size to expand.
- Increased crystalline nature
- Increases sensitivity over a wide range of frequencies.

Codoping

Codoping techniques using different donor and acceptor species combinations are frequently used to modify the electronic band structure, where a narrowed band gap is the result of both an increase in the valence band maximum and a decrease in the conduction band minimum. The material's responsiveness over a wider spectrum of the sun is improved by this band gap narrowing. Furthermore, a number of studies have documented the effective application of both metal and non-metal codoping techniques to enhance photocatalytic performance (**Figure 2.9**). Similar to conventional mono-doping with either metal or non-metal elements, codoping can successfully address several inherent host material limitations, such as low carrier mobility, inadequate absorption of visible light, high electron–hole recombination rates, and dopant solubility constraints (Yan et al., 2013).

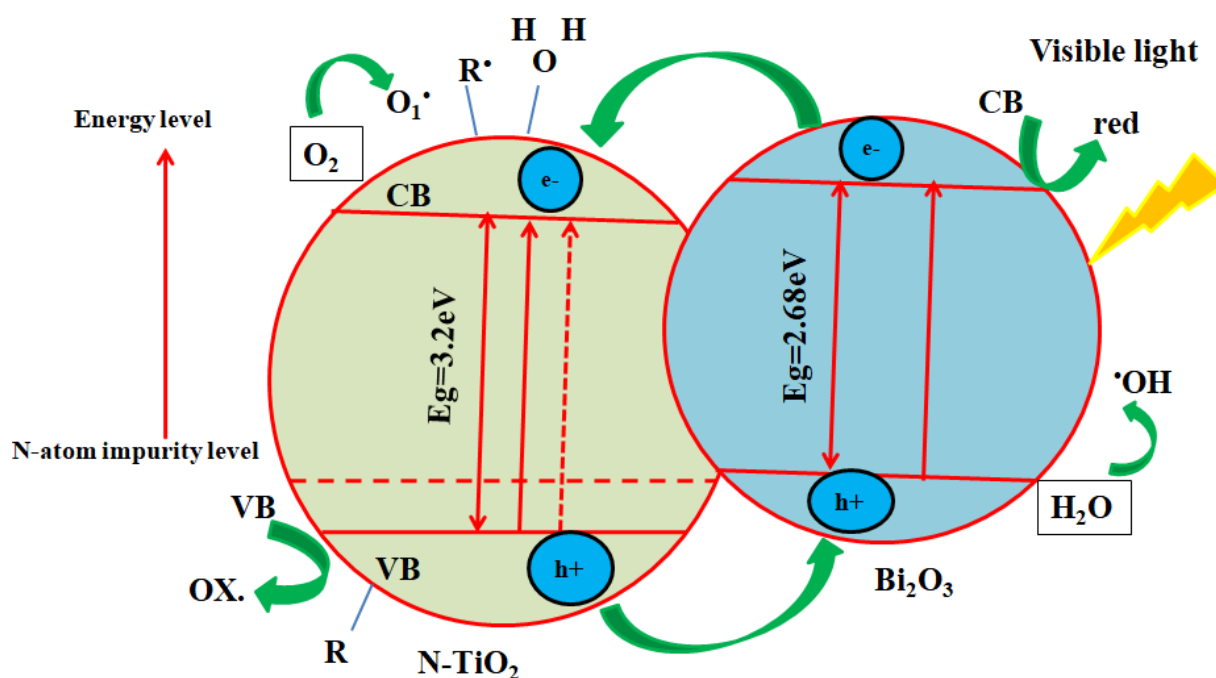


Figure 2.9 Codoping effect

Despite only slightly changing the conduction band edge, it has been shown that codoping with metal/non-metal pairs such as C–Mo, N–W, N–Nb, N–Ta, and Ce–F significantly increases photocatalytic efficiency. Huang et al. state that the codoping of Bi_2WO_6 with Ce and F modulates both the optical band gap and the microstructure of the material. It has also been demonstrated that the addition of a metal (Sm) and a non-metal (N) suppresses charge carrier recombination, restricts crystal growth, and prevents the anatase-to-rutile phase transformation. Hydrothermally generated zinc sulfide (ZnS) codoped with Ga and Cu showed enhanced stability under prolonged irradiation and a 58-fold increase in photocatalytic performance compared to undoped ZnS. In a different case, a hydrogel-assisted technique for creating N/F codoped anatase TiO_2 with exposed [001] facets showed better photocatalytic activity due to a stronger electron-driving force. More efficient electron injection from the dye's lowest unoccupied molecular orbital (LUMO) into the semiconductor's conduction band was made possible by this enhancement, which was attributed to a positively shifted flat-band potential. Additionally, TiO_2 functionalized with non-metal elements and plasmonic metals showed an extended photoresponse under solar, UV, and visible light irradiation, making it effective for the degradation of a range of organic pollutants (Yu et al., 2014).

Coupled Semiconductors or Composites/Coupling photocatalysts

The creation of semiconductor composites by means of strategic coupling of two or more semiconductors represents another efficient way to increase photo-responsivity and extend light absorption capacity in the visible light range. The semiconductors chosen for the composite preparation must have tunable band gaps. Usually, high band gap semiconductors are matched with smaller ones having more negative conduction band levels. Consequently, electrons from the conduction band of the narrow band gap semiconductor are effectively moved to the conduction band of the wide band gap semiconductor, enabling better charge separation and prolonged photoactivity.

Numerous photocatalyst combinations, including $\text{Ag}_3\text{PO}_4/\text{TiO}_2$, CdSe/TiO_2 , $\text{FeTiO}_3/\text{TiO}_2$, ZnO/CdS , CdS/TiO_2 , $\text{W}_{18}\text{O}_{49}/\text{TiO}_2$, $\text{NiTiO}_3/\text{TiO}_2$, $\text{CoTiO}_3/\text{TiO}_2$, ZnO/CdS , $\text{TiO}_2/\text{SnO}_2$, ZnO/TiO_2 , and ZnOAg_2S have all been coupled. The synergistic effect of such composites results in stronger photocatalytic activity than isolated ones. According to a report, Cr_2O_3 in combination with SnO_2 has been discovered to demonstrate improved photocatalytic activity when exposed to visible light due to its smaller crystal size, excellent crystalline nanoparticles, and enhanced reactivity to light. As subjected to visible light for 60 minutes, the sample breaks down 98% of the rhodamine B. Doping related photocatalysts with various mixtures of metals and non-metals can further improve the photocatalytic activity. Samadi and colleagues used Nd^{3+} and Zr^{4+} to codoped TiO_2 and SiO_2 nanocomposite.

Bhosale et al. investigated the influence of dopant incorporation on the morphology and uniformity of $\text{TiO}_2/\text{SiO}_2$ thin films. Their findings revealed that doping induces the formation of a spongy microstructure and promotes uniform particle dispersion with minimal agglomeration. This structural improvement contributes to a more efficient degradation of methyl orange, primarily due to the suppression of charge carrier recombination. Additionally, semiconductor coupling strategies may involve the incorporation of secondary metal oxides, such as TiO_2 or Al_2O_3 , onto the mesoporous surface of SnO_2 to further enhance photocatalytic activity (Ramasamy et al., 2010).

Substitution

The replacement of one metal with another is an additional method to alter the photocatalyst's activity. A $\text{CaFe}_2\text{O}_4\text{-MgFe}_2\text{O}_4$ bulk hetero-junction (BH) lattice photocatalyst was found to have more photocurrent after revealing the addition of Ti^{4+} at the Fe^{4+} position [Borse et al. 2012]. The Ti ion-doped sample's effective charge separation also resulted in an improved quantity quantum yield for the photo decomposition of the $\text{H}_2\text{OCH}_3\text{OH}$ combination.

Wang et al. (2012) examined the alterations in the band gap resulting from the substitution of various metals, such as Zr, Molybdenum, Hf, and Titanium, for tungsten in WO_3 . They said that when W in WO_3 is replaced by a metal of the same valency, such as Mo or Cr, the band gap is lowered by relocating the conduction band edge to the lower side. On the other hand, adding metals with lower valency, including Hf, Ti, and Zr, causes the conduction band edge to move higher, hence broadening the band gap. Substituting oxygen with sulphur creates localized occupied states above the valence band, which causes the band gap to close as the conduction band minimum moves upward. Both of these outcomes are beneficial purposes.

Long et al. also investigated the effect on band edge or electrical properties employing dopants of Sn, Ge, Pb, and Si. They noticed that distinct forms of the same dopant, such as rutile or anatase, transmit distinct electrical properties. Therefore, the effect on the band gap may be the same for different dopants. For example, rutile TiO_2 that is Pb-doped, Si-, Ge-, and Sn-doped exhibits a band gap reduction of around 0.1 with an approximate value of 0.55eV, while anatase form diminishes the band gap by 0.20 and 0.15eV and broadens it by 0.06 and 0.02eV, respectively.

Miscellaneous

Titanium is a pure crystalline metallic oxide with a band gap above 3.1 eV. Its wide band gap enables its application in renewable energy generation and environmental cleanup, as it is effective in the ultraviolet (UV) spectrum. During the synthesis of titania by the solution phase method, Yaghoubi et al. noted the formation of an energy gap attributed to midgap states. The photoreactivity is enhanced by the oxygen vacancy and extensive surface area of the undoped mixed-phase TiO_2 nanoparticles, which possess a bandgap of around 2.2 eV.

2.11. Methods used for preparation of nanomaterials:

Co-precipitation method

One easy way to make all sorts of nanoparticles is by using this method, which is widely utilized. This method calls for a liquid medium to facilitate the precipitation process. It is possible to create homogenous nanoparticles using this method. In a nutshell, coprecipitation is the process of mixing salts that are soluble in water, often of metal ions with trivalent or divalent charges. Trivalent metal ions are the usual form of salts that are soluble in these. These salts that dissolve in water undergo a reduction process and, in the end, produce a salt that does not dissolve in water, known as a precipitate. The reaction conditions and reducing agent dictate whether the solution must be stirred continuously or not in relation to the heat

conditions. Particles using this method typically display less crystalline nature. Using heat energy, the particles may be made more crystalline. Standard reducing agents like sodium hydroxide and ammonia solution are employed to maintain the required pH, ensuring that the entire process remains in an alkaline medium. Several factors influence the size of the nanoparticles, including the pH of the solution, the salt ratio, the sustained temperature of the reaction medium, and the kind of base employed. **Figure 2.10** shows the schematic diagram.

Filtration or centrifugation can separate the solvent, which can then be further purified and dried. Another way to make doped ferrites is to add different rare-earth elements to the ferrites. Ultrafine nanoparticles are required for use in biological applications. According to Kolahalam et al., this method may also be used to produce biocompatible nanoparticles.

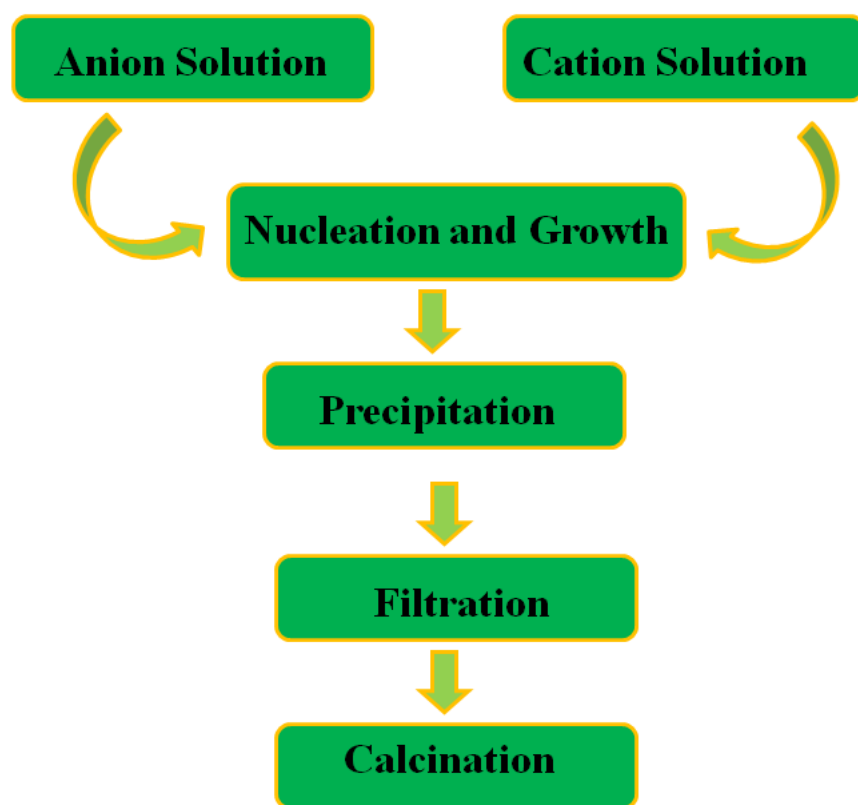


Figure 2.10 Schematic illustration of the co-precipitation method

Sol-gel method

Nowadays, nanoparticles are generated and produced through an array of approaches, including the vapor phase compression method, the mechanical alloying method, the sol-gel method, the plasma process, impact with high-energy pellets, and the electrochemical process. Even though

all of the aforementioned technologies may produce large amounts of nanomaterial, the sol-gel approach is the most popular and has more practical uses in the business world. Due to its unique properties, this technique may be used on an industrial scale to produce nanoparticles of consistent size and quality. It is possible to make two or more kinds of nanoparticles simultaneously using this method, which involves mixing metal (or metal oxide) precursors in certain proportions to generate alloy products. The fundamental distinction between the sol-gel technique and other methods, such as the electrochemical and plasma methods, is the latter's capacity to synthesize alloy products in a single step, while the former is not as large-scale as the latter. Furthermore, extremely homogenous, highly pure (99.99% pure) composites may be formed via the sol-gel method. This technique also has the benefit of producing metal and ceramic nanomaterials at temperatures between 70 to 320°C because of its lower process temperature when compared to traditional techniques. Nanomaterials with temperatures ranging from 1400 to 3600 degrees Celsius are produced via the various methods described. The sol-gel method is an example of a bottom-up synthesis approach. In this process, the end molecules are generated by means of a series of irreversible chemical events. The original, uniform molecules (sol) go through these changes to become a gel, which is a continuous, heavy, 3D molecule. **Figure 2.11** shows the sol-gel process flowchart, from precursor to aerogel.

The formation of binary or tertiary hybrid systems involves the utilization of a wide variety of salt combinations, each of which possesses a distinct chemical composition. Reaction rates vary among the major salts. Concentration, pH, temperature, and solvent type are some of the factors that influence the rate of salt reactions. A 3D structure called the polymer gel is formed from the density of the cells when the cavities are linked. Volumetric shrinkage causes the gel to solidify and harden as it dries. It is worth noting that by modifying the drying conditions of the gel, nanosized permeability may be attained. The main advantages of the sol-gel process are the low temperatures required, the homogeneous nanostructure that is produced, and the outstanding product purity. We know that there are a lot of steps involved in transitioning from sol to gel in the sol-gel process, the most common of which is slowly draining the solvent. The gel shrinks as it dries, so making sure the conditions are appropriate to prevent fractures from developing is an important part of this process. The sol-gel method may be used to create materials that can be used in composites or nanocomposite applications [Bokov et al., 2021].

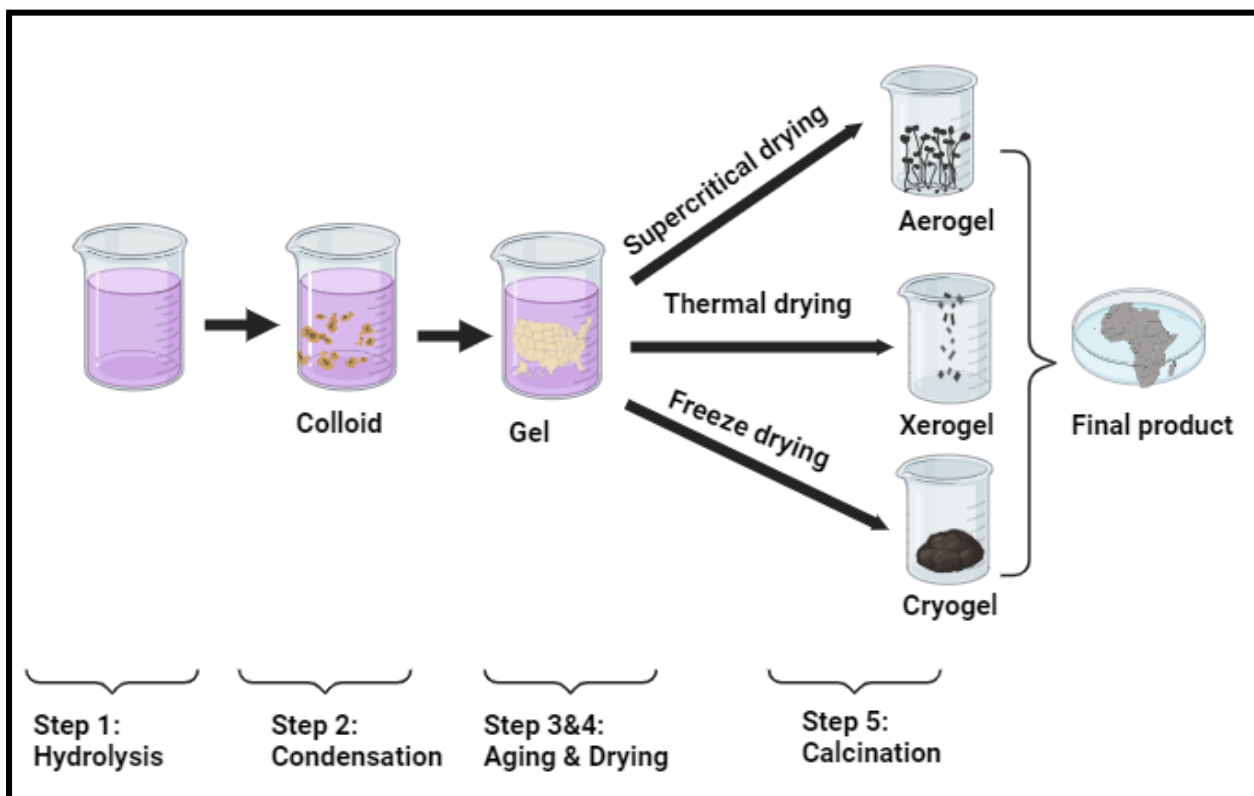


Figure 2.11 Diagram representing the several steps of the Sol-Gel process

Hydrothermal method

Any heterogeneous reaction that takes place at high pressure and temperature when mineralizers or aqueous solvents are present is typically referred to as hydrothermal. Autoclaves, which are pressure containers made of steel, may or may not have a Teflon lining and are usually used to perform this synthetic procedure (**Figure 2.12**). The reaction is carried out in aqueous solutions under regulated temperature and/or pressure. In order to obtain vapour saturation pressure, it is feasible to increase the temperature to a level that is higher than the point at which water boils. The temperature and the amount of solution that is provided are the primary factors that determine the internal pressure that is created in the autoclave during the process. The most crucial factors to consider when choosing an appropriate autoclave are the pressure and temperature circumstances throughout the experiment, as well as the solvent or hydrothermal fluid's resistance to corrosion within that pressure-temperature range. When selecting an autoclave material, corrosion resistance is a crucial consideration if the reaction is occurring inside the vessel itself. Strong materials that are resistant to corrosion include high-

strength alloys, iron, nickel, cobalt-based superalloys, titanium and its alloys, and stainless steel from the 300 series (austenitic).

The hydrothermal approach has been widely used by researchers to create nanoparticles with photocatalytic characteristics. By hydrothermally treating the peptized precipitates of a Ti precursor with H₂O, for instance, TiO₂ nanoparticles can be produced. Titanium butoxide was used as a precursor to create the precipitates when tetraalkylammonium hydroxide (a protease) was present. With longer alkyl chains, the particle size dropped at the same peptizer concentration. The shape of the particles was affected by the proteases and their concentrations. In another investigation, WO₃ was created using a hydrothermal approach for the photoelectrochemical solar water oxidation process as well as the breakdown of an aqueous solution of rhodamine B when exposed to sunlight [Medina-Ramírez et al., 2015].

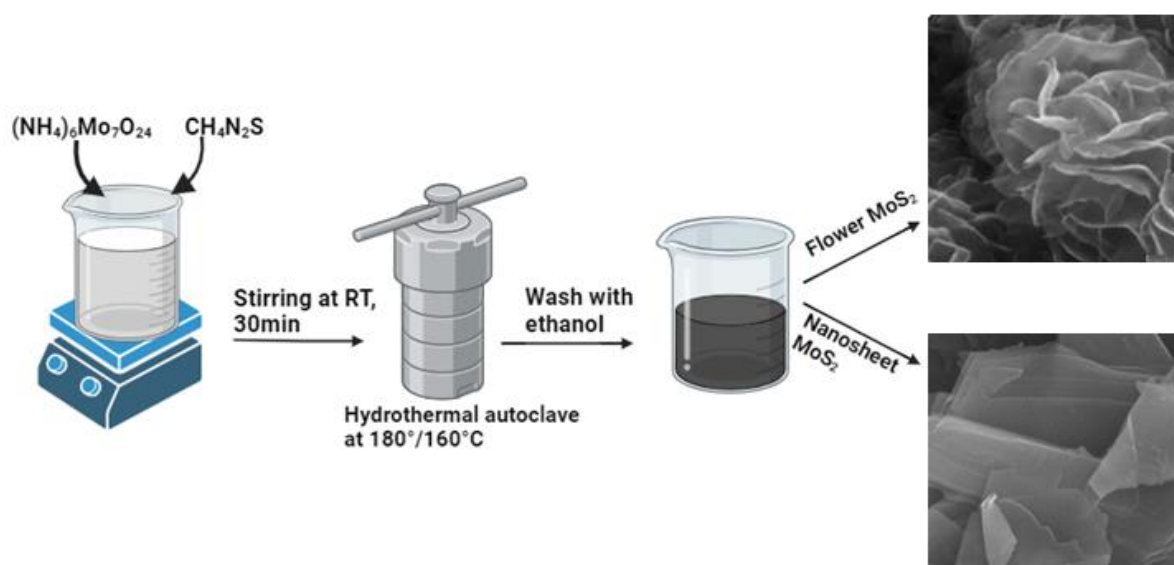


Figure 2.12 Schematic diagram of the hydrothermal method showing the synthesis of nanomaterials

Microwave method

Microwave (MW) radiation has been the subject of a significant amount of research because of its ability to activate energy and promote a wide range of chemical reactions. The utilization of this approach has been expanded to involve the formation of a wide variety of inorganic materials as a result of the advantages it offers in the field of organic chemistry. These advantages include a simpler workup, a cleaner atmosphere (i.e., reactions that do not require

the use of solvents), higher yields, and enhanced reaction speeds. An illustration of the microwave process is depicted in **Figure 2.13** as a schematic diagram.

There is an ongoing debate over the factors that lead to the amplification of chemical processes by microwave radiation, despite the many benefits of using microwave radiation to activate energy for chemical reactions. Impacts from both nonthermal and thermal microwave impacts are at the center of the controversy. The frequency range of microwaves is 0.3 to 300 GHz; reactors intended for chemical processes function at 2.45GHz, a frequency designated for heating system purposes. Since MW radiation cannot directly break bonds, it is known that it is insufficiently energetic to break covalent or hydrogen bonds. As a result, it is unable to trigger chemical processes. All reaction elements (solvents, reagents, containers, etc.) in microwave chemistry can interact with or disrupt the electromagnetic field. For microwave-assisted chemical processes to work, the reaction mixture must be able to absorb microwave energy efficiently, and the solvents utilized can have a significant impact on this capacity. The loss tangent (δ) is a measure of a solvent's or material's capacity to transform microwave energy into heat energy. It is anticipated that compounds (solvents, molecules) with high $\tan \delta$ values will be more susceptible to the thermal effects of microwave radiation since they have a good ability to absorb microwave radiation.

In addition to the clear macroscopic alteration in bulk reaction temperature, Kappe et al. conducted an in-depth analysis to elucidate the influence of electromagnetic radiation on a chemical alteration. Chemical processes were carried out in a silicon carbide tank, which has a high microwave absorptivity, to reduce the impact of the electromagnetic field. In order to execute the same reactions under similar reaction circumstances, a vessel that is non-absorbing of microwave radiation was employed for the comparison. Based on the collected data, the study group concluded that the increases in microwave chemistry are driven by the overheating phenomena and that the electromagnetic field has no direct effect on the chemical pathway.

Several publications on the fabrication of composite-ternary materials by the use of microwave irradiation have also been published in the appropriate literature. For instance, the photocatalytic activity of a composite called (RGO)-BiVO₄ (RGO: Reduced graphene oxide) was assessed in relation to the breakdown of ciprofloxacin. The MW approach is regarded as an easy, quick, economical, and clean way to produce photocatalytic compounds. Furthermore, minor adjustments to the reaction variables can readily enhance the materials' physicochemical

characteristics. Different sizes, forms, and morphologies of photocatalytic materials have been synthesized. These materials can be used in many different ways.

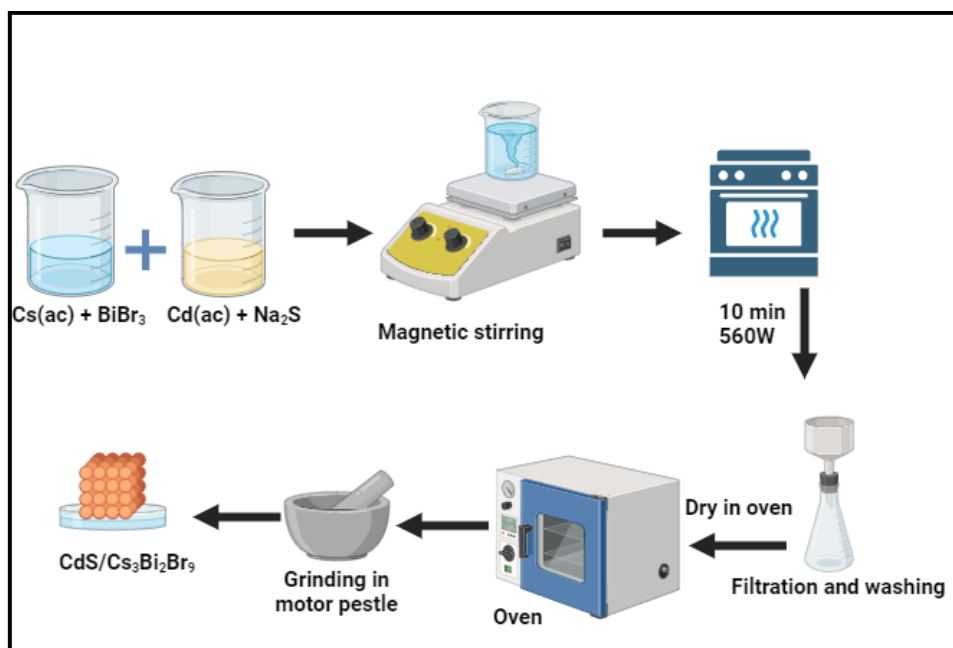


Figure 2.13 Diagram for the microwave-irradiation technique

2.12. Photocatalytic remediation of organic pollutants

The ecosystem has experienced numerous natural disasters. However, the greatest threat has occurred in the last 50 years, during which time air and water contamination levels have peaked. The most significant environmental factor that exists today is the "water age," and some people believe that future conflicts will take place on the water. There may soon be a lack of clean water due to the growing threat that organic contaminants pose to water resources. This is a result of population, urbanization, and industrialization growth that is out of control [Jing et al., 2013; Liu et al., 2017]. However, a large number of organic substances, including fertilizers, surfactants, solvents, synthetic pigments, and dyes, come from a variety of industries, including plastic, textile, pharmaceutical, leather, food, and farming. These compounds are stable and have a hard time decomposing naturally, which means they can harm people and animals over long or short periods. They may cause vomiting, Nausea, dizziness, anxiety, excessive perspiration, effects that are mutagenic and cancer-causing effects, dementia, kidney failure, high blood pressure, and other problems. As a result, it is necessary to create new technologies to safeguard the environment and public health.

To encourage the elimination or decomposition of contaminant species by redox processes, advanced oxidation processes have been established based on the elimination of contaminants

in wastewater. The Advanced Oxidation Process (AOP) has stood out for its exceptional performance and great efficiency. By using both direct and indirect methods, these procedures effectively remove persistent organic contaminants by utilizing $\cdot\text{OH}$ radicals and other active oxidizing agents. Among the most potent oxidizing agents, $\cdot\text{OH}$ has an extremely high standard potential [$E^\circ(\text{H}_2\text{O}/\cdot\text{OH}) = 2.80\text{V}/\text{SHE}$]. From its initial nonselective reaction with various pollutants to the subsequent breakdown of those products into water, carbon dioxide, and inorganic ions, it can yield hydroxylated or dehydrogenated compounds [Akerdi et al., 2017; Byrne et al., 2018].

Phenols

The issue of water pollution has grown more serious in recent years, and the phenomenon of inadequate industrial wastewater discharge is progressively endangering the environment and public health, particularly when it comes to industrial wastewater that contains phenols and their derivatives. The state has designated wastewater containing phenol as an essential control organic pollutant due to its wide range of contaminants, complex structure, and difficulty in degrading. Phenols and phenolic compounds are common pollutants of the aquatic system. Phenol is one of the most prevalent and hazardous phenolic chemicals found in wastewater.

Huang et al. reported the development of a new visible-light-reacting $\text{BiOI}/\text{Bi}_2\text{WO}_6$ hetero-junction photo catalyst by a hydrothermal procedure. The photocatalytic activity of $\text{BiOI}/\text{Bi}_2\text{WO}_6$ heterojunctions was greater than that of pristine BiOI and pristine Bi_2WO_6 , with $\text{BiOI}/\text{Bi}_2\text{WO}_6$ exhibiting the greatest efficiency for phenol. The effect of the BiOI and Bi_2WO_6 molar ratio on heterojunction photo-catalyst activity was investigated in this work [Huang et al., 2021]. Zhang et al. have studied how photocatalytic degradation causes the phenol solution to mineralize over BiPO_4 . After a 5-hour photocatalytic reaction, over 95% of the phenol (10 ppm, 100 ml) was mineralized, which is better than TiO_2 under the same conditions.

Modestor and Lev investigated the photo-catalytic efficiency of TiO_2 in suspension and on supported systems, as well as the photo-catalytic oxidation of 2, 4-dichlorophenoxyacetic acid using TiO_2 . Using TiO_2 and activated carbon in combination, [Herrmann et al., 2010] tried photocatalytic degradation of 4-chlorophenol.

Cláudia et al. synthesize zinc oxide nanomaterials incorporated with gold nanoparticles through a double impregnation approach. The Au-loaded catalysts showed higher activity when compared to bare ZnO ; this was measured using the pseudo-first-order kinetic constant and

phenol degradation. The Au-loaded ZnO samples made by thermal breakdown of zinc acetate (Zn ac) ($k_{app} = 5.6 \text{ min}^{-1} \text{ mg}^{-1} \text{ Au}$ for both materials) and chemical vapour deposition had the best activity, with mineralization of 82% and 92%, respectively.

The highest visible-light photocatalytic efficiency was demonstrated by ZnO nanorods with large surface flaws, which degraded 10 ppm phenol aqueous solution by 50% in 2.5 hours. This degradation rate was nearly four times faster than that of nanorods with smaller surface defects. Several photocatalytic byproducts, including carboxylic acids, benzoquinone, resorcinol, and catechol, evolved at different stages during the mineralization process of phenol during degradation, which was also studied [Jamal et al., 2016].

Dyes

Synthetic dyes represent a significant category of pollutants prevalent in contemporary wastewater due to their widespread use in industries such as textiles, printing, food and beverage, and medicines. These dyes, which often possess hazardous and carcinogenic properties, can block sunlight from penetrating water bodies, thereby disrupting aquatic processes such as biodegradation and photosynthesis [Sima and Hasal, 2013]. Commonly, dyes considered in photocatalysis include methylene blue, methyl orange, and Rhodamine B. The transformation of complex organic dyes in the environment can yield aromatic amines as intermediates, which are extremely toxic to marine life and must be removed before environmental discharge [Hickman et al., 2018]. Conventional wastewater treatment methods are generally inadequate for degrading these dyes due to their non-biodegradable and persistent nature.

Photocatalysis has become a successful method for the degradation of dyes. This process begins with hydroxyl radicals ($\cdot\text{OH}$) attacking the weak bonds in the dye compounds, like the azo bond ($-\text{N}=\text{N}-$), leading to the destruction of the conjugated structure. Subsequently, intermediates undergo radical chain reactions with oxygen, ultimately breaking down into water and carbon dioxide. Dye photodegradability is often lower for dyes with more complicated structures, as the degradation mechanism is sensitive to the chemical structure of dyes. The adsorption characteristics of dyes can also be affected by the existence of functional groups, which have been investigated by numerous scholars under visible and UV light (Khataee and Kasiri 2010). Though extensive research has been conducted on dye removal via photocatalytic degradation, studies focusing on real effluent are limited. Isari et al. (2018) examined the effect of various anions on the photo-catalytic elimination of rhodamine B using

FeTiO₂/rGO photocatalysts. The existence of sulfate, chloride, nitrate, and phosphate anions reduce elimination efficacy to 57%, 73%, 78%, and 48% respectively. Chloride and sulfate were found to adsorb quickly onto the photocatalyst, competing with dye molecules for radicals, whereas nitrate and phosphate showed less attachment. The application of the same photocatalyst in the treatment of real textile wastewater resulted in a total organic carbon reduction from 930-310mg/L, achieving a 66.6% decrease. Additionally, the chemical oxygen demand was reduced from 1550-634mg/L, reflecting a 59.1% reduction after a treatment duration of three hundred ninety minutes.

Conversely, Touati et al. found that titanium dioxide didn't have a significant impact on the degradation of dyes in textile effluent. Total organic carbon and color elimination efficiencies were comparable under UV irradiation and hydrogen peroxide, both with and without titanium dioxide. The addition of hydrogen peroxide and cerium ions to the titanium dioxide system significantly enhanced its performance, increasing total organic carbon removal from twenty-seven percent to forty percent and improving color elimination from around thirty percent to fifty-five percent after 24 hours of treatment. In order to identify chemicals in actual textile effluent, gas chromatography-mass spectrometry was employed [Jorfi et al., 2018]. Among the most important organic chemicals that were discovered were palmitic acid, fluoroacetamide, quinolone, dimethylquinoline, methylisoquinoline, and linoleic acid. A 300-minute photocatalytic treatment at pH 3 using a Manganese, Molybdenum, and La-doped TiO₂ catalyst supported on activated carbon (Mn, Mo, La/TiO₂/AC) resulted in the formation of additional oxygenated organic compounds, including acetamide, phenyl benzoic acid, and isoindole. This indicated the need for further oxidation of intermediates for complete conversion to non-toxic substances. In addition to TiO₂, ZnO that is commercially and organically generated was also investigated as a bulk photocatalyst in actual textile wastewater. In contrast, ZnO showed comparatively less decolorization (64.41%) after 150 minutes of UV light exposure than TiO₂ (95.29%). Amornpitoksuk et al. 2016 demonstrate that the precipitation solution at pH 6 yielded Ag₃PO₄ powders with a multifaceted structure and the best activity for decolorizing RhB and MB solutions when exposed to visible light. AgBr/Ag₃PO₄ powders were synthesized utilizing a one-pot ion-exchange technique with success.

Pesticide Degradation

Currently, one of the main causes of water contamination is pesticides. These are a combination of materials used to eradicate, prevent, or control pests. These include species of animals and plants that cause harm at any point in the production, storage, processing, or marketing of wood, wood products, food, animal feedstuffs, agricultural commodities, or that may be given to animals to control arachnids, insects, or other pests on their bodies. They can also include vectors of diseases that affect humans or animals. In addition to preventing degradation during storage or transportation, pesticides are employed as ripening regulators, defoliants, desiccants, growth regulators, and fruit thinning agents. They are sprayed on crops either prior to or following harvest. Numerous academic publications discuss various pesticide types, including nematicides, herbicides, fungicides, insecticides, and rodenticides. In terms of chemical composition, pesticides can be categorized as substituted urea, carbamates, organophosphates, and organochlorines (OCs). Organic contaminants (OCs) are regarded as persistent and harmful pollutants that pose a serious risk to the ecosystem [Vaya et al., 2020].

According to Nguyen et.al, Cu was added to the ZnO lattice in order to widen its responsiveness to visible light and narrow its band gap. In order to fabricate the CuZnO/gC₃N₄ Z-direct arrangement photocatalyst for enhanced atrazine elimination, the obtained CuZnO was constantly combined with gC₃N₄. Consequently, compared to single gC₃N₄ or Cu-ZnO materials, the as-prepared CuZnO/gC₃N₄ exhibited higher photocatalytic atrazine degradation [Truc et al., 2019]. Ahmad et al produced Ag – doped STO/gCN heterojunction, and the resulting heterostructures have been described. The pesticide Dicofol was broken down, and hydrogen was produced photocatalytically using the nanocomposites that were synthesized. Ag(3) STO/gCN was discovered to have a hydrogen generation rate of 645.62 $\mu\text{mol g}^{-1}\text{h}^{-1}$, which is approximately two times as high as that of pristine STO/g-CN. The produced nanocomposites demonstrated ultrafast photocatalytic activity, as evidenced by the data, which showed that 92.2% degradation occurred in less than 60 minutes.

To enhance the photocatalytic degradation of chlorpyrifos (CP), a widely used agricultural pesticide, composite photocatalysts were synthesized by integrating cobalt-aluminum layered double hydroxides (Co – Al LDH), graphitic carbon nitride, and cobalt ferrite (CoFe₂O₄). These Co – Al LDH/gC₃N₄ – CoFe₂O₄ nanocomposites demonstrated significantly improved photocatalytic performance compared to pure g-C₃N₄. This enhancement was primarily attributed to more efficient separation of photogenerated electron–hole pairs, which reduces recombination losses and boosts photocatalytic efficiency (Sheikhpour et al., 2021). However,

[Yadav et al., 2019] demonstrates that the ZnO/SnO₂ nano-composites were produced by the co-precipitation technique and were used for disintegrating Triclopyr, a persistent pesticide, with different Sn concentrations. Compared to pure ZnO or SnO₂, ZnO/SnO₂ nanocomposites exhibit greater activity towards the photodegradation of triclopyr. The development of heterojunctions, which in turn reduces charge carrier recombination and increases photodegradation efficiency, is primarily responsible for the increased activity in ZnO/SnO₂ nanocomposites.

Pharmaceutical compounds

Pharmaceutical waste often enters aquatic environments due to improper disposal, particularly from manufacturing facilities, hospitals, and residential areas. Although these pharmaceutical compounds are typically present in trace amounts, their continuous release into the environment leads to chronic exposure [Teixeira et al., 2016]. Common pharmaceuticals found in wastewater include macrolides, sulphonamides, quinolones, diclofenac, and ibuprofen. Due to the complex aromatic structures and environmental persistence of many pharmaceuticals, conventional wastewater treatment methods are generally unsuccessful at removing them. As a result, photocatalysis has emerged as a promising technique for degrading these complex compounds. The photodegradation mechanism for pharmaceutical residues is similar to that of dyes, with hydroxyl radicals playing a key role in the mineralization process. During this process, various intermediates are generated through dehydroxylation, deamination, and ring-opening reactions, which are eventually further mineralized into less persistent and more biodegradable by-products [Deng et al., 2018].

Recent research has been concentrating more and more on the question of whether or not it is possible to remove pharmaceutical chemicals in actual wastewater by employing photocatalytic techniques. An assortment of wastewater samples has been gathered from various sources, including rivers, municipal treatment plants, and pharmaceutical production sites. In India, Talwar et al. coupled aerobic biological processes and photocatalysis for pharmaceutical factory wastewater. A total of 96.5% COD was removed, of which 67% was due to photocatalysis with a commercial TiO₂ photocatalyst and the remainder to the RBC (rotating biological contactor). Teixeira et al. assessed the photocatalytic degradation of pharmaceutical medicines in a wastewater treatment plant in Germany using commercial ZnO and TiO₂ photocatalysts. The study found that ZnO could degrade 14 categories of pharmaceutical complexes in the effluent by about 95% within 40 minutes under UV

irradiation, while TiO₂ required over 6 times longer to achieve a similar elimination efficacy under identical conditions. This suggests that ZnO is more effective in utilizing the light source.

Lofrano et al. observed significant seasonal variability in the concentration of the macrolide spiramycin (SPY) in an Italian WWTP, with winter concentrations averaging 35 µg/L compared to 5 µg/L in summer. Photolysis removed more than 99.9% of SPY in summer within eighty minutes, and complete removal occurred in five minutes after adding 0.1 g/L titanium dioxide photo catalyst. In winter conditions, a removal efficiency of 91% was achieved within 80 minutes of treatment. Additionally, a study conducted in China demonstrated that combining ultrafiltration with ozonation could eliminate up to 99.9% of macrolide antibiotics, including spiramycin (SPY). Wajahat et al. (2019) compared the energy demands of various advanced oxidation processes, specifically photocatalysis, ozonation, and photolysis, for the removal of ciprofloxacin (CIP) from pharmaceutical wastewater. Their results showed that photocatalysis using 1 g/L of commercial TiO₂ achieved a 99.1% removal rate within 30 minutes. Although this was comparable to ozonation, which achieved a 98.7% removal rate, the energy consumption for photocatalysis was considerably lower at 8.7 kWh/m³ compared to 36.8 kWh/m³ for ozonation. It is worth noting, however, that the study did not assess additional costs such as operational or material expenses.

Oils

Hydrocarbon oil compounds are characterized by varying carbon chains and functional groups and are extensively utilized as solvents and raw materials across industries such as petroleum, petrochemicals, pharmaceuticals, and cosmetics [Emam and Aboul-Gheit, 2014]. These compounds can result in significant environmental impacts when released as effluents or during oil spills, including disruptions to aquatic photosynthesis and reductions in dissolved oxygen levels, leading to ecosystem imbalances. Aromatic hydrocarbons are generally more toxic than their aliphatic counterparts. In contrast to aliphatic hydrocarbons, which can be either saturated or unsaturated, aromatic compounds are characterized by the presence of a stable benzene ring or rings. The number of fused rings in an aromatic compound's structure affects its photodegradation resistance. For photocatalysis to work, these rings must be cut in order to convert the compounds into inert byproducts. Benzene rings are difficult to photodegrade due to their high stability; longer chains cause carbon dioxide degradation to occur at a slower rate [Kaneco et al., 2006]. After enough time has passed under the radiation lamp, the intermediates are dissolved into the carbon dioxide and water.

Traditional oil spill treatment methods, such as oil recovery, oil booms, oil absorption, and skimming, are not only costly but also require significant manpower [Hsu et al., 2008]. Thus, the alternative method, photocatalytic degradation, has been proposed. In the treatment of oily industrial wastewater characterized by an initial chemical oxygen demand of 1298 mg/L, the application of TiO_2 in conjunction with hydrogen peroxide (H_2O_2) and ferrous ions (Fe^{2+}) resulted in a COD removal efficiency exceeding 80%. The pH of the solution played a pivotal role in the photodegradation process, with the highest removal efficiency observed at the point of zero charge (PZC) of the TiO_2 photocatalyst. This behavior is attributed to the non-ionic nature of oil, which minimizes electrostatic interactions, thereby enhancing photocatalytic activity near the PZC. Both acidic and basic conditions impeded the photocatalysis process. Furthermore, self-decomposition of H_2O_2 occurred at greater temperatures in this investigation, even though temperature generally increases the collision between pollutant molecules and the photocatalyst.

Shivaraju et al. investigated the treatment of real-time wastewater from automobile service stations in India using coated polyscales fabricated from nitrogen-doped TiO_2 (N-TiO_2) particles embedded in ceramic beads and thermocol, facilitating easy separation and recovery of the photocatalyst after treatment. Being less dense than water, these polyscales floated on the surface, interacting with the floating oil and grease. With less than 24 hours of natural sunlight irradiation, oil and grease removal efficiencies were $86.57\% \pm 2$ with thermocol beads and $95.28\% \pm 29$ with ceramic beads. Chemical oxygen demand was condensed from 10,400 to 1396 mg/L with thermocol beads and attained 490 mg/L with ceramic beads, likely due to the advanced porosity and surface area of the ceramic beads, which enhanced interaction with oil molecules. Conversely, Saïen and Shahrezaei demonstrated that petroleum refinery wastewater with a comparatively reduced chemical oxygen demand of approximately 200 mg/L attained a 78% degradation efficiency following just 2 hours of UV irradiation.

Endocrine-disrupting chemicals

Freshwater is essential to the long-term, sustainable growth of wildlife as well as humans. The availability of safe and affordable drinking water has become a significant global environmental concern, with rapid urbanization and industrialization posing serious challenges to water supply. One major source of aquatic pollution is still the discharge of wastewater that has not been treated or has not been sufficiently treated [Nasrollahzadeh et al., 2021].

Pharmaceuticals and personal care products (PPCPs), dyes, heavy metals, pesticides, endocrine-disrupting chemicals (EDCs), and other organic and inorganic contaminants are among the many contaminants that are introduced into natural water bodies as a result of such inappropriate disposal [Schwarzenbach et al., 2006; Huang et al., 2014; Al Sharabati and Sabouni, 2020; Abhinaya et al., 2021]. These substances are known to be toxic and to be a significant risk to human and environmental health. They can cause endocrine system disruptions, liver, lung, and brain disorders, as well as carcinogenic effects and reproductive dysfunctions. Consequently, many international organizations and countries have imposed restrictions on the usage of these hazardous compounds, leading to intensified research on effective removal methods. **Table 2.3** shows various semiconductor-based heterojunction nanocomposites for photocatalytic degradation of EDCs.

An important environmental concern is the existence of endocrine-disrupting chemicals in water bodies, which include sewage, drinking water, and groundwater. EDCs are exogenous chemicals or chemical mixtures that disrupt endocrine functions in organisms [van der Meer et al., 2021]. These substances can be synthetic or natural and are released into the ecosystem through several sources, including domestic sewage, landfill leachates, livestock waste, and industrial effluents. There is an urgent need for efficient and cost-effective water treatment methods to address endocrine-disrupting chemicals, employing physical, chemical, and biological techniques. Traditional methods such as coagulation/flocculation, photocatalysis, separation membranes, ion exchange, adsorption by activated carbon, and AOPs are frequently used for wastewater treatment. While these conventional techniques offer various benefits, they often face limitations, such as low removal efficiencies, complex procedures, high operational costs, and the formation of toxic sludge or by-products. Advanced tertiary treatments (ATTs) have appeared as valid alternatives to address these challenges and improve treatment efficacy [Al Sharabati et al., 2021].

Repousi et al developed a range of photocatalysts by incorporating small amounts (0.5 wt.%) of noble metals, specifically platinum (Pt), ruthenium (Ru), palladium (Pd), and rhodium (Rh), onto commercial TiO₂ (P25) using a wet impregnation technique. These metal-doped catalysts were then evaluated for their effectiveness in breaking down Bisphenol A (BPA) under simulated sunlight. Among the different formulations, the Pt-loaded TiO₂ showed the most effective photocatalytic performance. Interestingly, the Rh/TiO₂ catalyst demonstrated a notable enhancement in BPA degradation when humic acid (HA) was present at a concentration of 20 mg/L, achieving about 2.5 times the activity compared to tests conducted in ultrapure

water. Additionally, when HA was included in the reaction medium, the rate at which BPA degraded increased steadily as the amount of catalyst used was raised from 50 to 400 mg/L.

The zirconium and silver codoped TiO₂ nanoparticles were synthesized for the effective degradation of two hazardous organic pollutants: AB-52 (Acid Black-52) and 17 α -ethinyl estradiol (EE2). The degradation pathways and potential intermediate compounds were analyzed using LC-MS. To assess the phytotoxicity of the middle products generated during the photodegradation process, toxicity tests were conducted using two different seed types, *Phaseolus vulgaris* and *Vigna radiata*. The toxicity analysis indicated that the metabolites formed during degradation were less toxic compared to the original compounds, EE2 and AB-52 [Naraginti et al., 2016]. To facilitate the photocatalytic destruction of Bisphenol A (BPA), several anatase TiO₂@MIL101Cr were produced by the solvothermal approach by [Tang et al. 2020]. The composites were characterized and found to have an octahedral structure resembling that of MIL-101(Cr), but with a reduced particle size of around 300–500 nm. Under ideal circumstances, 59% TiO₂@MIL101Cr might attain 99.4% bisphenol A remediation in 240 minutes under UV exposure. The quantity and surface area of TiO₂ in the composites both affected the photocatalytic degradation [Tang et al., 2020].

Audrey et al demonstrate that an inventive "domino" method was created for the remediation of endocrine-disrupting substances in highly concentrated aqueous effluents. An arene hydrogenation phase precedes a photocatalytic step in this method. The innovative aspect of this two-step treatment is based on the use of TiO₂-supported zerovalent Rh nanoparticles as multicatalytic materials (MCMs) for diethyl phthalate. This model aromatic pollutant is commonly found in the aquatic system. This novel nanocomposite material showed activity in the subsequent processes, the reduction of the aromatic ring, and the photodegradation step. It was simply manufactured using a green, wet impregnation technique. When it comes to photoresistive substances, this environmentally friendly method presents some interesting options., Jianan et al explored a novel approach to removing stubborn endocrine-disrupting chemicals by creating nitrogen-doped hydrochars (NHCs) from pinewood biomass. These materials were applied as carbocatalysts to activate peroxymonosulfate (PMS) in the degradation process. Mechanistic analysis revealed that the presence of graphitic nitrogen played a key role: it encouraged the generation of oxygen-centered persistent free radicals (PFRs) from structural imperfections, supporting a radical-driven degradation pathway. At the same time, graphitic nitrogen also enhanced electron transfer, enabling PMS activation through

a non-radical mechanism. Importantly, the PMS/NHC system not only showed strong pollutant degradation capability but also maintained good stability, making it suitable for practical water treatment applications.

Table 2.3: Photocatalytic degradation of various Endocrine Disrupting Chemicals by Semiconductors Heterojunctions

Photocatalyst	EDCs	Efficiency	Reference
ZnO	Bisphenol A	97.5%	[Alikarami et al., 2019]
Cu ₂ O/BiOI	Bisphenol A	99.9%	[Ponnaiah et al., 2019]
TiO ₂ @ACD@RGO	Bisphenol A	85%	[Wang et al., 2021]
Ag ₂ CO ₃ / BiOBr/CdS	Tetracycline	99%	[Perumal et al., 2023]
CMCD-Fe ₃ O ₄ @TiO ₂	PCBs	83%	[Khammar et al., 2020]
α -Fe ₂ O ₃	Dibutyl phthalate	93%	[Liu et al., 2018]
TiO ₂	Phenol	99.48%	[Zulfiqar et al., 2019]
Ag ₃ PO ₄ /TiO ₂	2,4-dichlorophenoxyacetic acid	98.4%	[Amiri et al., 2021]
BiOBr/Bi ₄ O ₅ Br ₂ /PDI	Bisphenol A 17 α -ethynyl estradiol (EE2) and 17 β -estradiol (E2)	90% 100%	[Wang et al., 2022]
CoFe ₂ O ₄ -GO	Bisphenol A	100%	[Görmez et al., 2022]
TiO ₂ @ZnFe ₂ O ₄ /Pd	Diclofenac	86.1%	[Ahmadpour et al., 2020]
C/N-codopedTiO ₂	Resorcinol	96%	[Al-Hajji et al., 2020]

β -CD-CoFe ₂ O ₄ /PMS	Bisphenol A	99.23%	[Ahmed et al., 2021]
ZnO/WO ₃ /Pt	Estriol (E3)	86%	[Yasir et al., 2022]
N-Bi ₂ O ₃ @SnO ₂	Endocrine-disrupting pesticides	96%	[Choudhary et al., 2022]
Bi ₂ O ₃ /TiO ₂ @rGO	Di(2-ethylhexyl) phthalate (DEHP)	89%	[Zhang et al., 2021]
APTES-modified BiVO ₄	17 α -Ethinylestradiol (EE2)	91.27%	[Pi et al., 2021]
PLA/TiO ₂ /HNT	17 α -Ethinylestradiol (EE2)	71.6%	[Ali et al., 2024]
Gd ³⁺ /BiVO ₄	Bisphenol A	77.02%	[Orona-Návar et al., 2021]
	Bisphenol S	44.36%	
	Bisphenol AF	74.11%	

2.13. Research Gap and Objectives of the Present Thesis

Research Gap

Although there has been considerable progress in wastewater treatment technologies, effective elimination of benevolent endocrine-disrupting chemicals (EDCs) has been a key environmental issue of concern because of their complicated chemical structures, low biodegradability, and the negative ecological and human health impacts. Photocatalytic degradation has been proposed as a novel green technology that can serve to mineralize EDCs by the irradiation of visible light using the generation of reactive oxygen radicals, thereby providing a green substitute to the traditional methods. Nevertheless, some of the drawbacks that exist with the photocatalysts include low visible light absorption, a short recombination of the photogenerated charge carriers, and inadequate surface-active sites, which limit their ability to degrade a variety of EDCs such as 2-chlorophenol, ciprofloxacin, ibuprofen, and paracetamol.

This thesis has filled these gaps through a new combination of transition metal sulfide-based catalysts, including copper sulfide (CuS), cadmium sulfide (CdS), and molybdenum disulfide

(MoS₂), with complementary optical and catalytic characteristics. These materials in isolation and as heterostructures have more visible light absorption, better charge separation, and more reactive sites, which greatly enhance the photocatalytic degradation of the selected EDCs. This study enhances the design of effective and sustainable photocatalytic systems that can be adapted to the degradation of difficult pollutant molecules common in Indian water bodies by incorporating these advanced catalysts.

Objectives

1. Synthesis of transition metal nanoparticles by conventional and microwave processes.
2. Fabrication of cesium-based perovskite materials and their modification by transition metal nanoparticles.
3. Structural characteristic analysis of functional perovskite materials.
4. Endocrine-disrupting chemicals degradation by transition metal nanoparticles-based perovskite functional materials from industrial aquatic waste.

CHAPTER 3

MATERIALS AND METHODS

3.1 MATERIALS:

The synthesis of nanoparticles can be done using a variety of techniques, including chemical co-precipitation, Microwave method, sol-gel method, chemical and physical vapour deposition, etc. This work is related to two synthesis-related methods: Sol-Gel and the Microwave method for the preparation of nanocomposite materials. This chapter discusses many approaches that have been utilized to examine recently synthesized materials CuS, CdS, MoS₂, CdS/Cs₃Bi₂Br₉, MoS₂/CdS, and MoS₂/Cs₃Bi₂Br₉ that are being exploited for photocatalytic degradation. Numerous spectroscopic methods are used to examine and describe the elements, functional groups, and oxidation state of the materials. Microscopic methods were used to characterize the lattice fringes, crystalline structure, and surface appearance of the as-synthesized materials.

3.1.1. Chemicals Required:

Cesium acetate (Sigma Aldrich), Cadmium acetate, sodium sulfide, thiourea, sodium molybdate dihydrate, thioacetamide, oxalic acid, diethylenetriamine pentaacetic acid (DTPA), bismuth tribromide, purchased from Loba Chemi PVT. Ltd India.

3.1.2. Reagents Required:

N, N-dimethylformamide (DMF), dimethyl sulfoxide (DMSO), ethanol, diethyl ether, and distilled water are used for synthesis and stock solution preparation.

3.1.3. Stock solutions of 2-chlorophenol, paracetamol and ciprofloxacin

The 2-chlorophenol, Paracetamol, Ciprofloxacin, and Ibuprofen were made individually by dissolving 0.1 gram of each organic component in a 100 milliliter volumetric flask with distilled water to produce a 100 mL or 1000 ppm stock solution. By dilution, various working concentrations of 2-chlorophenol, Paracetamol, Ciprofloxacin, and Ibuprofen were created from their corresponding stock solutions.

3.2. Preparation of Catalyst

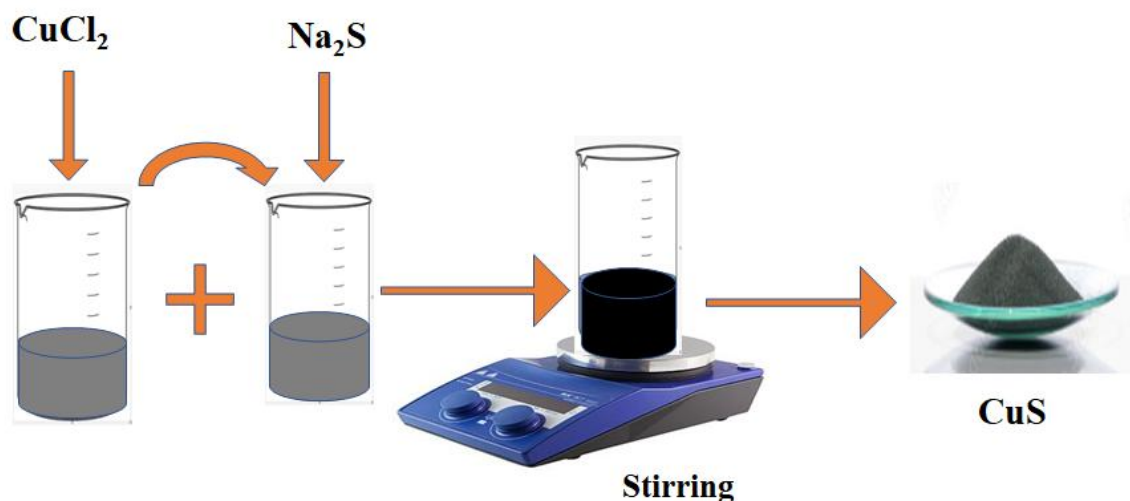
3.2.1. CuS nanoparticles synthesized by sol-gel method

Copper chloride (CuCl₂) and sodium sulfide (Na₂S) are the precursor substances utilized for the production of CuS nanoparticles. Dissolve 13g of CuCl₂ in 100 milliliters of distilled H₂O to get a 1M solution. After that, the solution is agitated for 30 minutes at 100 to 150 rpm at room temperature. The following step in the synthesis is the gelation process. This is achieved by combining sodium sulfide with copper chloride solution. A 1M solution of sodium sulfide (Na₂S) is obtained by dissolving 8g of Na₂S in 100 milliliters of distilled water. At room temperature, the mixture was stirred between 450 and 500 rpm. After 10 to 15 minutes of

constant stirring, the liquid solidified into a gel. After that, this gel was allowed to precipitate for 2 to 3 hours without being disturbed. The precipitate was subsequently dried out in a vacuum oven at 100 °C for an additional period. Following drying, the material was ground into a powder that would be used for future experiments.

3.2.2. CuS nanoparticle manufacturing via the wet chemical coprecipitation method

The present study employed the wet chemical co-precipitation approach to synthesize copper sulfide nanoparticles using CuCl_2 and Na_2S as raw materials. A standard synthesis involved making 1M CuCl_2 (13g) in 100 ml of distilled water, adding 1M sodium sulfide (8g) solution drop by drop, and continuously swirling the mixture on a magnetic stirrer at 70°C and pH 7. CuS nanoparticles are the end product of this process. Filtration was used to gather the nanoparticles, then washing and configuration separation at 2000 rpm for five minutes were used to further purify the final product see scheme 1.



Scheme 1 Schematic diagram for synthesis of CuS nanoparticles

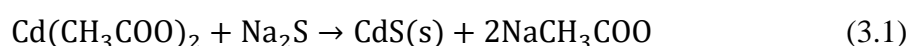
3.2.3. Synthesis of CdS nanoparticle by Sol-gel method

50 milliliters of aqueous solutions of (0.1 M) Cd (ac) and (0.1 M) Na_2S were prepared in order to produce CdS nanoparticles utilizing the Solgel method. The freshly prepared 0.1 M Na_2S aqueous solution was vigorously stirred for 20 minutes while being added drop by drop to the 0.1 M Cd (ac) solutions. The NaOH (1M) solution was added drop wise into the above

suspension under continuous stirring at 60°C until pH raised to 10–11. The mixture gradually changed color as the reaction started, going from translucent to light yellow or cream, and then turning dark yellow after the reaction was finished. After being repeatedly washed with ethanol, the precipitates were centrifuged and vacuum-dried for four hours at 70°C.

3.2.4. Synthesis of CdS nanoparticle by Microwave method

Microwave synthesis of CdS is used in the present study. In 50mL of distilled water, add 13.32g of Cd (ac), 3.9g of Na₂S, and 3.8g of thiourea. Stir for 20 minutes. The solution was microwaved at 80W for 5 minutes. The yellow precipitate was washed with ethanol or distilled water and oven-dried for six hours at 55°C, **Equation 3.1**.



3.2.5. Synthesis of MoS₂ nanoparticle by Solgel method

MoS₂ was synthesized by sol sol-gel method. Take 0.2g of sodium molybdate dihydrate in 8ml of deionized water, add 0.4g of thioacetamide, dissolve it properly on stirring, and then add 0.05g of diethylenetriamine pentaacetic acid (DTPA) and keep for heating at 180°C for 22h. The crystals were kept for drying in an oven for 6 h at 80°C.

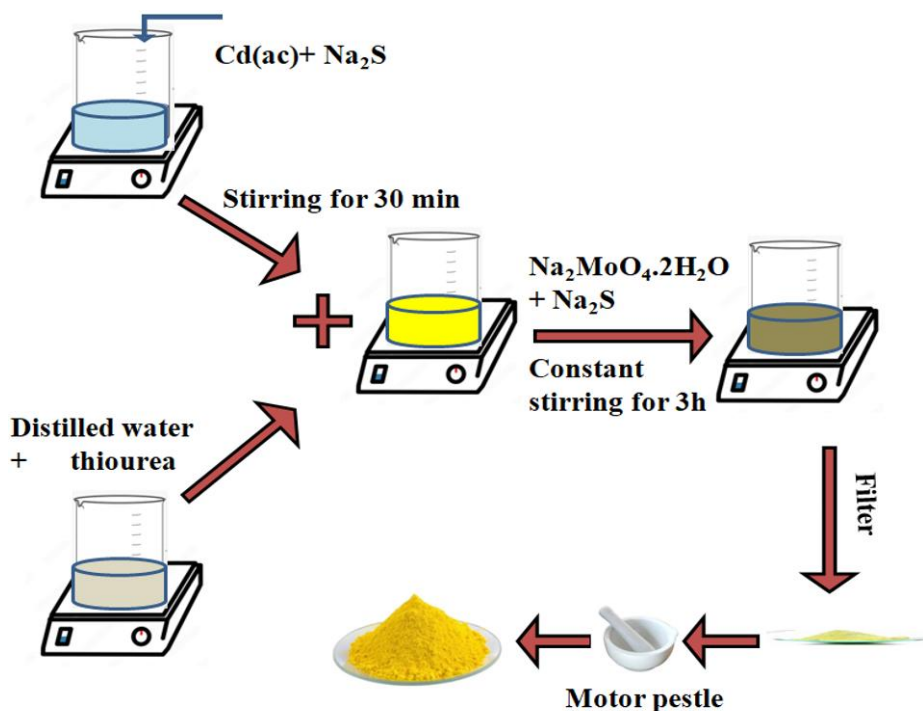
3.2.6. Synthesis of MoS₂ nanoparticle by Microwave method

Pure MoS₂ nanocomposites are synthesized using a microwave-assisted technique. After dissolving 1.33 M of thioacetamide and 0.17 M of Na₂MoO₄·2H₂O (sodium molybdate dihydrate) in 15 milliliters of distilled water and stirring for 20 minutes, oxalic acid (0.22 M) is added dropwise to this homogeneous solution. After that, the combined solution is poured into a 500-milliliter beaker. The solution is heated to 160 °C and subjected to 360 W of microwave radiation for ten minutes. The nanomaterial is washed with ethanol and cooled to room temperature overnight. The crystals that have been rinsed should be dried in an oven at 80°C for a period of 10 hours.

3.2.7. Synthesis of MoS₂/CdS nanocomposite by Solgel method

Dissolve 1M Cd (ac), sodium sulfide, and thiourea in 50 milliliters of deionised water. Stir the mixture until a homogeneous solution (Solution A) is formed. Dissolve 1M sodium molybdate dehydrate, thioacetamide, and Dpta in 15 milliliters of distilled water. Stir the mixture until a homogeneous solution (Solution B) is formed. Mix the Solution A and Solution B. Stir the combined solution at 60 degrees Celsius for 30 minutes until a gel is formed. Filter the gel using a suitable filter apparatus. Wash the obtained solid with ethanol several times to remove

impurities. Dry the washed solid in an oven at 60 degrees Celsius for 6 hours. The dried material is the MoS₂/CdS composite. The various catalyst composites labeled as 1:1M MoS₂/CdS, 1:2M MoS₂/CdS, and 2:1M MoS₂/CdS are shown in Scheme 2.



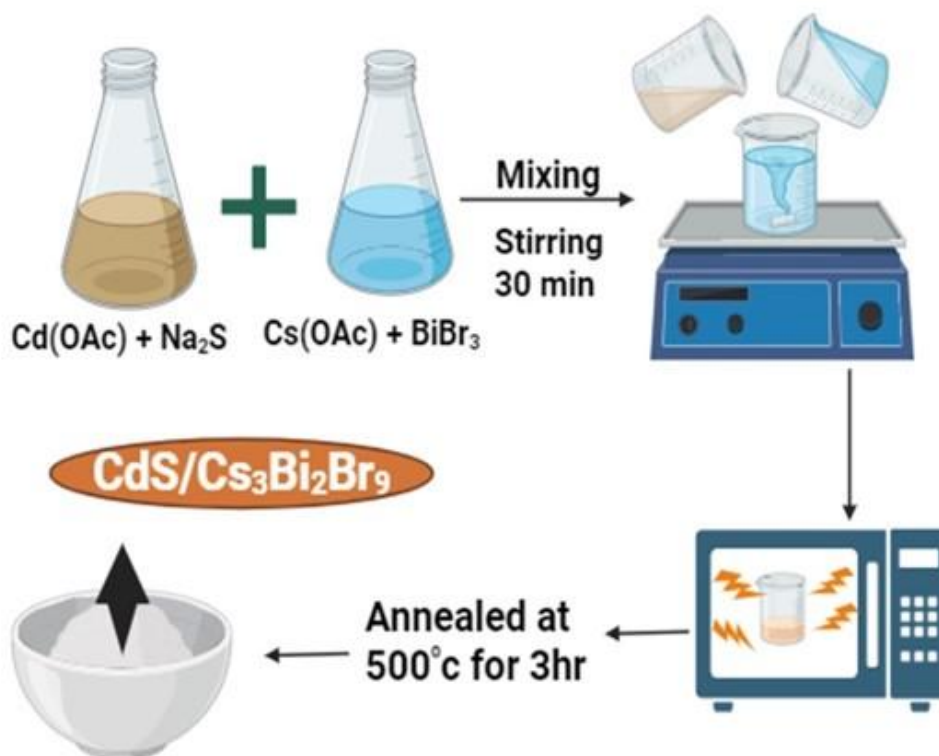
Scheme 2 Schematic diagram for the Synthesis of MoS₂/CdS nanocomposite

3.2.8. Synthesis of Cs₃Bi₂Br₉ nanoparticle by Microwave method

The synthesis of Cs₃Bi₂Br₉ by the Sol-Gel method. Take Cs (ac) (7.245M) and BiBr₃ (1.65M) into a round-bottom flask in DMF/DMSO₄ (7/3 volume) solvent. The mixture was kept in a microwave at 350 W for 10 minutes. To get rid of any remaining DMF, the solid was then dried and rinsed three times with water and diethyl ether. For later usage, store the resulting powder in the dark.

3.2.9. Synthesis of CdS-Cs₃Bi₂Br₉ nanocomposites by Microwave method

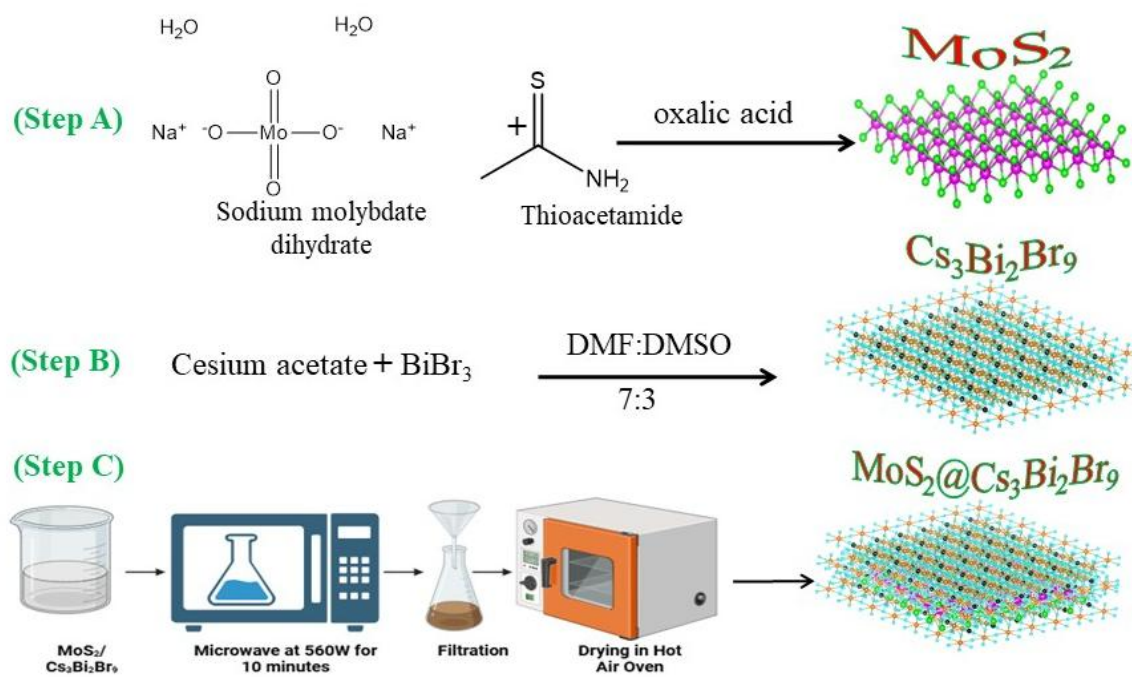
For the microwave method of producing the CdS/Cs₃Bi₂Br₉ nanocomposite. In 7/3 volume of N, N-dimethylformamide (DMF)/ dimethyl sulfoxide (DMSO₄), combine 2.475M of Cs(ac), 1.65M of BiBr₃, and CdS. After 20 minutes of stirring, put the mixture in a microwave set at 560 watts for 10 minutes. After repeatedly washing the composites with diethyl ether and water, it was dried out for six hours at 55 degrees Celsius. The generated products at several Cs₃Bi₂Br₉ doped percentages (1%CdS, 5%CdS and 10%CdS) were classified as 1%CdS/Cs₃Bi₂Br₉, 5%CdS/Cs₃Bi₂Br₉ and 10%CdS/Cs₃Bi₂Br₉ see scheme 3.



Scheme 3: This is a schematic design for the synthesis of nanocomposites

3.2.10. Synthesis of $\text{MoS}_2\text{-Cs}_3\text{Bi}_2\text{Br}_9$ nanocomposites by Microwave method

For the synthesis of $\text{MoS}_2/\text{Cs}_3\text{Bi}_2\text{Br}_9$ nanocomposite using the microwave method. Take 2.475 M Cesium acetate, 1.65 M BiBr_3 , and add MoS_2 in a 7/3 volume in N, N-dimethylformamide (DMF)/ dimethyl sulfoxide (DMSO_4). After 20 minutes of stirring, put the mixture in a microwave set at 560 watts for 10 minutes. After repeatedly washing the composites with diethyl ether and water, it was dried out for six hours at 55 degrees Celsius. The resulting products at several $\text{Cs}_3\text{Bi}_2\text{Br}_9$ doped percentages (1% MoS_2 , 5% MoS_2 and 10% MoS_2) were designated as 1% $\text{MoS}_2/\text{Cs}_3\text{Bi}_2\text{Br}_9$, 5% $\text{MoS}_2/\text{Cs}_3\text{Bi}_2\text{Br}_9$ and 10% $\text{MoS}_2/\text{Cs}_3\text{Bi}_2\text{Br}_9$ see scheme 4.



Scheme 4 Schematic Diagram for synthesis of MoS_2 , $\text{Cs}_3\text{Bi}_2\text{Br}_9$, and $\text{MoS}_2@\text{Cs}_3\text{Bi}_2\text{Br}_9$ nanocomposites.

3.3. Catalytic Characterization Analysis:

To establish a connection between the physicochemical characteristics of the materials and their catalytic activities, it is imperative to consider the physical, chemical, and structural aspects of catalysts. The produced and doped catalysts were characterized using various techniques, including FTIR, XRD, UV-vis, and FESEM/EDS. In this work, the following methods of physicochemical characterization have been explored.

3.3.1. Fourier Transform Infrared Spectroscopy Analysis

Fourier transform infrared spectroscopy is a multidisciplinary analytical method that provides insights into a material's structure. It may also be utilized to verify surface properties like acidity and isomorphism replacement by other material constituents. Infrared light is absorbed by molecules in the far-infrared spectrum, changing the vibrational energy of the molecule. This process is known as Fast Fourier analysis (FT-IR). When recognizing organic compounds with strong charge separation and polar chemical bonds like OH, NH, CH, etc., it is a useful and powerful technique. The IR spectra may be thought of as the fingerprints of each functional group because each one has a distinct vibrational energy. As-synthesized and calcined

materials' IR spectra were captured using the KBr pellet method on an FT-IR spectrometer (Nicolet Avatar 360). A hydraulic press was used to turn the mixture, which contained around 10 mg of the sample and 70 mg of spectral grade KBr, into a pellet. This pellet was utilized to record the infrared spectra in the $4000\text{--}400\text{ cm}^{-1}$ band by scanning it 50 times at a resolution of 4 cm^{-1} . **Figure 3.1** represents the FTIR spectroscopy.

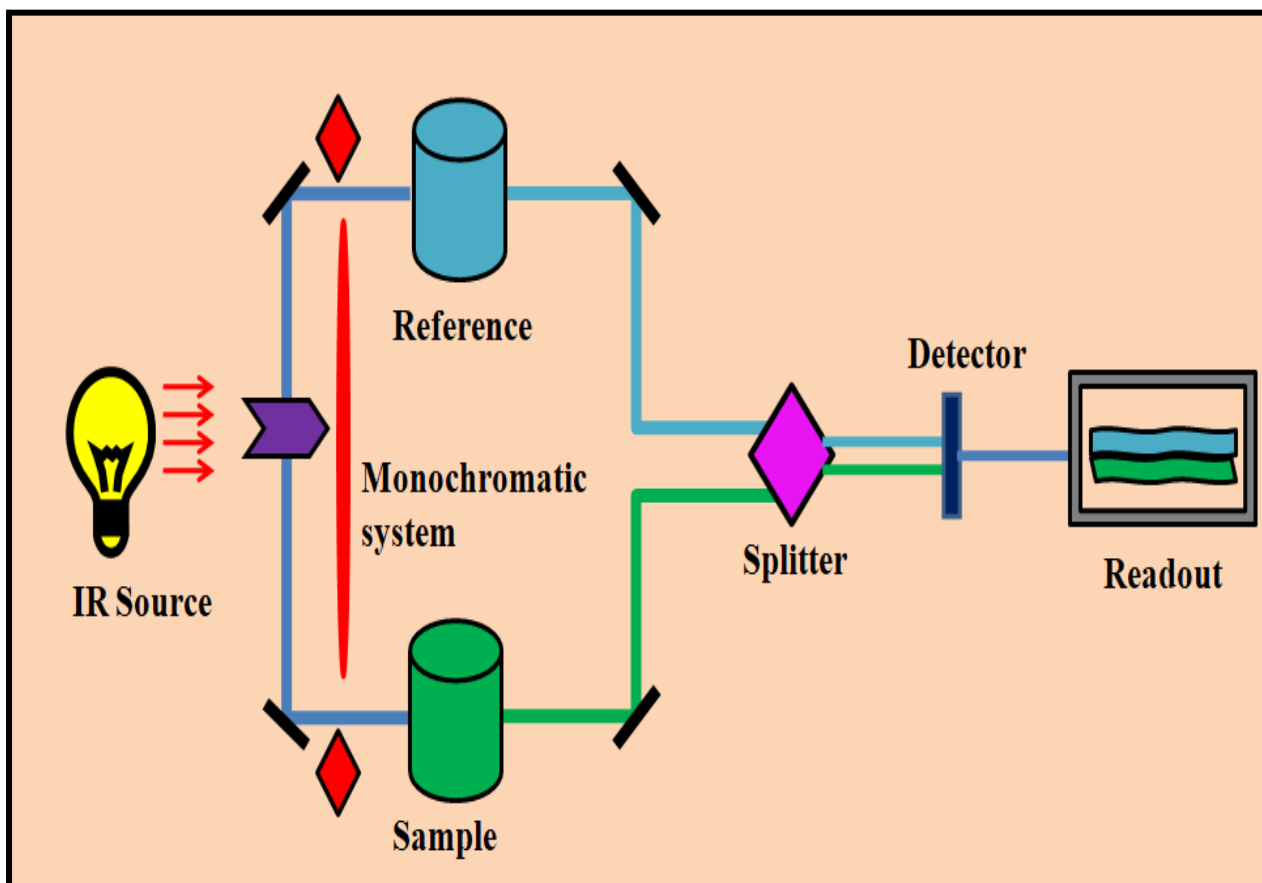


Figure 3.1 Schematic representation of FTIR spectroscopy

3.3.2. X-Ray Diffraction Analysis

The primary purposes of patterns obtained from XRD were to determine the catalyst's unit cell parameter, degree of crystallinity, crystallographic phase content, and crystallite size. High-energy electrons are launched into a target to create the traditional X-ray source. Typically, X-ray sources include $\text{CuK}\alpha$, $\text{CoK}\alpha$, $\text{FeK}\alpha$, and $\text{MoK}\alpha$. Generally, the X-ray source utilized is $\text{CuK}\alpha$ radiation, characterized by a wavelength of 0.154 nm and an energy of 8.04 keV . The X-ray diffraction technique studies how the atoms of a periodic lattice interact with the incident monochromatic X-ray. X-rays are effectively dispersed in the

directions indicated by Bragg's rule in **Equation (3.2)** by atoms arranged in an ordered lattice.

$$n\lambda = 2d\sin\theta \quad (3.2)$$

Where θ is the Bragg's angle, d is the distance between two lattice planes, λ is the X-ray wavelength, and $n = 1, 2, 3\ldots$ is the order of reflection. This rule establishes a relationship between the wavelength of electromagnetic radiation and the lattice spacing and diffraction angle in a crystalline sample. Numerous thousands of distinct reflections can form crystal formations; this unique arrangement is known as the diffraction pattern. It is possible to designate indicators (hkl) to every reflection, signifying its location within the spectrum of diffraction. The crystalline lattice and the unit cell in actual space are related to the pattern via a reciprocal Fourier transform.

Several significant and helpful details about the material were made available by the X-ray diffractogram.

- Whether the substance being examined is crystalline or amorphous.
- Alterations in the dimensions and form of the unit cell concerning the peak's location in an XRD profile.
- The process by which a substance crystallizes during synthesis.
- When a synthetic sample's fingerprints match those of a recognized sample, the presence of an impurity phase can be detected.
- By applying Scherrer **Equation (3.3)**, one may ascertain the crystallite size (D) of a solid sample based on the corrected line broadening (β).

$$D = K\lambda/\cos\theta \quad (3.3)$$

Where λ is the X-ray wavelength (1.54 Å), D is the catalyst's crystal size, K (equal to 0.89) is a constant, E is its full width at half maximum (FWHM), and θ is the Bragg angle (shown in **Figure 3.2** and **Figure 3.3**). The Bruker D8 advanced powder X-ray diffractometer was employed to record the low-angle X-ray diffraction patterns of the materials in the 2θ range of -0.5 - 6° , with a step size of 0.01° and a step time of 5s. $\text{CuK}\alpha$ ($\lambda=1.5418$ Å) was deployed as the radiation source.

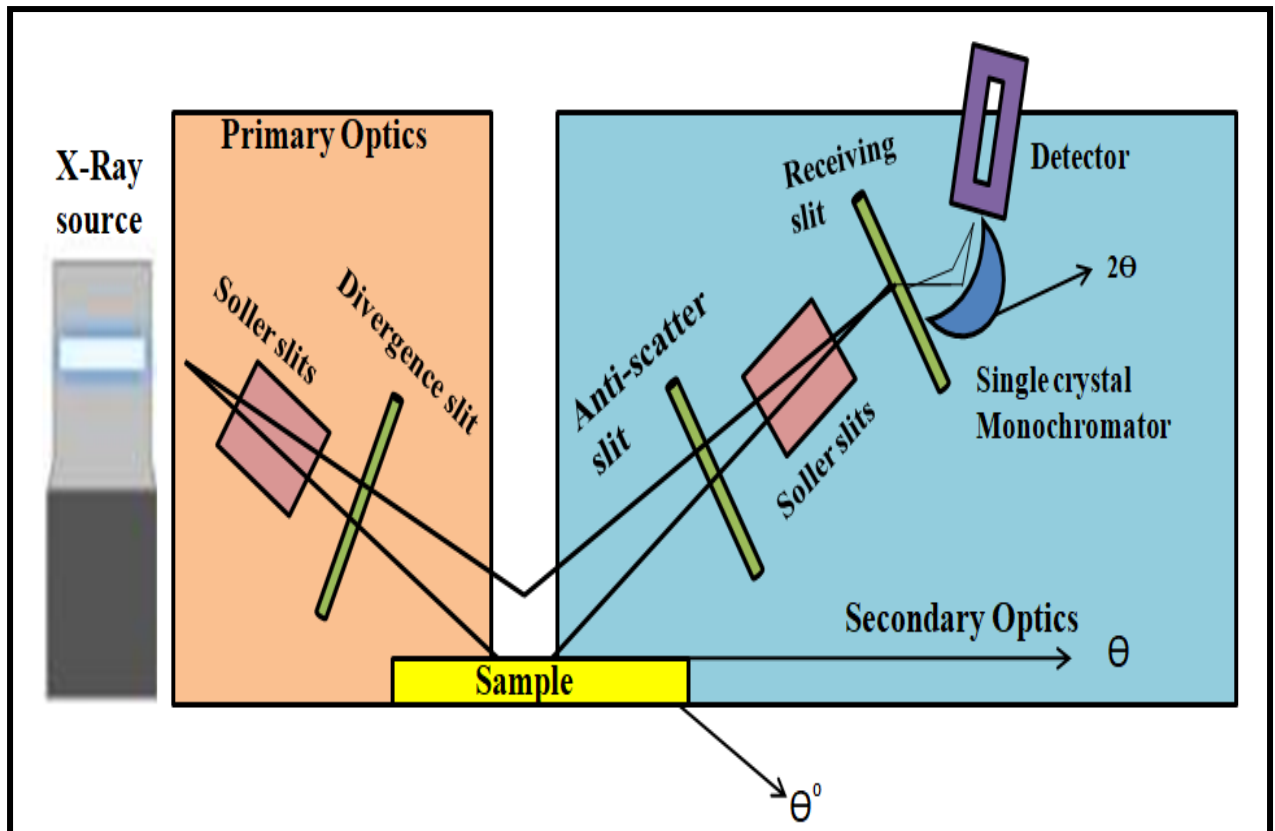


Figure 3.2 X-Ray Diffraction technique

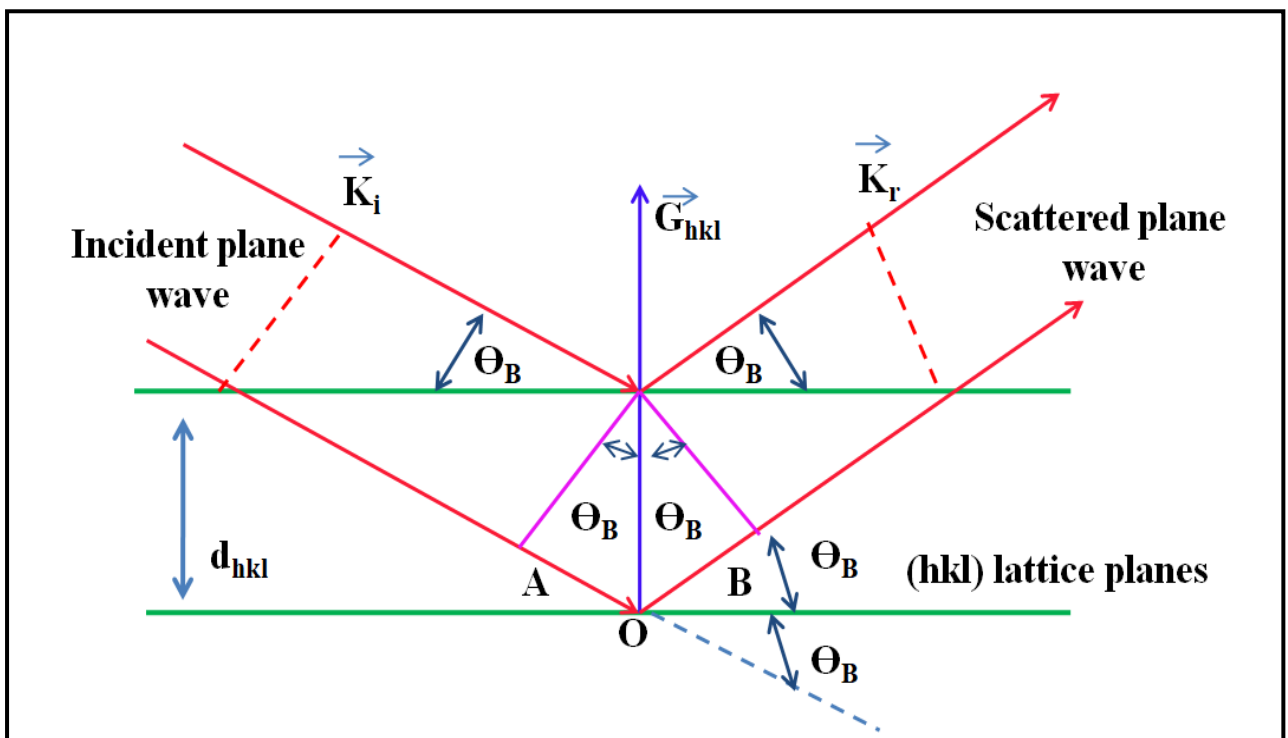


Figure 3.3 Braggs law and Geometrical drawing of crystal planes

3.3.3. Scanning Electron Microscopic Analysis

A scanning electron microscopy may be used to determine the exterior morphology of a material over a range of micrometers to nanoscale. Utilizing a high-energy electron beam, the sample's surface was examined. Inside the target lens are two electromagnetic coils that enable SEM scanning. One pair deflects the beam along the sample in the "x" direction, while the other pair deflects it in the "y" direction. For scanning to be controlled, an electrical signal must be received by at least one set of scan coils for the beam to reach the sample on one side of the lens's central axis. The beam is slightly deflected by employing an alternative set of coils (in this example, the y coils), which results in the beam being scanned again using the x coils. This is accomplished by varying the electrical signal sent to the current pair of coils (x coils) about time, after the first scan. When an electron beam contacts a material, it releases three distinct electrical signals: backscattered electrons, secondary electrons, and auger electrons. To get sample imaging, backscattered electrons were employed. When auger electrons are created, electrons in the visible X-ray region are de-excited. The quick mobility of the beam causes the whole sample surface to be often exposed to beam radiation. The image of the sample is produced by a detector's output. Studying materials that transmit electricity is simpler. Metallic coatings composed of gold, palladium, or platinum can be deposited over non-conductive samples to make them conductive for use in SEM applications. **Figure 3.4** and **Figure 3.5** depicts the SEM instrument image and principle of SEM instrument.

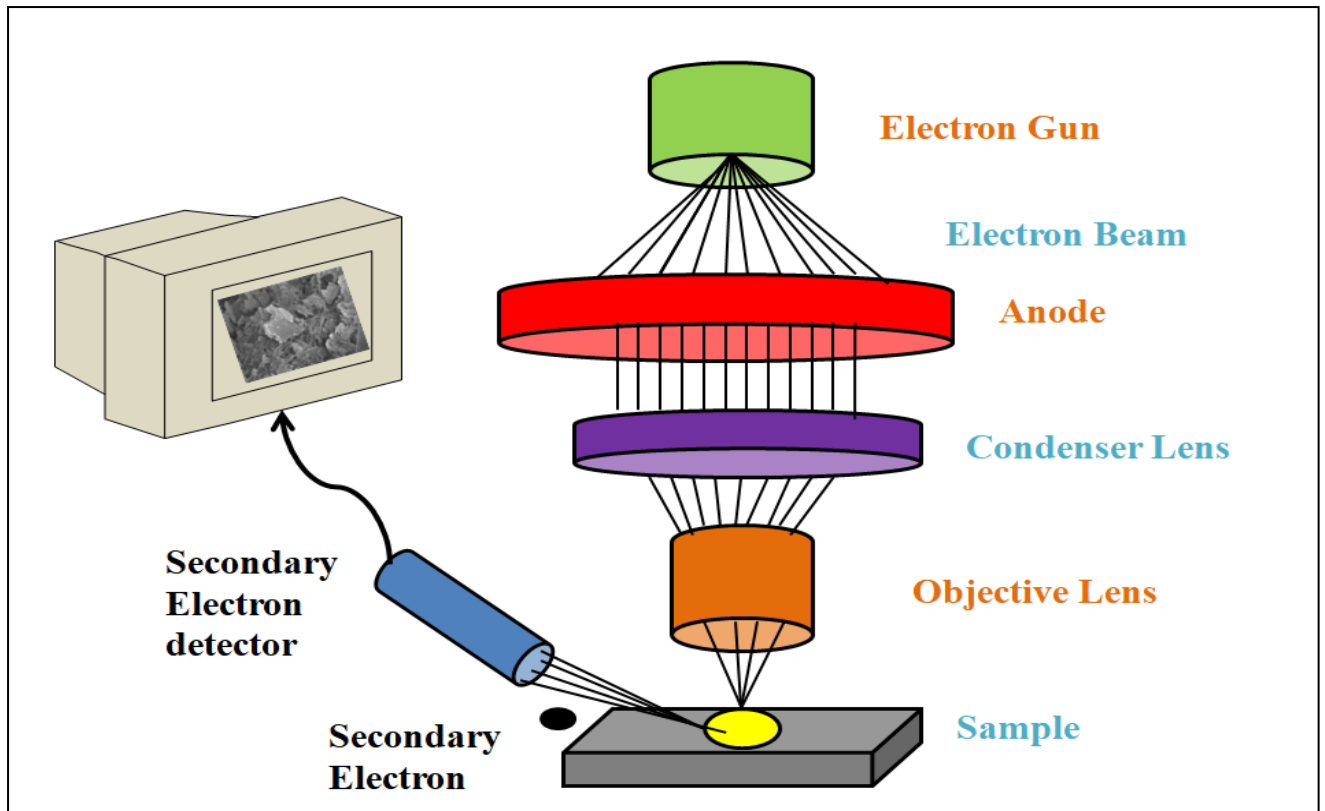


Figure 3.4 Illustration of SEM instrument

3.3.4. Energy Dispersive Spectra Analysis

The natural composition of a tiny cubic micron of material may be ascertained using energy dispersive X-ray spectroscopy (EDS), a potent yet essential instrument. For the purpose of getting natural data about the material under study, the hardware is connected to the SEM. EDS operates by identifying X-rays that an electron beam produces from a test set. The test's atoms are powered by the electron bar, which releases a lot of energy in the form of X-rays through emission. The ability to precisely regulate the electron pillar and gather EDX spectra from a particular spot or particle on the test allows for the examination of several cubic microns of material. However, the bar is visible in a selected set of tests to determine the elements at that place.

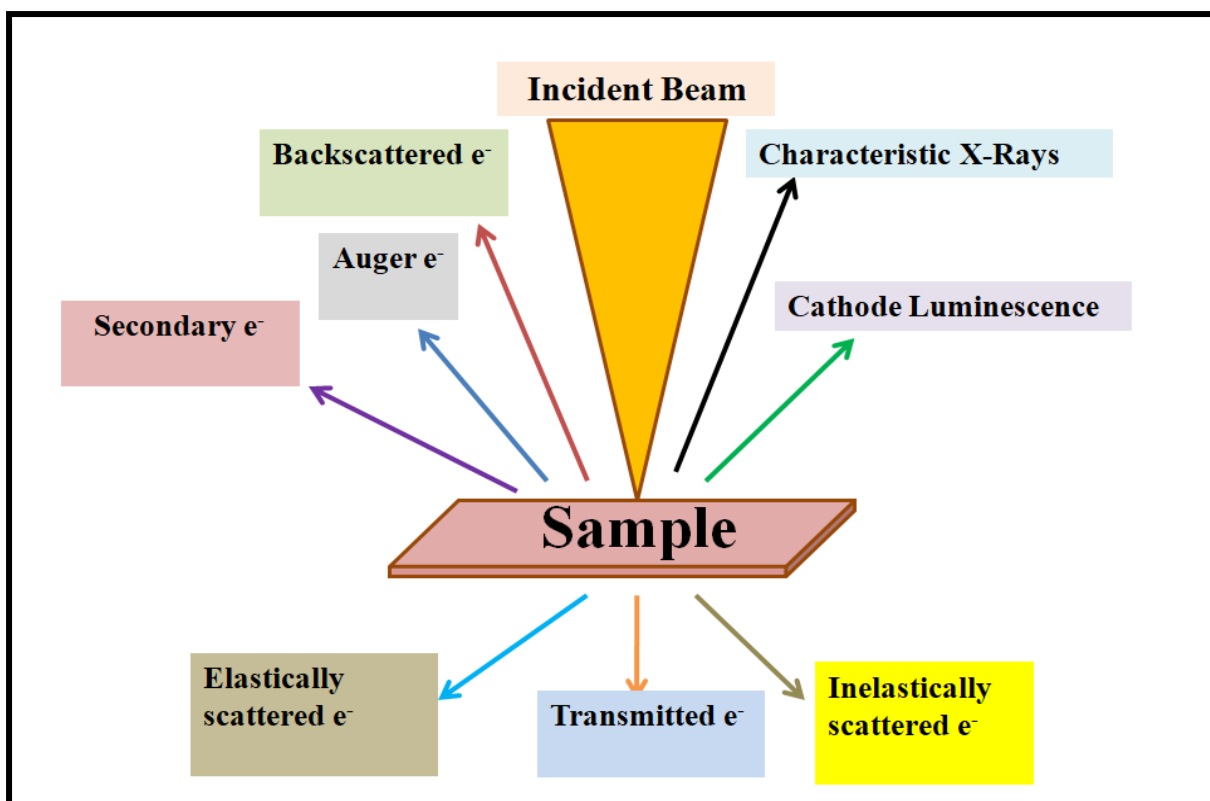


Figure 3.5 Principle of Scanning electron microscopy (SEM)

3.3.5. UV- Vis Spectroscopy Analysis

E-spectroscopy is UV-VIS spectroscopy. Visible (400–800 nm) and ultraviolet (200–400 nm) absorption spectroscopy measures light beam attenuation following penetration or reflection with a substance. **Figure 3.6** shows a schematic illustration of a UV-Vis spectrophotometer. It makes use of visible, neighbouring near-UV and near-infrared (NIR) light spectrums. Molecules experience electronic transitions in this area of energy space. Higher energy levels of outer (valence) electrons can be achieved by promoting them with visible and ultraviolet light. The three forms of electron orbitals that include valence electrons are non-bonding orbitals (n-lone pair electrons), σ bonding orbitals, and π bonding orbitals. The bonding orbitals of sigma (σ) are generally less energetic than those of (π) bonding orbitals, which are less energetic than non-bonding orbitals. The anti-bonding or empty orbitals (π^* and σ^*) have the highest energy. Electronic transitions are shown in **Figure 3.7**, an energy level diagram. Only the two lowest energy transitions the leftmost and blue-colored ones among the six are possible with the energies present in the 200–800 nm range. An excited state is the outcome of energetically advantageous electron promotion, which typically occurs from the highest occupied molecular orbital (HOMO) to the lowest unoccupied molecular orbital (LUMO).

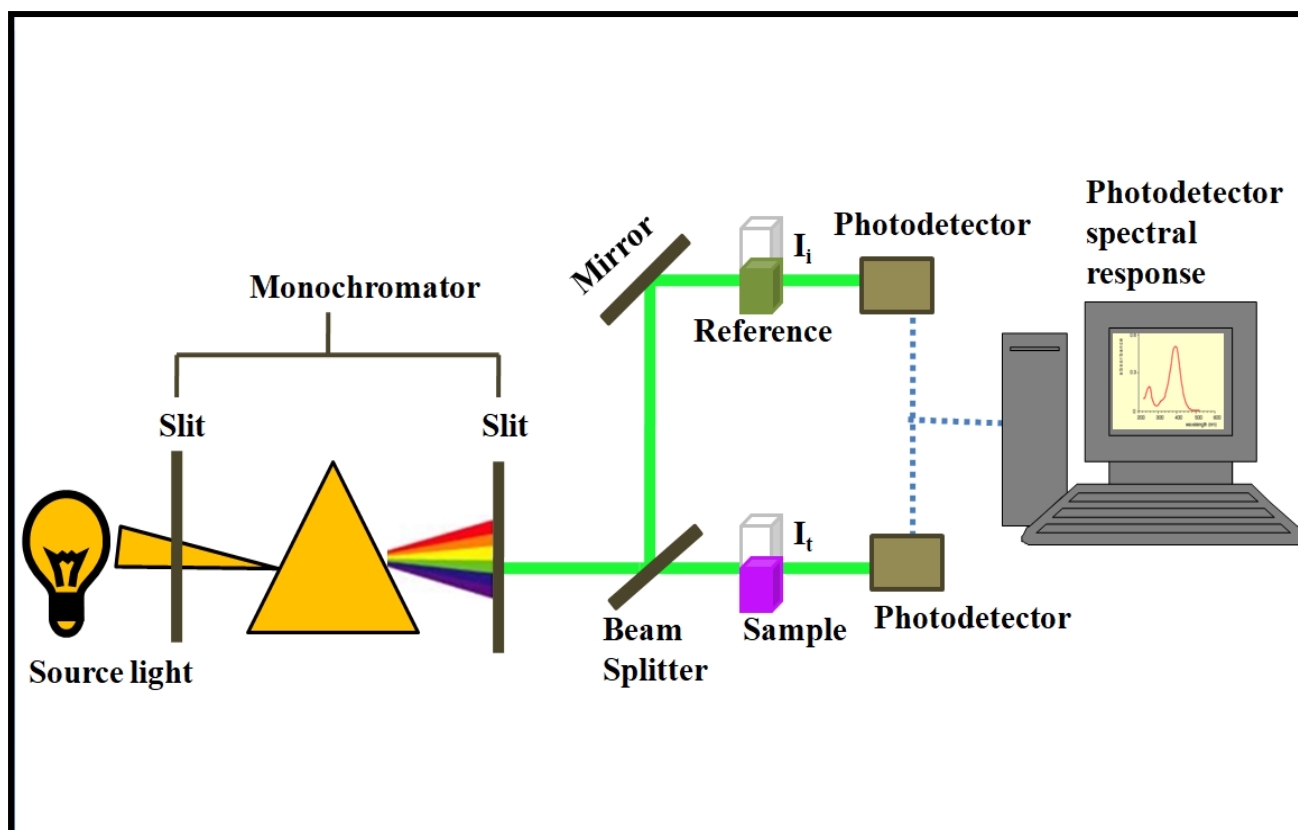


Figure 3.6 Schematic illustration of a UV-Vis spectrophotometer

UV-Vis spectroscopy is especially useful for finding conjugated systems with higher absorptions due to its ability to discriminate transitions ($\pi \rightarrow \pi^*$) and $n \rightarrow \pi^*$ involving lone pairs and orbitals. Additionally, compounds that need energy in the UV/Vis range to remove an electron from one atom and place it on another may give rise to absorption bands. The term "charge transfer excitation" refers to this procedure. Chromophores are defined as molecules that may display any of the above-mentioned kinds of electronic transitions. A chromophore is a unique functional group that stands alone, not connected to any other group, and it exhibits remarkable absorption in the visible or ultraviolet spectrum. The most dominant ones are (C=O) and (C=C), which demonstrate the transitions ($\pi \rightarrow \pi^*$ and $n \rightarrow \pi^*$, respectively). A set of chemicals will typically absorb light at almost the same wavelength if they all share the same functional group and no other complicating variables are present. Therefore, it is easy to see that a compound's spectrum may be a highly useful tool in identifying the functional groups included in the molecule when it is connected with information from the literature for known compounds.

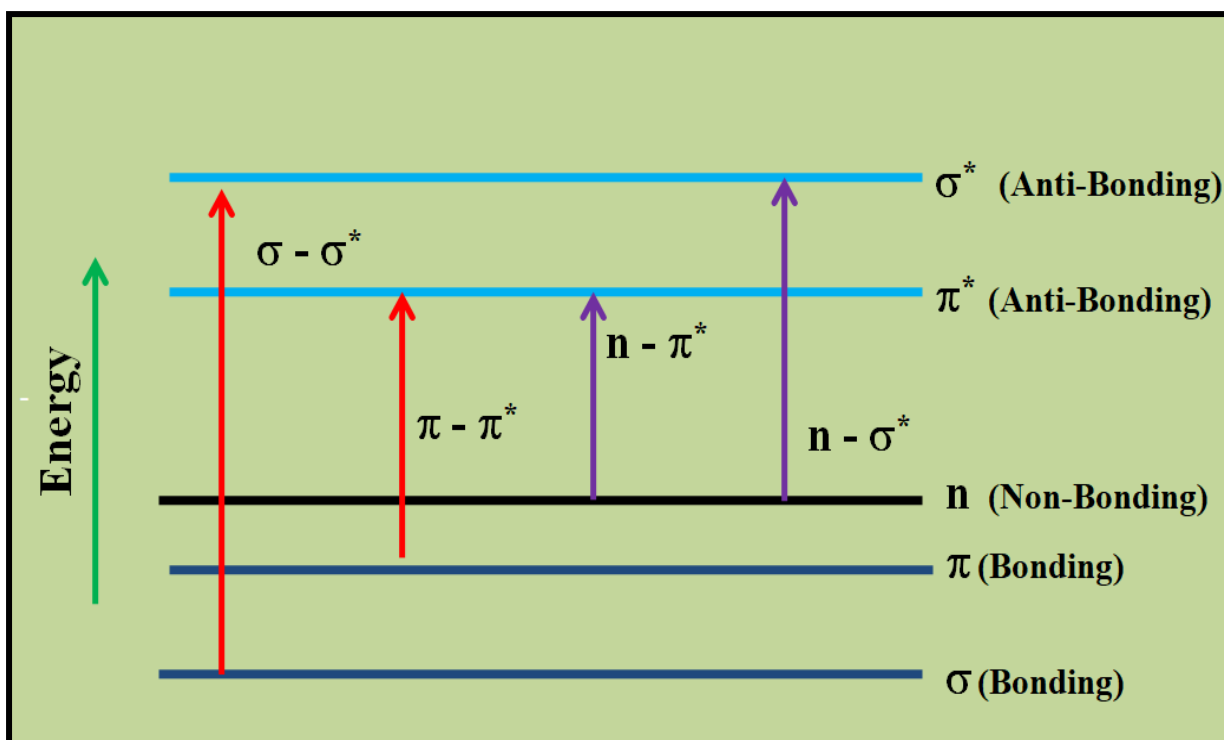


Figure 3.7 Energy level diagrams

3.3.6. Thermogravimetric Analysis

The thermoanalytical approach measures the change in sample weight while heating the sample steadily in an air or nitrogen environment. This method works well for quantitative investigation of thermal processes including mass changes brought on by dehydration, desorption, evaporation, decomposition and gas adsorption. It is common practice to investigate the structural stability of molecular sieves using Thermogravimetric analysis (TGA). It offers details on the range of temperatures needed to release adsorbed water, break down blocked organic cations, alter the structure of molecular sieves, and undergo phase shifts. The sample and the reference material were simultaneously heated or cooled at a constant rate. The measurement of transition or reaction temperatures was then done as a function of the temperature differential between the reference and sample. It gave important details on the materials' high-temperature endothermic and exothermic behaviours. Thermogravimetric analysis (TGA) graphic illustrations are shown in **Figure 3.8**. TGA of the materials (Perkin Elmer Diamond series) was carried out using 10 mg of the sample in the 50–800 °C temperature range, under N₂ environment and at a heating rate of 10 °C min⁻¹.

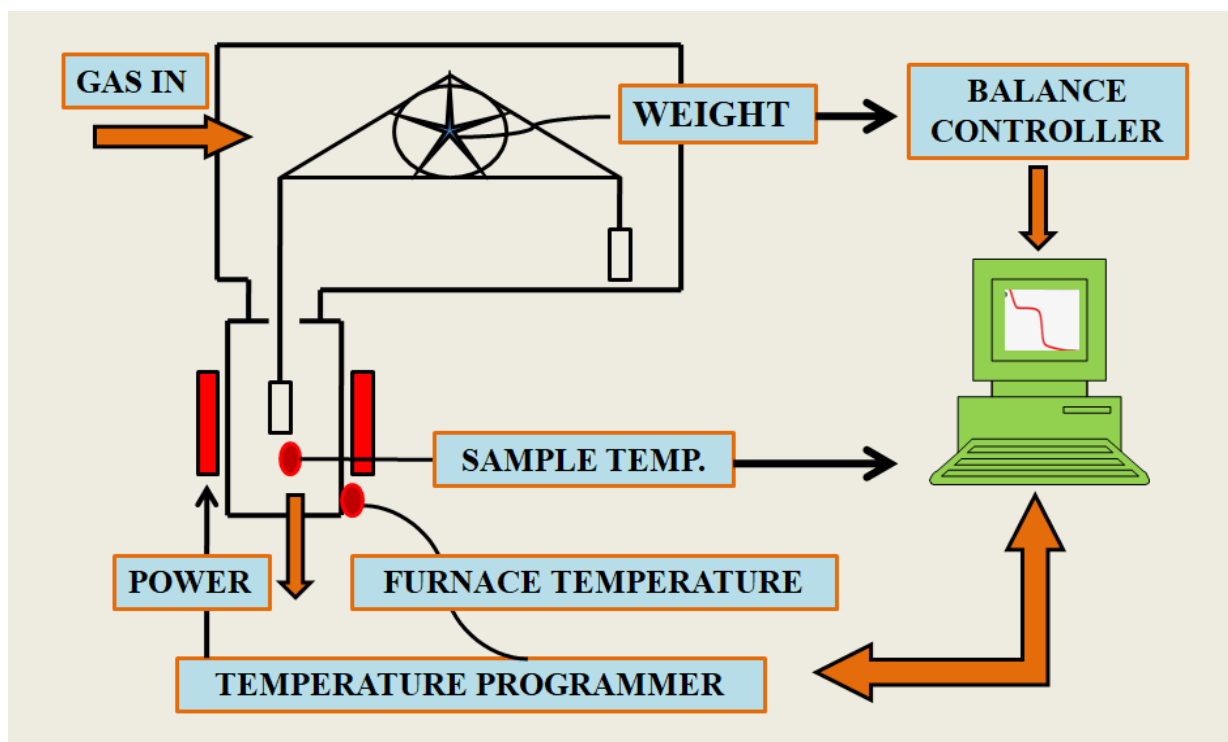


Figure 3.8 Thermogravimetric analysis (TGA) graphic illustrations

3.4. Photocatalytic degradation activity test/ Methodology of Various EDCs

To enable the photocatalytic degradation of pollutants at varying pH levels, all samples were subjected to the same amount of visible light (Xe lamp) in a thermostatically controlled water bath. The pH of the solution was maintained at a consistent level with a glass electrode, along with 0.1N NaOH and 0.1N M HCl. To examine the comparative degradation of pollutants, a 30 mL polluted solution containing 10 mg of catalytic material was subjected to UV-visible light at a shaking speed of 60rpm for 3 hours, respectively. The contaminated solution was filtered using Whatman filter paper after 3 hours of light irradiation, and absorbance was recorded at the peak wavelength of 243 nm using a UV-visible spectrophotometer. **Equation 3.4** was employed to ascertain the % degradation efficiency of the contaminated solution. The identical methodology was employed in the batch experiment to photodegrade 2-chlorophenol, paracetamol, ciprofloxacin, and ibuprofen solutions by as-prepared photocatalysts under irradiation of light.

$$\text{Percent degradation} = \left(\frac{C_0 - C_t}{C_0} \right) \times 100 \quad (3.4)$$

C_0 represents the beginning concentration of 2-chlorophenol, paracetamol, ciprofloxacin and ibuprofen while C_t is the concentration of Paracetamol remaining in solution at time t .



Scheme 5 Schematic diagram of the experimental set up for degradation of various EDCs

CHAPTER 4

RESULTS AND DISCUSSION

Chapter-4

Synthesis and characterization studies of CuS nanoparticles synthesised via the wet chemical coprecipitation method and their photo-degradation application of 2-chlorophenol

4.1. Introduction

In recent years, the increase of process industries utilizing significant pollutants, including nitrophenols, dyes, herbicides, and pesticides, has occurred due to population growth and urban development [Kumar et al., 2018]. According to Gaurav Sharma et al., one of the primary issues is the presence of extremely dangerous and deadly chemicals in the water and wastewater that the chemical factories release. Due to the severe bioaccumulation, persistence, and toxicity, chlorophenol substances, which are increasingly utilized in agriculture, manufacturing, and medical treatment, are being released into the environment in greater quantities. This hurts both human' health and the environment [Diao et al., 2020]. Additionally, CPs show toxicity towards the development and metabolism of microorganisms. Trace chlorophenol is ineffective in eliminating these compounds from water sources and drinking water, and it is crucial to acknowledge the risk to water quality safety posed by microbial leakage [Olaniran et al., 2011]. Physical adsorption facilitates the rapid transfer and concentration of chlorinated phenol contaminants, in contrast to the decomposition and full mineralization of pollutants, which may lead to secondary pollution [Alkaram et al., 2009; Zhou et al., 2010]. The primary way for diminishing CP pollutants is the traditional chemical reduction-oxidation process; yet, this technique experiences high operational costs and stringent requirements for the reaction apparatus. This procedure often produces by-products and is challenging to fully mineralize. Removing pollutants from water is a challenging issue [Yin et al., 2012]. Recently, Suman et al. demonstrated that ZnO and La-doped ZnO photocatalysts were employed to investigate the degradation of 2-chlorophenol (2-CP) under optimal pH, irradiation duration, and catalytic dosage. At an optimum pH of 2, ZnO and La-doped ZnO exhibited maximum degradation efficiencies of 75.85% and 83.92%, respectively, utilizing a catalytic dose of 10 mg and an irradiation duration of two hours.

The Advanced oxidation processes, including photo-Fenton technology, are currently proposed as effective methods for the degradation of chlorophenol contaminants [Della-Flora et al., 2020]. The photo-Fenton process offers a promising approach to effectively eliminate organic

pollutants by harnessing the power of accelerated electron transfer between H_2O_2 and iron- or copper-based photocatalysts under light stimulation. This process has the potential to generate even more active species like $\cdot\text{OH}$ [Dong et al., 2019]. The photo-Fenton method provides additional advantages such as cost-effectiveness, mild reaction conditions, high catalytic efficiency, and operational simplicity, effectively addressing the limitations of traditional techniques for eliminating chlorophenol pollutants [Han et al., 2020]. The field of photo-Fenton reactions has seen a surge in research on conventional Fe-based catalysts. Most photo-Fenton reactions exhibit a limited pH range (2.8-3.5), with the degradation efficacy significantly diminished at elevated pH levels due to the formation of iron hydroxide precipitates and the delayed reduction of Fe^{3+} to Fe^{2+} [Al Kausor et al., 2021]. Furthermore, it is important to note that these catalysts tend to pay higher costs, as they predominantly rely on UV radiation instead of utilizing sunlight or visible light. Researchers consistently seek innovative approaches to modify the catalysts to effectively tackle the previously mentioned challenges. Metal sulfide nanoparticles in the II–VI group of semiconductors have attracted a lot of interest as crucial materials for lithium-ion battery [Liou et al., 2004], solar cell [Li et al., 2017], light-emitting diode and antibacterial activity [Xu et al., 2014], electrocatalytic H_2 evolution [Gupta et al., 2014], and photocatalytic applications [Ayodhya et al., 2018]. Recently, there has been considerable interest in photocatalysis as a promising approach to tackle the various challenges related to aqueous environmental pollution. Among the challenges we face are the effective decomposition of detrimental substances such as dyes, insecticides, and antibiotics when subjected to sunlight [Seo et al., 2017; Sharma et al., 2018]. In addition, a class of metal sulfide nanomaterials has been designed for pollutant degradation in a range of shapes and sizes (flowers, rods, ribbons, etc.) due to their large surface-to-volume ratio and the quantum confinement effect, which gives them their distinctive structure, electrical, magnetic, and optical properties [Shahi et al., 2018; Chandrasekar et al., 2015]. Recent years have seen a surge in interest from the theoretical and experimental communities in the production of nanostructures. These materials have been the subject of substantial study because of their unique chemical and physical properties. The materials with nanostructures were created using copper sulfide nanostructures using various processes. Some examples of these methods are chemical bath deposition, sonochemical analysis, hydrothermal treatment, wet chemical treatment, and solvothermal treatment. A p-type semiconductor, such as copper sulfide (CuS), is inexpensive, non-toxic, environmentally benign, and has a narrow energy gap (1.63-2.5 eV) [Ayodhya et al., 2016]. The CuS nanoparticles display fascinating chemical and physical properties based on their size and structure. It can be triggered by visible light, significantly

enhancing the light's effectiveness for application and priming it for a Fenton-like catalyst. The implementation of CuS as a Fenton catalyst in practical scenarios remains challenging. Initially, CuS nanoparticles exhibit a tendency to agglomerate, hence diminishing their capacity for reusability as a catalyst. Furthermore, diminished catalytic degradation efficiency results from inadequate photogenerated carrier separation efficiency and low quantum yield [Zhang et al., 2023]. Ultimately, light exposure induces the rapid corrosion and oxidation of CuS nanoparticles.

This study estimated the photodegradation activity of the produced CuS nanoparticles by calculating the elimination efficiency of 2-CP in an aqueous solution under visible light. Researchers have looked at how catalyst crystallinity, optical absorbance, pH of the solution, and catalyst concentration all play a role in photodegradation.

4.2. Results and Discussion

4.2.1. Characteristics studies

Fourier transform infrared spectroscopy Analysis.

FTIR spectroscopy was employed to ascertain the presence of functional groups of vibration bands in the synthesized materials. **Figure 4.1** illustrates the FTIR spectra of the synthesized CuS nanoparticles, recorded at ambient temperature within the wavenumber range of 4000-500 cm^{-1} . An evident absorption band at 3500–3000 cm^{-1} , indicative of the associated hydroxyl groups, is observable in the FTIR spectra of each sample. The residual peaks, situated between 1630 and 1500 cm^{-1} , signify moisture-laden water and are linked to the stretching vibrations of a hydroxyl group. The stretching bands of CuS nanoparticles are shown by the peak observed between 750 and 500 cm^{-1} [Lai et al., 2019]. A comparative comparison of both approaches reveals analogous peaks for Cu-S within the range of 750 to 500 cm^{-1} .

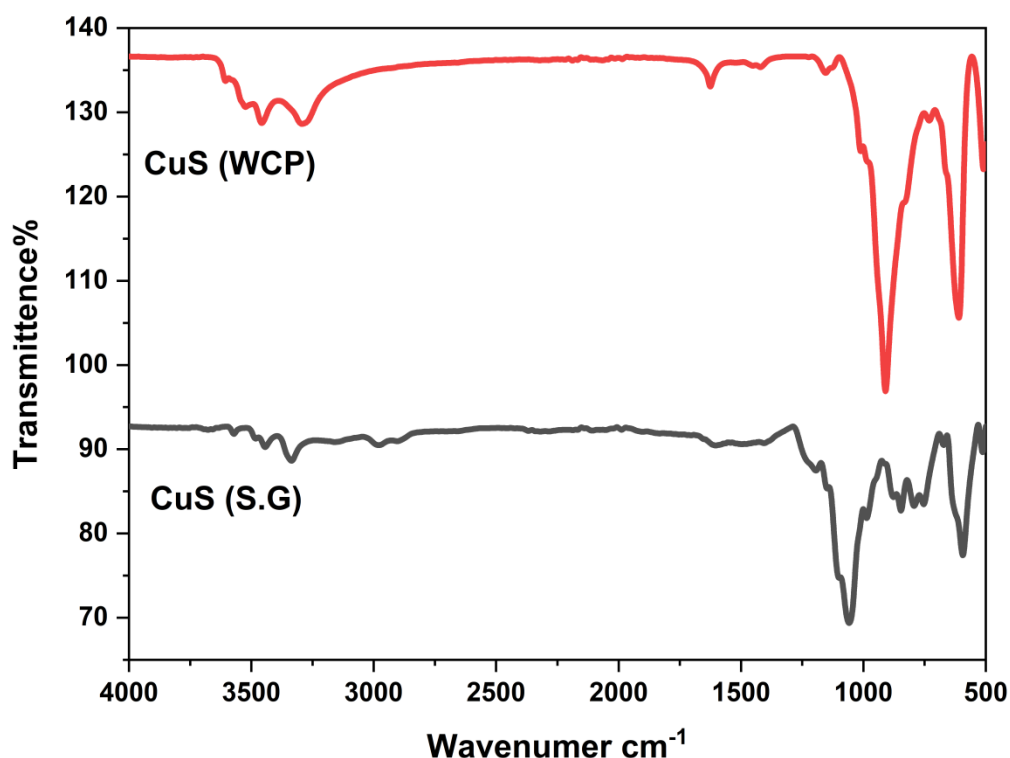


Figure 4.1 FTIR spectra of CuS nanoparticle

X-ray diffraction Analysis

The X-ray diffraction (XRD) analysis of CuS semiconductor nanoparticles confirmed their crystallization in a hexagonal phase. Distinct diffraction peaks were observed for CuS nanoparticles synthesized via wet chemical co-precipitation (CuS WCP) and sol–gel (CuS SG) routes at 2θ values of 27.51° , 31.46° , 32.26° , 39.54° , 49.11° , 53.15° , and 57.12° . These peaks correspond to the lattice planes (101), (102), (103), (106), (110), (108), and (203), in agreement with the standard JCPDS card no. 78-0876, thereby confirming high crystallinity (**Figure 4.2**). The slight broadening of the peaks and reduction in intensity are indicative of the nanoscale dimension of the particles. In addition, the presence of a few extra peaks can be attributed to moisture adsorption on the precursor surface during synthesis or during measurement [Ayodhya et al., 2019; Patil et al., 2023].

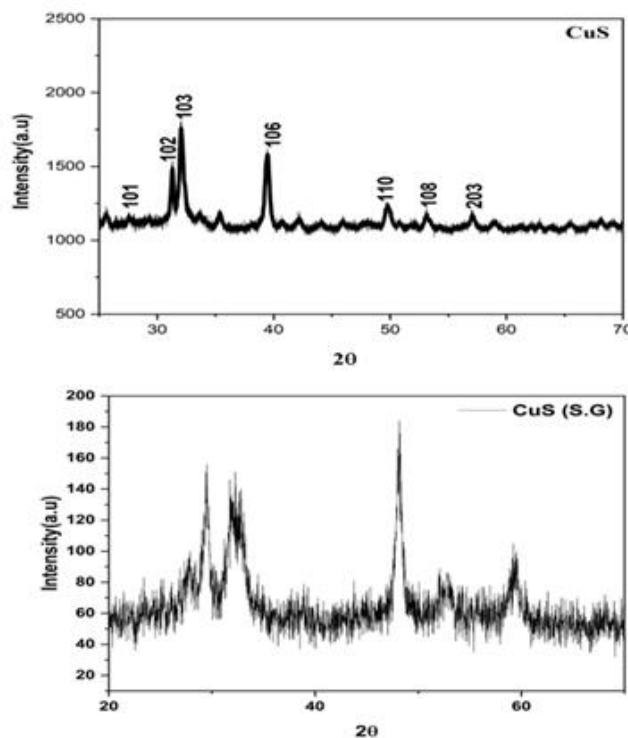


Figure 4.2 X-ray diffraction of CuS nanoparticles produced via sol-gel and wet chemical co-precipitation techniques

TGA/DSC

The CuS nanoparticles' thermal stability was investigated using TGA measurements, which were carried out in the range of 30 to 1000°C at a heating rate of 10°C/min (refer to **Figure 4.3**). According to Gupta et al., this method entails manipulating a sample's temperature in a controlled environment and then measuring the resulting mass change. Understanding a material's moisture content, degradation behaviors, thermal stability, and chemical transformations requires this technique. The samples' TGA curves show many distinct mass loss phases, which correspond to the gradual breakdown and destruction of the unreacted molecules. These steps start with the desorption of adsorbed atmosphere components and continue all the way to the production of absolute ash. A small decrease in mass is seen at around 272°C. The reduction in concentration is because some of the CuS is reduced to Cu₂S. At the same time, there is another peak in the -weight loss direction, which indicates that the water content of the sample has been removed. Near 380°C, there is also a noticeable exothermic peak and a small subsequent mass increase. The presence of oxysulfate and copper

sulfate compounds in the CuS sample is indicated by this. This peak's exothermic properties suggest that heat is being released during the transformation. Insights into the CuS material's thermal stability, phase transformations, and chemical reactions during heating are provided by these detailed thermal profiles acquired through TGA. In order to optimize the material's processing conditions and determine its suitability for various applications, it is crucial to understand these thermal behaviours [An et al., 2015].

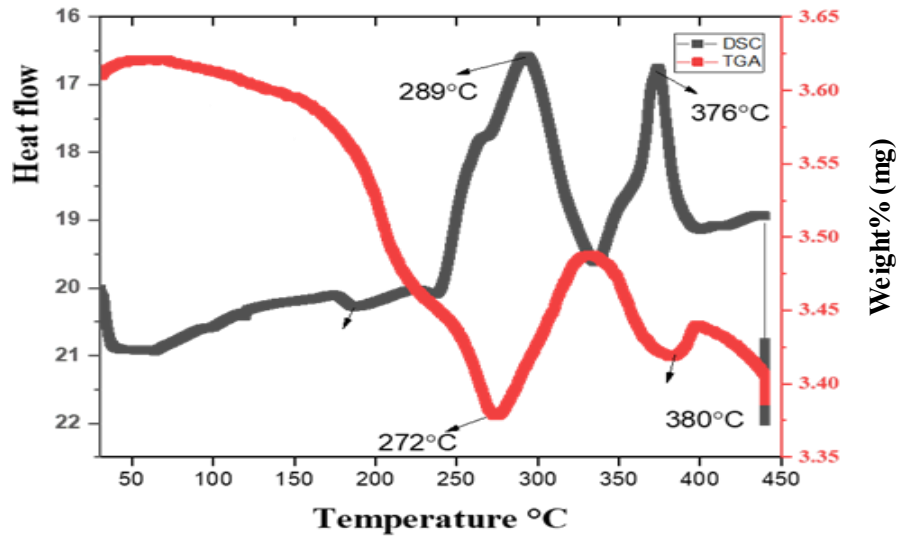


Figure 1.3 TGA/DSC of CuS nanoparticle (wet chemical co-precipitation method)

UV-Visible Spectroscopy

According to Riyaz et al., the band gap was determined to be 2.89 eV by applying the Solgel method and extrapolating the data. In contrast, our method for analyzing the UV-visible absorbance spectra of CuS nanoparticles produced by wet chemical co-precipitation (200 to 800 nm) allows one to use the spectra to determine the optical band gap using the Tauc equation (**Equation 4.1**) [Li et al., 2017; Nafees et al., 2012]. The anticipated bandwidth value of 2.1 eV is in good agreement with the previous finding in **Figure 4.4**. Our method minimizes the bandwidth gap, which allows it to find better outcomes than the present methodology.

$$(\alpha h\nu) A^{1/n} = (h\nu - E_g) \quad 4.1$$

For directly permitted transitions, where $n = 1/2$, the coefficient of absorption is denoted by $\alpha = -\ln T$, $h\nu$ is the photon's energy, A is the optical transition-dependent constant, and ν is the

incident beam's frequency, the intercept (E_g) is obtained by extending the linear segment of the curve until it intersects with the x-axis. Tauc's plot shows a direct relationship between $\alpha h\nu/2$ and $h\nu$, and the band gap for direct transitions is given by its intercept on the X-axis.

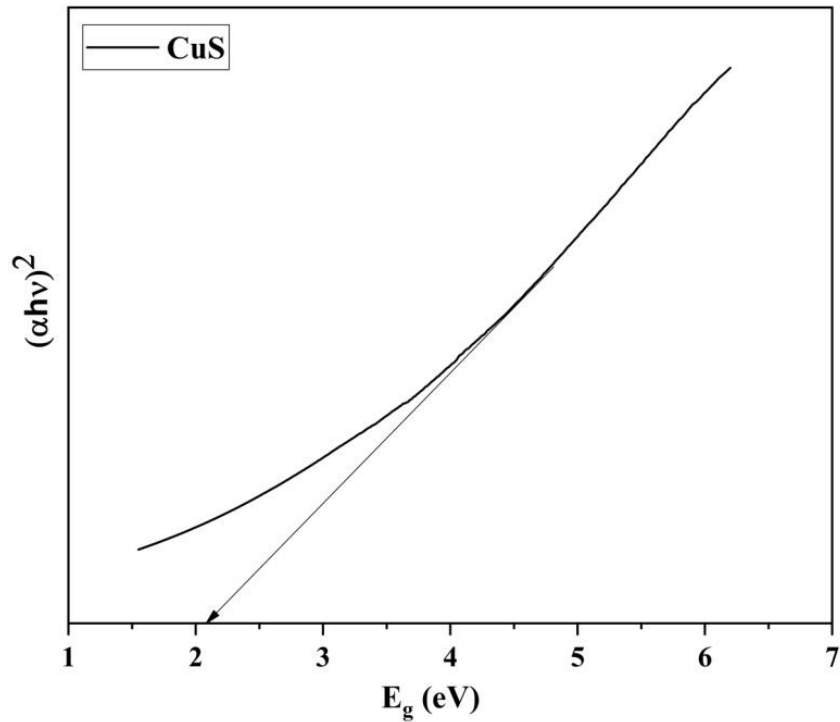


Figure 4.4 Tauc plot of CuS nanoparticle (wet chemical co-precipitation method)

SEM/EDX Spectrum

The morphology of the sample was investigated using a scanning electron microscope (SEM). Using its magnifications, the corresponding images show that the CuS nanoparticles are uniformly dispersed and have a spherical shape. In contrast, scanning electron microscopy (SEM) images of CuS produced using the sol-gel method reveal a larger particle size compared to CuS produced using the wet chemical co-precipitation method. In **Figure 4.5**. As you can see from the spectrum, Energy-dispersive X-ray spectroscopy (EDX) was used to conduct the elemental analysis. **Figure 4.6** shows the EDX spectra, which confirm the sample's Cu, S, and O concentrations. The elements found in the CuS nanostructures are graphically represented and subjected to quantitative analysis [An et al. 2015].

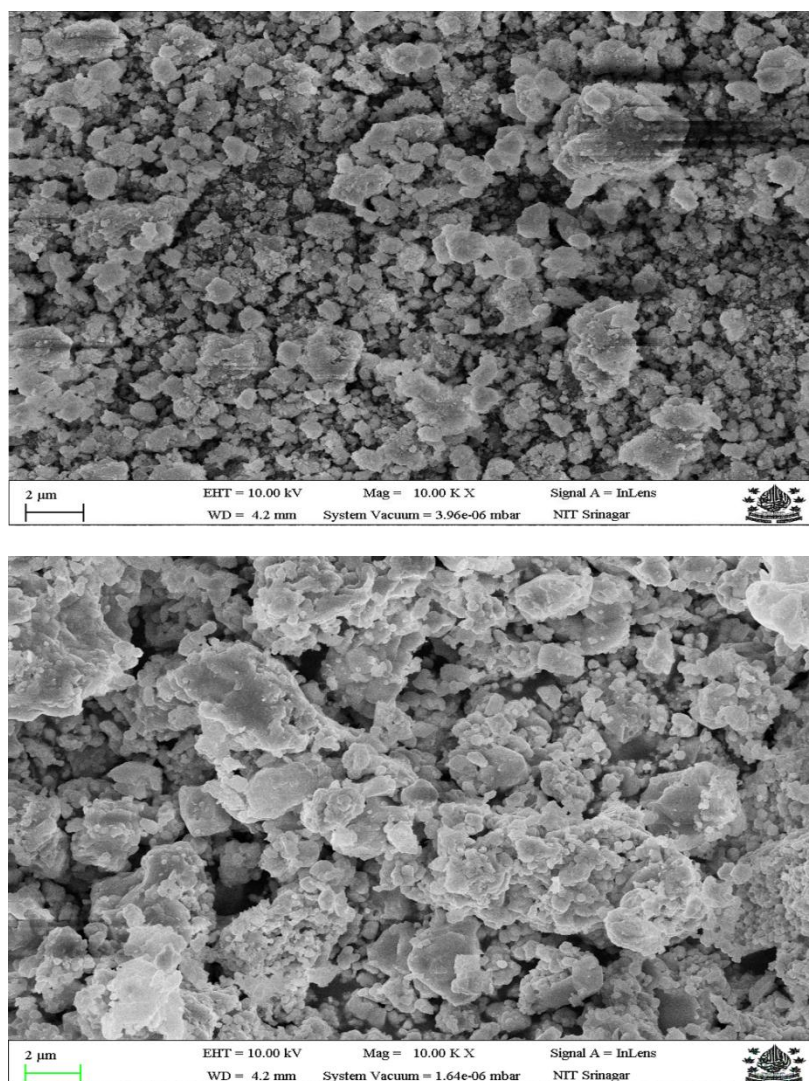


Figure 4.5 FESEM of CuS nanoparticle wet chemical co-precipitation and Sol-Gel method

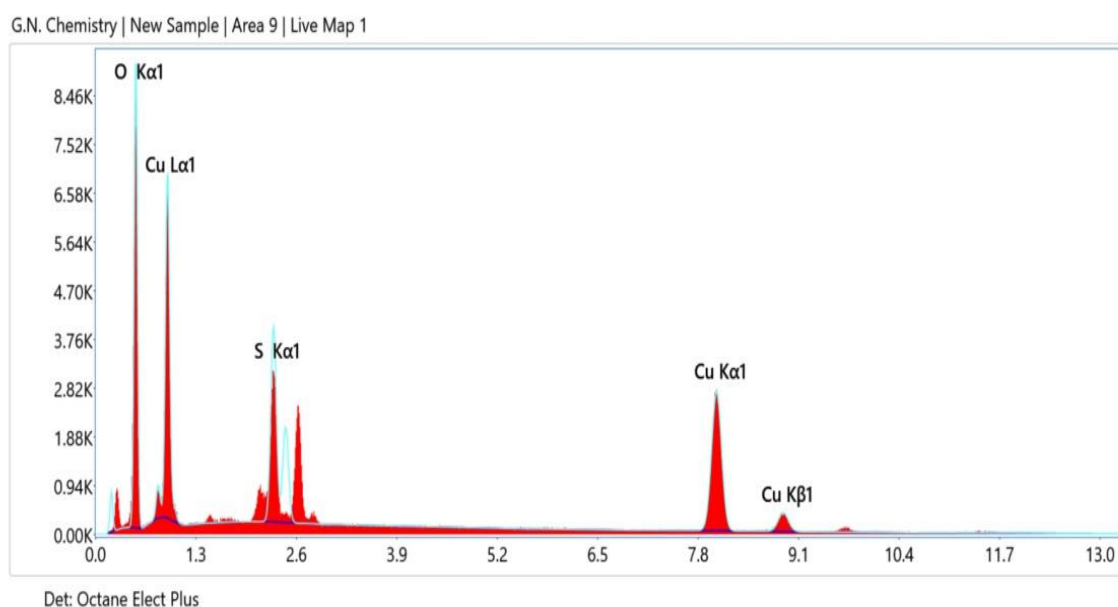


Figure 4.6 EDX spectrum of CuS nanoparticle (wet chemical co-precipitation method)

4.2.2. Photocatalytic degradation of 2-CP

Impact of pH

The degradation rate of 2-chlorophenol by copper sulphide nanoparticles was studied under visible light to determine the effect of pH. The elimination effectiveness of 2-CP rises with increasing pH values up to 6, as demonstrated in **Figure 4.7**, but then falls as pH increases to 10.0. The surface becomes positively charged, and an electrostatic repelling shift occurs in the direction of the cationic moiety when the pH of the photocatalyst material is acidic (pH 6). By changing the electrostatic repulsion between anionic molecules and making the photocatalyst's surface material negatively charged, the light power increases by 100 to 200 W at an alkaline pH. The photocatalytic elimination of 2-CP was enhanced from 27% to 77% and 30% to 80% using CuS nanoparticles made using the Sol-Gel method (CuS-SG) and the wet chemical coprecipitation method (CuS-WCP), respectively. Due to the considerable lowering of the bandgap from 2.89 to 2.1 eV, wet chemical co-precipitation displays the highest degradation of 2-CP when compared with the Solgel approach. The degradation of 2 chlorophenol utilizing different materials as a photocatalyst at different pH values is compared in **Table 4.1** with CuS [Ba-Abbad et al., 2016].

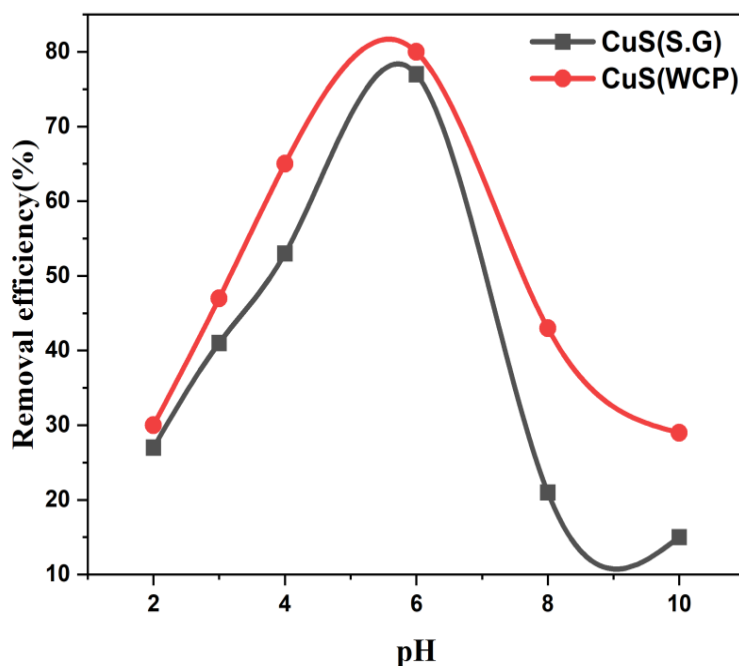


Figure 4.7 Effect of pH on degradation of 2-CP, reaction volume; 30 mL, Conc. of 2-CP; 100 mg/L, pH; 6, Temperature; 30°C catalyst dose; 10 mg, irradiating time; 2 h

Table 4.1: Treatment of wastewater with CuS and hybrid materials for photocatalytic destruction of organic contaminants

Material	Method	pollutant	% Degradation	Reference
CuS/Fe ₃ O ₄ /GO	Solgel/hydrothermal	Methylene Blue	90.3%	[Dustgeer et al., 2021]
rGO/CuS	facile co-precipitation technique	Malachite Green	97.6%	[Nasseh et al., 2021]
CuS	Hydrothermal	4-nitrophenol	25.6%	[Saranya et al., 2015]
		nitrobenzene	19.4 %	
CuS		CV	85%	[Ajibade et al., 2021]
		MB	100%	
		RhB	81%	

CuS/rGO	chemical reduction process	Cr (VI)	98%	[Pal et al., 2015]
CuS/CoFe ₂ O ₄	Hydrothermal method	Methylene blue Rhodamine B	100% 72%	[Bano et al., 2020]
CuS-CdS	Simple method	Rhodamine B Methylene blue	96% 94.7%	[Siadatnasab et al., 2018]
CuS-WO ₃	Solution method	Rhodamine B	49%	[Pandit et al., 2020]
FeNi ₃ /SiO ₂ /CuS		tetracycline	100%	[Song et al., 2020]
CuS-MoS ₂	Hydrothermal technique	Hydroquinone	83%	[Nasseh et al., 2018]
CuS@CNs	In situ	2,4-DCP	96%	[Chen et al., 2021]
Co-doped ZnO/CuS	Hydrothermal method	MO phenol		[Li et al., 2018]
CuS	Wet chemical co-precipitation process	2-CP	83.2%	Present work
CuS	Solgel process	2-CP	75%	Present work

Effect of Time

The reaction process was examined by means of a kinetic examination employing CuS (SG) and CuS (WCP). In about 2 hours when exposed to visible light, 2-CP was catalytically removed, with CuS (SG) nanoparticles removing about 75% and CuS (WCP) nanoparticles removing about 83% (15ppm), respectively (**Figure 4.8**). The elimination of 2-CP catalytically followed the pseudo-first order kinetic model (**Figure 4.9**) with statistical significance ($R^2 > 0.906$ and $R^2 > 0.943$) as shown in **Equation 4.2**.

$$\frac{\ln C_0}{C_t} = ak * t \quad 4.2$$

The above equation states that the concentrations at time t , C_0 , and C_t , are expressed in mg/L. The response rate constant k (min^{-1}) is shown in **Table 4.2**, which is formed by plotting $\ln(C_0/C_t)$ against time in a linear fashion. Ayodhya et al. and Dustgeer et al. found that the rate constant grows as the initial 2-CP concentration increases.

Table 4.2: Pseudo first order rate constant for 2-CP

Material	2-CP (mg/L)	k (min^{-1})	R^2
CuS (WCP)	15	0.722	0.943
CuS (S.G)	15	0.645	0.906

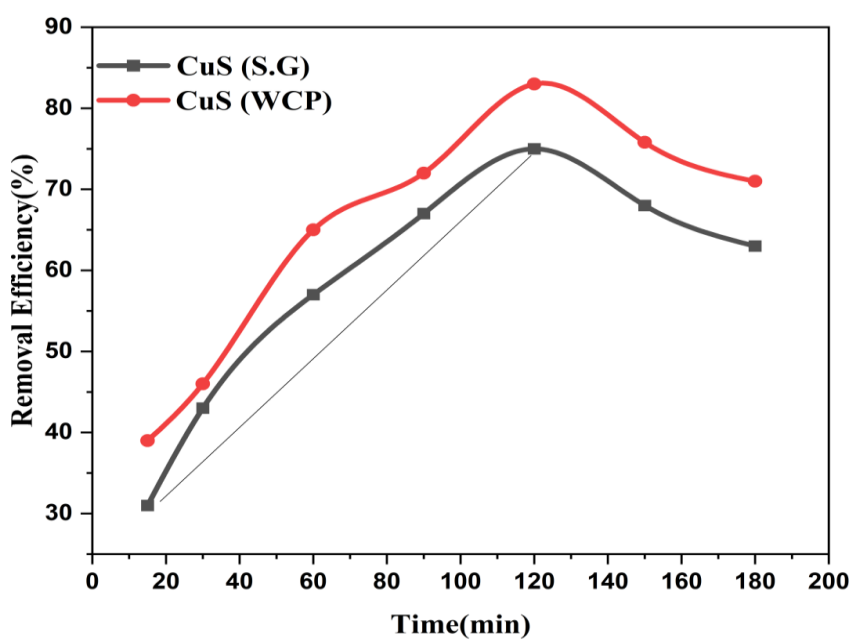


Figure 4.8 Effect of reaction time, Conc. of 2-CP; 100 mg/L, pH; 6, Reaction volume; 30 mL, catalyst dose; 10 mg, irradiating time; 2 h, Temperature; 30°C

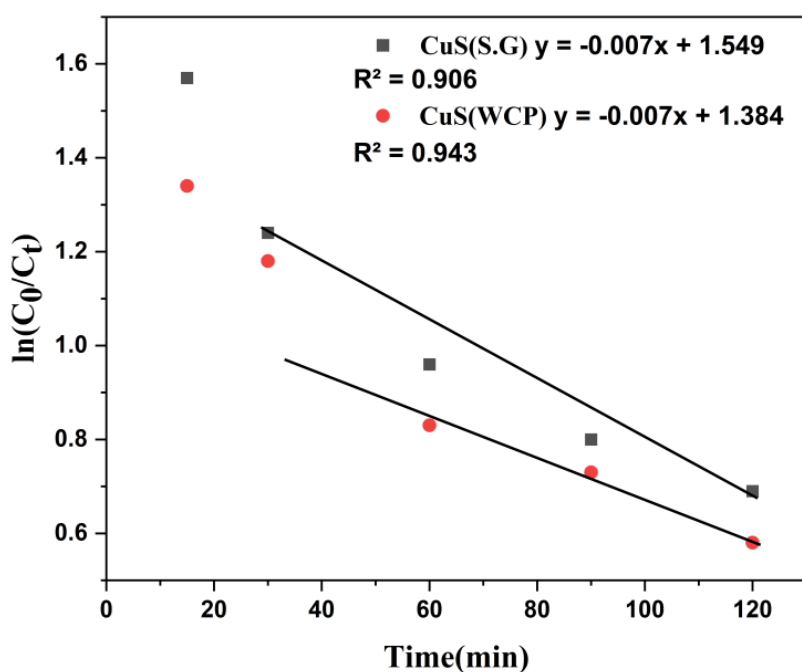


Figure 4.9 Pseudo i^{st} - order kinetics. Conc. of 2-CP; 100 mg/L, reaction volume; 30 mL, irradiating time; 2 h, catalyst dose; 10 mg, pH; 6, Temperature; 30°C

Catalyst dosage effect

A significant amount of the photocatalyst boosts the generation of e^-/h^+ couples, which in turn enhances the photocatalytic degradation process of 2-CP [Song et al., 2017]. To find the optimal photocatalyst dose, the CuS nanoparticle material was varied from 0.01 to 0.2 g/L in 30 mL of 2-CP (100 mg/L) under 100 W of light intensity on a pH value of 6.0 for two hours. **Figure 4.10** shows that with an increase in photocatalyst concentration from 0.01 to 0.05 g/L, the photocatalytic removal efficiency of 2-CP for CuS (SG.) increased from 37% to 69.5% and for CuS (WCP) from 43% to 72.8%. However, the removal effectiveness was not further enhanced by adding 0.2 g/L to the dose of CuS nanoparticles. Due to the photocatalyst's increased suspension, light penetration was found to be diminished with a high photocatalyst addition [Nasseh et al., 2021].

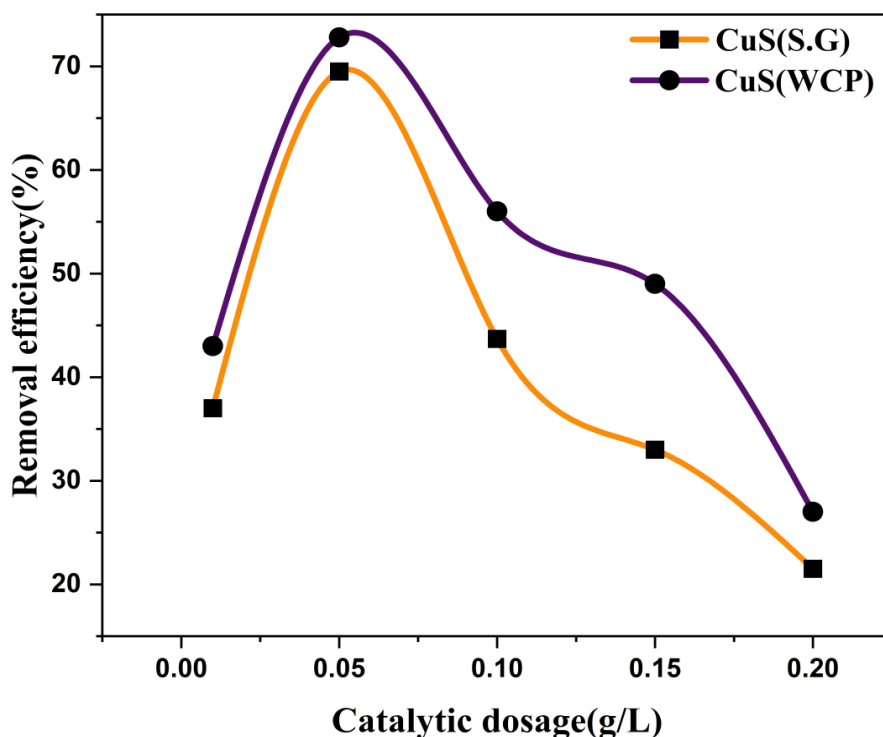


Figure 4.10 Effect of catalyst dosage, Conc. of 2-CP; 100 mg/L, pH; 6, reaction volume; 30 mL, irradiating time; 2 h, Temperature; 30°C

Effect of H₂O₂ concentration

Hydrogen peroxide improves photocatalytic elimination by increasing the quantity of accessible $\cdot\text{OH}$ radicals by the formation of vivid intermediates during the photocatalytic reaction. **Figure 4.11** shows the influence of hydrogen peroxide on the photocatalytic removal of 2-CP by CuS (SG) and CuS (WCP), with hydrogen peroxide levels affected by 0.001% to 0.4%. Without hydrogen peroxide, the photo-degradation efficiency was 72.8%. In contrast, increasing the hydrogen peroxide concentration from 0.001 to 0.1% resulted in an 84.4% rise for CuS (WCP) and a 75.2% increase for CuS (SG) in the photocatalytic removal of 2-CP. However, increasing the concentration to 0.4% caused a 42.6% decrease. The combination of hydroxyl radicals and abundant hydrogen peroxide acts as an inhibitor, which explains this decrease. By capturing photoinduced e⁻ ions with hydrogen peroxide, the linked e⁻/h⁺ can be stabilized. The $\cdot\text{OH}$ radicals can be generated by reacting hydrogen peroxide with e or O₂^{•-}. It was therefore hypothesized that 2-chlorophenol may be more effectively removed by incorporating hydrogen peroxide into the photocatalytic reaction system. Since the additional hydrogen peroxide caught the created $\cdot\text{OH}$ radicals to make weaker oxidant HO₂[•] radicals, the quantity of $\cdot\text{OH}$ radicals available for 2-CP elimination reduced as the concentration of added hydrogen peroxide increased [Pandit et al., 2020].

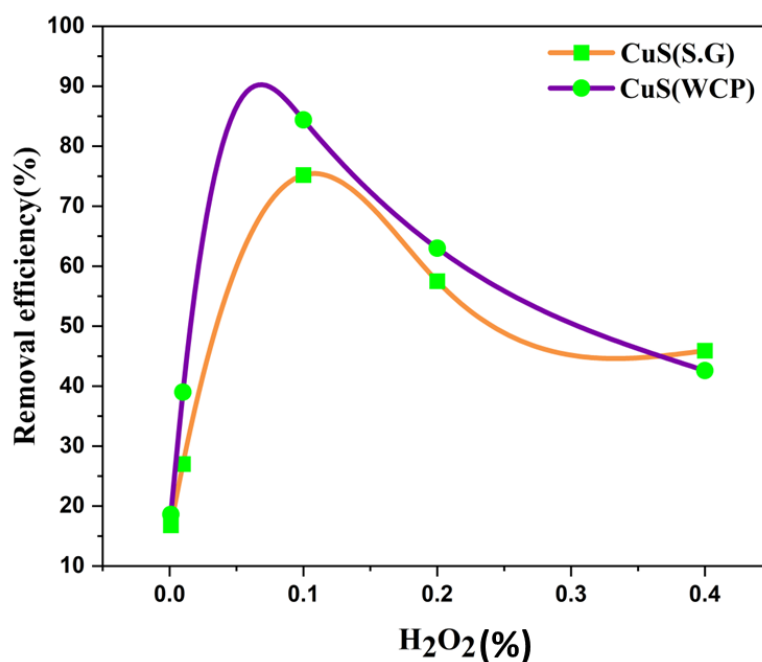


Figure 4.11 Effect of H₂O₂ (%), Conc. of 2-CP; 100 mg/L, reaction volume; 30 mL, pH; 6, irradiating time; 2 h, catalyst dose; 10 mg, Temperature; 30°C

Photocatalyst Regeneration

By reusing the photocatalyst that was produced for 'n' cycles, the financial viability of the catalyst will be improved. The employed photocatalyst was treated with a solution of thirty percent hydrogen peroxide for one hour while being agitated. This was done in order to renew the photocatalyst. The efficiency of 2-CP in eliminating the substance was 42.7% up until the fifth cycle, and it continued to decrease as the number of regeneration cycles rose (**Figure 4.12**). [Ba-Abbad et al., 2016] found that the hydrogen peroxide treatment can free the active sites and form a negatively charged surface, which in turn functions as a new photocatalyst CuS nanoparticle. This is accomplished by oxidizing the surface-trapped molecules to water and carbon dioxide.

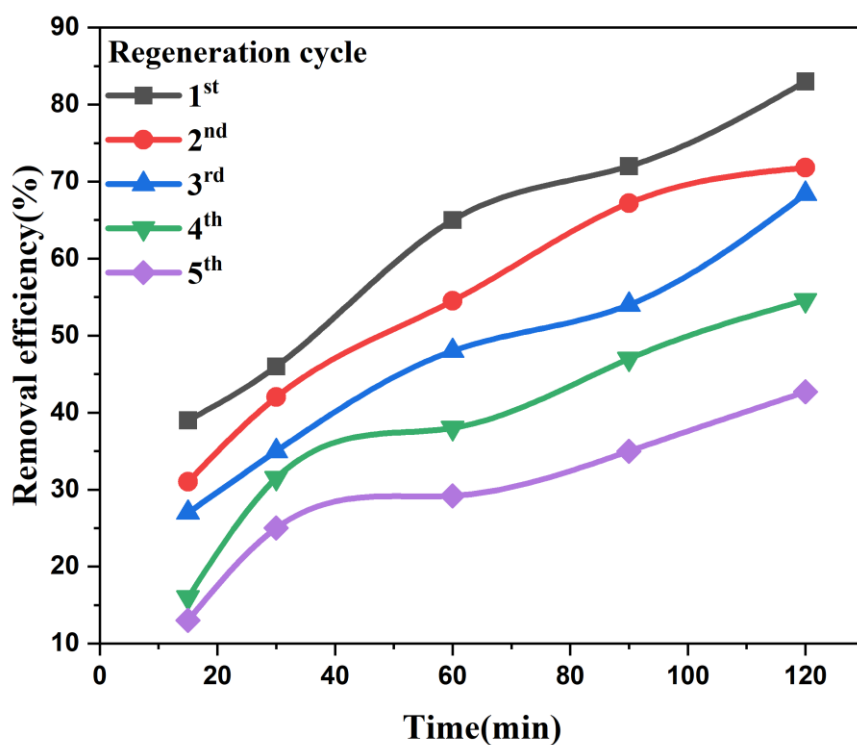


Figure 4.12 Regeneration of CuS (WCP) photo-catalyst (reaction condition: 2-CP concentration; 100 mg/L, catalyst dose; 10 mg, reaction volume; 30 mL, H₂O₂; 0.01%, pH; 6.0, temperature; 30° C)

4.2.3. Batch absorption experiment

Spiking process/ Photodegradation of 2-Cp from aquatic wastewater

The sample of wastewater was collected from the sewerage treatment plant located at Lovely Professional University Phagwara, Punjab, 144411. The wastewater samples were analyzed using standard analytical methods as soon as they were collected, which was shortly after receiving them. The pH of wastewater is 7.8, its color is yellowish, its total soluble solids (TSS) is 164 mg/l, its total dissolved solids (TDS) is 231 mg/l, and its conductivity is 1.11 Ohm⁻¹m⁻¹

During the photocatalytic process, one of the most important variables is the dose of the catalyst. The optimum value is to optimize photocatalytic activity (PCA) at the lowest feasible catalyst dose. This means that the creation of hydroxyl radicals is connected with an increase in catalyst concentration up to a certain point. On the other hand, agglomeration might take place after that point, and the PCA might fall as a consequence of the decreased light penetration. Both the likelihood of a higher electron-to-hole pair recombination rate and the probability of agglomeration from higher doses than the optimal value could be factors that contribute to the decrease in degradation rate that is brought about by increasing the catalyst dose. This could, in the end, lead to a reduction in the amount of light that penetrates [Singh et al., 2009]. For the purpose of determining the optimal concentration for the maximal degradation of 2-CP, CuS (WCP) nanoparticles were utilized at a variety of concentrations ranging from 0.01 to 0.2 g/L. It was discovered that a lower concentration of photocatalyst had no discernible impact on photodegradation. On the other hand, increasing the concentration of the catalyst increased the rate of degradation, reaching up to 72.8%, 64%, and 67.2% for wastewater, spiking, and synthetic solution degradation, respectively, at the optimal value of the catalyst (**Figure 4.13**).

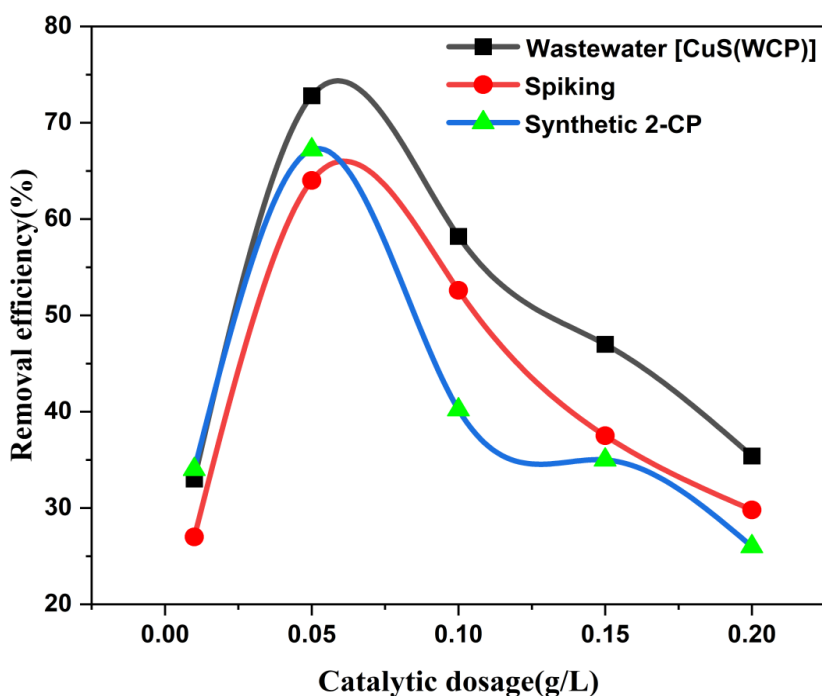


Figure 4.13 Effect of catalyst dosage, Conc. of 2-CP; 100 mg/L, pH; 6, reaction volume; 30 mL, Temperature; 30°C, irradiating time; 2 h

4.2.4. Schematics mechanism of CuS for 2-CP degradation

The formation of photogenerated charge carriers, namely holes and electrons, transpired when photons of light impinged upon the photocatalytic material CuS compound [Borthakur et al., 2021]. **Figure 4.14** demonstrates that the degradation process encompasses both electrons and holes. Reduction transpires in the presence of electrons, whereas oxidation occurs in the presence of holes. Superoxide radical anion and other highly reactive species are produced on the surface of the active catalyst [Lai et al., 2019]. The low electrode potential of hydroxyl radicals renders them highly reactive species. Two pathways are feasible for the breakdown of 2-chlorophenol (2-CP). In mechanism-I (M-I), an electron in the conduction band interacts with 2-CP, resulting in the elimination of the chlorine group as a radical and the formation of phenol as an intermediate. In mechanism II (M-II), the reactive OH radical and conduction band electrons assault the Ortho-position, substituting the Cl group with the OH group to yield the catechol intermediate. The conduction band electron subsequently decomposed catechol to yield phenol. Numerous investigations have demonstrated that the OH radical targets the aromatic rings of phenol owing to its electrophilic nature. This leads to the production of fumaric acid and maleic acid, which then decompose into the simpler molecule acetic acid

[Turchi et al., 1990]. Consequently, at the end of the process, 2-CP completely mineralizes into CO_2 and H_2O .

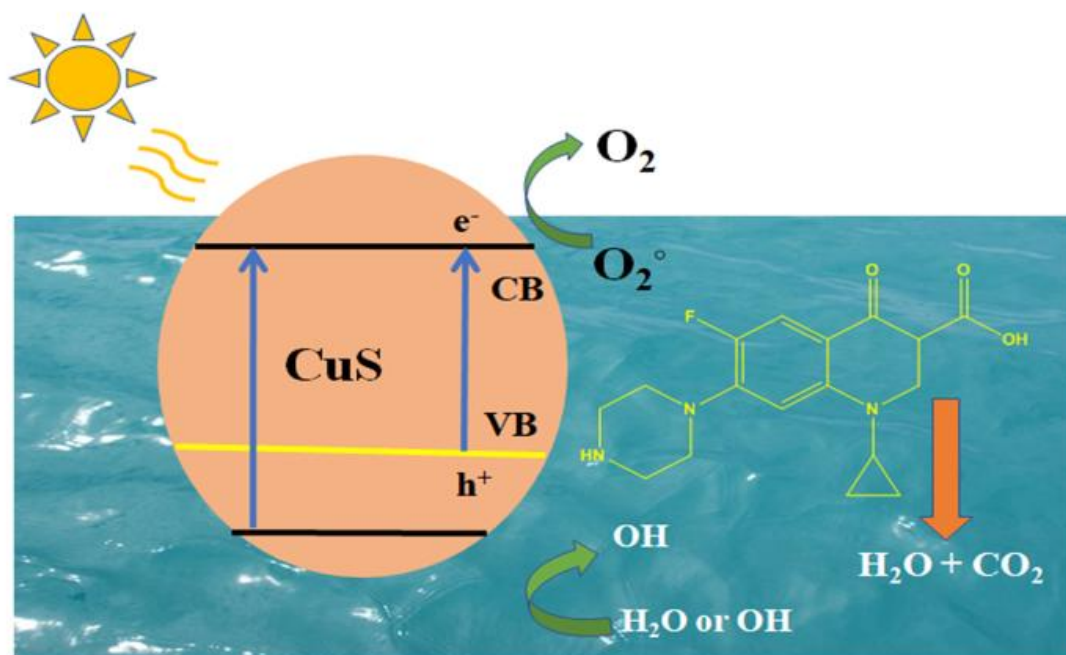


Figure 4.14 Mechanism of CuS (WCP) nanoparticles used for degradation of 2-CP

Chapter-5

Photocatalytic Degradation of Ciprofloxacin Using Microwave-Assisted $\text{CdS}/\text{Cs}_3\text{Bi}_2\text{Br}_9$ Nanocomposite in Industrial Aquatic Waste

5.1.Introduction

The increasing prevalence of persistent pharmaceutical chemicals in aquatic environments is mainly due to the extensive use of antibiotics and the inadequacies of traditional water treatment methods [Agladze et al., 2007]. Fluoroquinolones (FQs), a prevalent class of antibiotics, have been consistently identified in environmental samples [An et al. 2010]. FQs demonstrate significant stability, with more than 70% of the molecule being excreted unaltered or as active metabolites, underscoring their potential for environmental persistence [Barros et al., 2014].

Antibiotics belonging to the β -lactam category are commonly employed in the treatment of infectious diseases in both animals and humans. The antibacterial action against both Gram-positive and Gram-negative bacteria is exhibited by the β -lactam antibiotic family, which comprises amoxicillin (AMX). AMX has a greater rate of absorption in living organisms compared to other β -lactam antibiotics, and it blocks the synthesis of peptidoglycans, the main component of bacterial cell walls. Its persistent usage in biological fluids and animal feed is a direct outcome of its widespread usage, which in turn causes certain harmful consequences on people. One of the side effects of antibiotics is colitis, which can also cause rashes, nausea, and vomiting. Finding any trace of it in foodstuffs and bodily fluids is, hence, of the utmost importance [Nosuhi et al., 2017]. Metoclopramide (MCP) is a famous dopamine antagonist with antiemetic and analgesic effects; it is especially useful for a variety of gastrointestinal problems. MCP is a derivative of 4-aminobenzoic acid and substituted benzamide. Not only does it alleviate GERD and gastroparesis, but it also reduces labor pain and migraine attacks, acts as a local anesthetic and alleviates hiccup symptoms, prevents nausea and vomiting after surgery, eliminates vomiting caused by chemotherapy, and speeds up the emptying of the stomach. Due to its short half-life of a few hours and efficient absorption, approximately 80% of an oral dose of MCP (in its unmodified molecule and conjugate form) is eliminated in the urine within 24 hours. N-4 glucuronide and metoclopramide-N-4 sulfate account for less than 2% of MCP discharged in urine. According to Fazaeli et al, individuals with renal disease have a decrease of at least 30% in their ability to eliminate MCP.

Ciprofloxacin (CIP) is an efficient fluoroquinolone antibiotic that is commonly administered to treat bacterial infections. Because of its inappropriate disposal in direct drainage and wastewater effluents, however, it has contaminated the environment due to its extensive use. Consequences of CIP contamination in human water include lowered immunity, gastrointestinal distress (vomiting, nausea, and vomiting), headaches, and skin and mouth problems (stomatitis, eczema, and other dermatological difficulties) [Brillas et al., 1995]. According to Martínez-Huitle et al, CIP also has phytotoxic effects, which mean it hinders plant growth and development, damages DNA, stops higher plants like spinach from making photosynthesis, and causes morphological abnormalities.

Research conducted by Pérez et al. found that treated waterways and groundwater can include amounts of up to mg L⁻¹ of CIP, whereas hospital effluents can contain values ranging from ng L⁻¹. Because CIP degrades slowly, it can remain in solution at high concentrations for a long time. Activated sludge treatment and sludge digestion can get rid of CIP, but even then,

over 70% of the chemical is still in the treated effluent sludge [Cotillas et al., 2019]. As a result of residue detection in sewage effluent, CIP experiences secondary environmental harm as a result of phase transfer during sewage treatment, according to studies [Cotillas et al., 2018]. Several strategies have been devised to eradicate CIP from the environment in order to lessen these environmental repercussions and the emergence of resistance bacteria [Shanmugaraj et al., 2023].

According to Chankhanittha et al, several methods have been used to eliminate organic pollutants. These include coagulation, chemical precipitation, adsorption, ozone oxidation, and electrochemical strategies. Another biological option for reducing antibiotic contamination of water is biodegradation, which is a process that bacteria and fungus can do [Cheng et al., 2018]. To further remove contaminants, non-biological techniques such hydrolysis, oxidation, and reduction have been employed [Huang et al., 2019]. Nevertheless, the practical use of these procedures is limited due to their high costs, low stability, and limited efficiency, among other constraints. As a result, there is an urgent and fascinating need to find new techniques to remove contaminants, especially antibiotics, from the environment.

Recent decades have seen semiconductor-based (heterogeneous) photocatalysis emerge as the gold standard for AOPs. This technology is widely recognized as safe, cost-effective, ecologically friendly, and capable of rapidly decomposing a wide range of organic compounds with potential toxicity. This method relies on the production of powerful hydroxyl radicals and superoxide radical oxidants by exposing a semiconducting material to intense ultraviolet or visible light. Chemical pollutants can be targeted by these radicals, which can then break them down into smaller bits and convert them into water and carbon dioxide. The main problem with this method, according to Derikvandi et al, is that photogenerated electron-hole (e^-/h^+) pairs recombine, significantly diminishing the efficacy of photodegradation.

Hence, many methods have been used to reduce the level of e^-/h^+ recombination. With the nano-sized method, the photoinduced e^-/h^+ couples no longer have to travel the full length of the semiconductor from its bulk to its surface. The outcome is a faster transit time to the surface for the e^-/h^+ couples. They may, therefore, undergo photodegradation before recombining. Doping the semiconductor with metals or non-metals is another strategy that can be employed to introduce new or mixed energy levels to the systems. Consequently, the photogenerated e^-/h^+ couples in the CB/VB of the main semiconductor can reach these new energy levels, and e^-/h^+ recombination tends to diminish. Distributing the semiconductor species across their

surface is possible with the help of a suitable support, like zeolite, silica, or alumina. As a result, the effective surface area increases and the aggregation of semiconductor species is prevented. To further decrease e^-/h^+ recombination, hybrid or hetero-junction systems can be employed. These systems comprise two or more semiconductors that are strategically placed to take advantage of the right possible positions for CB and VB. Internal redox (reduction-oxidation) processes occur between the CB and VB levels of the semiconductors in these systems. Recombination between e^- and h^+ is greatly inhibited by these redox processes. Several photodegradation mechanisms, including the direct Z-scheme and type II heterojunction, have been studied and proven in this regard [Yousefi et al., 2021; Rezaei et al., 2024; Rezaei et al., 2024].

The potential of semi-conducting photocatalysts to clean water and air has piqued a lot of people's interests in these materials [Mirsalari et al., 2021; Chankhanittha et al., 2022]. By removing dangerous pollutants without producing harmful byproducts, photocatalytic processes provide a proactive approach for contaminant removal. Additionally, this method is easy to manage, doesn't harm the environment, and doesn't cost a fortune [Kaur et al. 2018, Patidar et al., 2021]. An innovative age in effective pollution removal has begun with cadmium sulfide (CdS), a noteworthy example of visible light-active photocatalysts with a band gap energy of about 2.4 eV. The photocatalytic degradation of organic contaminants makes considerable use of CdS. But there are two big drawbacks to CdS. To start with, it isn't very useful because electron-hole couples recombine so quickly. Additionally, its usefulness is further limited by photo-corrosion, which happens during the photodegradation of contaminants [Senasu et al., 2017; Senasu et al., 2018; Senasu et al., 2021]. Using the right sacrificial agent can fix this semiconductor's disadvantage. According to Nezamzadeh-Ejhi et al, a sacrificial agent frequently used to inhibit CdS photocorrosion is a mixture of Na_2S and Na_2SO_3 . Using eggshell membranes, CdS nanoparticles were synthesized at different pH values in an additional experiment. Increasing the pH results in a large amount of the smallest possible nanoparticles. The photodegradation effectiveness of the toluidine blue dye was demonstrated by the produced nanoparticles.

Recent research has increasingly focused on perovskite materials and their derivatives, such as Rudorffite-type compounds, owing to their easy synthesis, adjustable bandgap, remarkable charge carrier mobility, high defect tolerance, and wide range of applications [Chen et al.,

2015; Ye et al., 2020]. Rudorffites differ from conventional perovskites (ABX_3) by exhibiting edge-shared AX_6 and BX_6 octahedra, and they adopt a structural formula of $A_aB_bX_x$ (where $x = a + 3b$). The distinctive architecture facilitates the development of bismuth-based Rudorffite nanomaterials [Tie et al., 2020; Turkevych et al., 2017]. The vacancy-ordered triple perovskite variant, $A_3B_2X_9$, has attracted considerable attention in the field of photovoltaics due to its moderate power conversion efficiency. The $A_3B_2X_9$ Rudorffite-type structure demonstrates significant stability and presents an opportunity to substitute toxic lead with less harmful elements in traditional perovskites, positioning it as a highly promising candidate [Park et al., 2015].

This study reports the successful synthesis of a novel $CdS/Cs_3Bi_2Br_9$ nanocomposite with increased photocatalytic capabilities using a microwave-assisted method. Ciprofloxacin is a common antibiotic contaminant, and the $CdS/Cs_3Bi_2Br_9$ nanocomposite showed remarkable photocatalytic activity in degrading it from water. This study demonstrates the promise of a $CdS/Cs_3Bi_2Br_9$ nanocomposite prepared by microwave synthesis as a photocatalyst for the elimination of antibiotics.

5.2. Results and Discussion

5.2.1. Characteristics studies

Fourier Transform Infrared spectroscopy (FTIR)

Figure 5.1 illustrates the FTIR spectra of $Cs_3Bi_2Br_9$ nanocomposites incorporated with CdS . The absorption band observed near 700 cm^{-1} is assigned to $Cd-S$ bonding, arising from strong sulfide vibrations. A weaker band at 882.52 cm^{-1} is attributed to $O-H$ vibrations of water molecules. The characteristic stretching modes of thiourea appear at 1002.54 cm^{-1} ($C=S$) and 1143.83 cm^{-1} ($C-N$). An asymmetric scissoring vibration is evident at 1404.22 cm^{-1} , while weak asymmetric $C-H$ vibrations occur as a doublet at 2359.68 cm^{-1} . Two additional peaks, located at 2016.05 cm^{-1} and 2182.64 cm^{-1} , correspond to $N=C$ stretching or the isothiocyanate ($-NCS$) group, generated from thiourea hydrolysis during the synthesis process [Kumar et al. 2016; Senobari et al., 2018]. Peaks at 531 , 641 , 1015 , 1405 , 1633 , and 3358 cm^{-1} are associated with $Cs_3Bi_2Br_9$, reflecting distinct bonding arrangements or structural vibrations of the compound. In particular, bands at 531 and 641 cm^{-1} indicate $Cs-Bi$ bonding, while those at 1015 cm^{-1} and 1633 cm^{-1} correspond to $N-O$ and $C=N$ groups, respectively. The broad band

at 3358 cm^{-1} is attributed to O–H stretching, suggesting the presence of hydroxyl groups or absorbed moisture [Mirsalari et al., 2021; Wang et al., 2021].

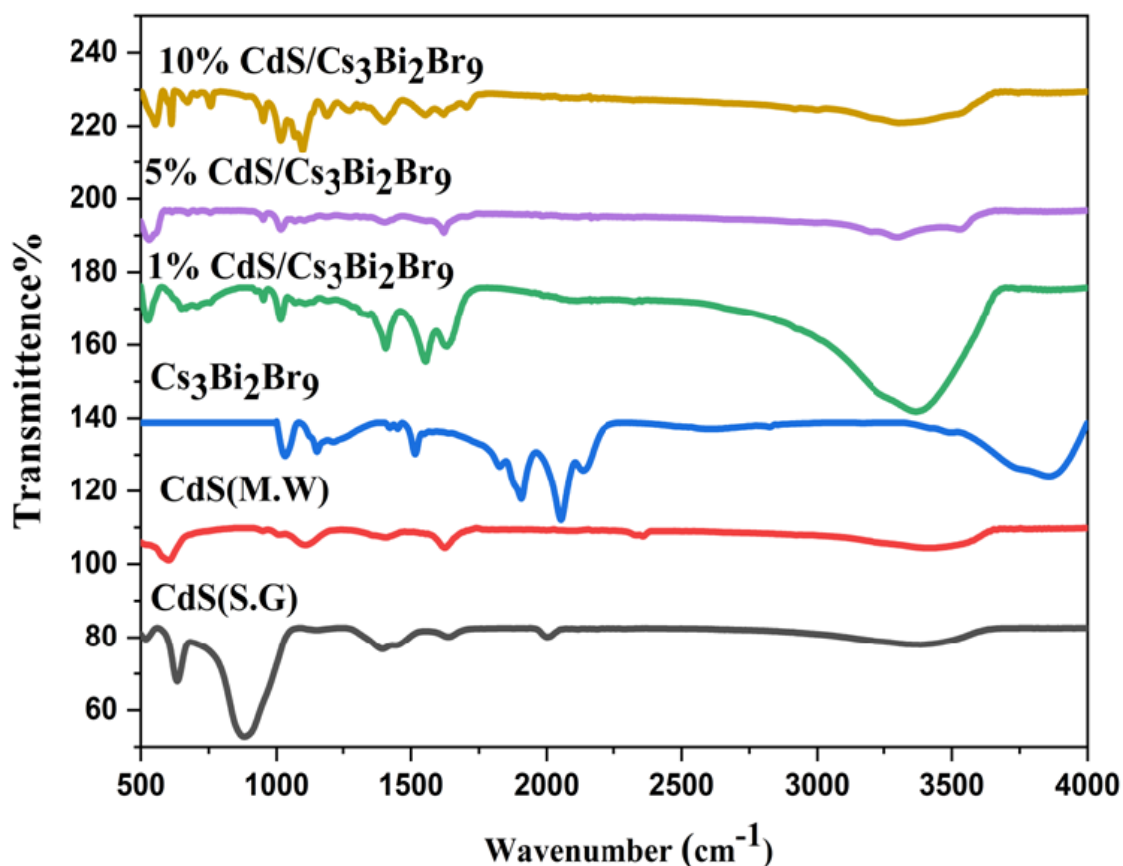


Figure 5.1 Fourier transform infrared spectra of CdS (S.G). CdS (M.W), $\text{Cs}_3\text{Bi}_2\text{Br}_9$ and their several composites

XRD Analysis

The powder X-ray diffraction (XRD) patterns were utilized to analyze the crystallinity and crystal structure of CdS and $\text{Cs}_3\text{Bi}_2\text{Br}_9$ nanocomposites. The CdS exhibited diffraction peaks at 2θ values of 24.81° , 26.50° , 28.40° , 30.80° , 34.39° , 45.83° , 51.91° , and 53.10° , corresponding to the (100), (002), (101), (220), (102), (110), (311), and (112) planes of the cubic CdS crystal lattice (JCPDS card no. 00-001-0647) [Khan et al., 2011; Tailor et al., 2021]. The distinctive diffraction peaks of $\text{Cs}_3\text{Bi}_2\text{Br}_9$ indicate its unique hexagonal structure within the $P\bar{3}m1$ space group (JCPDS card no 44-0714). The pronounced peaks at 12.78° , 15.68° , and 31.69° correspond to the (100), (101), and (202) planes of its hexagonal structure, respectively. In comparison to pure $\text{Cs}_3\text{Bi}_2\text{Br}_9$, the hybrid $\text{Cs}_3\text{Bi}_2\text{Br}_9/\text{CdS}$ samples demonstrate a

considerable enhancement in intensity. The increase in intensity indicates significant alterations in the material's structural composition, paving the possibility for future breakthroughs in both application and performance. This finding indicates that the content of CdS nanospheres in the structure influences the alignment of $\text{Cs}_3\text{Bi}_2\text{Br}_9$ platelets, particularly for the lateral dimensions of the lattice. This behavior indicates that the included nanospheres substantially influence the material's structural configuration, potentially unlocking unprecedented opportunities for precise manipulation and enhancement of its properties.

Figure 5.2 [Hemmatpour et al., 2022].

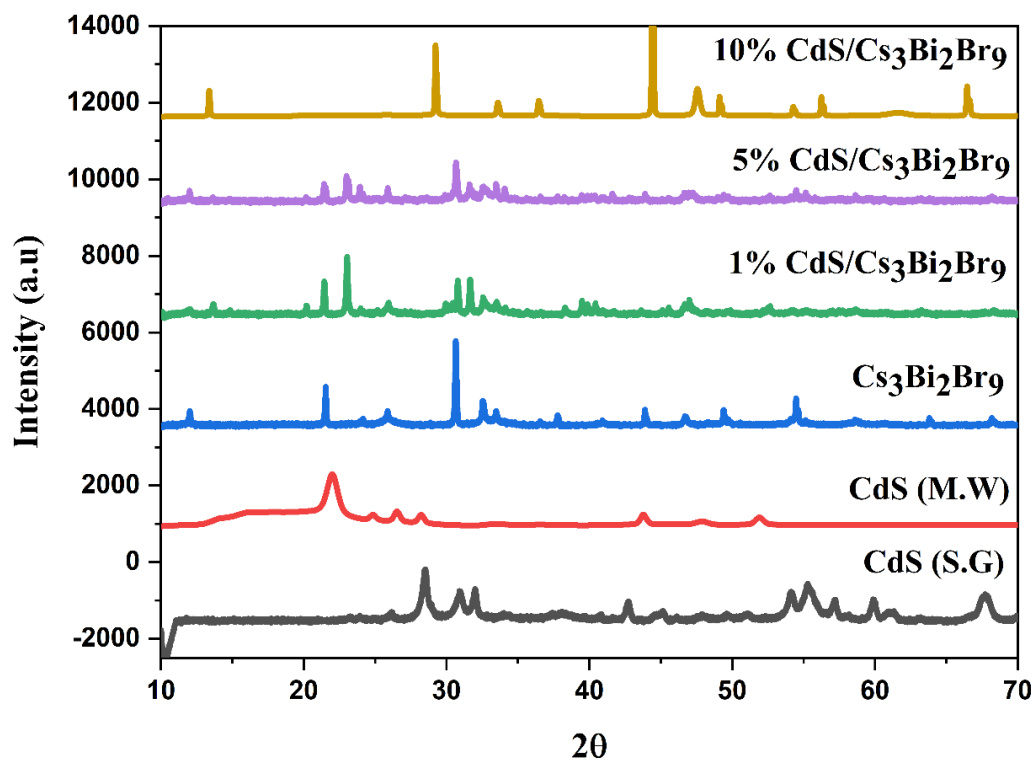


Figure 5.2 X-ray diffraction graphs of CdS (S.G), CdS (M.W), $\text{Cs}_3\text{Bi}_2\text{Br}_9$ and their several composites

The Scherrer equation states that a crystallite with a narrower diffraction peak (a larger β -value, where β is the total width at half maximum in radians) results in a smaller crystallite with diameter (d). Although the Scherrer constant (k) can take on values between 0.8 and 1.4, a value of 0.94 is commonly used. The variables θ and κ in **Equation 5.1** stand for the Bragg (diffraction) angle and the wavelength of the X-ray photon, or Cu-K α radiation, respectively.

$$d = k\lambda / \beta \cos\theta \quad 5.1$$

The average crystallite size for prepared CdS (S.G), CdS (M.W), Cs₃Bi₂Br₉, and 5%CdS/Cs₃Bi₂Br₉ was around 14.3, 16.82, 11.72, and 7.02 nm, respectively. Several experimental factors, including lattice defects, different stresses produced for several grains, and crystallite size, might affect the width β of a typical diffraction peak. The Williamson-Hall (W-H) equation (**Equation 5.2**) evaluates the combined impacts of size and induced strain (η). The WH equation is composed of the strain broadening Stokes and Wilson expression and the size broadening Scherrer formula. Hence, in the case of strain-free broadening ($\eta = 0$), the W-H equation yields a net Scherrer formula. Crystallite size changes in relation to the $1/\cos(\theta)$ value in the W-H model. As stated in several studies [Azimi et al., 2015; Tamiji et al., 2019, Zhao et al., 2021], the strain is affected by any variation in $\tan(Q)$. By utilizing the intercept value, one may approximate the average size of the crystallites (**Table 5.1**).

$$\beta \cos\theta = \left(k\lambda / d \right) + (\eta \sin\theta) \quad 5.2$$

Table 5.1: CdS (S.G), CdS (M.W), Cs₃Bi₂Br₉ and (1, 5 and 10%) CdS/Cs₃Bi₂Br₉ nanocomposite crystallite size, lattice strain and FWHM.

Material	FWHM	Crystallite size(nm)	Strain
CdS (SG)	0.536	14.36	9.21
CdS (MW)	4.718	16.82	442.2
Cs ₃ Bi ₂ Br ₉	0.65	11.72	10.31
1% CdS/Cs ₃ Bi ₂ Br ₉	1.79	4.26	28.15
5%CdS/Cs ₃ Bi ₂ Br ₉	1.09	7.02	17.22
10% CdS/Cs ₃ Bi ₂ Br ₉	0.48	15.16	5.09

Scanning Electron Microscopy and Energy Dispersive X-ray spectroscopy (SEM/EDX) Analysis

These scanning electron micrographs show the morphologies and microstructures of the materials. **Figure 5.3 A1, B1, and C1** show the morphology of the pure CdS, Cs₃Bi₂Br₉, and 5%CdS/Cs₃Bi₂Br₉ composites, which were characterized by a spherical shape and reasonably regular aggregates. During the microwave synthesis of the CdS/Cs₃Bi₂Br₉ composite, the active photocatalyst is close to Cs₃Bi₂Br₉, which makes it easier for charges to move between them. Cs₃Bi₂Br₉ is not the main photocatalyst; instead, it is an absorber and sensitizer for visible light. Element's mapping and energy dispersive X-ray spectroscopy were used to investigate the chemical component distribution and elemental composition of the 5%CdS/Cs₃Bi₂Br₉ photocatalyst. The scanning electron micrograph (SEM) of the mapping area and the EDX elementary mapping **Figure 5.3 A2, B2, C2** demonstrate that all elements, particularly bismuth (Bi), oxygen (O), bromine (Br), cadmium (Cd), and sulfur (S), are color-distributed evenly over the scanning region of the composite. **Figure 5.3 A3, B3, and C3** of the EDX spectrum shows that the CdS and Cs₃Bi₂Br₉ nanoparticles that were synthesized are pure. The elements cadmium, sulfur, cesium, bismuth, and bromine are all present in these nanoparticles, with a ratio of about 78.5:21.5 for CdS and 38.6:40.0:0.8 for Cs₃Bi₂Br₉ that approaches the nominal value [Farsi et al., 2022].

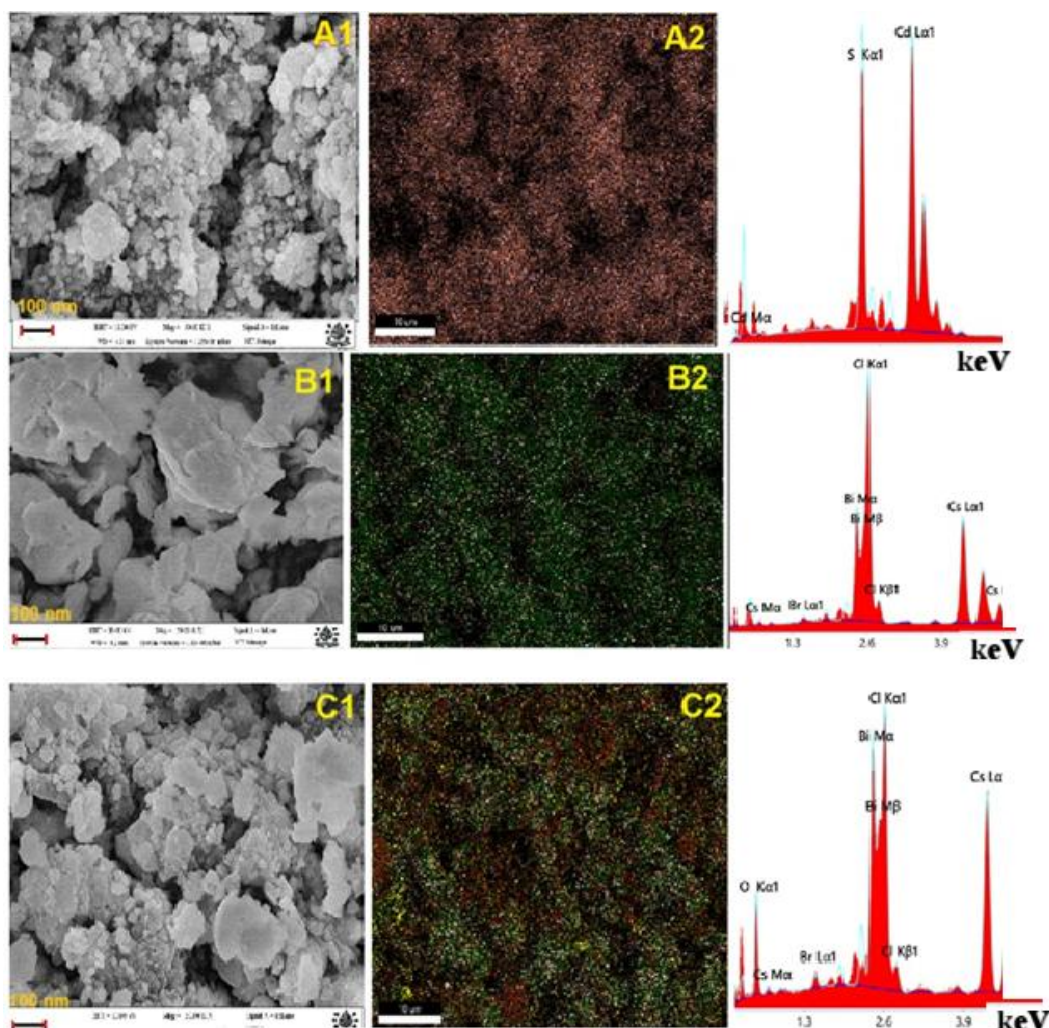


Figure 5.3 Scanning Electron Microscopy/Mapping/EDX graphs of CdS (A1, A2, A3), $\text{Cs}_3\text{Bi}_2\text{Br}_9$ (B1, B2, B3) and 5% CdS/ $\text{Cs}_3\text{Bi}_2\text{Br}_9$ composites (C1, C2, C3)

UV-visible spectroscopy Analysis

The optical properties of the binary composite catalyst, CdS/ $\text{Cs}_3\text{Bi}_2\text{Br}_9$, as well as the synthesized CdS and $\text{Cs}_3\text{Bi}_2\text{Br}_9$ nanoparticles, were examined by capturing and evaluating their UV-Vis diffuse reflectance spectra (DRS). We calculated the band gap energies and looked at the samples' absorption edge wavelengths in the first part of the work. Here, we will use the retrieved Kubelka-Munk, reflectance spectra, and Tauc plots to find the band gap energies of the samples. Materials' macroscopic optical properties, including their dispersiveness, total reflectance, and absolute absorption characteristics, can be investigated using DRS. Materials' macroscopic optical properties, including their dispersiveness, total reflectance, and absolute absorption characteristics, can be investigated using DRS. In simpler terms, the absorption

futures of the samples are related to their optical properties, ratio, and particle size distribution, which in turn are associated to the dispersed reflected (re-emitted) photons.

In other words, the absorption futures of the samples determine the relationship between the samples' optical properties, particle size dispersion, and filling factor, and the diffused reflected (re-emitted) photons. The absorption spectra of semiconducting materials provide important information about their optical features, including the band gap energy (E_g), which is the electrical motivation between the valence (VB) and conduction (CB) bands of the materials. To estimate this value, one can utilize the Kubelka-Munk theory in conjunction with the absorption edge wavelength (λ_{AE}). Here we see some quick illustrations of tauc plots and the Kubelka-Munk model. Using the absolute reflectance value (R , in the 0-1) of an opaque material, the converted reflectance (K) for this mathematical model can be predicted using (**Equation 5.3**). The total reflectance of a sample is defined by its scattering and absorption processes within a certain thickness.

$$k = (1 - R)^2 / 2R \quad 5.3$$

$$(\alpha h\nu) = \beta(h\nu - E_g)^n \quad 5.4$$

Sample thickness (t) and light transmission (T , $1/t = \ln(1/T)$) are the two variables that determine the absorption coefficient "a" in the standard method for generating Tauc plots (**Equation 5.4**). To determine bandgap values for electronic transitions, plot $(\alpha h\nu)^n$ versus photon energy (ν). This approach is applicable for authorized direct ($n = 1/2$) and indirect ($n = 2$) transitions, as well as banned direct ($n = 3/2$) and indirect ($n = 3$). **Figure 5.4** displays the generated Tauc graphs. To get the E_g -values at which $(\alpha h\nu)^n = 0$, we extrapolated the rising slopes towards the photon energy axis. **Table 5.2** displays the results.

In comparison to pure CdS, the coupled binary CdS/Cs₃Bi₂Br₉ catalyst had a somewhat narrower band gap. According to published research, there is a direct correlation between particle size and $f(R)$.

The possible positions of valence band and conduction band for the individual semiconductors used were predicted using the following equations (**Equations 5.5 and 5.6**) using the E_g values for the direct electronic transition, the energy of the free electrons (E_e : approximately 4.5 eV

compared to NHE), and χ [Omrani et al., 2020; Mehrabanpour et al., 2023; Ghattavi et al., 2019; Ghattavi et al., 2020; Rani et al., 2020].

$$E_{VB} = \chi - E_e + 0.5E_g \quad 5.5$$

$$E_{CB} = E_{VB} - E_g \quad 5.6$$

Table 5.2 The samples' electronic transition band gap energy and VB and CB potential locations were determined.

Catalyst	χ (eV)	E_g (eV)	E_{VB}	E_{CB}
CdS	5.48	3.4	2.69	-0.71
Cs ₃ Bi ₂ Br ₉	5.77	3.5	3.02	-0.8
5%CdS/ Cs ₃ Bi ₂ Br ₉	NA	3	NA	NA

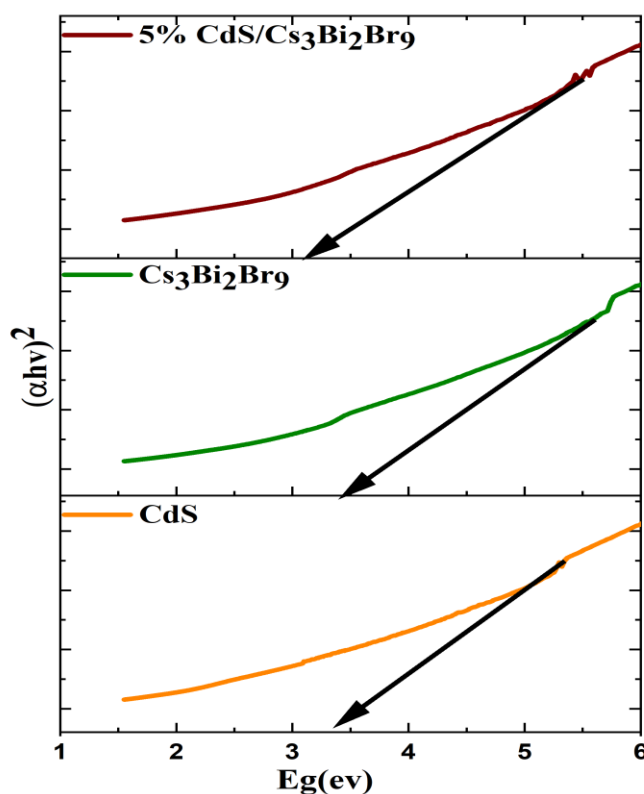


Figure 5.4 Tauc plot of CdS, $\text{Cs}_3\text{Bi}_2\text{Br}_9$ and 5% $\text{CdS}/\text{Cs}_3\text{Bi}_2\text{Br}_9$ for $n=2$

Zeta potential Analysis

One of the physical characteristics of all particles that are suspended is called the zeta potential, and the magnitude of this potential can be used as a measurement for the stability of the colloidal system. When nanoparticles in suspension exhibit a zeta potential with a magnitude that is adequate to produce interparticle electrostatic repulsion, the aggregation of nanoparticles in suspension is prevented. This results in the colloidal dispersion being stabilized. On the other hand, if the zeta potential values of the particles are low, there is no force that prevents them from aggregating and flocculating. **Figure 5.5** shows that the zeta potential of the composite, which is -4 mV, is closer to neutral than the zeta potentials of cesium bismuth bromide, which is -19.5 mV, and CdS, which is -5 mV. This could be an indication of enhanced adsorption and degradation as a result of less electrostatic repulsion between the composite material and the molecules of ciprofloxacin that are existing in solution. $\text{Cs}_3\text{Bi}_2\text{Br}_9$ has an extremely negative zeta potential of -19.5 mV, which may result in higher electrostatic repulsion with ciprofloxacin (assuming that it bears a similar charge in the experimental pH) [Rao et al., 2017, Sankhla et

al. 2016]. This may make it more difficult for cesium bismuth bromide to be used for effective adsorption and photocatalytic activity.

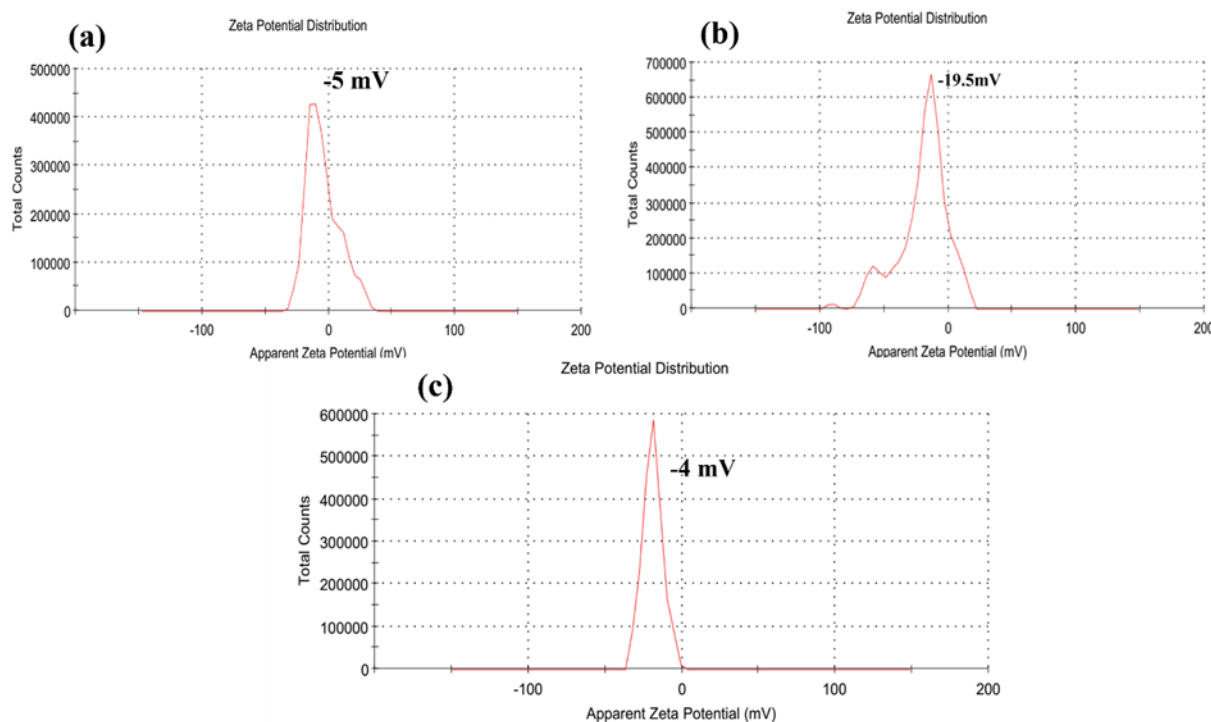


Figure 5.5 Zeta potential of (a) CdS, (b) Cs₃Bi₂Br₉ and (c) 5% CdS/Cs₃Bi₂Br₉

5.2.2. Degradation of Ciprofloxacin (CIP) by Photocatalysis process

The photo-degradation of Ciprofloxacin was studied utilizing a customized batch reactor and visible light LED sources for CdS, Cs₃Bi₂Br₉, and CdS/Cs₃Bi₂Br₉ photocatalysts, with the goal of achieving uniform light intensity. At regular intervals, 0.1 N HCl and 0.1 N NaOH were added to the stock solution to maintain a consistent pH. For the same three-hour radiation run, the identical batch investigation was performed using 10 mg CdS, Cs₃Bi₂Br₉, and 5% CdS/Cs₃Bi₂Br₉ in a 10 ppm Ciprofloxacin solution. Two passes via Whatman filter paper were performed on the mixture following radiation exposure. Following this, a UV-Visible spectrophotometer was used to measure the Ciprofloxacin concentration at 278 nm. It was investigated in the study by Ejhieh et al. how several experimental parameters, such as pH levels, concentrations of hydrogen peroxide, dosages of photocatalysts, and intensity of visible light, affected the elimination of ciprofloxacin. The efficiency of ciprofloxacin degradation was determined using the following equation (**Equation 5.7**):

$$\% \text{degradation efficiency} = \left(\frac{C_0 - C_t}{C_t} \right) \times 100 \quad 5.7$$

The initial Ciprofloxacin concentration is C_0 , while the solution concentration at time t is C_t .

Effect of pH

The photocatalytic efficacy of nanomaterials is significantly pretentious by the pH of the solution, which changes the surface interaction among CIP molecules and pure or doped CdS and $\text{Cs}_3\text{Bi}_2\text{Br}_9$ nanomaterial. The pace of photodegradation is controlled by the amount and reactivity of OH radicals. Reacting with adsorbed oxygen and water, the photogenerated charge carriers' low electrode potential value produced highly reactive OH free radicals. The molecule eventually mineralizes due to the oxidative breakdown of CIP into intermediates, which is initiated by the hydroxyl free radicals. Using a Ciprofloxacin solution with a concentration of 10 ppm and a pH range of 2–10, we conducted experiments on photocatalytic degradation. The catalyst concentrations employed in the trials were 10 mg each of CdS (Solgel), CdS (Microwave), $\text{Cs}_3\text{Bi}_2\text{Br}_9$, 1% CdS/ $\text{Cs}_3\text{Bi}_2\text{Br}_9$, 5% CdS/ $\text{Cs}_3\text{Bi}_2\text{Br}_9$, and 10% CdS/ $\text{Cs}_3\text{Bi}_2\text{Br}_9$. They were then revealing to visible light for 3 hrs. **Figure 5.6** shows an interesting trend: when the acidity of the medium increases, the photocatalytic degradation efficiency also increases. The article highlights that the optimal pH for the breakdown of CdS (Solgel), CdS (Microwave), $\text{Cs}_3\text{Bi}_2\text{Br}_9$, 1% CdS/ $\text{Cs}_3\text{Bi}_2\text{Br}_9$, 5% CdS/ $\text{Cs}_3\text{Bi}_2\text{Br}_9$, and 10% CdS/ $\text{Cs}_3\text{Bi}_2\text{Br}_9$ is 8. How well a catalyst degraded was affected by its surface charge properties as well as its concentration of OH-ions. The charge transfer between the catalyst surfaces and CIP is affected by both the solution pH and the catalyst's pH_{pzc} (point of zero charge) values. Placing the pH of the catalyst surface below the pH_{pzc} (point of zero charge) causes it to be positively charged, and vice versa when the pH is greater than pH_{pzc}. Because of this, catalyst surfaces display a positive charge in acidic environments and a negative charge in basic zones. The degradation efficiencies of CdS (Solgel), CdS (Microwave), $\text{Cs}_3\text{Bi}_2\text{Br}_9$, 1% CdS/ $\text{Cs}_3\text{Bi}_2\text{Br}_9$, 5% CdS/ $\text{Cs}_3\text{Bi}_2\text{Br}_9$, 10% CdS/ $\text{Cs}_3\text{Bi}_2\text{Br}_9$, 80%, 50%, and 61.3 percent correspondingly reach their maximum at very alkaline conditions (pH 8). The phenolate anion catalyzes a sequence of processes with explosive efficiency through its dynamic electrostatic contact with the positively charged catalyst surface, leading to improved efficiency. The bulk of the catalysts mentioned in **Table 5.3** exhibit the highest degradation efficiency in acidic

media. The production of carbonate ions basically hinders the photocatalyst's ability to scavenge OH^- ions and decrease its catalytic activity.

At high quantities of OH^- , two reactions can take place, rendering $\cdot\text{OH}$ inactive, as we have already shown. It is possible to synthesize H_2O_2 and $\text{HO}_2\cdot$ molecules through the reaction of $\cdot\text{OH}$ with OH^- . These compounds have a very low reactivity with organic pollutants as compared to $\cdot\text{OH}$. Because there are more $\cdot\text{OH}$ radicals in solution at higher pH values, the radical-radical reaction also occurs at these levels. The conjugated basic $\text{HClO}^{\cdot-}$ is formed in an acidic solution when HCl is introduced, thanks to an interaction between Cl^- and $\cdot\text{OH}$. The equilibrium constant of this base in the solution is $k=4.3\times 10^9 \text{ L mol}^{-1} \text{ s}^{-1}$. The inorganic radical anions mentioned in the studies by Tabasum et al. (2023), Sun et al. (2024), and Gupta et al. (2021) are not involved in photodegradation because of their much lower reactivity.

Table 5.3 Efficiency Comparison of Photocatalysts for Ciprofloxacin Degradation.

pH	Photocatalyst	Ciprofloxacin concentration (mg/L)	Degradation efficiency (%)	References
7	ZnO	4	50	[El-Kemary et al., 2010]
7	UV/ I^-	100	61.4	[Aghdasi et al., 2016]
6.8	ZnO	10	69.5	[Sarkhosh et al., 2019]
8	CdS	10	49	Present study
8	$\text{Cs}_3\text{Bi}_2\text{Br}_9$	10	53	Present study
8	5% $\text{CdS/Cs}_3\text{Bi}_2\text{Br}_9$	10	98	Present study

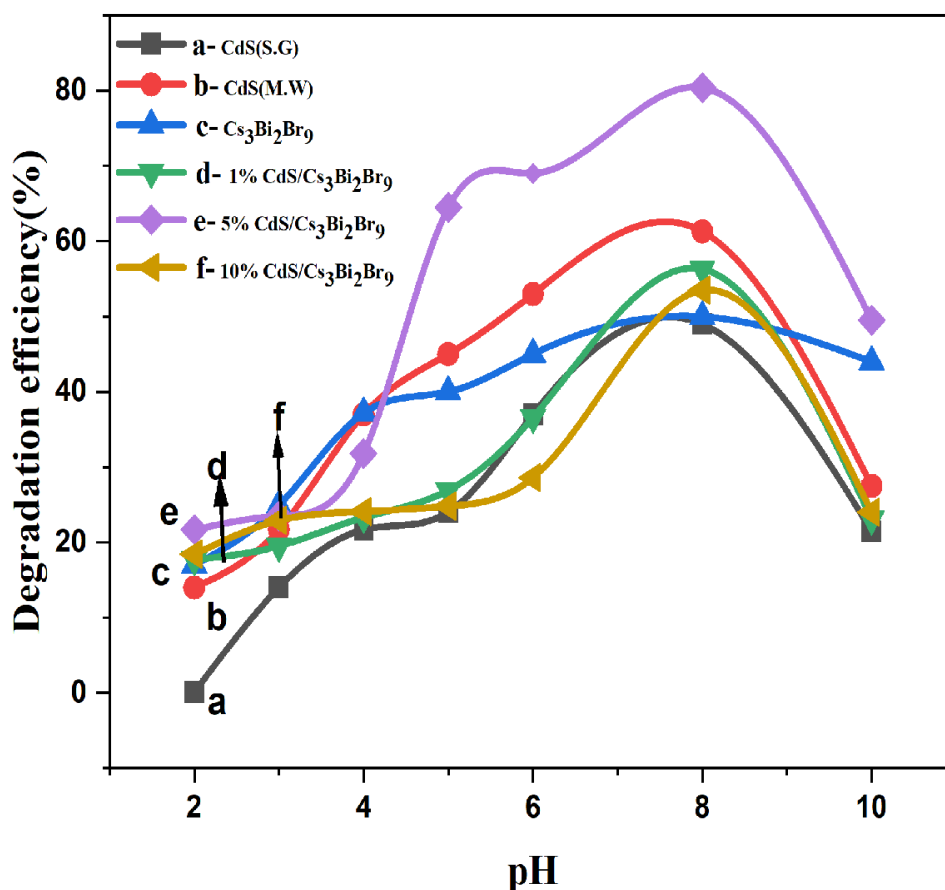


Figure 5.6 Effect of pH on Ciprofloxacin. Conc. of CIP; 100mg/L, Reaction volume; 30mL, Catalyst dose; 10mg, irradiation time; 3h, pH; 8, Temperature; 30°C

Impact of kinetic study

Performing kinetic experiments on CdS (Solgel), CdS (Microwave), Cs₃Bi₂Br₉, and 5% CdS/Cs₃Bi₂Br₉ was crucial for comprehending reaction rates and underlying mechanisms. The 10 ppm Ciprofloxacin solution was photocatalytically degraded in 210 minutes by using a 10 mg catalyst dosage for CdS (Solgel), CdS (Microwave), Cs₃Bi₂Br₉, and 5% CdS/Cs₃Bi₂Br₉, respectively. This was achieved with an astounding 60%, 80%, 65.5%, and 98.4% of the solution, respectively. The degrading efficiency of 5% CdS/Cs₃Bi₂Br₉ is higher in the visible range than that of CdS and Cs₃Bi₂Br₉ alone, as shown in **Figure 5.7**. Research shows that when subjected to visible light irradiation, the CIP solution remains stable even without catalysts. Catalyst addition to CIP solution caused a major shift in photocatalytic degradation rate, with substantial variation across photocatalysts [Amiri et al., 2015]. Increasing the CdS ratio significantly boosts the photocatalytic activity of the composite photocatalysts. Conversely, as the CdS ratio grows more, the photocatalytic activity becomes progressively less. This effect is caused by an excess of CdS, which coats the surface of Cs₃Bi₂Br₉

nanoparticle and makes photocorrosion worse during photodegradation. The graph between $\ln(C_0/C_t)$ and $t(\text{time})$, with rate constants ($k \text{ min}^{-1}$), is shown in **Figure 5.8**, which follows the first-order kinetic model for CdS, $\text{Cs}_3\text{Bi}_2\text{Br}_9$, and 5% CdS/ $\text{Cs}_3\text{Bi}_2\text{Br}_9$ mention in **Table 5.4**. The photo catalytic degradation of Ciprofloxacin follows the 1st order kinetic rate equation, as shown in **Equation 5.8**.

Here, C_0 and C_t stand for the beginning and final concentrations of Ciprofloxacin, respectively, and k is the reaction rate constant.

$$\ln\left(\frac{C_0}{C_t}\right) = k * t \quad 5.8$$

Table 5.4: Apparent 1st Order Rate Constant for photo catalytic degradation of Ciprofloxacin.

Materials	Ciprofloxacin (mg/L)	k (min ⁻¹)	R ²
CdS	10	0.583	0.847
$\text{Cs}_3\text{Bi}_2\text{Br}_9$	10	0.76	0.94
5%CdS/ $\text{Cs}_3\text{Bi}_2\text{Br}_9$	10	0.80	0.963

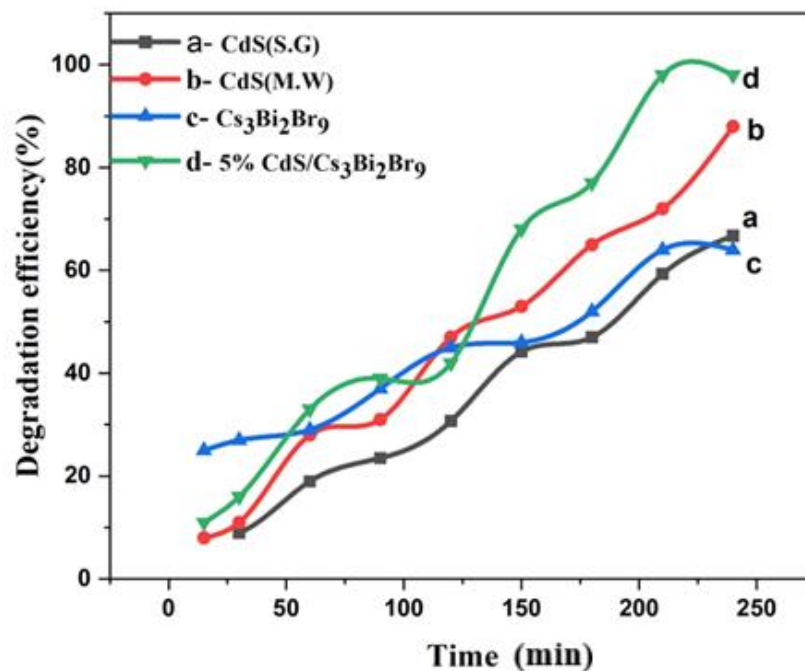


Figure 5.7 Effect of time. Conc. of CIP; 100mg/L, Reaction volume; 30mL, Catalyst dose; 10mg, irradiation time; 3h, pH; 8, Temperature; 30°C

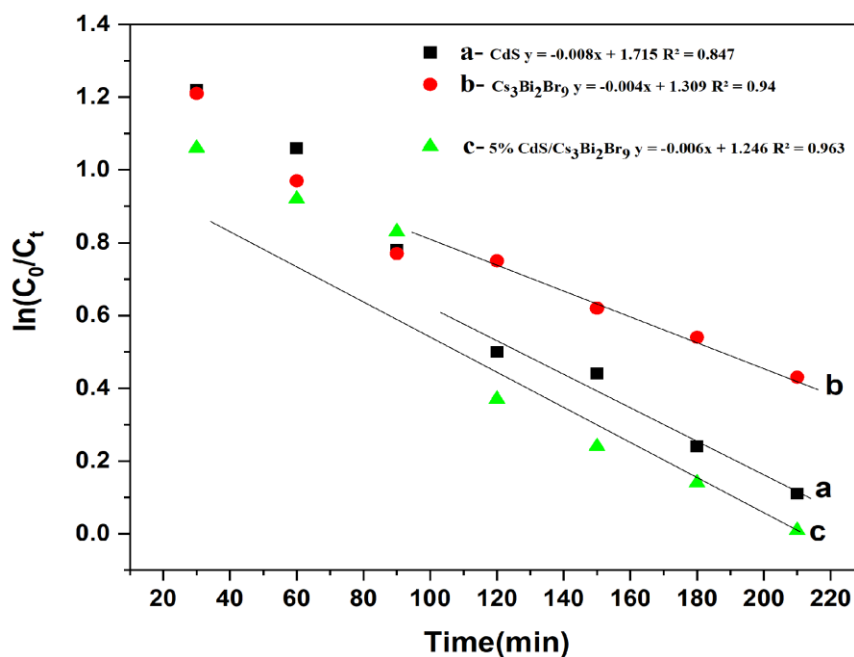


Figure 5.8 Rate of CIP photocatalytic degradation reaction. Conc. of CIP; 100mg/L, Reaction volume; 30mL, Catalyst dose; 10mg, irradiation time; 3h, pH; 8, Temperature; 30°C

Impact of H₂O₂ Concentration

Producing a significant volume of OH⁻ radicals, H₂O₂ can enhance the efficacy of photocatalytic elimination and create vivid by products. The photocatalytic degradation of

Ciprofloxacin by CdS, Cs₃Bi₂Br₉, and 5% CdS/Cs₃Bi₂Br₉ was evaluated in response to varying H₂O₂ concentrations, which ranged from 0.001 to 0.4% (**Figure 5.9**). The photodegradation efficiencies were 19%, 17%, and 65% in the absence of H₂O₂. When H₂O₂ concentration was raised from 0.01 to 0.1%, Ciprofloxacin photocatalytic degradation efficiency increased from 19%, 17%, and 65% to 51%, 47%, and 100%. The rate of elimination reduced to an even more noticeable 29, 37, and 60% when the amount of H₂O₂ was increased to an astonishing 0.4%. Because H₂O₂ has a stronger inhibitory effect when paired with hydroxyl radicals, this is likely the cause of the diminished removal efficacy. It is possible to stabilize the synergy between electron-hole pairs by efficiently trapping photoinduced electrons in H₂O₂. By reacting with H₂O₂, oxygen or electrons can create hydroxyl radicals ([•]OH). (Arabpour et al., 2016; Sharma et al., 2016). A faster degradation of Ciprofloxacin was anticipated upon adding H₂O₂ to the photocatalytic reaction setup.

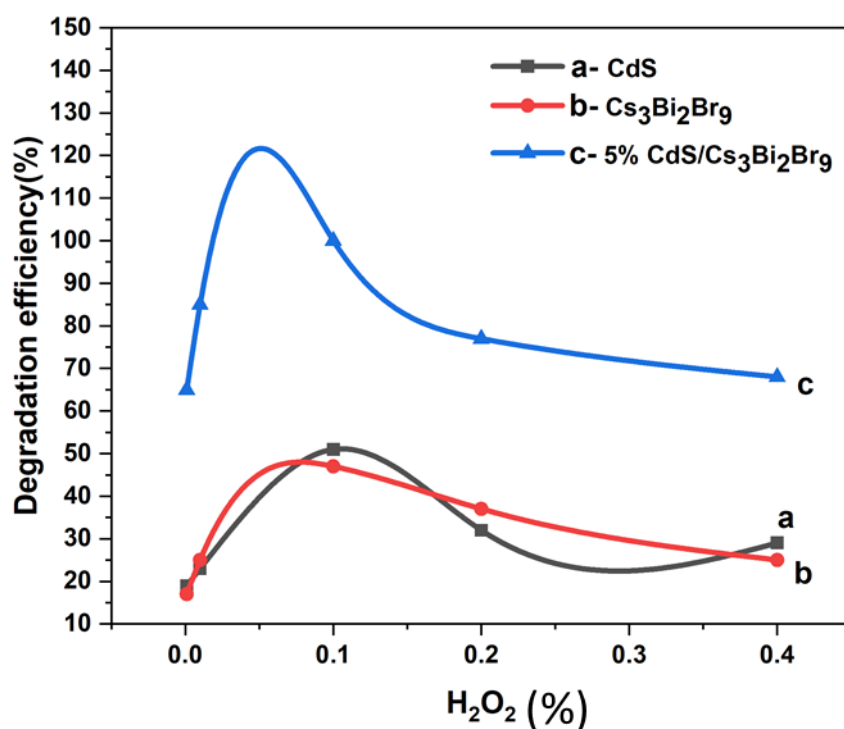


Figure 5.9 Effect of H₂O₂ (%). Conc. of CIP; 100mg/L, Reaction volume; 30mL, pH; 8, irradiation time; 3h, Catalyst dose; 10mg, Temperature; 30°C

Effects of Catalyst Dosage

Improving the efficiency of Ciprofloxacin degradation is largely dependent on optimizing the amount of photocatalyst used, since this parameter determines the rate of generation of

photogenerated electrons and holes charge carriers. Various quantities of CdS, Cs₃Bi₂Br₉, and 5% CdS/Cs₃Bi₂Br₉ nanocomposites were tested in a 180 ml CIP solution with 0.1% H₂O₂ and a pH of 8.0 to find the best photocatalytic dosage. The efficiency of degradation of ciprofloxacin using photocatalytic processes rose from 35 to 88.5% as the dosage of the photocatalyst was raised from 0.001 to 0.5 g/l. Visual representation in **Figure 5.10**. It's worth mentioning that the elimination efficiency persistently remained below the 0.5g/l barrier, even when administered at greater dosages. This indicates a crucial saturation threshold beyond which further increases in dosage won't have much of an effect. According to the research, light penetration was reduced due to the increased suspension of photocatalysts caused by the large amount of photocatalytic nanocomposite [Khodami et al., 2015; Meky et al., 2025; Nezamzadeh-Ejhieh et al., 2012].

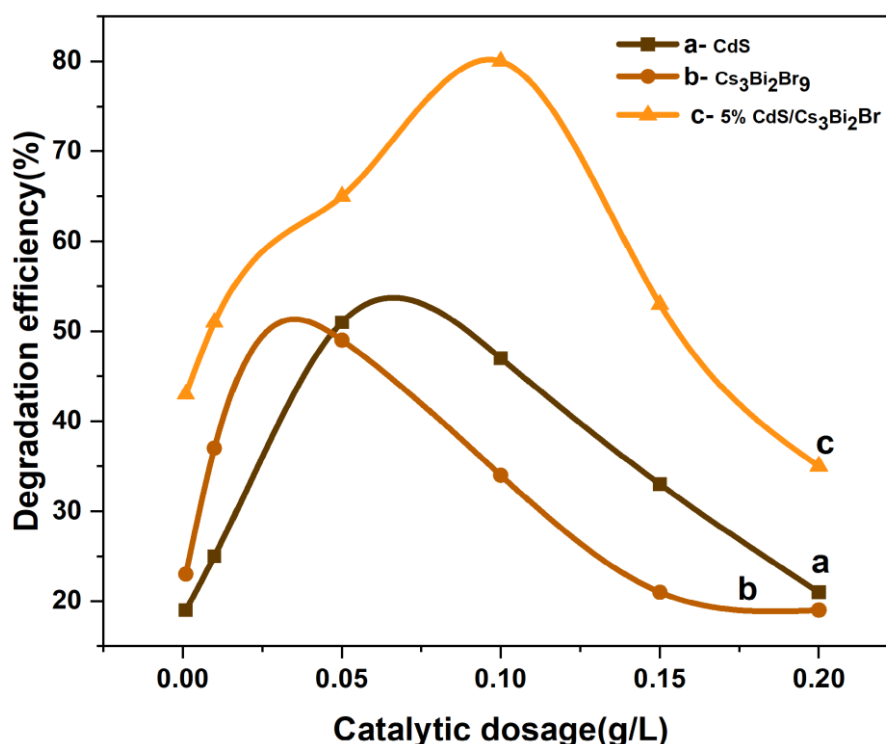


Figure 5.10 Effect of catalyst dosage. Conc. of CIP; 100mg/L, Reaction volume; 30mL, irradiation time; 3h. Catalyst dose; 10mg, pH; 8, Temperature; 30°C

Impact of Temperature on photocatalytic breakdown of ciprofloxacin

The impact of temperature on the removal of CIP from water utilizing CdS, Cs₃Bi₂Br₉, and 5% CdS/Cs₃Bi₂Br₉ nanocomposites was assessed by examining the photocatalytic efficiency at various temperatures (10, 20, 30, 40, and 60°C). The rate of CIP photodegradation increased from 10 to 40 °C, reaching a maximum at 40 °C (75% for CdS, 69% for Cs₃Bi₂Br₉, and 92.34% for 5% CdS/Cs₃Bi₂Br₉) after 120 minutes, subsequently declining at 60°C (**Figure 5.11 (a)**,

(b), (c)). The enhanced effectiveness of the removal process with increasing temperature is likely to adhere to Arrhenius' equation, which posits that elevated temperatures can improve catalyst particle mobility and interaction potential with ciprofloxacin ions. The minimal deterioration efficacy was observed at these temperatures, as elevated temperatures diminish the efficacy of the degradation process by prompting radicals to interact with each other rather than with the CIP molecule. A temperature increase diminishes the solubility of oxygen in water, which is unfavourable. In the experiments, the solution will evaporate markedly at elevated temperatures. Consequently, temperatures exceeding 50 °C are not recommended [Salesi et al., 2022; Narenuch et al., 2021; Mohapatra et al., 2012].

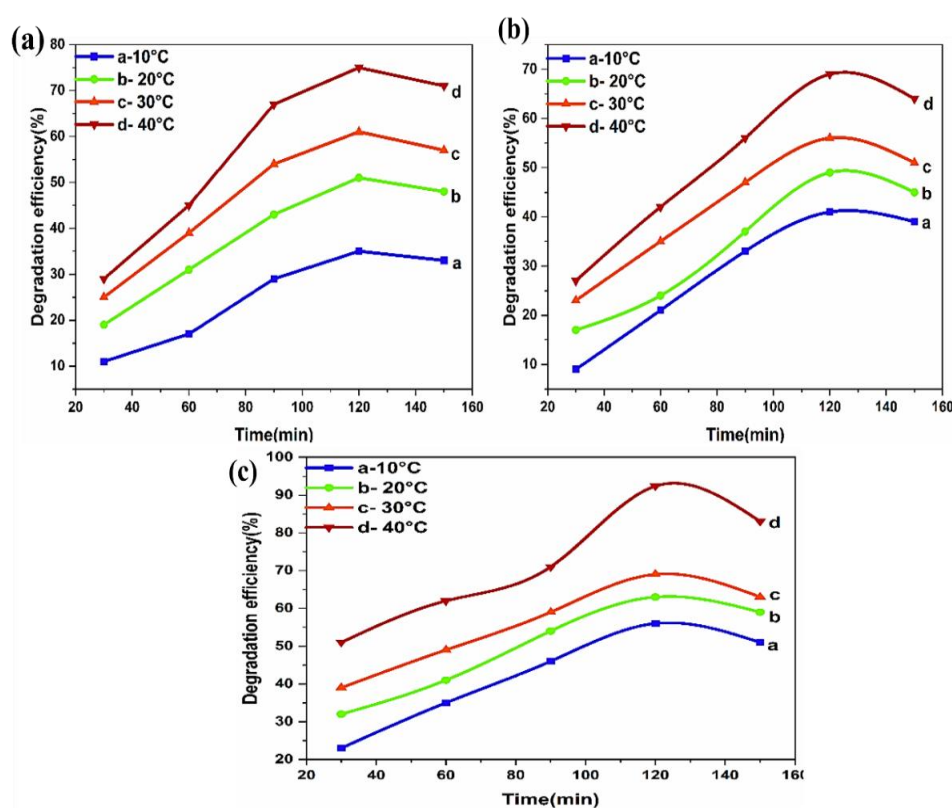


Figure 5.11 Effect of Temperature on degradation of CIP by (a) CdS, (b) Cs₃Bi₂Br₉, (c) 5% CdS/Cs₃Bi₂Br₉. Conc. of CIP; 100mg/L, Reaction volume; 30mL, Catalyst dose; 10mg, pH; 8, irradiation time; 2.5h

Effect of concentration of pollutant

In the CdS, Cs₃Bi₂Br₉, and 5% CdS/Cs₃Bi₂Br₉ system, a number of batch experiments were carried out with CIP concentrations of 10, 20, 30, and 50 mg/L to evaluate the impact of CIP concentration on its degradation (**Figure 5.12 (a), (b), (c)**). The efficacy of Ciprofloxacin

degradation diminished from 57.33% to 49% for CdS, from 52% to 35.9% for Cs₃Bi₂Br₉, and from 90.25% to 65.4% for 5% CdS/Cs₃Bi₂Br₉ as the CIP concentration increased from 10 mg/L to 50 mg/L. The deuterogenic byproducts and CIP molecules may exert a greater competitive influence on the limited reactive oxygen species, thereby impeding CIP degradation. In addition, there are limited adsorption sites, and Ciprofloxacin compounds and their degradation intermediates compete for them. The rivalry diminishes the reaction rate by obstructing the active sites of CdS on the catalyst surface. The collected data were subsequently input into the Langmuir-Hinshelwood model **Equation 5.9**, with its corresponding plot illustrated in **Figure 5.13**. Substituting the value of k into the calculation $t_{1/2} = (0.693/k)$ yields $t_{1/2} = 77.86$ min for CdS, $t_{1/2} = 95.98$ min for Cs₃Bi₂Br₉, and $t_{1/2} = 63$ min for 5% CdS/Cs₃Bi₂Br₉ [Narenuch et al., 2021; Mohapatra et al., 2012].

$$\ln(C_t) = -kt + \ln C_0 \quad 5.9$$

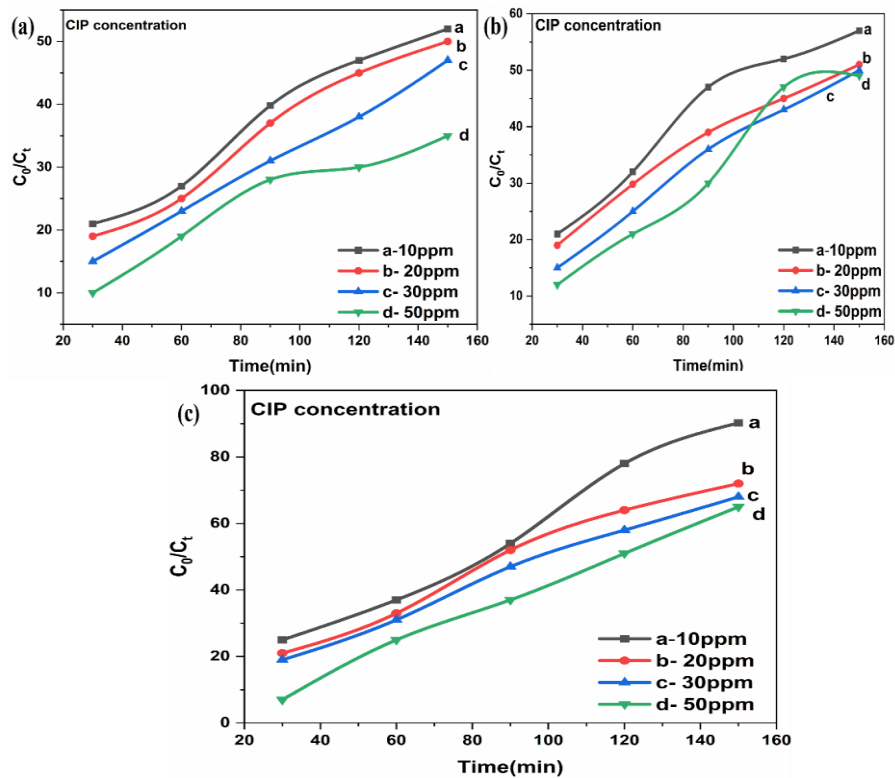


Figure 5.12 Effect of initial concentration on degradation of CIP by (a) CdS, (b) Cs₃Bi₂Br₉, (c) 5% CdS/Cs₃Bi₂Br₉. Conc. of CIP; 100mg/L, Reaction volume; 30mL, pH; 8, Catalyst dose; 10mg, Temperature; 30 irradiation time; 2.5h

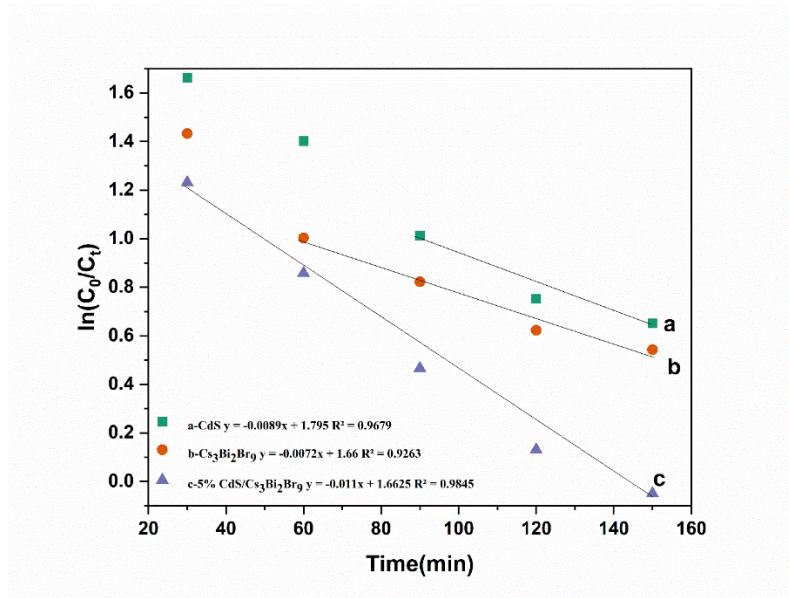


Figure 5.13 Hinshelwood model for degradation of CIP by (a) CdS, (b) Cs₃Bi₂Br₉, (c) 5% CdS Cs₃Bi₂Br₉. Conc. of CIP; 100mg/L, Reaction volume; 30mL, Catalyst dose; 10mg, irradiation time; 2.5h, pH; 8

Regeneration study

The catalyst becomes more profitable when the produced photocatalyst is reused for "n" cycles. The employed photocatalyst was subjected to a 30% H₂O₂ solution for one hour under stirring to facilitate regeneration (0.1 g/10 mL). Until the 5th cycle, the elimination efficacy of Ciprofloxacin was 50.01%, and with an increase in the number of regeneration cycles, the elimination efficacy of Ciprofloxacin diminished (**Figure 5.14**). The H₂O₂ treatment can oxidize surface-trapped compounds to H₂O and CO₂ by providing free active sites and a negatively charged surface, functioning as a novel photocatalyst 5% CdS/Cs₃Bi₂Br₉ [Khodami et al., 2015].

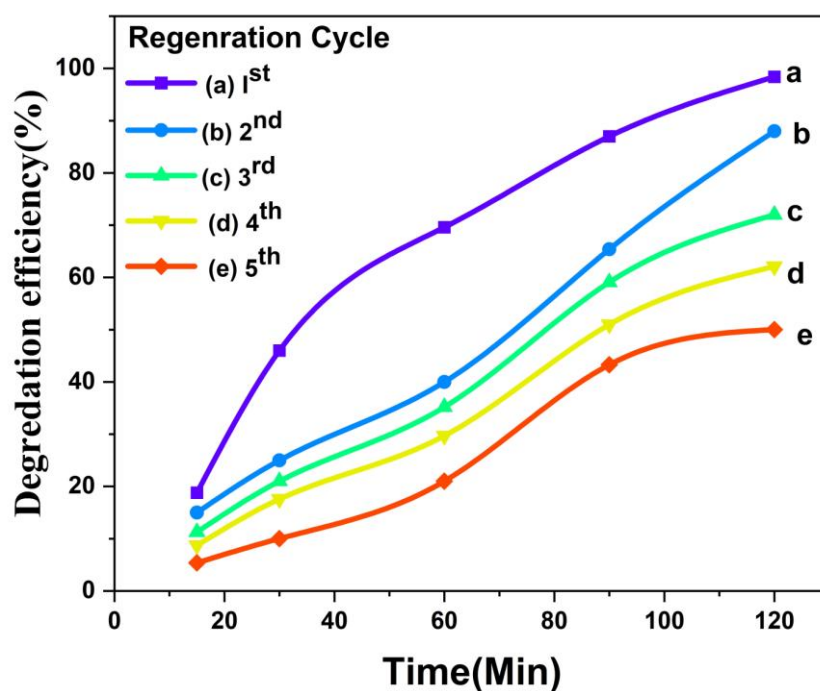
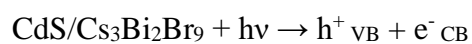


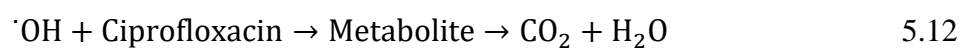
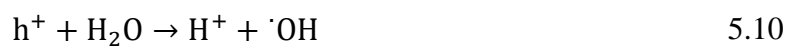
Figure 5.14 The regeneration rate of 5% CdS/Cs₃Bi₂Br₉. Conc. of CIP; 100mg/L, Reaction volume; 30mL, Catalyst dose; 10mg, irradiation time; 3h, pH; 8, Temperature; 30°C

5.2.3. Ciprofloxacin Photocatalytic Degradation: A Comprehensive Overview

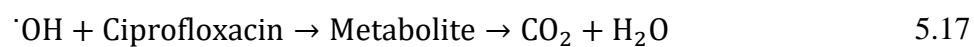
Based on experimental results and prior literature regarding the photocatalytic degradation of organic compounds, we hypothesized that the exposure of CdS/Cs₃Bi₂Br₉ nanocomposites to visible light would promote electron excitation from the valence band to the conduction band, resulting in the formation of electron holes. The preliminary phase of semiconducting material photocatalysis has conventionally been perceived as the transport of generated electrons (holes) to the pollutant situated on the nanoparticle's surface. **Figure 5.15**. Scheme 1 depicts the oxidation of the medication at the CdS/Cs₃Bi₂Br₉ interface by photogenerated hydroxyl radicals and holes. The medication may undergo oxidation both directly and indirectly due to the substantial oxidative potential of the holes. Hydroxide reactive radicals are generated during the indirect oxidation of drug molecules when the valence band hole interacts with water and/or hydroxide anions (OH⁻), as illustrated in **Equations 5.10 and 5.11**. Subsequent to further modifications, the principal photoproducts radical ions resulting from interfacial electron (hole) transfer are established as definitive photoproducts, as illustrated by **Equation 5.17**. The subsequent mechanism for drug degradation employing photocatalysts (P) was given [Wen et al., 2018; El-Kemary et al., 2010].



Equation for oxidative reaction



Degradation of Ciprofloxacin via Reductive Photocatalysis:



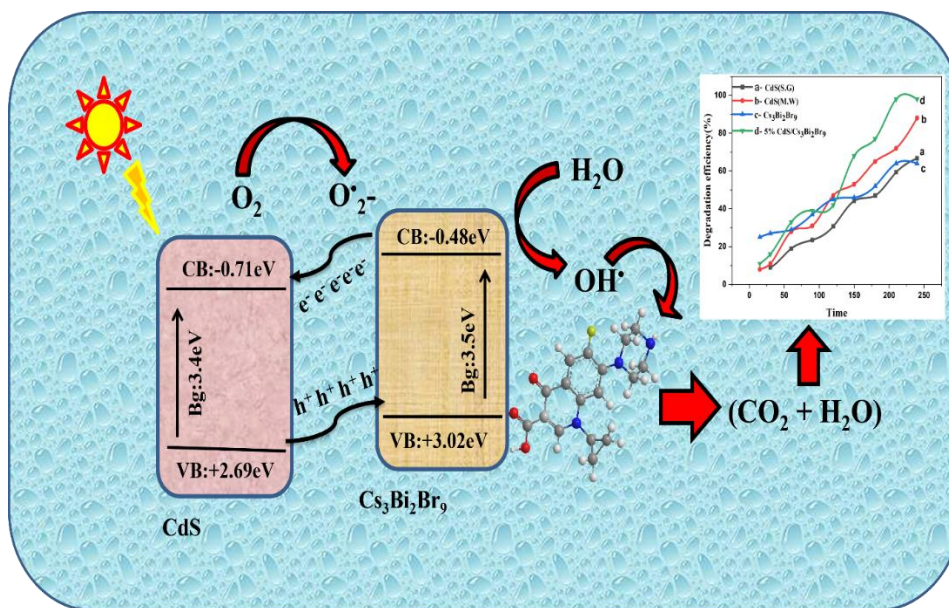
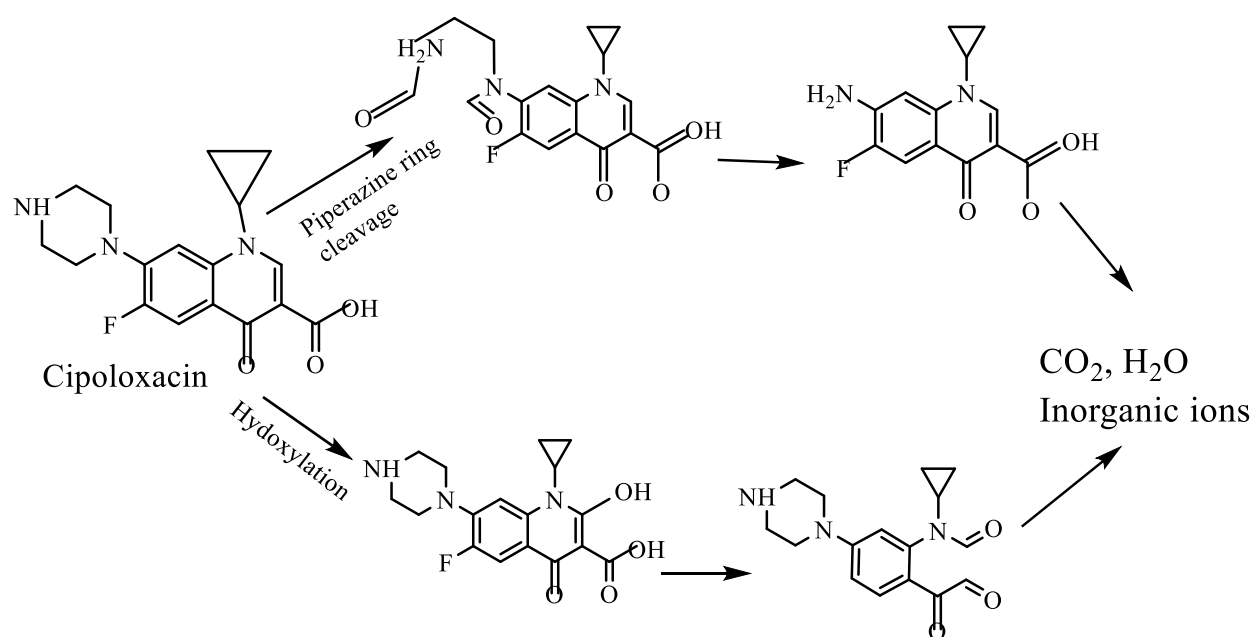


Figure 5.15 An approach to Ciprofloxacin degradation

Possible degradation pathway of ciprofloxacin

In the first part, the piperazine ring is cleaved in a methodical manner. Reactive radicals like hydroxyl can easily produce cation radicals by oxidizing the lone pair of electrons by electron transfer. Afterwards, peroxy radicals are produced when the α -carbon of the cation radicals undergoes deprotonation and reacts with oxygen in the solution. The production of dialdehyde derivative A occurs upon the breaking of the piperazine ring. The increasing disappearance of formaldehyde groups is caused by increased compound oxidation A. Oxidation, CO_2 loss, and amine extraction lead to the end product at this stage. Breaking the quinolone ring is the second step. To begin, the intermediate molecule is formed when $\cdot\text{OH}$, which have been generated through photocatalysis, attack carbon atom C of CIP. Along with it, hydroxylation and decarboxylation will occur. The second pathway concludes in the production of the final product through hydroxyl substitution. You can see the progression of the degradation process in the pathway below (Scheme 6). Water, carbon dioxide, and inorganic ions are the expected byproducts of AOP, as mentioned earlier [Mohapatra et al., 2012; Wen et al., 2018].



Scheme 6 Schematic Pathway for degradation of Ciprofloxacin.

Chapter-6

MoS₂/CdS Nanocomposites for Enhanced Visible Light Photocatalytic Degradation of Paracetamol in Synthetic Pharmaceutical Wastewater

6.1. Introduction

Water is an indispensable resource crucial for supporting life on our planet. However, the escalating demand for water in domestic, agricultural, and industrial sectors has significantly compromised its quality [Michael et al., 2013]. Recent studies and reports have drawn attention to the persistence of elevated concentrations of emerging contaminants, specifically pharmaceutical compounds, in various environmental compartments such as water bodies, soil, sediment, and plants [Hou et al., 2020]. The contamination of these water bodies by pharmaceutical compounds stems primarily from two pathways: the discharge of effluents containing pharmaceutical residues from the pharmaceutical industry into water streams, and the improper disposal of substantial quantities of unused drugs into the environment [Massima et al., 2021]. These practices have led to the presence of higher concentrations of antibiotics, notably in drinking water sources, highlighting the limitations of current water treatment technologies in effectively eliminating antibiotics from aqueous mediums [Dao et al., 2018]. The concerning aspect of this issue lies in the fact that antibiotics play a significant role in fostering the emergence of antibiotic-resistant bacteria and genes. This, in turn, poses substantial threats to aquatic ecosystems and human health [Wang et al., 2018]. The proliferation of antibiotic-resistant bacteria and genes can disrupt the balance of aquatic systems and, if transmitted to humans, can significantly impact health by rendering antibiotics less effective in combating infections [Sharma et al., 2017]. To address this pressing environmental and public health concern, numerous techniques have been developed for the removal of antibiotics from aqueous mediums. Among these methods, "heterogeneous photocatalysis" has emerged as a promising solution [Boczkaj et al., 2017]. This process is considered more viable compared to conventional processes and advanced oxidation methods as it enables the degradation of antibiotics without relying on an external supply of hydrogen peroxide (H₂O₂) [Serpone et al., 2012]. This approach, recognized as a "green approach," involves the utilization of semiconductor-type photocatalysts that, upon absorbing light energy exceeding their band gap, spontaneously generate various reactive oxygen species (ROS) like hydroxyl radicals, superoxide radicals, singlet oxygen, and H₂O₂ [Wang et al., 2021].

Acetaminophen, commonly known as paracetamol, is a prevalent active compound in various pharmaceuticals, serving as an anti-inflammatory and analgesic medication for both humans and animals [Bhembe et al., 2020]. However, its widespread presence in the environment and its tendency to accumulate in water bodies pose concerns. Acetaminophen has been detected in surface waters, wastewater, and even in drinking water. A significant percentage, around 58 to 68%, is excreted from the human body after therapeutic use, emphasizing the risks associated with excessive intake, including liver failure and potential fatality [Crabb et al., 2019]. To address these limitations, researchers are focusing on developing nanomaterials from different waste products. These nanomaterials offer economic viability, effectiveness, and efficiency in both heavy metal adsorption and the photodegradation of organic pollutants, offering a promising avenue for mitigating the challenges associated with traditional adsorption methods [Gloria et al., 2023]. Photocatalysis stands as a prominent advanced oxidation method utilized for breaking down toxic and persistent organic compounds found in various sources like pharmaceuticals, textile dyes, and pesticides within wastewater. Its efficacy lies in generating potent reactive radicals, particularly hydroxyl radicals, capable of mineralizing a broad spectrum of organic pollutants [Garrido-Cardenas et al., 2020].

Semiconducting optoelectronic materials play a pivotal role in various applications due to their exceptional optical, electrical, magnetic, and piezoelectric properties. Alterations in semiconductor materials' optical, electrical, magnetic, and physical attributes are intricately linked to their sizes, structures, and morphologies [Pant et al., 2019]. Researchers have increasingly focused on synthesizing semiconductor particles within the few nanometres range, approaching the dimensions comparable to the Bohr radius. At this scale, semiconductor nanoparticles exhibit distinct size-dependent properties, holding potential for applications like quantum dot lasers, single electron transistors, and various biological applications [Singh et al., 2024]. Efforts have been directed towards synthesizing semiconductor nanoparticles of desired sizes with a narrow size distribution, employing manageable conditions concerning precursors, solvents, and temperatures. Metal-oxide semiconductors have emerged as particularly effective photocatalysts in this context. Notably, semiconductors like WO_3 , TiO_2 , CdS , MoS_2 and ZnO have demonstrated outstanding photocatalytic capabilities. CdS , and MoS_2 in particular, holds distinction due to its small band gap of 2.42 [Bharti et al., 2018] and 1.84 [Hussain et al., 2020] eV respectively, enabling it to absorb visible light effectively and efficiently degrade organic pollutants, making it a promising candidate for photocatalytic applications

Cadmium sulfide (CdS) stands out as a noteworthy semiconductor material, boasting a direct band gap at room temperature and demonstrating remarkable physical and chemical properties.

Its applications span diverse technical fields, encompassing photochemical catalysis, gas sensors, laser and infrared detectors, solar cells, nonlinear optical materials, luminescence devices, and optoelectronic devices, among others [Wang et al., 2021]. CdS particularly excels in visible light detection among semiconductor materials [Cao et al., 2019]. Over the past decades, numerous techniques have been explored for synthesizing CdS nanoparticles [Yu et al., 2023]. Researchers strive to discover novel experimental methodologies capable of producing nanoparticles with minimal cost, low size dispersion, and precise control over size and shape. Recent research has focused on developing high-quality CdS nanoparticles via a simple chemical route employing cadmium nitrate and sodium sulfide inorganic precursors.

In our current research, we detail the synthesis of MoS₂ and CdS nanocomposites using a Solgel method. Our study centres on an in-depth analysis of the structural modifications within the MoS₂ and CdS nanocomposite host matrix. We aim to comprehensively investigate the structural, optical, and spectroscopic properties of MoS₂ and CdS nanocomposites, emphasizing the capabilities and alterations achieved through the Solgel technique. This method allows precise control over composition and crystalline structure, offering tailored properties suitable for specific applications. Our manuscript provides a detailed exploration facilitated by the microwave synthesis approach, enabling a nuanced understanding of MoS₂ and CdS nanocomposites characteristics. We employ various analytical techniques such as X-ray diffraction and photoluminescence (PL) to conduct a comprehensive analysis. The primary objective of this research is to elucidate the material's attributes and potential functionalities. Furthermore, our study focuses on the degradation of paracetamol for wastewater treatment, aiming to leverage the unique properties of CdS synthesized through the Solgel method in addressing environmental challenges related to pharmaceutical contaminants in water.

6.2.Result and Discussion

6.2.1. Characterization studies

XRD Analysis

The X-ray diffraction analysis of MoS₂, CdS, and their various composites, as depicted in **Figure 6.1 (a, b, c, d and e)**, delivers valuable info about the crystalline phases, crystallite size, and purity of the materials. The X-ray diffraction patterns of MoS₂ and CdS match well with the corresponding entries in the JCPDS database (JCPDS card No. 101122 for MoS₂ and No. 23323 for CdS). MoS₂ is identified as existing in the hexagonal phase [Gupta et al., 2022], while CdS is identified as having a cubic phase [Dey et al., 2020]. This information is crucial for understanding the structural characteristics of the individual materials. The XRD patterns of the various composites, with different ratios of MoS₂ and CdS, are reported to match the

hexagonal and cubic phases, respectively. The presence of sharp peaks in the XRD patterns indicates the crystalline nature of the samples.

The crystallite size of the materials is calculated using the Scherrer formula. The obtained values confirm that the average crystallite size for all materials is below 50 nm. The absence of impurity peaks in the XRD patterns confirms the single crystal phase of both pristine MoS₂ and CdS, as well as their various composites.

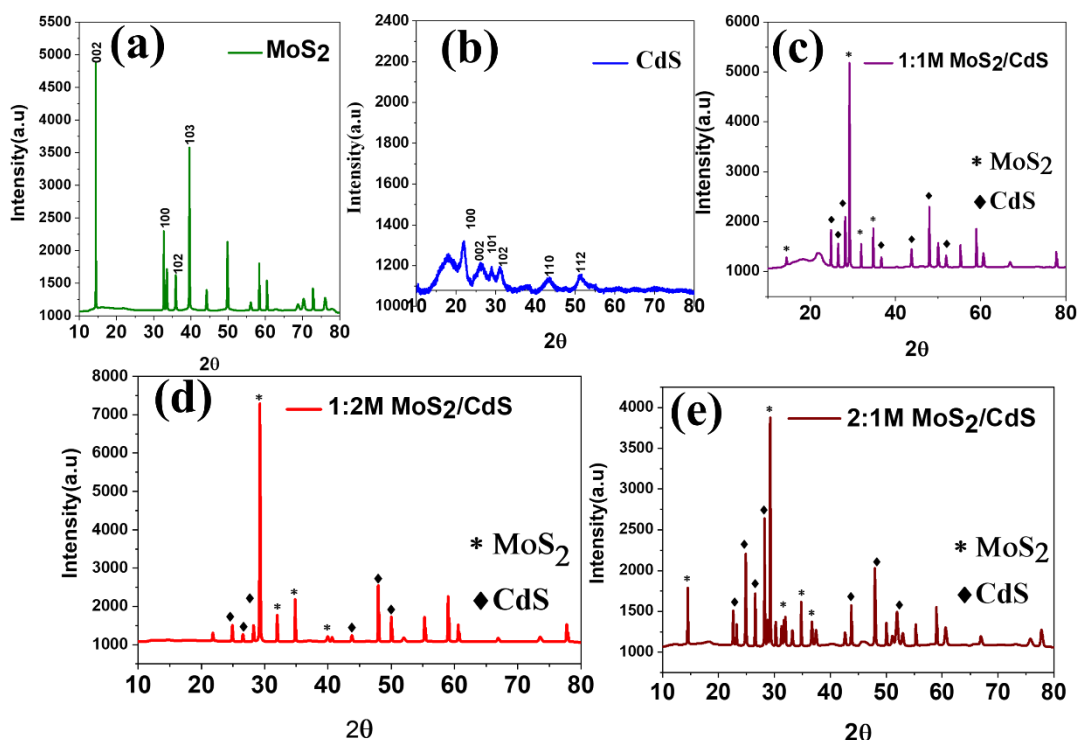


Figure 6.1 XRD pattern of (a) MoS₂, (b) CdS, (c) 1:1M MoS₂/CdS, (d) 1:2M MoS₂/CdS and (e) 2: 1M MoS₂/CdS

FTIR Analysis

The FTIR (Fourier-transform infrared spectroscopy) spectra of MoS₂, CdS, and MoS₂/CdS nanocomposite are shown in **Figure 6.2 (a, b and c)**. The peaks correspond to specific functional groups or bonds present in the sample. The peak at 593 cm⁻¹, 739 cm⁻¹, 1075 cm⁻¹, 2346 cm⁻¹ and 3093 cm⁻¹ are attributed to MoS₂ and are likely related to its structural vibrations or specific bonding configurations [Liu et al., 2012]. This peak at 593 cm⁻¹ is associated with the S–S bond, indicating the presence of sulfur-sulfur bonds in the MoS₂ nanoparticles. The peak at 3093 is indicative of the O–H group, which could suggest the presence of hydroxyl groups or moisture absorbed on the surface of the nanoparticles. Understanding these peaks

helps in characterizing the chemical composition and structure of the MoS₂ nanoparticles. The peaks at 636 cm⁻¹, 882 cm⁻¹, 1397 cm⁻¹, 3386 cm⁻¹ are due to the CdS [Martin et al., 1982]. The distinctive signals of CdS originate from the stretching vibrations of its C–H bonds, exhibiting three well-defined peaks centered around 1397 cm⁻¹ in the infrared (IR) spectroscopy spectrum. The peak at 3386 cm⁻¹ is due to the O–H group, which could suggest the presence of hydroxyl groups or moisture absorbed on the surface of the CdS.

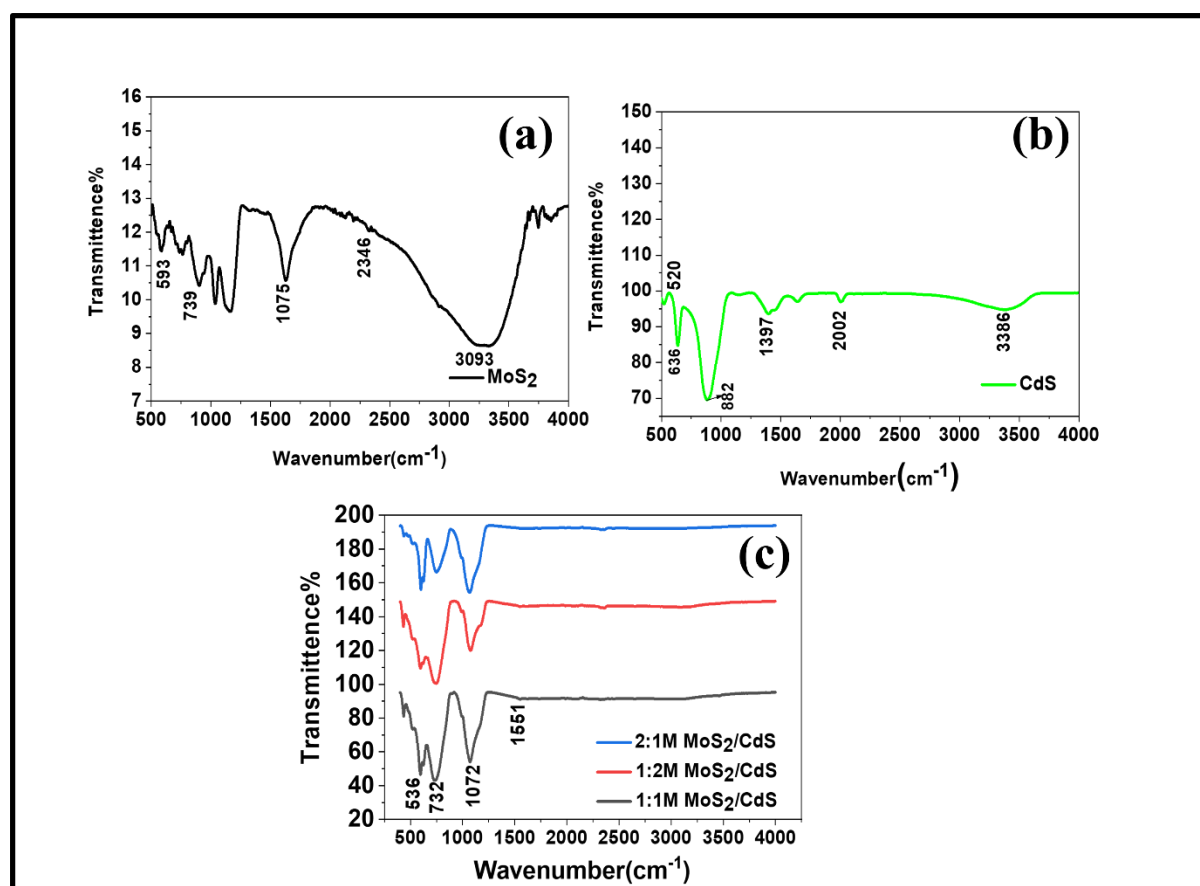


Figure 6.2 FTIR spectra of (a) MoS₂, (b) CdS and (c) MoS₂/CdS nanocomposites

SEM/EDS Analysis

Understanding the morphology is crucial in materials science, especially for nanomaterials and composites, as it influences various properties and behaviours, such as mechanical strength, electrical conductivity, and catalytic activity [Raja et al., 2022]. The scanning electron microscopy (SEM) micrographs presented in **Figure 6.3 (a, b and c)** for the pure MoS₂, CdS and 1:1 MoS₂/CdS composite provide insights into the morphological characteristics of the material. The observations suggest a degree of nonuniformity throughout the sample, marked by the formation of irregular shapes that subsequently agglomerate to form sheet-like structures. The SEM micrographs reveal the presence of irregular morphology and subsequent

agglomeration observed in materials like MoS₂ (molybdenum disulfide) and CdS (cadmium sulfide) can be attributed to various factors related to their synthesis and properties [Liu et al., 2021]. During the synthesis process, nucleation and subsequent growth of particles occur. Irregularities may arise if the nucleation sites are not uniformly distributed or if there are variations in the growth rates of different crystal faces. Non-uniform growth can result in irregular shapes. Further the kinetics of nucleation and growth processes can result in non-uniformities. Rapid nucleation or growth in certain regions may lead to irregular shapes, and subsequent agglomeration could be influenced by the kinetics of these processes.

The Energy-Dispersive X-ray Spectroscopy (EDS) spectra, as depicted in **Figure 6.3 (a, b and c)**, provide information about the elemental composition of the material under examination, likely the pure MoS₂, CdS and 1:1 MoS₂/CdS composite. The statement indicates that the EDS analysis supports the purity of the material, revealing no detectable impurities. Additionally, the elemental composition obtained from EDS is reported to be in good agreement with the expected composition based on the empirical formula.

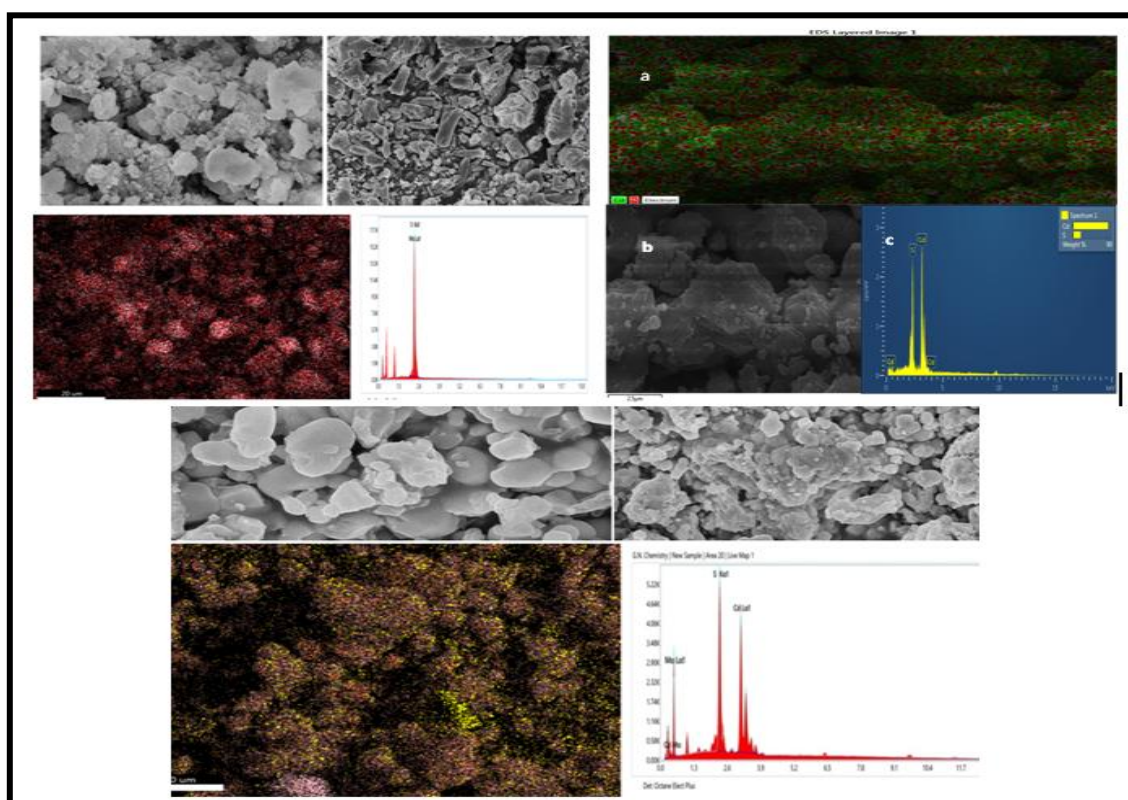


Figure 6.3 SEM/EDX of (a) pure MoS₂, (b) pure CdS and (c) 1:1M MoS₂/CdS nanocomposite

UV Absorption

The absorption spectrum provides information about how a material absorbs light at different wavelengths. For MoS₂, CdS, and their 1:1 composite, the absorption lies in the visible region near 500 nm, indicating strong light absorption within the visible range of the electromagnetic spectrum. The peak observed around 500 nm is associated with characteristic electronic transitions or the bandgap of these materials [Wamsley et al., 2023]. The composite exhibits absorption behaviour similar to its individual components, as the absorption peaks of CdS and MoS₂ remain unchanged in the 1:1 mixture. This suggests that the intrinsic electronic properties of each material are preserved in the composite. The composite of CdS and MoS₂ does not shift the absorption peak but instead allows their beneficial features to coexist without undesirable modifications. This stability is advantageous for tailoring material properties and enhances the potential for integrating the composite into optoelectronic technologies.

The optical bandgap (E_g) of the MoS₂/CdS (1:1) composite was determined using the Tauc equation:

$$(\alpha h\nu)^n = A(h\nu - E_g)$$

where α is the absorption coefficient, $h\nu$ is the photon energy, A is a constant, and E_g is the bandgap energy. Since both materials exhibit direct band gaps, an exponent value of $n = 1/2$ was applied. **Figure 6.4 (a-c)** depicts the optical bandgap of MoS₂, CdS and their 1:1 composite. The calculated bandgap values were 1.84 eV for MoS₂, 2.42 eV for CdS, and 1.78 eV for the composite, representing the energy gap between the valence and conduction bands [Ebnonnasir et al., 2014]. The identification of narrow bandgap in as-synthesised materials underscores their promise for optoelectronic applications, where effective light absorption and high energy efficiency are crucial for advancing device performance.

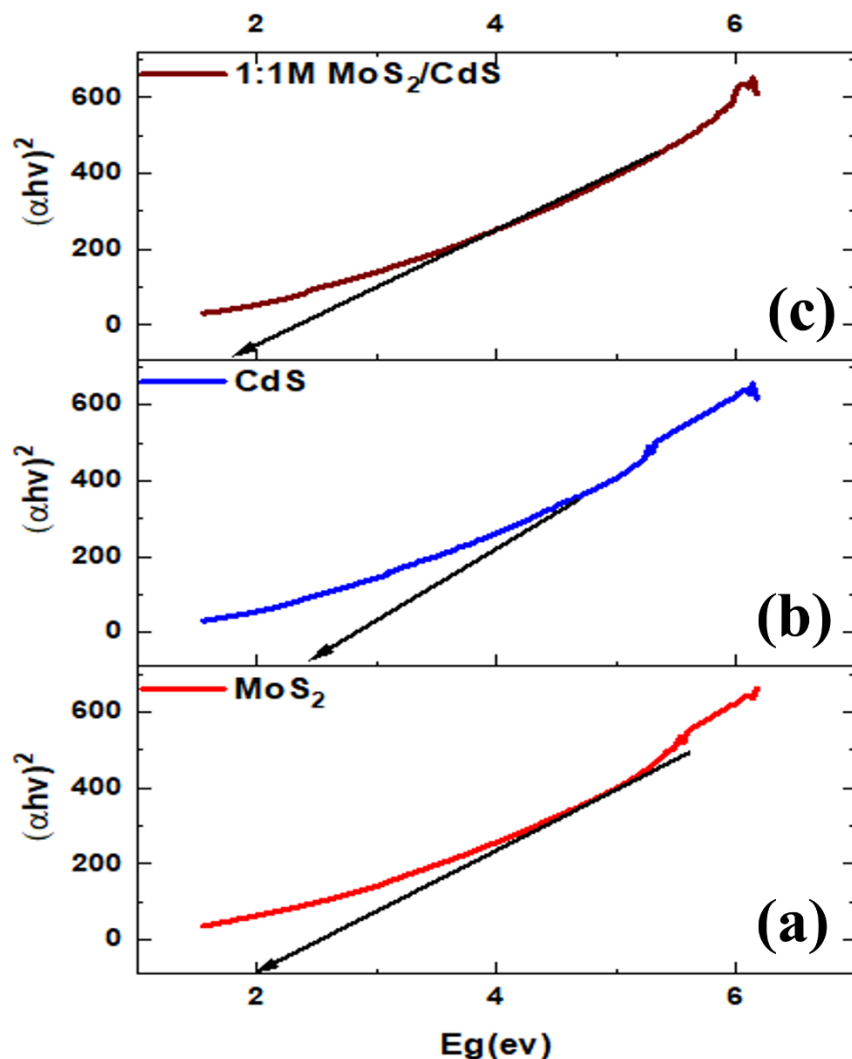


Figure 6.4 Optical band gap of (a) MoS_2 , (b) CdS and (c) 1:1M MoS_2/CdS

6.2.2. Photocatalytic Degradation of Paracetamol

To optimize the photocatalytic degradation of paracetamol (PCM) across different pH levels, all samples were subjected to an identical amount of visible light (Xe lamp) in a thermostatic water bath utilizing CdS , MoS_2 , and 1:1 CdS/MoS_2 photocatalytic nanomaterials. The pH of the solution was maintained at a consistent level with a glass electrode along with 0.1N NaOH and 0.1N HCl . In order to examine the comparative degradation of CdS , MoS_2 and 1:1 CdS/MoS_2 nanomaterials, a 30 milliliter Paracetamol solution containing 10mg of catalytic material was exposed to UV and visible light for 3h respectively. The degraded Paracetamol solution underwent filtering using Whatman filter paper after 3 hours of light irradiation, and absorbance was measured at the maximum wavelength of 243 nm using a UV-

visible spectrophotometer [Zhang et al., 2019]. The degradation efficiency percentage of paracetamol was calculated using **Equation 6.1**. In the batch experiment, a solution containing 10 ppm of paracetamol was photodegraded using a 1:1 CdS/MoS₂ nanomaterials photocatalyst and three hours of light irradiation, following the same approach.

$$\% \text{ Degradation Efficiency} = \left(\frac{C_0 - C_t}{C_t} \right) \times 100 \quad 6.1$$

The initial Paracetamol concentration is C_0 , and the solution concentration at time t is C_t .

Effect of pH

The pH is an essential variable that influences the CdS, MoS₂ and 1:1CdS/MoS₂ catalyst contact with the surface on Paracetamol molecules, which in turn influences the degradation of Paracetamol in several ways. Therefore, it is essential to investigate how pH affects photodegradation. Degradation process efficiency is adversely affected by highly reactive OH radicals. Paracetamol is initially oxidized into metabolites by the OH-free radical, which leads to total mineralization. The pH of the solution influences the degradation of Paracetamol by modifying the amount of OH radical produced during the acid-base equilibrium process and by influencing the surface contact between the photocatalyst and Paracetamol through the deprotonation and protonation of Paracetamol. In this work, 10 mg of CdS, MoS₂ and 1:1 CdS/MoS₂ nanocatalyst were used to photocatalyzed the degradation of 10 ppm of Paracetamol solution under visible region light, respectively, at pH 3, 4, 5, 6, 8 and 10 i.e., acidic to basic medium. The maximal degradation efficiencies for CdS, MoS₂, and 1:1 CdS/MoS₂ nanomaterials at pH 4 are 70%, 68%, and 98.7%, respectively. **Figure 6.5**, illustrates the degradation efficiency rise in acidic medium. A higher concentration of H^+ is generated in an acidic medium, where it transforms into an $\cdot OH$ and H_2O_2 . Both the concentration of OH^- ions and the surface charge characteristic of the catalyst had an impact on the rate of degradation process. The pH_{pzc} values and pH of the solution of the catalyst have an impact on the electrostatic interaction among the Paracetamol and catalyst surface. Since Paracetamol and the positively charged catalyst surface interact electrostatically, CdS, MoS₂ and 1:1 CdS/MoS₂ nanomaterials exhibit maximum efficiency in degradation at pH 4. Paracetamol degrades less efficiently in a basic media because hydroxide ions capture the $\cdot OH$ and produce less h^+ . Comparing the degradation of Paracetamol at different pH values using TiO₂ as a photocatalyst

and CdS, MoS₂ and 1:1 CdS/MoS₂ [Sharma et al., 2016] is shown in **Table 6.1**. It indicates that the highest photodegradation efficiency is achieved by 1:1 CdS/MoS₂ nanocomposite.

Table 6.1: Research chart for Paracetamol showing photocatalytic degradation efficiency.

pH	Photocatalyst	Paracetamol conc.(mg/L)	Degradation efficiency (%)	Reference
pH 6.5	TiO ₂	< 20	99	[Lozano-Morales et al., 2019]
pH 7.8	TiO ₂ -PES	30	80	[Chijioke-Okere et al., 2021]
pH 7.28	TiO ₂	15	97	[Chekira et al., 2022]
pH 4	CdS	10	70	This study
pH 4	MoS ₂	10	68	This study
pH 4	1:1M MoS ₂ /CdS	10	98.7	This study

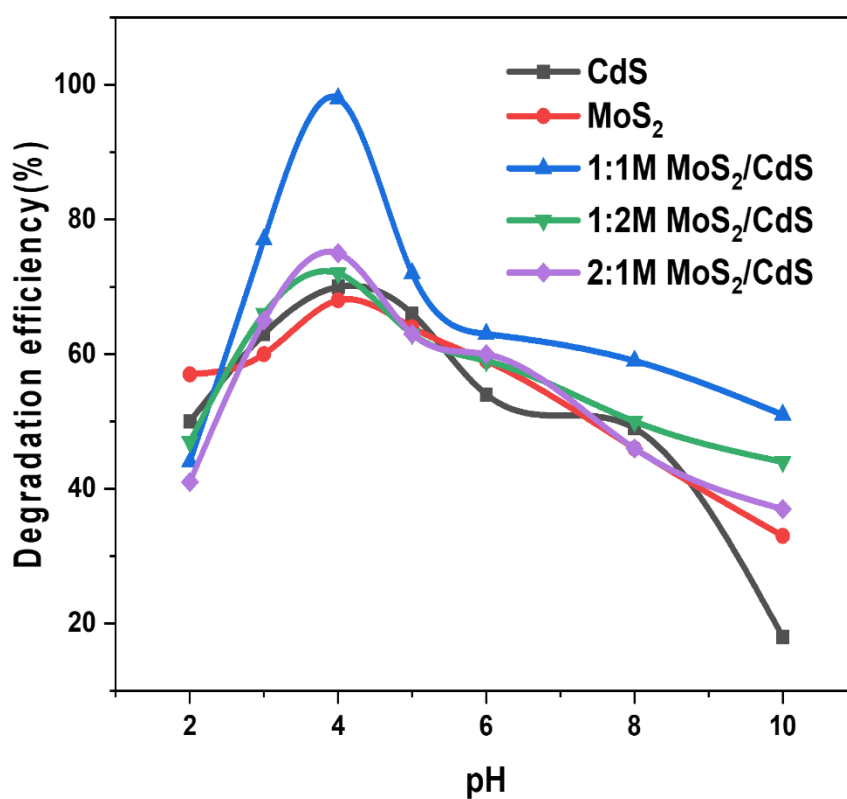


Figure 6.5 Effect of pH on PCM, Conc. of PCM;10mg/L, reaction volume; 30mL, catalyst dose;10mg, irradiation time; 3.5h, temperature; 30°C

Kinetic studies

Kinetic investigations of CdS, MoS₂ and 1:1M MoS₂/CdS were evaluated to investigate the mechanism of Paracetamol degradation. When exposed to visible light for 3 hours, a 10 mg catalyst dosage of CdS, MoS₂ and 1:1M MoS₂/CdS nanomaterials resulted in 89% 85% and 95% photocatalytic degradation of the Paracetamol solution, respectively (Rani et al., 2023).

Figure 6.6 demonstrates that 1:1M MoS₂/CdS nanocomposite had higher degrading efficiencies than CdS and MoS₂ nanoparticles with respective values of 46%, 61%, 68%, 79%, 81%, 85%, 88% and 90% in 15, 30, 60, 90, 120, 150, 180, 210 and 240 minutes. According to the literature review, the decomposition of Paracetamol exhibits pseudo-first-order kinetics (Parveen et al., 2023). A pseudo 1st order reaction kinetic was used to linearize the CdS, MoS₂ and 1:1M MoS₂/CdS nanomaterials curves between $\ln(C_0/C_t)$ and t (time), as shown in **Figure 6.7**. The graph of CdS, MoS₂ and 1:1M MoS₂/CdS substitution is a straight line. According to the linearized version of Langmuir Hinshelwood [Sharma et al., 2016] **Equation 6.2**, the degradation process of Paracetamol takes place on the CdS, MoS₂ and 1:1M MoS₂/CdS surface, where the Paracetamol adsorbed together with the reactive OH radical as well.

$$R_{PCM} = -\frac{dC_{eq}}{dt} = kKC_{eq}/1 + KC_{eq} \quad 6.2$$

Where k is the rate constant, t is the illumination constant, K is the Langmuir-Hinshelwood adsorption coefficient, C_{eq} is the equilibrium constant of the PCM and R_{PCM} is the rate of photocatalytic degradation. **Table 6.2** shows the rate constant reaction k (min⁻¹) determined from $\ln(C_0/C_t)$ Vs 't'.

Table 6.2: Rate constants of Pseudo-first order for catalytic elimination of Paracetamol using CdS, MoS₂ and 1:1M MoS₂/CdS.

Materials	Paracetamol(mg/L)	k(min ⁻¹)	R ²
CdS	10	1.733	0.972

MoS ₂	10	1.02	0.894
1:1M MoS ₂ /CdS	10	2.07	0.880

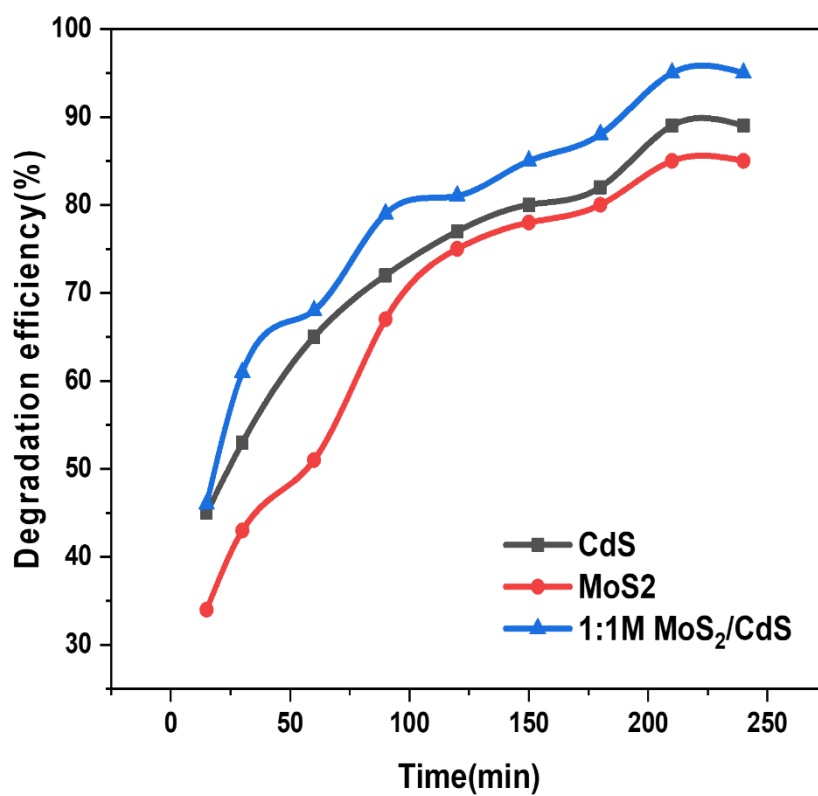


Figure 6.6 Kinetic studies of PCM Conc. of PCM; 10mg/L, reaction volume; 30mL, catalyst dose;10mg, pH; 4, temperature; 30°C

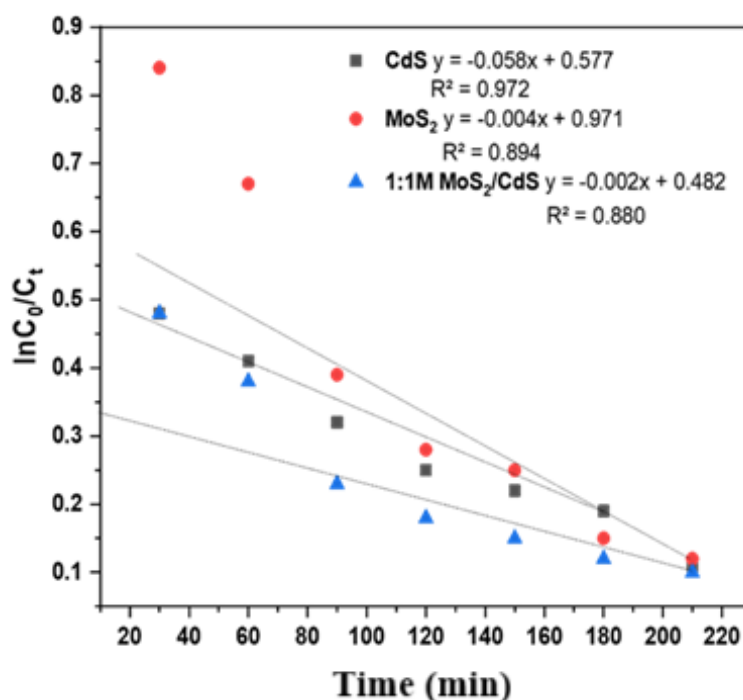


Figure 6.7 Photodegradation of PCM. Conc. of PCM; 10mg/L, reaction volume; 30mL, catalyst dose;10mg, irradiation time; 3.5h, pH; 4, temperature; 30°C

Effect of H₂O₂ of concentration

More sustainable intermediates and improved photocatalytic elimination result from H₂O₂'s capacity to produce more OH radicals (Aggelopoulos et al., 2020). **Figure 6.8** demonstrates the effect of variable hydrogen peroxide from 0.001 to 0.4% on the photocatalytic removal of Paracetamol by CdS, MoS₂ and 1:1M MoS₂/CdS. Without H₂O₂, the rate of photocatalytic degradation is 88%, 85% and 90% by CdS, MoS₂ and 1:1M MoS₂/CdS. An increase in hydrogen peroxide concentration from 0.001 to 0.1% leads to enhance 90–93% elimination of Paracetamol by photocatalytic degradation. The rate of elimination was reduced to 68% as the concentration of H₂O₂ was raised to 0.4%. The reduction was attributed to an increase in hydrogen peroxide, which inhibits hydroxyl radicals. Hidden photoinduced electron in hydrogen peroxide to stabilize electron/hole. Hydroxyl radicals are the by-product of the interaction between O₂ and H₂O₂. The elimination of Paracetamol from the system was therefore thought to be improved by adding H₂O₂ to the photocatalytic process. The provided quantity of hydrogen peroxide (H₂O₂) reduced the concentration of hydroxyl (OH) radicals, thereby diminishing their capacity to neutralize Paracetamol through the sorting of the OH

radicals. This process resulted in their transformation into less potent oxidants known as hydroperoxyl (HO_2) radicals [Tabasum et al., 2023].

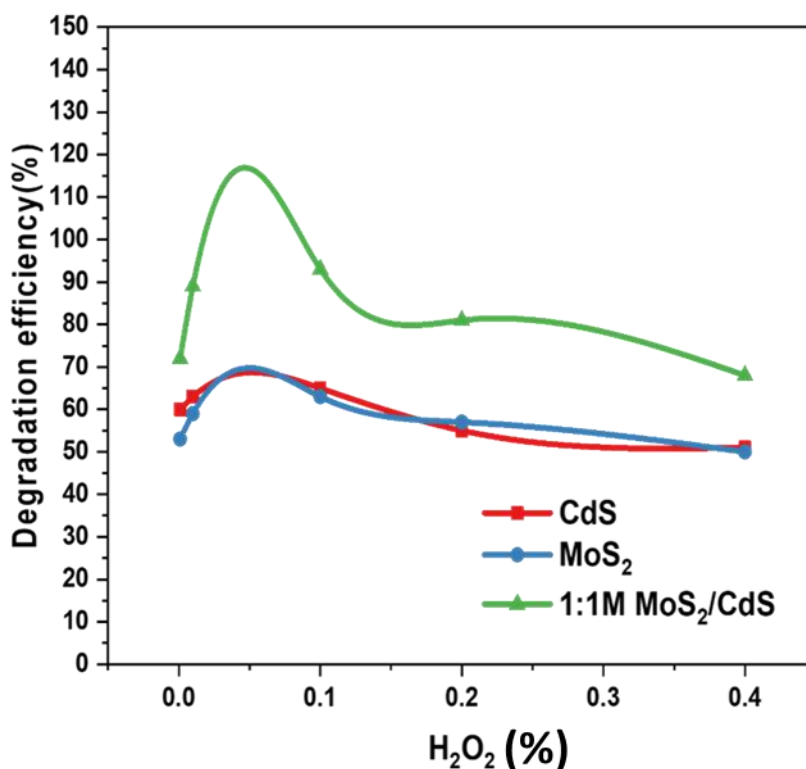


Figure 6.8 Effect of H_2O_2 (%), Conc. of PCM; 10mg/L, reaction volume; 30mL, catalyst dose; 10mg, irradiation time; 3.5h, pH; 4, temperature; 30°C

Effect of Catalyst Dosage

Paracetamol can be metabolized more effectively when its photo catalyst is easily accessible and present in adequate quantities (Yun et al., 2019). The photocatalytic performance of the nanomaterials is influenced by the dose of the photocatalyst, as shown in **Figure 6.9**. The concentration of CdS, MoS₂ and 1:1M MoS₂/CdS was diverse from 0.001g/L to 0.2 g/L in 210 milliliter of paracetamol solution with 0.1% hydrogen peroxide to govern the optimum quantity of photocatalyst. The Paracetamol photocatalytic elimination rate improved from 56% to 77% when the photocatalyst dosage was raised from 0.001 to 0.05 g/L. Nevertheless, there was no further impact on elimination efficiency when the dose was increased. This finding revealed that when a significant amount of photocatalyst was present, the greater concentration of the photocatalyst restricted the amount of light penetration [Noorisepehr et al., 2019].

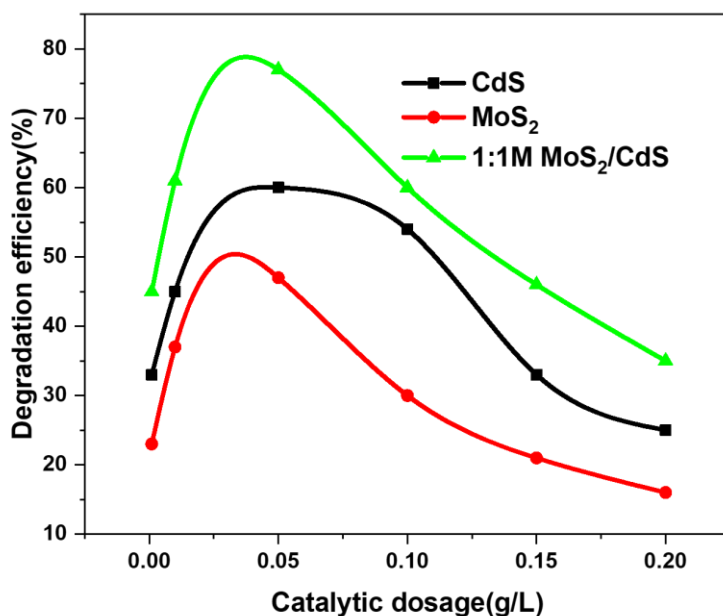


Figure 6.9 Effect of Photocatalyst dosage, Conc. of PCM; 10mg/L, reaction volume; 30mL, irradiation time; 3.5h, pH; 4, temperature; 30°C

6.2.3. Mechanism for photocatalytic degradation of Paracetamol

Fig. 6.10 shows the process of photocatalytic degradation of paracetamol entails the absorption of paracetamol molecules onto a photocatalyst surface, which is then exposed to light to generate electron-hole pairs. Reactive oxygen species (ROS) produced during the process or adsorbed paracetamol molecules engage in redox reactions with these electron-hole pairs. Superoxide radicals are created when photogenerated electrons break down oxygen molecules that have been deposited on the surface of the photocatalyst. These radicals then react with paracetamol to form intermediate products. The initial by-product of the dehydrogenation of Paracetamol was N-phenylacetamide, which was then converted by decarboxylation to a molecule termed aniline. Additionally, aniline denitrification generated toluene, which was then followed by the synthesis of (Z)-buta-1, 3-dien-1-ol due to bond breakage triggered by hydroxyl attack. The final products, but-1-ene (alpha-butylene), as well as a few other basic compounds, including H₂O, CO₂, NO²⁻, and NO³⁻ are formed upon the elimination of the aldehyde. In the meantime, paracetamol or other organic intermediates are oxidized by the holes in the valence band, which leads to the mineralization of paracetamol into less toxic and simpler molecules like water and carbon dioxide. The photocatalyst serves as a mediator during

the whole process, assisting in the breakdown of paracetamol in the presence of light [Puri et al., 2021].

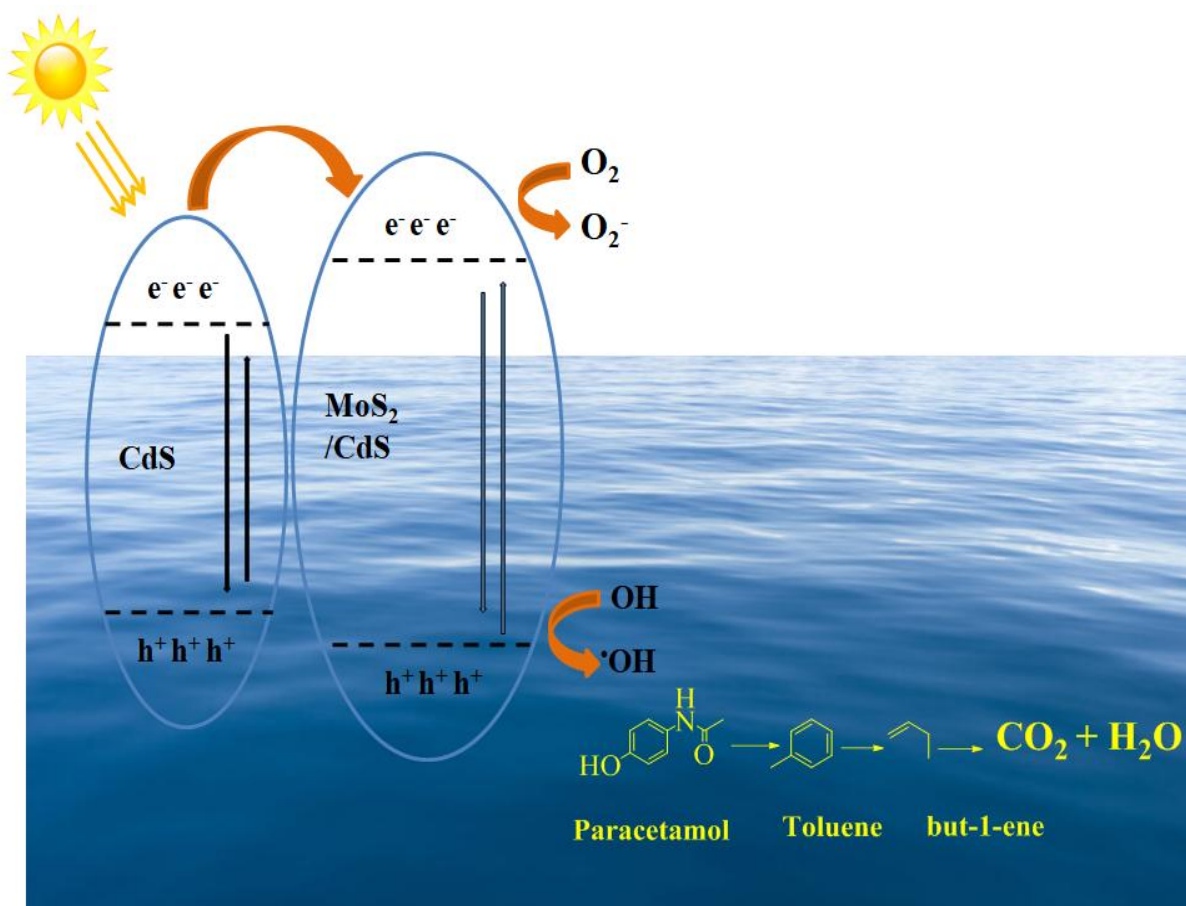


Figure 6.10 Mechanism of photocatalytic degradation process for Paracetamol

Chapter-7

Photocatalytic Removal of Ibuprofen from Wastewater using Novel $\text{MoS}_2@\text{Cs}_3\text{Bi}_2\text{Br}_9$ Nanocomposites

7.1. Introduction

The contamination of freshwater systems globally by a vast array of industrial and natural compounds has emerged as a significant environmental issue. Pharmaceuticals and personal care products, in particular, are among the most alarming emerging pollutants and have been frequently detected in natural water sources in recent years [Schwarzenbach et al., 2006; Boxall et al., 2012]. Ibuprofen (IBF), a widely utilized nonsteroidal anti-inflammatory drug, is produced in several thousand tons annually due to its effective antipyretic and analgesic properties. Despite its relatively low toxicity, IBF demonstrates both non-photodegradability and non-biodegradability, leading to its accumulation in aquatic environments and biological organisms [Kezzim et al., 2017; Garg et al., 2021]. This persistence poses potential risks to human health and ecological systems. Conventional wastewater treatment methods are insufficient in completely eliminating IBF, and can sometimes result in the formation of more hazardous intermediate by-products. Therefore, it is crucial to develop effective and environmentally friendly technologies for the removal of IBF from contaminated water. The IBF, known for its endocrine-disrupting and potential carcinogenic properties, poses serious threats to both human and environmental health. Chronic exposure to IBF concentrations exceeding $1\text{ }\mu\text{g/L}$ in water bodies has been linked to disruption in aquatic organisms, antibiotic resistance in microbial communities, and potential risks to human health through contaminated drinking water sources [Langenhoff et al., 2013]. Conventional wastewater treatment has been able to remove nearly 95% of ibuprofen, but it has severe side effects, including the creation of hydroxyl-IBF and carboxy-IBF, which are sometimes much more harmful than IBF.

Photocatalysis has emerged as a promising advanced oxidation process (AOP) characterized by high efficiency, low energy consumption, and minimal pollution. This technology leverages the strong oxidative properties of reactive oxygen species (ROS), including superoxide radicals (O_2^-), hydroxyl radicals (OH^\bullet), and holes, to unconditionally oxidize and mineralize a wide range of pollutants. As a method that converts solar energy into chemical energy, advancing photocatalysts that respond to visible light is essential for enhancing the utilization of solar energy in water treatment applications [Mao et al., 2021, Jagannathan et al., 2010]. Transition metal dichalcogenides (TMDC) have garnered significant

interest due to their unique structural, electrical, optical, and mechanical properties [Mearaj et al., 2024]. Their electrical, catalytic, and photo-corrosion resistance characteristics make these materials suitable for a variety of applications, including energy storage and conversion, catalysis, and lubrication [Sheikh et al., 2024; Chackrabarti et al., 2024; Upadhyay et al., 2024]. Among various TMDC, molybdenum disulfide (MoS_2) is a layered material having possible uses in the domains of catalysis, storage materials, nanoelectronics. In two-dimensional form, it shows direct band gap of 1.8 eV with an as indirect bandgap of 1.2 eV. MoS_2 has a layered structure with hexagonal arrangement of Mo and S atoms with consequent S–Mo–S interaction [Buscema et al., 2013]. This allows the MoS_2 with almost $500 \text{ cm}^2 \text{ V}^{-1} \text{ s}^{-1}$. Seebeck coefficient of -4.10^2 and $-1.10^5 \mu\text{V K}^{-1}$. Apart from this, the stacked layers of bulk MoS_2 let foreign atoms to be easily intercalated between them. Under coordinated sulfur edges it has been seen that the catalytic activity of MoS_2 originates. But MoS_2 's basic planes are catalytically inactive [Lau et al., 2018]. Van-der-Waals interaction causes the monolayers to interact and helps them to cope with one another during MoS_2 preparation; bilayer creation may therefore help to lower the catalytic reactivity. Therefore, the preparation technique of MoS_2 is crucial to make it an effective photocatalytic material. Different techniques including solid-state reaction, pulsed laser deposition, liquid exfoliation, and ball milling produce MoS_2 nanostructures. Few studies, meantime, on the literature for the efficient degradation of organic pollutants utilizing MoS_2 as a photocatalytic material are accessible. Under visible light irradiation generated by an optimal sol–gel method, Peitao et al. synthesized flower-like N-doped MoS_2 for the degradation of RhB [Zhang et al., 2019]. Studies of density functional theory (DFT) are quite useful for clarifying material properties without experimental preparation. Using DFT, the electronic structure and photocatalytic activity of MoS_2 have been investigated in great detail; these values are reported in the literature. This study focuses on synthesizing MoS_2 nanoparticles via a straightforward slow evaporation technique and evaluating their photocatalytic performance against two industry-standard organic dyes: Methylene Blue (MB) and Malachite Green (MG). Furthermore, basic mechanism of the photocatalytic activity of MoS_2 by density functional theory (DFT) has been investigated using simulation research [Zhang et al., 2019].

The growing concern over organic pollutants in environmental waters has catalyzed the exploration of innovative remediation technologies. Among these, photocatalysis has emerged as a promising solution due to its unique advantages [Taghilou et al., 2024]. Photocatalysis harnesses light energy to activate semiconductor materials, leading to the generation of highly reactive species capable of degrading a wide range of organic pollutants into harmless byproducts. This process is not only effective but also offers several advantages over traditional

remediation methods [Bahadoran et al., 2024; Bashardoust et al., 2024]. One of the primary benefits of photocatalysis is its ability to operate under mild conditions, often at room temperature and atmospheric pressure, reducing energy consumption compared to thermal treatments. Furthermore, photocatalytic degradation leads to complete mineralization of organic compounds, resulting in non-toxic end products like carbon dioxide and water. Unlike adsorption or chemical oxidation techniques, which may require extensive operational costs and generate secondary waste, photocatalysis presents a sustainable and environmentally friendly approach to water treatment. In contrast, other remediation methods, such as biological treatment and activated carbon adsorption, face significant limitations [Kakavandi et al., 2024]. Biological treatments are often hindered by the toxicity of certain pollutants to microbial communities, leading to reduced efficiency and longer treatment times. Additionally, these methods may not effectively address certain recalcitrant compounds. Similarly, activated carbon, while effective for some contaminants, comes with high operational costs and requires regeneration or disposal of spent carbon, which poses logistical challenges and potential environmental risks.

Halide perovskite materials have lately attracted a lot of interest, especially for their remarkable efficiency in photovoltaics and optoelectronics [Singh et al., 2024]. Large absorption coefficients are attributed to their favorable band gap, point defects, grain boundaries, and extended electron-hole diffusion lengths, which lower the recombination of electron-hole pairs. These materials show several important characteristics that make them interesting candidates for photocatalytic applications. Furthermore, the synthesis of these materials is somewhat affordable and easily repeatable. Lead halide perovskites have shown historically exceptional efficiency as solar energy collectors [Zai et al., 2017]. Lead-based perovskites are therefore unfit for wastewater treatment uses since these materials are unstable, particularly under high humidity conditions, and the possible leakage of Pb^{2+} ions poses toxicity hazards. By comparison, bismuth-based perovskites show encouraging benefits like better moisture and water stability. Different techniques have been used thus far to create effective modified photocatalysts, with special attention to increasing visible-light activity [Singh et al., 2024]. Important work has been focused on building heterojunctions and synthesizing bismuth-based nanomaterials. Notwithstanding these developments, their whole potential has yet not be fully investigated. While bismuth-based photocatalysts now show significant improvement in their photocatalytic activity, more study and development are required to attain ideal performance. In this study, we introduce a novel composite photocatalyst, $\text{MoS}_2@\text{Cs}_3\text{Bi}_2\text{Br}_9$, and investigate its potential applications for photocatalysis

under visible light irradiation. This research marks the first instance of synthesizing and evaluating the photocatalytic performance of the $\text{MoS}_2@\text{Cs}_3\text{Bi}_2\text{Br}_9$ hybrid structure using microwave-assisted synthesis, which leverages electrostatic interactions for the spontaneous assembly of its components. The significant findings from our work demonstrate that the 5% $\text{MoS}_2@\text{Cs}_3\text{Bi}_2\text{Br}_9$ composite exhibits a remarkable degradation efficiency of 96.77% for ibuprofen, a prominent pharmaceutical contaminant, under optimal conditions of pH 6.0 and 0.1% H_2O_2 after three hours of visible light irradiation. This enhanced photocatalytic performance is attributed to the effective generation of hydroxyl and superoxide radicals, affirming the potential of our novel photocatalyst in environmental remediation efforts.

7.2. Results and Discussion

7.2.1. Characterization studies

Fourier Transform Infrared spectroscopy (FTIR)

One characterization approach used to look into the functional groups and bonding interaction of synthetic materials is FTIR. The far-infrared spectrum of the synthetic MoS_2 and $\text{Cs}_3\text{Bi}_2\text{Br}_9$ is displayed in **Figure 7.1**. The peaks at 593 cm^{-1} , 739 cm^{-1} , 1075 cm^{-1} , 2346 cm^{-1} , and 3093 cm^{-1} are attributed to MoS_2 and are likely related to its structural vibrations or specific bonding configurations. This peak at 593 cm^{-1} is associated with the S–S bond, indicating the presence of sulfur-sulfur bonds in the MoS_2 nanoparticles. The peak at 3093 is indicative of the OH group, which could suggest the presence of hydroxyl groups or moisture absorbed on the surface of the nanoparticles [Bhat et al., 2021]. These peaks belong to MoS_2 synthesized by the sol-gel method. The Mo = S functional group is represented by the bands at 896 cm^{-1} and 1416 cm^{-1} , which are the result of compound sulfur forming with the active sites in MoS_2 . The stretching vibration of the O-H group is responsible for the bands located at 1615 cm^{-1} , caused by the stretching of the C–H bond, which is produced by the Microwave process. The additional peaks at 531 , 641 , 1015 , 1405 , 1633 cm^{-1} , and 3358 cm^{-1} are ascribed to $\text{Cs}_3\text{Bi}_2\text{Br}_9$ and are probably connected to certain bonding arrangements or structural vibrations of the compound [Musiienko et al., 2021]. The peaks at 531 and 641 cm^{-1} are illustrated for CsBi in $\text{Cs}_3\text{Bi}_2\text{Br}_9$. The peaks observed at 1015 and 1633 cm^{-1} belong to the N-O and C=N group. The O-H group

is responsible for the peak at 3358 cm^{-1} , which may indicate the presence of hydroxyl groups or moisture [Ding et al., 2017].

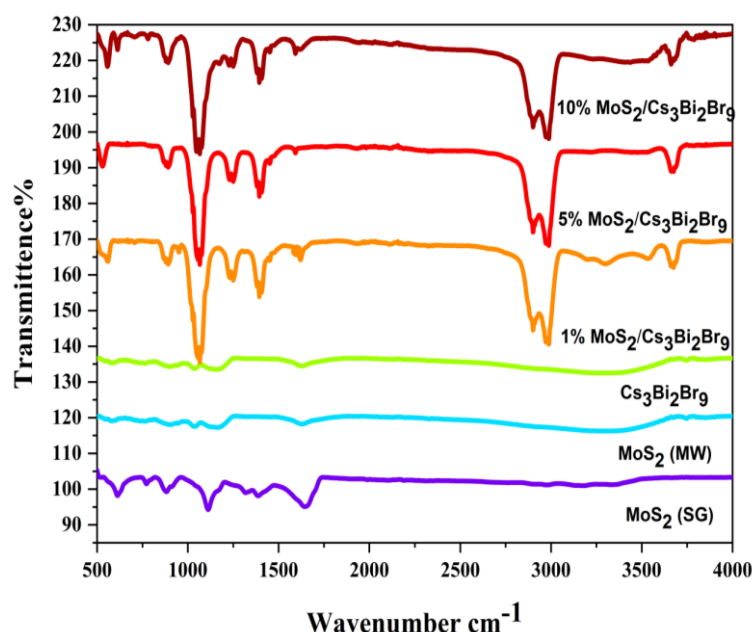


Figure 7.1 FTIR spectra of MoS_2 (SG), MoS_2 (MW), $\text{Cs}_3\text{Bi}_2\text{Br}_9$ and their various composites

XRD Analysis

The X-ray diffraction (XRD) spectrum of MoS_2 synthesized through both Sol-Gel and Microwave methods is illustrated in **Figure 7.2**. Notably, the peaks observed in the XRD pattern generated by the Microwave method exhibit greater intensity compared to those produced by the sol-gel method. This difference in peak intensity can be attributed to the variation in the crystallization efficiency and structural integrity of the MoS_2 formed through these two synthesis routes. **Figure 7.2** shows the XRD graphs of MoS_2 (SG), MoS_2 (MW), $\text{Cs}_3\text{Bi}_2\text{Br}_9$, and their various composites. On the contrary, the diffraction peaks of $\text{Cs}_3\text{Bi}_2\text{Br}_9$ were narrower, consistent with a crystalline particle structure. The primary diffraction peaks, which corresponded to the planes (100), (102), (201), (112), (202), (212), and (220), were centered at 12.1 , 21.45 , 24.16 , 26.04 , 30.75 , 36 , 39.4 , and 43.74° (2θ), (ICSD 112997) respectively. The diffractogram corresponded to the trigonal $P\bar{3}m1$ space group and matched patterns found in published literature [Bresolin et al., 2020]. The presence of composites was confirmed by the XRD diffractograms, which displayed convoluted peaks resulting from the proportional production of wide MoS_2 diffraction peaks and narrower $\text{Cs}_3\text{Bi}_2\text{Br}_9$ peaks. The XRD analysis of the $\text{MoS}_2@\text{Cs}_3\text{Bi}_2\text{Br}_9$ composite reveals distinct peaks corresponding to both

the rhombohedral phase of MoS₂ (JCPDS 06-0097) and the cubic phase of Cs₃Bi₂Br₉. This observation indicates that the composite retains the structural features of both individual components, confirming the formation of a heterogeneous mixture of MoS₂ and Cs₃Bi₂Br₉ phases within the sample. The XRD patterns exhibit characteristic diffraction peaks for both phases, consistent with their respective Joint Committee on Powder Diffraction Standards (JCPDS) references. The XRD analysis reveals distinctive peaks associated with a rhombohedral structure at 2θ values of 14.51°, 32.69°, 36.16°, 39.62°, 44.17°, 49.87° and 58.54° for pure MoS₂. These peaks correspond to the specific hkl planes (002), (100), (102), (103), (006), (105), and (110), respectively, and they are accurately indexed according to the JCPDS card number (06-0097) [Sathiyar et al., 2015]. The presence of these peaks signifies the crystalline nature of MoS₂, which is essential for its effectiveness as a photocatalyst.

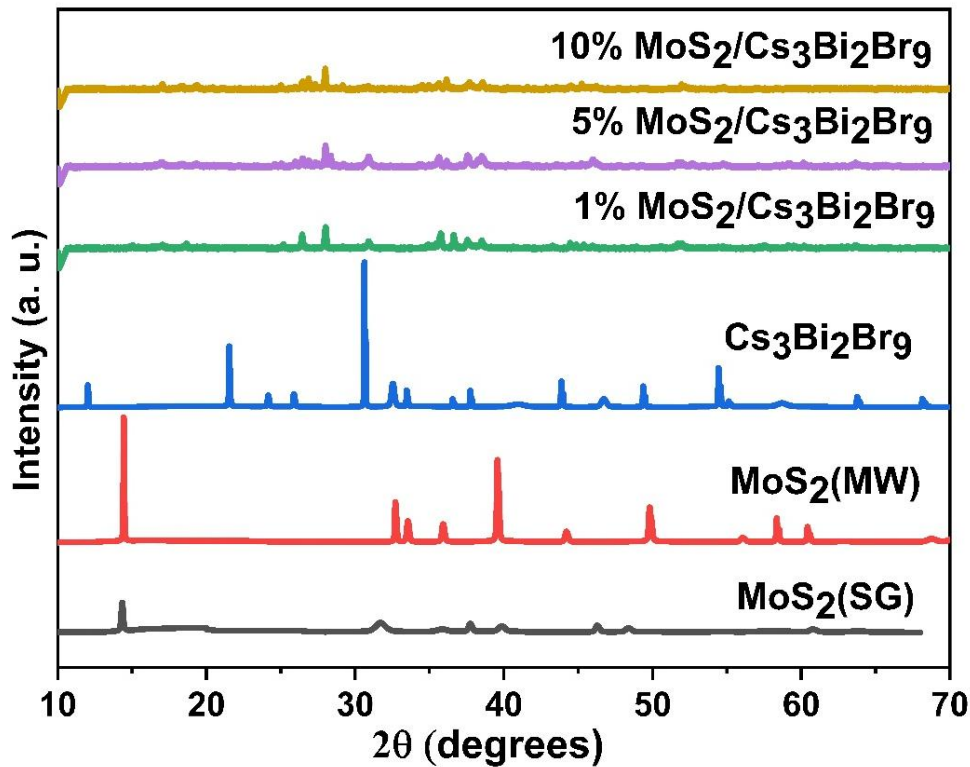


Figure 7.2: XRD graphs of MoS₂ (SG), MoS₂ (MW), Cs₃Bi₂Br₉, and their various composites.

The Scherrer equation is utilized to calculate the crystallite size, where “D” represents the crystallite size, “θ” is the Bragg diffraction angle, “λ” is the wavelength of the X-ray, and “β” is the full width at half maximum (FWHM) and is expressed as **Equation 7.1**.

$$D = \frac{0.9\lambda}{\beta \cos\theta} \quad 7.1$$

The resulting crystallite size provides important insights into the crystalline quality and structural properties of the $\text{MoS}_2@\text{Cs}_3\text{Bi}_2\text{Br}_9$ nanocomposite material. The intensity of the XRD peaks is indicative of the degree of crystallinity and the quality of the material produced. Strongly intense peaks usually suggest larger and more well-defined crystallites, which can enhance the electronic properties and photocatalytic activity of the material. A higher degree of crystallinity may facilitate better charge carrier mobility and separation during photocatalytic reactions, leading to improved efficiency in applications such as the degradation of pollutants. In contrast, weaker peaks can indicate smaller crystallite sizes or the presence of amorphous phases, which may hinder the effectiveness of the photocatalyst.^{38,39} In photocatalytic applications, a balance is often sought between crystallinity and surface area; while larger crystalline structures may harbor better electronic properties, finer structures could provide enhanced surface reactivity due to their higher surface area-to-volume ratio. The improved peak intensity associated with the Microwave method suggests a more advantageous crystalline structure, which potentially translates into superior photocatalytic performance when applied under visible light irradiation.

Specifically, the average crystallite sizes calculated from the most intense peak (002) using the Scherrer equation are approximately 55 nm for MoS_2 , 170 nm for $\text{Cs}_3\text{Bi}_2\text{Br}_9$, and ~50-70 nm for the different $\text{MoS}_2@\text{Cs}_3\text{Bi}_2\text{Br}_9$ nanocomposites as mentioned in **Table 7.1**. These results suggest that while the crystallite sizes of the individual components vary, the dimensions of the crystallites in the composite remain comparable to those of pure MoS_2 . Crystallite size significantly influences the intensity of XRD peaks. Smaller crystallite sizes tend to result in reduced peak intensities due to peak broadening effects. This broadening occurs as a result of increased relative surface area and potential strain effects within the materials. Therefore, the crystallite sizes observed in this study imply that the smaller dimensions of the MoS_2 crystallites (55 nm) contribute to wider and less intense peaks when compared to the larger $\text{Cs}_3\text{Bi}_2\text{Br}_9$ crystallites (170 nm). Moreover, the relatively lower average crystallite size of the composite (~50-70 nm) suggests that the interactions within the composite may lead to further reductions in peak intensity compared to the individual components. This is likely due to the presence of increased surface areas and potential lattice distortions that could arise from the interactions between the two materials [Lee et al., 2024]. The phase composition of the $\text{MoS}_2@\text{Cs}_3\text{Bi}_2\text{Br}_9$ composite also plays a critical role in determining peak intensities. When one phase is present in a higher proportion, its corresponding diffraction peaks typically exhibit greater intensity.

Table 7.1: FWHM, crystallite Size, and Lattice strain for MoS₂, Cs₃Bi₂Br₉, and (1, 5 and 10%) MoS₂@Cs₃Bi₂Br₉ nanocomposite

S. No	FWHM	Crystallite Size	Strain
MoS ₂ (SG)	0.15	55 nm	0.0052
MoS ₂ (MV)	0.07	104 nm	0.0028
Cs ₃ Bi ₂ Br ₉	0.05	172 nm	0.0008
1% MoS ₂ /Cs ₃ Bi ₂ Br ₉	0.16	53 nm	0.0028
5% MoS ₂ /Cs ₃ Bi ₂ Br ₉	0.12	71 nm	0.0021
10% MoS ₂ /Cs ₃ Bi ₂ Br ₉	0.13	65 nm	0.0023

Consequently, the observed peak intensities in the MoS₂@Cs₃Bi₂Br₉ sample reflect the relative concentrations of MoS₂ and Cs₃Bi₂Br₉ within the hybrid nanostructure. Furthermore, differences in atomic number and electron density between MoS₂ and Cs₃Bi₂Br₉ lead to variations in X-ray scattering and absorption, which can also impact the observed peak intensities in the XRD patterns. This highlights the importance of considering the unique structural and electronic characteristics of each component when analyzing composite materials. The XRD analysis of the MoS₂@Cs₃Bi₂Br₉ nanocomposite not only illustrates the retention of the distinct phases of both materials but also emphasizes the intricate relationships between crystallite size, phase composition, and peak intensity.

Scanning Electron Microscopy and Energy Dispersive X-ray spectroscopy (SEM/EDX) Analysis

The SEM analysis was conducted to examine the morphologies and distribution of MoS₂@Cs₃Bi₂Br₉ nanocomposites with varying weight percentages of Cs₃Bi₂Br₉, as presented in **Figure 7.3 (a, c, e)**. In 5% MoS₂@Cs₃Bi₂Br₉ composites, the SEM micrographs revealed that the crystal morphology of MoS₂@Cs₃Bi₂Br₉ remained akin to that of the pristine form, characterized by well-defined shapes as shown in **Figure 7.3 (e)**. Notably, the Cs₃Bi₂Br₉ crystals were observed to be uniformly dispersed across the surface of MoS₂, indicating minimal aggregation. However, with increased concentration of MoS₂@Cs₃Bi₂Br₉ nanocomposite, the micrographs exhibited the formation of larger clusters [Baghdadi et al., 2023]. This clustering was accompanied by a decreased interfacial interaction between the

(a) SEM image of Bi₂S₃ at 10.00 kV, 10.00 kV, 10.00 kV, 10.00 kV, 10.00 kV, 10.00 kV, 10.00 kV, 10.00 kV, 10.00 kV, 10.00 kV.

(b) EDS spectrum of Bi₂S₃ showing peaks for S Kα1 and Mo Lα1. MO: 59.9%, S: 40.1%.

(c) SEM image of Bi₂S₃ at 10.00 kV, 10.00 kV, 10.00 kV, 10.00 kV, 10.00 kV, 10.00 kV, 10.00 kV, 10.00 kV, 10.00 kV, 10.00 kV.

(d) EDS spectrum of Bi₂S₃ showing peaks for Cl Kα1, Bi Mo, Br Kβ, Cs La1, Cs Lβ2, Br Kα1, Bi Lβ2, and Br Kβ1. CS: 40.1%, BI: 40.1%, BR: 3.6%, CL: 17.8%.

(e) SEM image of Bi₂S₃ at 10.00 kV, 10.00 kV, 10.00 kV, 10.00 kV, 10.00 kV, 10.00 kV, 10.00 kV, 10.00 kV, 10.00 kV, 10.00 kV.

(f) EDS spectrum of Bi₂S₃ showing peaks for Cs Mo, Br La1, Bi Mo, Br Kβ, S Kα1, Mo Lα1, Cs La1, Cs Lβ2, Br Kα1, Bi Lβ2, and Br Kβ1. CS: 39.3%, BI: 47.4%, BR: 3.1%, MO: 9.5%, S: 0.7%.

photocatalyst. Overall, the SEM analysis elucidates the structural characteristics and the influence of $\text{Cs}_3\text{Bi}_2\text{Br}_9$ weight percentage on the photocatalytic activity of the $\text{MoS}_2@\text{Cs}_3\text{Bi}_2\text{Br}_9$ composites, highlighting the importance of maintaining a balance in the loading to optimize photocatalytic performance.

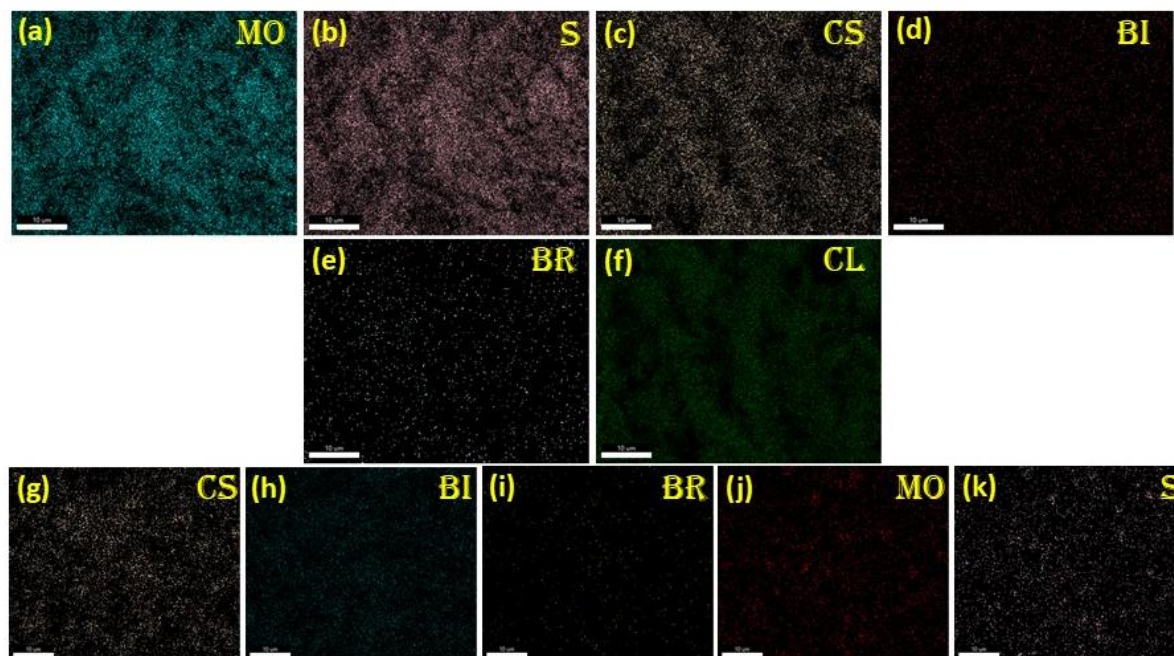


Figure 7.4 Elemental mapping of MoS_2 , $\text{Cs}_3\text{Bi}_2\text{Br}_9$, and 5% $\text{MoS}_2@\text{Cs}_3\text{Bi}_2\text{Br}_9$ nanocomposites.

UV Absorption Analysis

The optical properties of MoS_2 , $\text{Cs}_3\text{Bi}_2\text{Br}_9$, and their composite $\text{MoS}_2@\text{Cs}_3\text{Bi}_2\text{Br}_9$ nanocomposite were analyzed using UV-Visible spectroscopy, focusing on the absorption characteristics over the solar spectrum. The corresponding optical absorption spectra and their associated band gap values are presented in **Figure 7.5**. The UV-Visible analysis reveals that all three samples exhibit distinct absorption characteristics [Bhat et al., 2021]. $\text{Cs}_3\text{Bi}_2\text{Br}_9$

nanocomposite shows a pronounced absorption band in the UV region, specifically within the wavelength range of approximately 380-390 nm.

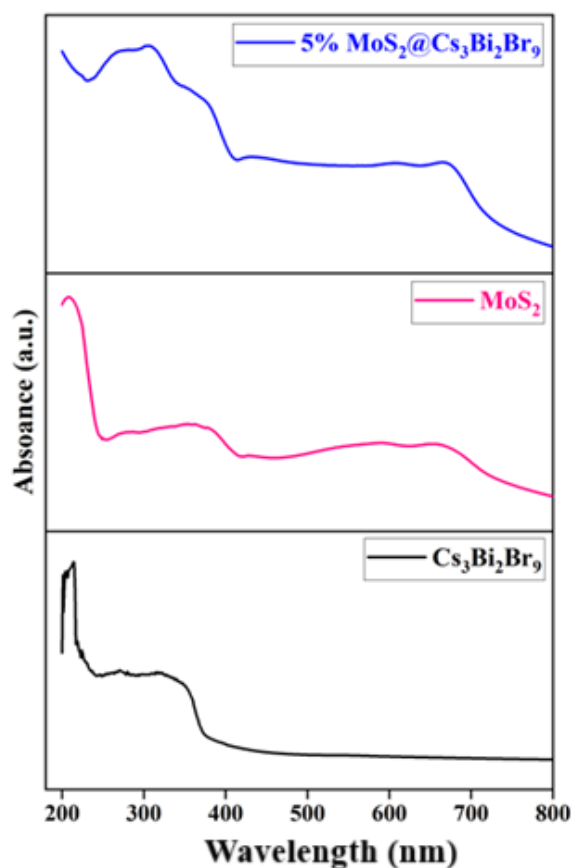


Figure 7.5 UV visible spectra of $\text{Cs}_3\text{Bi}_2\text{Br}_9$, MoS_2 , and 5% $\text{MoS}_2@\text{Cs}_3\text{Bi}_2\text{Br}_9$ nanocomposite.

This absorption is attributed to the inherent electronic transitions associated with its perovskite structure, which facilitates the excitation of electrons from the valence band to the conduction band. In contrast, MoS_2 displays absorption in the visible region, particularly between 500-600 nm. The absorption in this range can be ascribed to the direct bandgap transitions in the MoS_2 lattice, which, however, is also influenced by excitonic effects that arise from its two-dimensional (2D) structure. This characteristic absorption behavior is indicative ability of MoS_2 to utilize visible light, a desirable property for photocatalytic applications. The $\text{MoS}_2@\text{Cs}_3\text{Bi}_2\text{Br}_9$ nanocomposite demonstrates a combination of both absorption peaks. The presence of distinct bands in both the UV and visible regions confirms the successful formation of the composite material. This dual absorption behavior signifies that the composite can harness a broader spectrum of solar energy, enhancing its potential photocatalytic performance. The overlapping absorption bands suggest improved electronic interactions between MoS_2 and $\text{Cs}_3\text{Bi}_2\text{Br}_9$, facilitating efficient charge separation and transfer during photocatalytic processes.

The UV-Visible spectroscopy analysis delineates the optical properties of the individual components and their composite, indicating that the synergistic interactions between MoS₂ and Cs₃Bi₂Br₉ may lead to enhanced photocatalytic capabilities due to their complementary light absorption characteristics.

The solid-state UV-Visible (UV-Vis) analysis was conducted to assess the optical properties of the synthesized samples, specifically focusing on the determination of band gap energies associated with the MoS₂ and MoS₂@Cs₃Bi₂Br₉ nanocomposites. The UV-Vis spectra for each generated sample were measured, and the Tauc plots were derived from the reflectance data obtained for all compositions. To calculate the reflectance (R) of an infinitely thick specimen, the Kubelka-Munk **equation 7.2** was employed, where K and S represent the Kubelka-Munk absorption and scattering coefficients, respectively [Ding et al., 2017]:

$$F(R_{\infty}) = \frac{K}{S} = \frac{(1 - R_{\infty})^2}{2R_{\infty}} \quad 7.2$$

By plotting $[F(R_{\infty}) \text{ hv}]^{1/2}$ against the energy corresponding to the wavelength, the band gap energy (E_g) for MoS₂@Cs₃Bi₂Br₉ nanocomposite could be determined. A line was extended along the steep/linear portion of the plot until it intersected the x-axis; this point of intersection provides the value of the band gap energy (E_g) for the specific nanoparticles. As depicted in **Figure 7.6**, the band gap values exhibited a downward trend, decreasing from 2.83 eV to 2.36 eV with an increase in the concentration of the dopant, Cs₃Bi₂Br₉. This reduction in band gap energy can be attributed to several factors, including enhanced charge carrier dynamics and modifications in the electronic structure resulting from the incorporation of Cs₃Bi₂Br₉ into the MoS₂ matrix. The presence of the perovskite Cs₃Bi₂Br₉ can introduce additional energy states within the band gap, lowering the overall energy required for electronic transitions. The band gap energy is critically related to photocatalytic activity, particularly for the removal of pollutants such as drugs. A lower band gap energy enables the material to absorb a broader spectrum of visible light, thus enhancing its photocatalytic efficiency under solar irradiation. This improved light absorption leads to increased electron-hole pair generation, which is vital for driving the photocatalytic reactions that facilitate the degradation of organic contaminants. Consequently, the tunable band gap of the MoS₂@Cs₃Bi₂Br₉ nanocomposites makes them promising candidates for effective photocatalysts in the removal of pharmaceutical contaminants from wastewater, showcasing their potential for sustainable environmental applications.

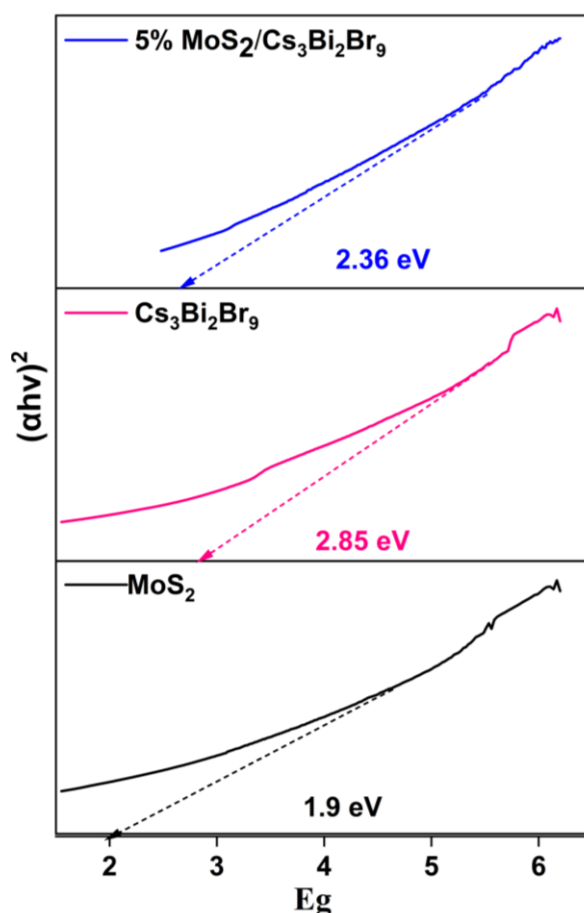


Figure 7.6 Optical band gap of MoS₂, Cs₃Bi₂Br₉, and 5%MoS₂@Cs₃Bi₂Br₉ nanocomposite.

7.2.2. Photocatalytic Degradation of Ibuprofen

Impact of pH

Figure 7.7 illustrates the impact of pH on the photodegradation efficiency of Ibuprofen under visible light exposure across various photocatalysts. The data reveal that the degradation efficiency of Ibuprofen increases within the acidic pH range of 05 to 06 across all photocatalysts. However, a decline in efficiency is observed when the pH is further increased from 7.0 to 11.0. The optimal pH for Ibuprofen removal was identified as 6.0, where slightly acidic conditions yielded maximum degradation efficiencies of 53%, 68%, 65%, 69%, 83%, and 60% for the MoS₂ (S.G.), MoS₂ (M.W.), Cs₃Bi₂Br₉, 1% MoS₂@Cs₃Bi₂Br₉, 5% MoS₂@Cs₃Bi₂Br₉, and 10% MoS₂@Cs₃Bi₂Br₉ nanocomposites, respectively, under visible light.

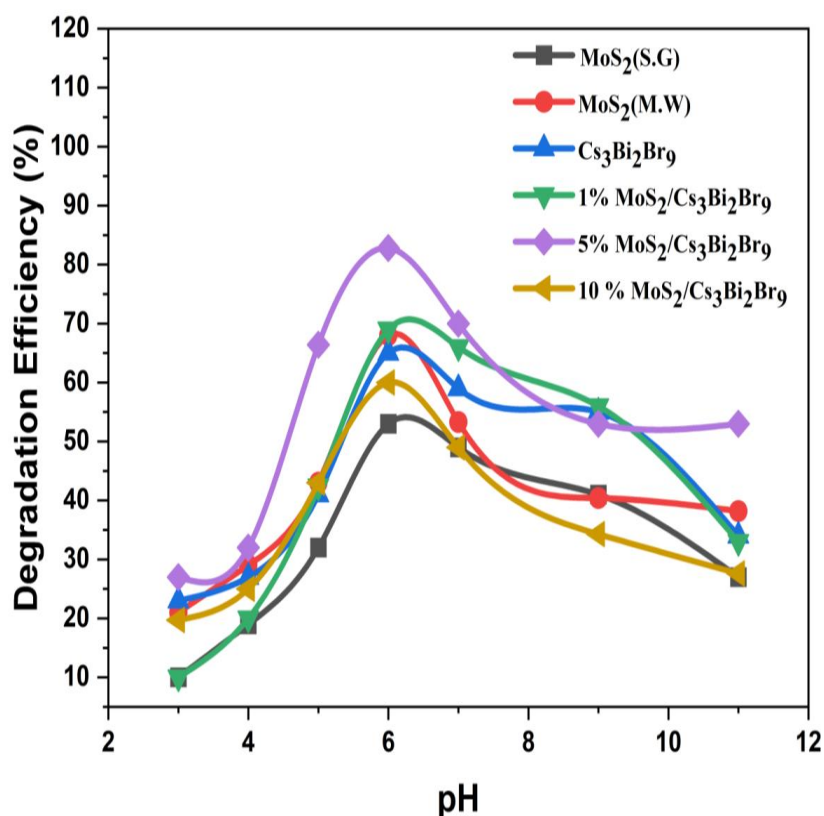


Figure 7.7 Effect of pH on Ibuprofen. Conc. of IBF; 100mg/L, Reaction volume; 30mL, Catalyst dose; 10 mg, irradiation time; 3h, pH; 6, Temperature; 30° C.

The point of zero charge (pH_{zpc}) of the 5% $\text{MoS}_2@\text{Cs}_3\text{Bi}_2\text{Br}_9$ nanocomposite was experimentally determined using the pH drift method. The pH_{zpc} was found to be pH 3.4, which aligns with the optimal pH (6.0) for maximum degradation efficiency [Lv et al., 2024; Jing et al., 2024]. This value confirms that the catalyst surface is positively charged at $\text{pH} < 3.4$, facilitating electrostatic attraction with the anionic Ibuprofen species. At $\text{pH} > 3.4$, the surface becomes negatively charged, leading to repulsion and reduced efficiency. Among the photocatalysts studied, the 5% $\text{MoS}_2@\text{Cs}_3\text{Bi}_2\text{Br}_9$ nanocomposite demonstrated the highest Ibuprofen removal efficiency. This can be attributed to the likely involvement of hydroxyl ions (OH^-) and water molecules (H_2O) in localized hole-induced electron transfer reactions, which generate an abundance of hydroxyl radicals. These radicals play a crucial role in accelerating the breakdown of Ibuprofen under visible light irradiation.

Kinetic studies

Figure 7.8 illustrates the effect of contact (irradiation) time on the photocatalytic degradation of Ibuprofen. The **Figure** shows a direct correlation between increased irradiation time and the

enhancement of degradation efficiency. Specifically, extending the irradiation period from 15 to 180 minutes resulted in a significant increase in the degradation percentage from 14.52% to 93.77% for the as-synthesized nanocomposite. This increase can be attributed to the prolonged exposure of Ibuprofen molecules to the photocatalyst's surface, allowing more time for interaction and the subsequent generation of hydroxyl radicals. These radicals play a crucial role in accelerating the photocatalytic process, thereby enhancing the overall degradation efficiency [Wang et al., 2023]. The kinetics of Ibuprofen removal are demonstrated in **Figure 7.9** with the pseudo-first order reaction shown in **Equation 7.3**.

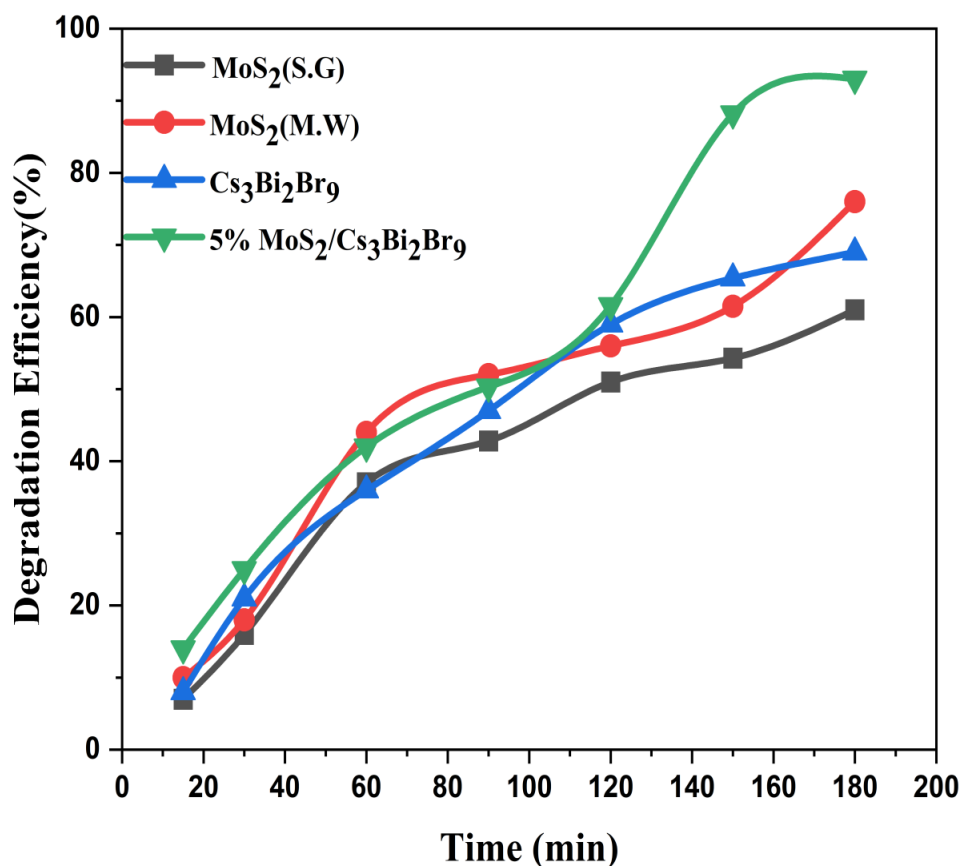


Figure 7.8 Effect of time. Conc. of IBF; 100mg/L, Reaction volume; 30mL, Catalyst dose; 10mg, irradiation time; 3h, pH; 6, Temperature; 30° C.

$$\ln C_0/C_t = K \times t \quad 7.3$$

Where, at a time “t”, C_0 and C_t are the initial and final concentrations, respectively (mg/L). The reaction rate constant k (min^{-1}) was calculated by the linear graph of $\ln (C_0/C_t)$ vs. “t”. The

reaction rate constant increased up to 0.1 mg/L and then decreased with increasing Ibuprofen concentration (**Table 7.2**).

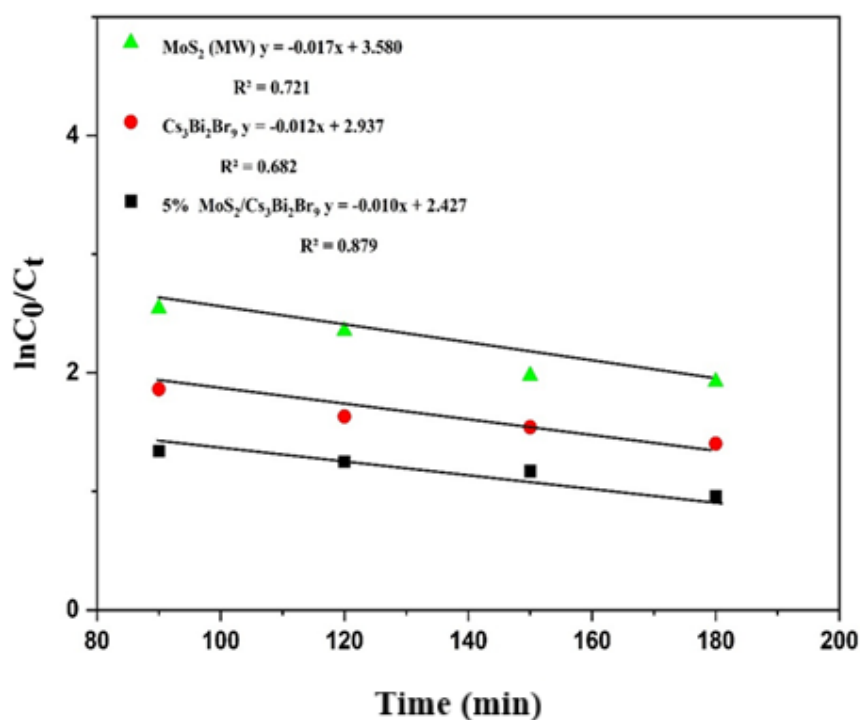


Figure 7.9 Rate of IBF photocatalytic degradation reaction. Conc. of IBF; 100mg/L, Reaction volume; 30mL, Catalyst dose; 10mg, irradiation time; 3h, pH; 6, Temperature; 30° C.

Table 7.2: Ibuprofen Photodegradation Estimated First-Order Rate Constant

Material	Ibuprofen (mg/L)	k (min ⁻¹)	R ²
MoS ₂ (MW)	20	0.27	0.721
Cs ₃ Bi ₂ Br ₉	20	0.34	0.682
5% MoS ₂ /Cs ₃ Bi ₂ Br ₉	20	0.41	0.879

Effect of H₂O₂ concentration

The effect of H₂O₂ on the photocatalytic degradation of Ibuprofen using 5% MoS₂@Cs₃Bi₂Br₉ is demonstrated in **Figure 7.10**. The presence of H₂O₂ is known to enhance the generation of hydroxyl radicals (•OH), which are crucial for improving photocatalytic degradation and

potentially leading to the formation of colorful intermediate products. When the H_2O_2 concentration was increased from 0.001% to 0.04%, a notable impact on the degradation efficiency was observed. In the absence of H_2O_2 , the photodegradation efficiency was recorded at 93.77%. However, with the introduction of H_2O_2 at a concentration of 0.01% to 0.1%, the degradation efficiency of Ibuprofen improved from 93.77% to 96.76%. Interestingly, a further increase in H_2O_2 concentration to 1% led to a decrease in the degradation efficiency to 46.1%. This reduction in efficiency is likely due to the dual role of H_2O_2 , where at higher concentrations, it may act as an inhibitor by reacting with hydroxyl radicals and stabilizing the coupled electron-hole pairs (e^-/h^+) through the trapping of photoinduced electrons (e^-). The interaction between H_2O_2 and e^- or O_2 can still generate hydroxyl radicals, yet an excess of H_2O_2 may impede the overall photocatalytic process. Thus, while the addition of H_2O_2 is anticipated to enhance the elimination of Ibuprofen, its concentration must be carefully optimized to avoid inhibitory effects [Oad et al., 2023].

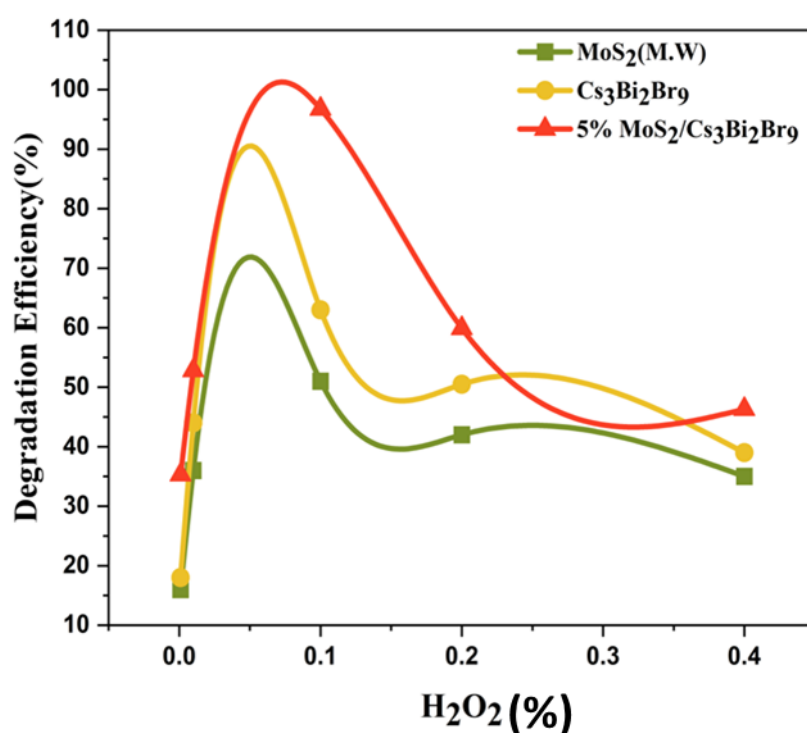


Figure 7.10 Effect of H_2O_2 (%). Conc. of IBF; 100mg/L, Reaction volume; 30mL, Catalyst dose; 10mg, irradiation time; 3h, pH; 6, Temperature; 30° C.

Effect of Catalyst Dosage

The impact of varying photocatalyst dosage on the photocatalytic efficiency of the nanocomposites is depicted in **Figure 7.11**. The experiment involved varying the amounts of

the MoS₂ (S.G.), MoS₂ (M.W.), Cs₃Bi₂Br₉, 1% MoS₂@Cs₃Bi₂Br₉, 5% MoS₂@Cs₃Bi₂Br₉, and 10% MoS₂@Cs₃Bi₂Br₉ nanocomposites from 0.001 to 0.2 mg/L in a 100 mL Ibuprofen solution, supplemented with 0.1% H₂O₂, under 100 W light intensity at pH 6.0 for up to 3 hours to determine the optimal photocatalyst dosage. As depicted in **Figure 7.11**, the photocatalytic degradation efficiency of Ibuprofen increased significantly from 27.44% to 83.69% as the photocatalyst dose was increased from 0.001 to 0.05 mg/L. However, further increases in the photocatalyst dose beyond 0.05 mg/L did not enhance the degradation efficiency. This outcome suggests that adding an excessive amount of photocatalyst leads to diminished light penetration due to increased turbidity, resulting from the suspension of a larger quantity of photocatalyst particles in the solution. Consequently, the optimal photocatalyst dosage was determined to be 0.05 mg/L, beyond which additional photocatalyst does not contribute to improved efficiency [Cai et al., 2022].

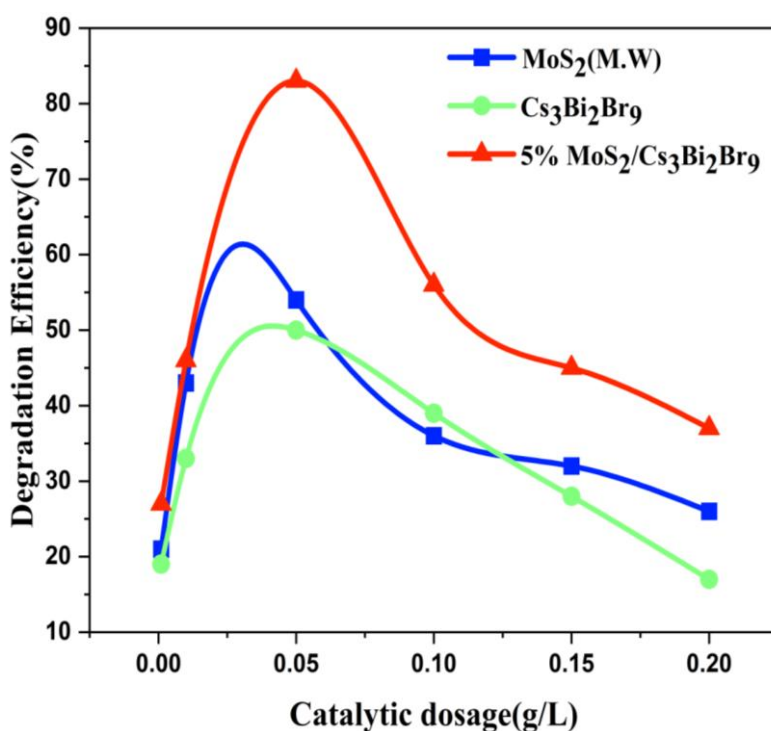


Figure 7.11 Effect of catalytic dosage. Conc. of IBF; 100 mg/L, Reaction volume; 30mL, Catalyst dose; 10mg, irradiation time; 3h, pH; 6, Temperature; 30° C.

7.2.3. Mechanism for photocatalytic degradation of Ibuprofen

The photocatalytic reaction mechanism (**Figure 7.12**) begins with the excitation of the MoS₂@Cs₃Bi₂Br₉ heterojunction under light irradiation ($h\nu \geq \text{bandgap energy}$). This promotes electrons (e^-) from the valence band (VB) to the conduction band (CB), leaving

photogenerated holes (h^+) in the VB (**Equation 7.4**) The h^+ in the VB oxidizes adsorbed water molecules to generate hydroxyl radicals ($\cdot\text{OH}$), while the e^- in the CB reduces dissolved oxygen (O_2) to superoxide anion radicals ($\cdot\text{O}_2^-$) (**Equations. 7.5 to 7.7**). These reactive oxygen species (ROS) drive the degradation of ibuprofen (IBP) into smaller intermediates or mineralized products (**Equation 7.8**). The $\text{MoS}_2@\text{Cs}_3\text{Bi}_2\text{Br}_9$ heterojunction enhances charge separation due to Fermi-level alignment at the interface (thermal equilibrium), where electrons transfer from $\text{Cs}_3\text{Bi}_2\text{Br}_9$ to MoS_2 , suppressing recombination. This synergistic effect increases the availability of e^- and h^+ for redox reactions, improving photocatalytic efficiency [Fauzi et al., 2018].

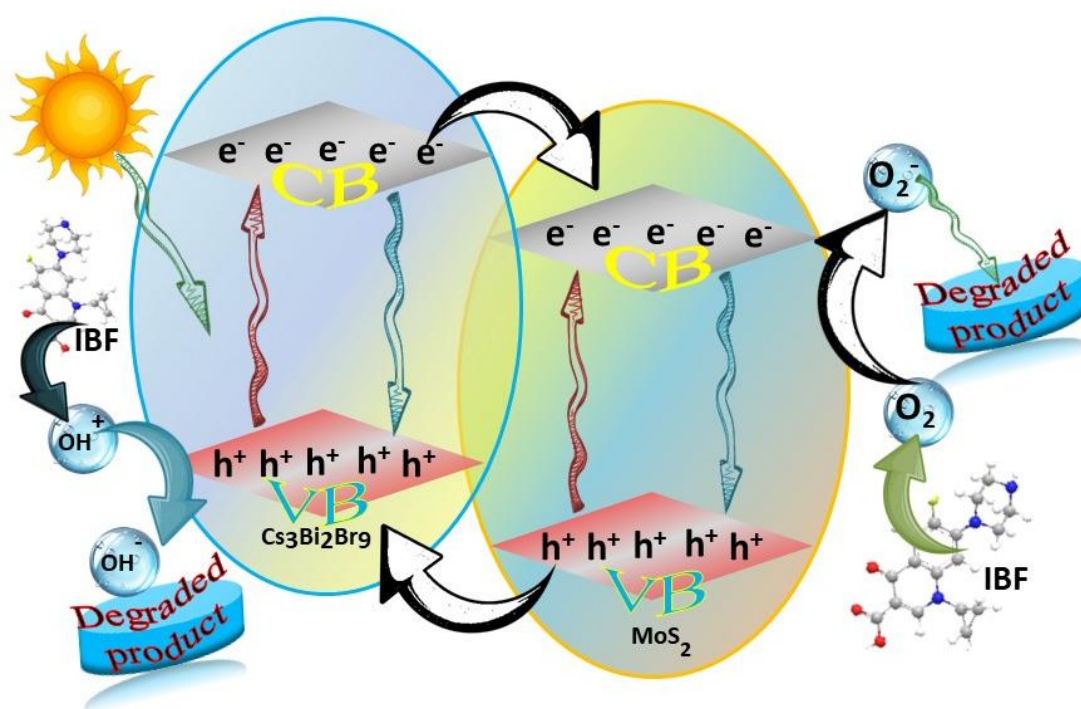
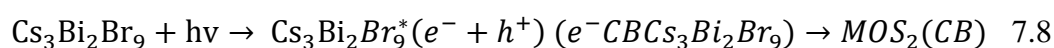
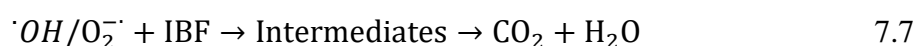
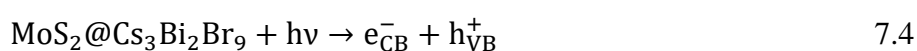


Figure 7.12 A proposed mechanism for IBF degradation.

CHAPTER 8

SUMMARY OF WORK AND FUTURE SCOPE

According to the latest studies, endocrine-disrupting chemicals have been found in industrial, sewage, municipal, and agricultural wastes. It has been demonstrated that EDCs alter the endocrine system, which could have detrimental consequences on both people and animals. Therefore, it is crucial to purify wastewater that contains these endocrine-disrupting substances. It is now necessary to use greener technologies and eco-friendly procedures due to the strict environmental restrictions. Since conventional remediation techniques only transfer contaminants from one phase to another, they are typically unsuccessful in eliminating EDCs. Furthermore, intermediates that are generated throughout the process have a higher level of toxicity than the original substance. So, a non-selective treatment approach that promotes quick and thorough mineralization would be optimal for removing EDCs.

Advanced oxidation procedures (AOP) can be used to remediate wastewater containing pharmaceuticals as well as other organic contaminants. Over the past twenty years, the removal of organic contaminants from wastewater has been made possible by the attractive and promising technology of photocatalytic degradation, which uses semiconductors as the photocatalyst. It has been determined that the most efficient and feasible photocatalysts are CdS and MoS₂. Their excellent physical and chemical characteristics allow them to be used in a multitude of applications. However, the rapid recombination of electron-hole pairs and their broad bandgap, which corresponds to UV light, have hindered the use of CdS and MoS₂. Consequently, one of the current hotspots in photocatalyst research is the investigation of altering CdS and MoS₂ to decrease electron-hole recombination and sensitization to visible light. From this perspective, studies on the doping of semiconductor material perovskite are currently being addressed. The current research focuses on the synthesis, characterization, and photocatalytic activity of CuS, CdS, MoS₂, Cs₃Bi₂Br₉, and doped CdS/Cs₃Bi₂Br₉, CdS/MoS₂, and MoS₂/Cs₃Bi₂Br₉ photocatalysts by Solgel and Microwave process. The degrading efficiency of Cs₃Bi₂Br₉-doped CdS and MoS₂ was higher than that of CdS and MoS₂ alone. This is because electron-hole recombination has been suppressed.

As compared to pure CdS, MoS₂, and Cs₃Bi₂Br₉, the as-obtained nanocomposites exhibit better photocatalytic performance of ciprofloxacin, paracetamol, and ibuprofen. According to their preparation, the CdS/Cs₃Bi₂Br₉, CdS/MoS₂, and MoS₂/Cs₃Bi₂Br₉ nanocomposites exhibit greater photocatalytic performance than CdS, MoS₂, and Cs₃Bi₂Br₉, respectively.

- ❖ CuS nanoparticles had an X-ray diffraction pattern that essentially matched with hexagonal phase of the metal. Strong copper sulphide diffraction peaks for CuS

nanoparticles synthesized by wet chemical co-precipitation method (CuS WCP) can be seen at 27.51° , 31.46° , 32.26° , 39.54° , 49.11° , 53.15° and 57.12° respectively, which correspond to the diffraction planes of (101), (102), (103), (106), (110), (108) and (203) (JCPDS # 78-0876) and demonstrate a high degree of crystallinity.

- ❖ The morphology of the sample was investigated using a scanning electron microscope (SEM). Using its magnifications, the corresponding images show that the CuS nanoparticles are uniformly dispersed and have a spherical shape. In contrast, scanning electron microscopy (SEM) images of CuS produced using the sol-gel method reveal a larger particle size compared to CuS produced using the wet chemical co-precipitation method.
- ❖ The X-ray diffraction analysis of MoS₂, CdS, and their various composites delivers valuable info about the crystalline phases, crystallite size, and purity of the materials. The X-ray diffraction patterns of MoS₂ and CdS match well with the corresponding database (JCPDS card No. **101122** for MoS₂ and No. **23323** for CdS). MoS₂ is identified as existing in the **hexagonal phase**, while CdS is identified as having a **cubic phase**. This information is crucial for understanding the structural characteristics of the individual materials. The XRD patterns of the various composites, with different ratios of MoS₂ and CdS, are reported to match the **hexagonal and cubic phases**, respectively. The presence of sharp peaks in the XRD patterns indicates the crystalline nature of the samples.
- ❖ The crystal structure and crystallinity of CdS and Cs₃Bi₂Br₉ nanocomposites were investigated using the patterns of powder X-ray diffraction (XRD) analysis. The CdS exhibited diffraction peaks with 2θ values of 24.81° , 26.50° , 28.40° , 30.80° , 34.39° , 45.83° , 51.91° , and 53.10° , corresponding to the (100), (002), (101), (220), (102), (110), (311), and (112) planes of the cubic CdS crystal lattice, respectively. The pronounced peaks at 12.78° , 15.68° , and 31.69° correspond to the (100), (101), and (202) planes of its hexagonal structure, respectively. In comparison to pure Cs₃Bi₂Br₉, the hybrid Cs₃Bi₂Br₉/CdS samples demonstrate a significant enhancement in intensity.
- ❖ One characterization approach used to look into the functional groups and bonding interaction of synthetic materials is FTIR. The far-infrared spectrum of the synthetic MoS₂ and Cs₃Bi₂Br₉. The peak at 593 cm^{-1} , 739 cm^{-1} , 1075 cm^{-1} , 2346 cm^{-1} , and 3093 cm^{-1} are attributed to MoS₂ and are likely related to its structural vibrations or specific

bonding configurations.⁴⁷ This peak at 593 cm^{-1} is associated with the S–S bond, indicating the presence of sulfur-sulfur bonds in the MoS_2 nanoparticles.

- ❖ The SEM analysis was conducted to examine the morphologies and distribution of $\text{MoS}_2@\text{Cs}_3\text{Bi}_2\text{Br}_9$ nanocomposites with varying weight percentages of $\text{Cs}_3\text{Bi}_2\text{Br}_9$. In 5% $\text{MoS}_2@\text{Cs}_3\text{Bi}_2\text{Br}_9$ composites, the SEM micrographs revealed that the crystal morphology of $\text{MoS}_2@\text{Cs}_3\text{Bi}_2\text{Br}_9$ remained akin to that of the pristine form, characterized by well-defined shapes

Enhanced photocatalytic degradation efficiency of nanocomposites

- ❖ The degradation rate of copper sulphide nanoparticles in 2-chlorophenol was studied below visible light to determine the effect of pH. The elimination effectiveness of 2-CP rises with increasing pH values up to 6. The photocatalytic elimination of 2-CP was enhanced from 27% to 77% and 30% to 80% using CuS nanoparticles made using the Sol-Gel method (CuS-SG) and the wet chemical coprecipitation method (CuS-WCP), respectively.
- ❖ The spiking process was done by CuS nanoparticles; sample of wastewater was collected from the sewerage treatment plant located at Lovely Professional University, Phagwara, Punjab, 144411. The wastewater samples were analyzed using standard analytical methods as soon as they were collected, which was shortly after receiving them. The pH of wastewater is 7.8, its color is yellowish, its total soluble solids (TSS) is 164 mg/l, its total dissolved solids (TDS) is 231 mg/l, and its conductivity is $1.11\text{ ohm}^{-1}\text{m}^{-1}$.
- ❖ The pH is an essential variable that influences the CdS, MoS_2 , and 1:1CdS/ MoS_2 catalyst contact with the surface of Paracetamol molecules, which in turn influences the degradation of Paracetamol in several ways. The maximal degradation efficiencies for CdS, MoS_2 , and 1:1 CdS/ MoS_2 nanomaterials at pH 4 are 70%, 68%, and 98.7%, respectively, in the visible region.
- ❖ Kinetic investigations of CdS, MoS_2 , and 1:1M MoS_2/CdS were evaluated to investigate the mechanism of Paracetamol degradation. When exposed to visible light for 3 hours, a 10 mg catalyst dosage of CdS, MoS_2 , and 1:1M MoS_2/CdS nanomaterials resulted in 89% 85% and 95% photocatalytic degradation of the Paracetamol solution, respectively.

- ❖ More sustainable intermediates and improved photocatalytic elimination result from H_2O_2 's capacity to produce more OH radicals. The effect of altering hydrogen peroxide from 0.001 to 0.4% on the photocatalytic degradation of Paracetamol by CdS, MoS_2 , and 1:1M MoS_2/CdS . Without H_2O_2 , the rate of photocatalytic degradation is 88%, 85% and 90% by CdS, MoS_2 , and 1:1M MoS_2/CdS . An increase in hydrogen peroxide concentration from 0.001 to 0.1% leads to an enhanced 90–93% elimination of Paracetamol by photocatalytic degradation.
- ❖ The concentration of CdS, MoS_2 and 1:1M MoS_2/CdS was diverse from 0.001 to 0.2 g/L in 210 ml of Paracetamol solution with 0.1% H_2O_2 to determine the optimal quantity of photocatalyst. The Paracetamol photocatalytic elimination rate improved from 56% to 77% when the dosage of photocatalyst was elevated from 0.001 to 0.05 g/L.
- ❖ The pH of the solution significantly influences the photocatalytic performance of pure and doped CdS and $\text{Cs}_3\text{Bi}_2\text{Br}_9$ catalysts by altering the surface interaction between Ciprofloxacin molecules and the nanomaterials. The catalysts utilized in the studies included CdS (Solgel), CdS (Microwave), $\text{Cs}_3\text{Bi}_2\text{Br}_9$, 1%CdS/ $\text{Cs}_3\text{Bi}_2\text{Br}_9$, 5%CdS/ $\text{Cs}_3\text{Bi}_2\text{Br}_9$, and 10%CdS/ $\text{Cs}_3\text{Bi}_2\text{Br}_9$, with each dosage set at 10 mg. These were subjected to visible light exposure for a duration of three hours at a pH of 8.
- ❖ Kinetic experiments on CdS (Solgel), CdS (Microwave), $\text{Cs}_3\text{Bi}_2\text{Br}_9$, and 5% CdS/ $\text{Cs}_3\text{Bi}_2\text{Br}_9$ were necessary for comprehending reaction rates and underlying mechanisms. The 10 ppm Ciprofloxacin solution was photocatalytically degraded in 210 minutes by using a 10 mg catalyst dose for CdS (Solgel), CdS (Microwave), $\text{Cs}_3\text{Bi}_2\text{Br}_9$, and 5% CdS/ $\text{Cs}_3\text{Bi}_2\text{Br}_9$, respectively. This was achieved with an astounding 60%, 80%, 65.5%, and 98.4% of the solution, respectively.
- ❖ The concentration of H_2O_2 was elevated from 0.01 to 0.1%, resulting in an enhancement of the photocatalytic degradation of Ciprofloxacin, with efficiency increasing from 19, 17, and 65% to 51, 47, and 100% respectively.
- ❖ The quantity of CdS, $\text{Cs}_3\text{Bi}_2\text{Br}_9$, and 5% CdS/ $\text{Cs}_3\text{Bi}_2\text{Br}_9$ nanocomposites was changed from 0.001 to 0.2 g/l in 180 ml of Ciprofloxacin solution with 0.1% H_2O_2 at a pH of 8.0. This was done in order to identify the best photocatalytic dosage. It was shown that the photocatalytic degradation effectiveness of Ciprofloxacin rose from 35 to 88.5% when the dose of the photocatalyst was raised from 0.001 to 0.5 g/l.

- ❖ The data reveal that the degradation efficiency of Ibuprofen increases within the acidic pH range of 05 to 06 across all photocatalysts. However, a decline in efficiency is observed when the pH is further increased from 7.0 to 11.0. The optimal pH for Ibuprofen removal was identified as 6.0, where slightly acidic conditions yielded maximum degradation efficiencies of 53%, 68%, 65%, 69%, 83%, and 60% for the MoS₂ (S.G.), MoS₂ (M.W.), Cs₃Bi₂Br₉, 1% MoS₂@Cs₃Bi₂Br₉, 5% MoS₂@Cs₃Bi₂Br₉, and 10% MoS₂@Cs₃Bi₂Br₉ nanocomposites, respectively, under visible light.
- ❖ The experiment involved varying the amounts of the MoS₂ (S.G.), MoS₂ (M.W.), Cs₃Bi₂Br₉, 1% MoS₂@Cs₃Bi₂Br₉, 5% MoS₂@Cs₃Bi₂Br₉, and 10% MoS₂@Cs₃Bi₂Br₉ nanocomposites from 0.001 to 0.2 mg/L in a 100 mL Ibuprofen solution, supplemented with 0.1% H₂O₂, under 100 W light intensity at pH 6.0 for up to 3 hours to determine the optimal photocatalyst dosage. The photocatalytic degradation efficiency of Ibuprofen increased significantly from 27.44% to 83.69% as the photocatalyst dose was increased from 0.001 to 0.05 mg/L.

For the degradation of 2-chlorophenol, ciprofloxacin, paracetamol, and ibuprofen, the as-prepared material was synthesized by microwave process and sol-gel process. This study shows how to synthesize a hybrid heterojunction between Cs₃Bi₂Br₉ and CdS, MoS₂ at various ratios. SEM-EDX pictures were used to assess morphological investigations and the composition of the dopants, demonstrating the existence of CdS, MoS₂ in the Cs₃Bi₂Br₉ nanostructured hybrid. Powder XRD was used to confirm the crystalline structures of CuS, CdS, MoS₂, Cs₃Bi₂Br₉, CdS/Cs₃Bi₂Br₉, and MoS₂/Cs₃Bi₂Br₉ nanocomposites, respectively. The bandgap energies for CuS, CdS, and Cs₃Bi₂Br₉ were determined by UV-vis spectroscopy. The as-prepared material CuS, CdS, Cs₃Bi₂Br₉, CdS/Cs₃Bi₂Br₉, and MoS₂/Cs₃Bi₂Br₉ photocatalysts were used to study the degradation of 2-chlorophenol, ciprofloxacin, paracetamol, etc, at the irradiation time, ideal pH, and H₂O₂ conc. Catalytic dosage and effect of temperature. Unexpectedly, at an ideal pH of 8, CdS, Cs₃Bi₂Br₉, and 5% CdS/Cs₃Bi₂Br₉ demonstrated maximum degradation efficiency of 80%, 65.5% and 98.4 % respectively, as compared to the Solgel method-based CdS, which is 60%, with a catalytic dosage of 10 mg and an irradiation period of three hours.

Moreover, the binary nanocomposites demonstrated enhanced absorption capacity of visible light, reduced crystalline size, a narrower band gap, efficient separation and transfer of interfacial charge carriers (e^-/h^+), and a recombination rate established by the prompt transference of organic contaminants to the photocatalyst surface. Previously, we have focused heavily on the reaction mechanism, which is supported by spectroscopic data. Its increased

photocatalytic activity may be due to its existence in an environment with a high biological reactant. All binary nanocomposites often contain OH reactive species, which are crucial to the photodegradation process and, in turn, the oxidative elimination of organic contaminants. These nanocomposites of binary photocatalysts seem like intriguing possibilities for intensive practical investigation for large-scale, reusable applications, which would ultimately lead to the utilization of freely accessible solar energy.

SCOPE FOR FUTURE WORK

Our research explores the synthesis of metal sulfides from metal oxides, transforming them into perovskite materials with tailored properties for environmental remediation. Building on this foundation, our future projects aim to harness these materials for sustainable energy production. Key objectives include:

- Water splitting for hydrogen production
- Methane evolution from CO₂ reduction
- Development of sustainable electrodes for applications in health, energy, and environment

By advancing perovskite-based technologies, we seek to address pressing challenges in energy and environmental sustainability. Our goal is to create innovative solutions that contribute to a cleaner and more sustainable future. With a focus on practical applications and scalability, our research has the potential to drive meaningful impact in various fields, from renewable energy to environmental protection and human health.

REFERENCES

1. Zubair, M., Arshad, M., & Ullah, A. (2020). Chitosan-based materials for water and wastewater treatment. In *Handbook of chitin and chitosan* (pp. 773-809). Elsevier.
2. Dhote, J., Ingole, S., & Chavhan, A. (2012). Review of wastewater treatment technologies. *Int. J. Eng. Res. Technol*, 1(5), 1-10.
3. Halder, S., & Bose, S. (2024). Addressing water scarcity challenges through rainwater harvesting: A comprehensive analysis of potential zones and model performance in arid and semi-arid regions—A case study on Purulia, India. *HydroResearch*, 7, 201-212.
4. Katoch, S. (2024). Water crisis in India: A study. *The Geo Journal*, 4(1), 78–89.
5. Panda, R. (2011). A growing concern: How soon will India run out of water?. *Journal of global health*, 1(2), 135.
6. Rakkasagi, S. B., Rawat, A., Singh, S., & Kumar, S. (2025). A review of India's water policy and implementation toward closing water scarcity gaps. *Journal of Water and Climate Change*, 16(2), 493–507.
7. Singh, R., & Kumar, S. (2021). The suitability of water scarcity indicators to the Indian context. *Environmental Advances*, 4, 100146.
8. Du, H., Yang, Z., Tian, Z., Huang, M., Yang, W., Zhang, L., & Li, A. (2018). Enhanced removal of trace antibiotics from turbid water in the coexistence of natural organic matters using phenylalanine-modified-chitosan flocculants: effect of flocculants' molecular architectures. *Chemical Engineering Journal*, 333, 310-319.
9. Yang, Y., Ok, Y. S., Kim, K. H., Kwon, E. E., & Tsang, Y. F. (2017). Occurrences and removal of pharmaceuticals and personal care products (PPCPs) in drinking water and water/sewage treatment plants: A review. *Science of the Total Environment*, 596, 303-320.
10. Anderson, P. D., D'Aco, V. J., Shanahan, P., Chapra, S. C., Buzby, M. E., Cunningham, V. L., ... & Schwab, B. W. (2004). Screening analysis of human pharmaceutical compounds in US surface waters. *Environmental Science & Technology*, 38(3), 838-849.
11. Hirsch, R., Ternes, T. A., Haberer, K., Mehlich, A., Ballwanz, F., & Kratz, K. L. (1998). Determination of antibiotics in different water compartments via liquid chromatography–electrospray tandem mass spectrometry. *Journal of chromatography A*, 815(2), 213-223.

12. Hignite, C., & Azarnoff, D. L. (1977). Drugs and drug metabolites as environmental contaminants: chlorophenoxyisobutyrate and salicylic acid in sewage water effluent. *Life Sciences*, 20(2), 337-341.
13. Daughton, C. G., & Ternes, T. A. (1999). Pharmaceuticals and personal care products in the environment: agents of subtle change?. *Environmental health perspectives*, 107(suppl 6), 907-938.
14. Lucaccioni, L., Trevisani, V., Marrozzini, L., Bertoncelli, N., Predieri, B., Lugli, L., ... & Iughetti, L. (2020). Endocrine-disrupting chemicals and their effects during female puberty: a review of current evidence. *International Journal of Molecular Sciences*, 21(6), 2078.
15. Saggioro, E. M., Chaves, F. P., Felix, L. C., Gomes, G., & Bila, D. M. (2019). Endocrine disruptor degradation by UV/chlorine and the impact of their removal on estrogenic activity and toxicity. *International Journal of Photoenergy*, 2019(1), 7408763.
16. Dodson, R. E., Nishioka, M., Standley, L. J., Perovich, L. J., Brody, J. G., & Rudel, R. A. (2012). Endocrine disruptors and asthma-associated chemicals in consumer products. *Environmental health perspectives*, 120(7), 935-943.
17. Staples, C. A., Dome, P. B., Klecka, G. M., Oblock, S. T., & Harris, L. R. (1998). A review of the environmental fate, effects, and exposures of bisphenol A. *Chemosphere*, 36(10), 2149-2173.
18. Flint, S., Markle, T., Thompson, S., & Wallace, E. (2012). Bisphenol A exposure, effects, and policy: a wildlife perspective. *Journal of Environmental Management*, 104, 19-34.
19. Birkett, J. W., & Lester, J. N. (Eds.). (2002). *Endocrine disrupters in wastewater and sludge treatment processes*. IWA Publishing.
20. Brooke, L. T., & Thursby, G. B. (2005). *Ambient Aquatic Life Water Quality Criteria, Nonylphenol: Final*. US Environmental Protection Agency, Office of Water.
21. Waltman, E. L., Venables, B. J., & Waller, W. T. (2006). Triclosan in a North Texas wastewater treatment plant and the influent and effluent of an experimental constructed wetland. *Environmental Toxicology and Chemistry: An International Journal*, 25(2), 367-372.
22. D'Ascenzo, G., Di Corcia, A., Gentili, A., Mancini, R., Mastropasqua, R., Nazzari, M., & Samperi, R. (2003). Fate of natural estrogen conjugates in municipal sewage transport and treatment facilities. *Science of the Total Environment*, 302(1-3), 199-209.

23. Tan, B. L., Hawker, D. W., Müller, J. F., Leusch, F. D., Tremblay, L. A., & Chapman, H. F. (2007). Comprehensive study of endocrine-disrupting compounds using grab and passive sampling at selected wastewater treatment plants in South East Queensland, Australia. *Environment international*, 33(5), 654-669.
24. Diamanti-Kandarakis, E., Bourguignon, J. P., Giudice, L. C., Hauser, R., Prins, G. S., Soto, A. M., ... & Gore, A. C. (2009). Endocrine-disrupting chemicals: an Endocrine Society scientific statement. *Endocrine reviews*, 30(4), 293-342.
25. Azimi, Y., Talaeian, M., Sarkheil, H., Hashemi, R., & Shirdam, R. (2022). Developing an evolving multi-layer perceptron network by genetic algorithm to predict full-scale municipal wastewater treatment plant effluent. *Journal of Environmental Chemical Engineering*, 10(5), 108398.
26. Li, Z., & Zhang, Y. (2023). Photocatalytic degradation of ciprofloxacin using novel nanomaterials: Mechanism and environmental implications. *Environmental Science & Technology*, 57(4), 2234–2248.
27. Agarwal, N. (2021). Paracetamol-A contaminant of high concern: Existence in environment and adverse effects. *Pharm. Drug Regul. Aff. J*, 4(000128), 10-23880.
28. Thacharodi, A., Hassan, S., Hegde, T. A., Thacharodi, D. D., Brindhadevi, K., & Pugazhendhi, A. (2023). Water a major source of endocrine-disrupting chemicals: An overview on the occurrence, implications on human health and bioremediation strategies. *Environmental Research*, 231, 116097.
29. Ashraf, M. A., & Wilson, M. (2019). Endocrine Disrupting Chemicals: Sources, Effects and Treatments. *Acta Chemica Malaysia*, 3(2), 39-47.
30. Heindel, J. J., Newbold, R., & Schug, T. T. (2015). Endocrine disruptors and obesity. *Nature Reviews Endocrinology*, 11(11), 653-661.
31. Montano, L. (2020). Reproductive biomarkers as early indicators for assessing environmental health risk. *Toxic Waste Management and Health Risk*; Marfe, G., Di Stefano, C., Eds, 113-145.
32. Montano, L., Bergamo, P., Volpe, M. G., Lorenzetti, S., Mantovani, A., Notari, T., ... & Iannuzzi, L. (2016). Human semen as an early, sensitive biomarker of environmental exposure: Preliminary results of the ECOFOODFERTILITY Project. *Reproductive Toxicology*, 100(64), 43-44.
33. Quesada, I., Fuentes, E., Viso-León, M. C., Soria, B., Ripoll, C., & Nadal, A. (2002). Low doses of the endocrine disruptor Bisphenol-A and the native hormone 17 β -

- estradiol rapidly activate the transcription factor CREB. *The FASEB Journal*, 16(12), 1671-1673.
34. Kojima, H., Katsura, E., Takeuchi, S., Niiyama, K., & Kobayashi, K. (2004). Screening for estrogen and androgen receptor activities in 200 pesticides by in vitro reporter gene assays using Chinese hamster ovary cells. *Environmental health perspectives*, 112(5), 524-531.
 35. Martyniuk, C. J., Mehinto, A. C., & Denslow, N. D. (2020). Organochlorine pesticides: Agrochemicals with potent endocrine-disrupting properties in fish. *Molecular and cellular endocrinology*, 507, 110764.
 36. Goldner, W. S., Sandler, D. P., Yu, F., Hoppin, J. A., Kamel, F., & LeVan, T. D. (2010). Pesticide use and thyroid disease among women in the Agricultural Health Study. *American journal of epidemiology*, 171(4), 455-464.
 37. Muñoz, J. P., Bleak, T. C., & Calaf, G. M. (2021). Glyphosate and the key characteristics of an endocrine disruptor: A review. *Chemosphere*, 270, 128619.
 38. Bustamante-Montes, L. P., Hernandez-Valero, M. A., Garcia-Fabila, M., Halley-Castillo, E., Karam-Calderon, M. A., & Borja-Aburto, V. H. (2008). Prenatal phthalate exposure and decrease in ano-genital distance in Mexican male newborns. *Epidemiology*, 19(6), S270.
 39. Calaf, G. M., Ponce-Cusi, R., Aguayo, F., Muñoz, J. P., & Bleak, T. C. (2020). Endocrine disruptors from the environment are affecting breast cancer. *Oncology letters*, 20(1), 19-32.
 40. Street, M. E., Angelini, S., Bernasconi, S., Burgio, E., Cassio, A., Catellani, C., ... & Amarri, S. (2018). Current knowledge on endocrine disrupting chemicals (EDCs) from animal biology to humans, from pregnancy to adulthood: highlights from a national Italian meeting. *International journal of molecular sciences*, 19(6), 1647.
 41. Gore, A. C. (2010). Neuroendocrine targets of endocrine disruptors. *Hormones*, 9(1), 16-27.
 42. Sargis, R. M., & Simmons, R. A. (2019). Environmental neglect: endocrine disruptors as underappreciated but potentially modifiable diabetes risk factors. *Diabetologia*, 62, 1811-1822.
 43. Basak, S., Das, M. K., & Duttaroy, A. K. (2020). Plastics-derived endocrine-disrupting compounds and their effects on early development. *Birth defects research*, 112(17), 1308-1325.

44. Hayes, T. B., Anderson, L. L., Beasley, V. R., De Solla, S. R., Iguchi, T., Ingraham, H., ... & Willingham, E. (2011). Demasculinization and feminization of male gonads by atrazine: consistent effects across vertebrate classes. *The Journal of steroid biochemistry and molecular biology*, 127(1-2), 64-73.
45. Grilo, T. F., & Rosa, R. (2017). Intersexuality in aquatic invertebrates: prevalence and causes. *Science of the Total Environment*, 592, 714-728.
46. Guillette Jr, L. J., Gross, T. S., Masson, G. R., Matter, J. M., Percival, H. F., & Woodward, A. R. (1994). Developmental abnormalities of the gonad and abnormal sex hormone concentrations in juvenile alligators from contaminated and control lakes in Florida. *Environmental health perspectives*, 102(8), 680-688.
47. Palma, P., Palma, V. L., Matos, C., Fernandes, R. M., Bohn, A., Soares, A. M. V. M., & Barbosa, I. R. (2009). Assessment of the pesticides atrazine, endosulfan sulphate, and chlorpyrifos for juvenoid-related endocrine activity using *Daphnia magna*. *Chemosphere*, 76(3), 335-340.
48. Vom Saal, F. S. (2016). TRIENNIAL REPRODUCTION SYMPOSIUM: Environmental programming of reproduction during fetal life: Effects of intrauterine position and the endocrine-disrupting chemical bisphenol A. *Journal of animal science*, 94(7), 2722-2736.
49. Lemaire, G., Terouanne, B., Mauvais, P., Michel, S., & Rahmani, R. (2004). Effect of organochlorine pesticides on human androgen receptor activation in vitro. *Toxicology and applied pharmacology*, 196(2), 235-246.
50. Combarnous, Y. (2017). Endocrine Disruptor Compounds (EDCs) and agriculture: The case of pesticides. *Comptes Rendus. Biologies*, 340(9-10), 406-409.
51. Galoppo, G. H., Tavalieri, Y. E., Schierano-Marotti, G., Osti, M. R., Luque, E. H., & Muñoz-de-Toro, M. M. (2020). Long-term effects of in ovo exposure to an environmentally relevant dose of atrazine on the thyroid gland of *Caiman latirostris*. *Environmental research*, 186, 109410.
52. Yang, F. W., Fang, B., Pang, G. F., & Ren, F. Z. (2019). Organophosphorus pesticide triazophos: A new endocrine disruptor chemical of the hypothalamus-pituitary-adrenal axis. *Pesticide biochemistry and physiology*, 159, 91-97.
53. Wu, S., Li, X., Liu, X., Yang, G., An, X., Wang, Q., & Wang, Y. (2018). Joint toxic effects of triazophos and imidacloprid on zebrafish (*Danio rerio*). *Environmental Pollution*, 235, 470-481.

54. Diamanti-Kandarakis, E., Bourguignon, J. P., Giudice, L. C., Hauser, R., Prins, G. S., Soto, A. M., ... & Gore, A. C. (2009). Endocrine-disrupting chemicals: an Endocrine Society scientific statement. *Endocrine reviews*, 30(4), 293-342.
55. Golub, M. S., & Doherty, J. D. (2004). Triphenyltin as a potential human endocrine disruptor. *Journal of Toxicology and Environmental Health, Part B*, 7(4), 281-295.
56. Mazur, C. S., Marchitti, S. A., & Zastre, J. (2015). P-glycoprotein inhibition by the agricultural pesticide propiconazole and its hydroxylated metabolites: Implications for pesticide–drug interactions. *Toxicology letters*, 232(1), 37-45.
57. Wadzinski, T. L., Altowaireb, Y., Gupta, R., Conroy, R., & Shoukri, K. (2014). Luteoma of pregnancy associated with nearly complete virilization of genetically female twins. *Endocrine Practice*, 20(2), e18-e23.
58. Gore, A. C., Chappell, V. A., Fenton, S. E., Flaws, J. A., Nadal, A., Prins, G. S., ... & Zoeller, R. T. (2015). EDC-2: the Endocrine Society's second scientific statement on endocrine-disrupting chemicals. *Endocrine reviews*, 36(6), E1-E150.
59. Walker, C. L. (2016). Minireview: epigenomic plasticity and vulnerability to EDC exposures. *Molecular Endocrinology*, 30(8), 848-855.
60. Zhang, Y., Wu, L., Zhang, G., Guan, Y., & Wang, Z. (2016). Effect of low-dose malathion on the gonadal development of adult rare minnow *Gobiocypris rarus*. *Ecotoxicology and environmental safety*, 125, 135-140.
61. Zhou, Q., Miao, M., Ran, M., Ding, L., Bai, L., Wu, T., ... & Li, D. K. (2013). Serum bisphenol-A concentration and sex hormone levels in men. *Fertility and sterility*, 100(2), 478-482.
62. Bansal, R., & Zoeller, R. T. (2008). Polychlorinated biphenyls (Aroclor 1254) do not uniformly produce agonist actions on thyroid hormone responses in the developing rat brain. *Endocrinology*, 149(8), 4001-4008.
63. Sangeetha, S., Vimalkumar, K., & Loganathan, B. G. (2021). Environmental contamination and human exposure to select endocrine-disrupting chemicals: A review. *Sustainable Chemistry*, 2(2), 343-380.
64. Patel, N. A. V. E. E. N., Khan, M. D., Shahane, S., Rai, D., Chauhan, D., Kant, C., & Chaudhary, V. K. (2020). Emerging pollutants in aquatic environment: source, effect, and challenges in biomonitoring and bioremediation-a review. *Pollution*, 6(1), 99-113.
65. Richardson, S. D., & Ternes, T. A. (2018). Water analysis: emerging contaminants and current issues. *Anal. Chem*, 90(1), 398-428.

66. Guarino, F., Motta, O., Turano, M., Proto, A., & Vigliotta, G. (2020). Preferential Use of the Perchlorate over the Nitrate in the Respiratory Processes Mediated by the Bacterium *Azospira* sp. OGA 24. *Water*, 12(8), 2220.
67. Ricciardi, M., Pironti, C., Motta, O., Miele, Y., Proto, A., & Montano, L. (2021). Microplastics in the aquatic environment: occurrence, persistence, analysis, and human exposure. *Water*, 13(7), 973.
68. Fiorentino, A., Rizzo, L., Guilloteau, H., Bellanger, X., & Merlin, C. (2017). Comparing TiO₂ photocatalysis and UV-C radiation for inactivation and mutant formation of *Salmonella typhimurium* TA102. *Environmental Science and Pollution Research*, 24, 1871-1879.
69. Bilal, M., & Iqbal, H. M. (2019). An insight into toxicity and human-health-related adverse consequences of cosmeceuticals—a review. *Science of the total environment*, 670, 555-568.
70. Kasonga, T. K., Coetzee, M. A., Kamika, I., Ngole-Jeme, V. M., & Momba, M. N. B. (2021). Endocrine-disruptive chemicals as contaminants of emerging concern in wastewater and surface water: A review. *Journal of Environmental Management*, 277, 111485.
71. Proto, A., Zarrella, I., Capacchione, C., & Motta, O. (2014). One-year surveillance of the chemical and microbial quality of drinking water was conducted in the Eolian Islands. *Water*, 6(1), 139-149.
72. Pironti, C., Motta, O., Ricciardi, M., Camin, F., Cucciniello, R., & Proto, A. (2020). Characterization and authentication of commercial cleaning products formulated with biobased surfactants by stable carbon isotope ratio. *Talanta*, 219, 121256.
73. Flint, S., Markle, T., Thompson, S., & Wallace, E. (2012). Bisphenol A exposure, effects, and policy: a wildlife perspective. *Journal of Environmental Management*, 104, 19-34.
74. Zoeller, R. T., Brown, T. R., Doan, L. L., Gore, A. C., Skakkebaek, N. E., Soto, A. M., ... & Vom Saal, F. S. (2012). Endocrine-disrupting chemicals and public health protection: a statement of principles from The Endocrine Society. *Endocrinology*, 153(9), 4097-4110.
75. Sharma, V. K., Anquandah, G. A., & Nesnas, N. (2009). Kinetics of the oxidation of endocrine disruptor nonylphenol by ferrate (VI). *Environmental Chemistry Letters*, 7, 115-119.

76. Colborn, T., Vom Saal, F. S., & Soto, A. M. (1993). Developmental effects of endocrine-disrupting chemicals in wildlife and humans. *Environmental health perspectives*, 101(5), 378-384.
77. Yilmaz, B., Terekeci, H., Sandal, S., & Kelestimur, F. (2020). Endocrine-disrupting chemicals: exposure, effects on human health, mechanism of action, models for testing and strategies for prevention. *Reviews in endocrine and metabolic disorders*, 21, 127-147.
78. Caliman, F. A., & Gavrilescu, M. (2009). Pharmaceuticals, personal care products, and endocrine-disrupting agents in the environment—a review. *CLEAN—Soil, Air, Water*, 37(4-5), 277-303.
79. Tijani, J. O., Fatoba, O. O., Babajide, O. O., & Petrik, L. F. (2016). Pharmaceuticals, endocrine disruptors, personal care products, nanomaterials, and perfluorinated pollutants: a review. *Environmental chemistry letters*, 14, 27-49.
80. Gröger, T. M., Käfer, U., & Zimmermann, R. (2020). Gas chromatography in combination with fast high-resolution time-of-flight mass spectrometry: Technical overview and perspectives for data visualization. *TrAC Trends in Analytical Chemistry*, 122, 115677.
81. Yang, F. W., Zhao, G. P., Ren, F. Z., Pang, G. F., & Li, Y. X. (2020). Assessment of the endocrine-disrupting effects of diethyl phosphate, a nonspecific metabolite of organophosphorus pesticides, by in vivo and in silico approaches. *Environment International*, 135, 105383.
82. Wan, Y., Tran, T. M., Nguyen, V. T., Wang, A., Wang, J., & Kannan, K. (2021). Neonicotinoids, fipronil, chlorpyrifos, carbendazim, chlorotriazines, chlorophenoxy herbicides, bentazon, and selected pesticide transformation products in surface water and drinking water from northern Vietnam. *Science of the Total Environment*, 750, 141507.
83. Bergman, Å., Heindel, J. J., Kasten, T., Kidd, K. A., Jobling, S., Neira, M., ... & Woodruff, T. J. (2013). The impact of endocrine disruption: a consensus statement on the state of the science. *Environmental health perspectives*, 121(4), a104-a106.
84. Mukherjee, R., Pandya, P., Baxi, D., & Ramachandran, A. V. (2021, December). Endocrine disruptors—‘food’ for thought. In *Proceedings of the Zoological Society* (Vol. 74, No. 4, pp. 432-442). New Delhi: Springer India.
85. Basile, T., Petrella, A., Petrella, M., Boghetich, G., Petruzzelli, V., Colasuonno, S., & Petruzzelli, D. (2011). Review of endocrine-disrupting-compound removal

- technologies in water and wastewater treatment plants: an EU perspective. *Industrial & Engineering Chemistry Research*, 50(14), 8389-8401.
86. Larsson, D. J., de Pedro, C., & Paxeus, N. (2007). Effluent from drug manufacturers contains extremely high levels of pharmaceuticals. *Journal of hazardous materials*, 148(3), 751-755.
 87. Praveena, S. M., Mohd Rashid, M. Z., Mohd Nasir, F. A., Wee, S. Y., & Aris, A. Z. (2021). Occurrence, human health risks, and public awareness level of pharmaceuticals in tap water from Putrajaya (Malaysia). *Exposure and Health*, 13, 93-104.
 88. Sharma, B. M., Scheringer, M., Chakraborty, P., Bharat, G. K., Steindal, E. H., Trasande, L., & Nizzetto, L. (2023). Unlocking India's potential in managing endocrine-disrupting chemicals (EDCs): importance, challenges, and opportunities. *Exposure and Health*, 15(4), 841-855.
 89. Sharma, B. M., Bharat, G. K., Tayal, S., Nizzetto, L., Čupr, P., & Larssen, T. (2014). Environment and human exposure to persistent organic pollutants (POPs) in India: A systematic review of recent and historical data. *Environment international*, 66, 48-64.
 90. Bornman, M. S., Aneck-Hahn, N. H., De Jager, C., Wagenaar, G. M., Bouwman, H., Barnhoorn, I. E., ... & Heindel, J. J. (2017). Endocrine disruptors and health effects in Africa: a call for action. *Environmental health perspectives*, 125(8), 085005.
 91. Dutta, D., & Khadgawat, R. (2015). Endocrine disruptors: Can they be the missing link explaining the diabetes epidemic in India?. *Journal of Social Health and Diabetes*, 3(01), 016-021.
 92. Xue, J., Wu, Q., Sakthivel, S., Pavithran, P. V., Vasukutty, J. R., & Kannan, K. (2015). Urinary levels of endocrine-disrupting chemicals, including bisphenols, bisphenol A diglycidyl ethers, benzophenones, parabens, and triclosan in obese and non-obese Indian children. *Environmental research*, 137, 120-128.
 93. Sharma, B. M., Bharat, G. K., Chakraborty, P., Martiník, J., Audy, O., Kukučka, P., ... & Nizzetto, L. (2021). A comprehensive assessment of endocrine-disrupting chemicals in an Indian food basket: Levels, dietary intakes, and comparison with European data. *Environmental Pollution*, 288, 117750.
 94. Singare, P. U. (2016). Distribution and risk assessment of suspected endocrine-disrupting pesticides in the creek water of Mumbai, India. *Marine pollution bulletin*, 102(1), 72-83.
 95. Geetha, T. (2021). Endocrine disruptors in boiled drinking water carried in plastic containers: a pilot study in Thrissur, Kerala, India. *Applied Water Science*, 11(12), 188.

96. Okonkwo, J. O., Sibali, L. L., McCrindle, R., & Senwo, Z. N. (2007). An improved activated carbon method to quantify dichlorodiphenyltrichloroethane (DDT) in surface water. *Environmental Chemistry Letters*, 5, 121-123.
97. Artham, T., & Doble, M. (2012). Bisphenol A and metabolites released by biodegradation of polycarbonate in seawater. *Environmental chemistry letters*, 10, 29-34.
98. Vieira, W. T., de Farias, M. B., Spaolonzi, M. P., da Silva, M. G. C., & Vieira, M. G. A. (2020). Removal of endocrine disruptors in waters by adsorption, membrane filtration and biodegradation. A review. *Environmental Chemistry Letters*, 18(4), 1113-1143.
99. Djebri, N., Boutahala, M., Chelali, N. E., Boukhalfa, N., & Larbi, Z. (2017). Adsorption of bisphenol A and 2, 4, 5-trichlorophenol onto organo-acid-activated bentonite from aqueous solutions in single and binary systems. *Desalination and water treatment*, 66, 383-393.
100. Goyal, N., Barman, S., & Bulasara, V. K. (2016). Quaternary ammonium salt assisted removal of genistein and bisphenol S from aqueous solution by nanozeolite NaY: equilibrium, kinetic and thermodynamic studies. *Journal of Molecular Liquids*, 224, 1154-1162.
101. Zhang, L., Lv, J., Xu, T., Yang, L., Jiang, X., & Li, Q. (2013). High efficiency removal and recovery of an endocrine disrupting compound–bisphenol AF from wastewaters. *Separation and Purification Technology*, 116, 145-153.
102. Maia, G. S., de Andrade, J. R., da Silva, M. G., & Vieira, M. G. (2019). Adsorption of diclofenac sodium onto commercial organoclay: kinetic, equilibrium and thermodynamic study. *Powder technology*, 345, 140-150.
103. de Souza, F. M., Lazarin, A. M., Vieira, M. G. A., & dos Santos, O. A. A. (2018). Kinetic, equilibrium, and thermodynamic study on atrazine adsorption in organophilic clay. *Desalination and Water Treatment*, 123, 240-252.
104. Coelho, C. M., de Andrade, J. R., da Silva, M. G. C., & Vieira, M. G. A. (2020). Removal of propranolol hydrochloride by batch biosorption using remaining biomass of alginate extraction from *Sargassum filipendula* algae. *Environmental Science and Pollution Research*, 27, 16599-16611.
105. Sahu, O., & Singh, N. (2019). Significance of bioadsorption process on textile industry wastewater. In *The impact and prospects of green chemistry for textile technology* (pp. 367-416). Woodhead Publishing.

106. Crini, G., Lichtfouse, E., Wilson, L. D., & Morin-Crini, N. (2019). Conventional and non-conventional adsorbents for wastewater treatment. *Environmental Chemistry Letters*, 17, 195-213.
107. Ahsan, M. A., Islam, M. T., Imam, M. A., Hyder, A. G., Jabbari, V., Dominguez, N., & Noveron, J. C. (2018). Biosorption of bisphenol A and sulfamethoxazole from water using sulfonated coffee waste: Isotherm, kinetic and thermodynamic studies. *Journal of Environmental Chemical Engineering*, 6(5), 6602-6611.
108. Rodriguez-Narvaez, O. M., Peralta-Hernandez, J. M., Goonetilleke, A., & Bandala, E. R. (2017). Treatment technologies for emerging contaminants in water: A review. *Chemical Engineering Journal*, 323, 361-380.
109. Si, X., Hu, Z., & Huang, S. (2018). Combined process of ozone oxidation and ultrafiltration as an effective treatment technology for the removal of endocrine-disrupting chemicals. *Applied Sciences*, 8(8), 1240.
110. Kamaz, M., Wickramasinghe, S. R., Eswaranandam, S., Zhang, W., Jones, S. M., Watts, M. J., & Qian, X. (2019). Investigation into micropollutant removal from wastewaters by a membrane bioreactor. *International Journal of Environmental Research and Public Health*, 16(8), 1363.
111. Schmidt, N., Page, D., & Tiehm, A. (2017). Biodegradation of pharmaceuticals and endocrine disruptors with oxygen, nitrate, manganese (IV), iron (III) and sulfate as electron acceptors. *Journal of contaminant hydrology*, 203, 62-69.
112. Hu, J. Y., Aizawa, T., & Ookubo, S. (2002). Products of aqueous chlorination of bisphenol A and their estrogenic activity. *Environmental Science & Technology*, 36(9), 1980-1987.
113. Roccuzzo, S., Beckerman, A. P., & Trögl, J. (2021). New perspectives on the bioremediation of endocrine disrupting compounds from wastewater using algae-, bacteria-and fungi-based technologies. *International Journal of Environmental Science and Technology*, 18(1), 89-106.
114. Grelska, A., & Noszczyńska, M. (2020). White rot fungi can be a promising tool for removal of bisphenol A, bisphenol S, and nonylphenol from wastewater. *Environmental Science and Pollution Research*, 27(32), 39958-39976.
115. Varma, K. S., Tayade, R. J., Shah, K. J., Joshi, P. A., Shukla, A. D., & Gandhi, V. G. (2020). Photocatalytic degradation of pharmaceutical and pesticide compounds (PPCs) using doped TiO₂ nanomaterials: A review. *Water-Energy Nexus*, 3, 46-61.

116. Irmak, S., Erbatur, O., & Akgerman, A. (2005). Degradation of 17 β -estradiol and bisphenol A in aqueous medium by using ozone and ozone/UV techniques. *Journal of hazardous materials*, 126(1-3), 54-62.
117. Kohantorabi, M., Giannakis, S., Gholami, M. R., Feng, L., & Pulgarin, C. (2019). A systematic investigation on the bactericidal transient species generated by photo-sensitization of natural organic matter (NOM) during solar and photo-Fenton disinfection of surface waters. *Applied Catalysis B: Environmental*, 244, 983-995.
118. Hu, C., Huang, D., Zeng, G., Cheng, M., Gong, X., Wang, R., ... & Liu, Y. (2018). The combination of Fenton process and *Phanerochaete chrysosporium* for the removal of bisphenol A in river sediments: mechanism related to extracellular enzyme, organic acid and iron. *Chemical Engineering Journal*, 338, 432-439.
119. Ferroudj, N., Nzimoto, J., Davidson, A., Talbot, D., Briot, E., Dupuis, V., ... & Abramson, S. (2013). Maghemite nanoparticles and maghemite/silica nanocomposite microspheres as magnetic Fenton catalysts for the removal of water pollutants. *Applied Catalysis B: Environmental*, 136, 9-18.
120. Patil, S. S., Shedbalkar, U. U., Truskewycz, A., Chopade, B. A., & Ball, A. S. (2016). Nanoparticles for environmental clean-up: a review of potential risks and emerging solutions. *Environmental Technology & Innovation*, 5, 10-21.
121. Mohammad, A. T., Abdulhameed, A. S., & Jawad, A. H. (2019). Box-Behnken design to optimize the synthesis of new crosslinked chitosan-glyoxal/TiO₂ nanocomposite: methyl orange adsorption and mechanism studies. *International journal of biological macromolecules*, 129, 98-109.
122. Goh, P. S., Matsuura, T., Ismail, A. F., & Hilal, N. (2016). Recent trends in membranes and membrane processes for desalination. *Desalination*, 391, 43-60.
123. Jain, S., Jain, A. P., Jain, S., Gupta, O. N., & Vaidya, A. (2013). Nanotechnology: An emerging area in the field of dentistry. *J Dent Sci*, 10, 1-9.
124. Appelbaum, R. P., Gebbie, M. A., Han, X., Stocking, G., & Kay, L. (2016). Will China's quest for indigenous innovation succeed? Some lessons from nanotechnology. *Technology in Society*, 46, 149-163..
125. Anjum, M., Miandad, R., Waqas, M., Gehany, F., & Barakat, M. A. (2019). Remediation of wastewater using various nano-materials. *Arabian journal of chemistry*, 12(8), 4897-4919.

126. Khan, S., Wu, Y., Zhang, X., Hu, S., Li, T., Fu, Y., & Li, Q. (2013). Influence of dissolved organic matter from corn straw on Zn and Cu sorption to Chinese loess. *Toxicological & Environmental Chemistry*, 95(8), 1318-1327
127. Tahir, M. B., Sohaib, M., Sagir, M., & Rafique, M. (2022). Role of nanotechnology in photocatalysis. *Encyclopedia of smart materials*, 578
128. Coronado, J. M., Fresno, F., Hernández-Alonso, M. D., & Portela, R. (Eds.). (2013). *Design of advanced photocatalytic materials for energy and environmental applications* (Vol. 71). London: Springer.
129. Chimmikuttanda, S. P., Naik, A., Akple, M. S., & Singh, R. (2022). Processing of hybrid TiO₂ semiconducting materials and their environmental application. In *Advanced Materials for Sustainable Environmental Remediation* (pp. 277-300). Elsevier.
130. Fujishima, A., & Honda, K. (1972). Electrochemical photolysis of water at a semiconductor electrode. *nature*, 238(5358), 37-38.
131. Linsebigler, A. L., Lu, G., & Yates Jr, J. T. (1995). Photocatalysis on TiO₂ surfaces: principles, mechanisms, and selected results. *Chemical reviews*, 95(3), 735-758.
132. He, F., Jeon, W., & Choi, W. (2021). Photocatalytic air purification mimicking the self-cleaning process of the atmosphere. *Nature Communications*, 12(1), 2528.
133. Glaze, W. H., Kang, J. W., & Chapin, D. H. (1987). The chemistry of water treatment processes involving ozone, hydrogen peroxide and ultraviolet radiation.
134. Kurian, M., & Nair, D. S. (2015). Manganese zinc ferrite nanoparticles as efficient catalysts for wet peroxide oxidation of organic aqueous wastes. *Journal of Chemical sciences*, 127, 537-546.
135. Wols, B. A., & Hofman-Caris, C. H. M. (2012). Review of photochemical reaction constants of organic micropollutants required for UV advanced oxidation processes in water. *Water research*, 46(9), 2815-2827.
136. Nair, D. S., & Kurian, M. (2017). Heterogeneous catalytic oxidation of persistent chlorinated organics over cobalt substituted zinc ferrite nanoparticles at mild conditions: Reaction kinetics and catalyst reusability studies. *Journal of environmental chemical engineering*, 5(1), 964-974.
137. Fenton, H. J. H. (1894). LXXIII.—Oxidation of tartaric acid in presence of iron. *Journal of the Chemical Society, Transactions*, 65, 899-910.

138. Nogueira, R. F. P., Trovó, A. G., Silva, M. R. A. D., Villa, R. D., & Oliveira, M. C. D. (2007). Fundamentos e aplicações ambientais dos processos Fenton e foto-Fenton. *Química nova*, 30, 400-408.
139. Rodríguez, R., Espada, J. J., Pariente, M. I., Melero, J. A., Martínez, F., & Molina, R. (2016). Comparative life cycle assessment (LCA) study of heterogeneous and homogenous Fenton processes for the treatment of pharmaceutical wastewater. *Journal of Cleaner Production*, 124, 21-29.
140. Bae, S., Gim, S., Kim, H., & Hanna, K. (2016). Effect of NaBH₄ on properties of nanoscale zero-valent iron and its catalytic activity for reduction of p-nitrophenol. *Applied Catalysis B: Environmental*, 182, 541-549.
141. Ribeiro, R. S., Silva, A. M., Tavares, P. B., Figueiredo, J. L., Faria, J. L., & Gomes, H. T. (2017). Hybrid magnetic graphitic nanocomposites for catalytic wet peroxide oxidation applications. *Catalysis Today*, 280, 184-191.
142. Van Geluwe, S., Braeken, L., Vinckier, C., & Van der Bruggen, B. (2009). Ozonation and perozone oxidation of humic acids in nanofiltration concentrates. *Desalination and Water Treatment*, 6(1-3), 217-221.
143. Wang, M., Fang, G., Liu, P., Zhou, D., Ma, C., Zhang, D., & Zhan, J. (2016). Fe₃O₄@ β -CD nanocomposite as heterogeneous Fenton-like catalyst for enhanced degradation of 4-chlorophenol (4-CP). *Applied Catalysis B: Environmental*, 188, 113-122.
144. Lai, C., He, T., Li, X., Chen, F., Yue, L., & Hou, Z. (2019). Catalytic wet air oxidation of phenols over porous plate Cu-based catalysts. *Applied Clay Science*, 181, 105253.
145. Chong, M. N., Jin, B., Chow, C. W., & Saint, C. (2010). Recent developments in photocatalytic water treatment technology: a review. *Water research*, 44(10), 2997-3027.
146. Ruppert, G., Bauer, R., & Heisler, G. (1994). UV-O₃, UV-H₂O₂, UV-TiO₂ and the photo-Fenton reaction-comparison of advanced oxidation processes for wastewater treatment. *Chemosphere*, 28(8), 1447-1454.
147. Fujishima, A., & Honda, K. (1972). Electrochemical photolysis of water at a semiconductor electrode. *nature*, 238(5358), 37-38.
148. Arana, J., Rendón, E. T., Rodríguez, J. D., Melián, J. H., Díaz, O. G., & Peña, J. P. (2001). Highly concentrated phenolic wastewater treatment by the Photo-Fenton reaction, mechanism study by FTIR-ATR. *Chemosphere*, 44(5), 1017-1023.

149. Verma, P., & Samanta, S. K. (2018). Microwave-enhanced advanced oxidation processes for the degradation of dyes in water. *Environmental chemistry letters*, 16, 969-1007.
150. Ince, N. H. (2018). Ultrasound-assisted advanced oxidation processes for water decontamination. *Ultrasonics sonochemistry*, 40, 97-103.
151. Reddy, D. R., Dinesh, G. K., Anandan, S., & Sivasankar, T. (2016). Sonophotocatalytic treatment of Naphthol Blue Black dye and real textile wastewater using synthesized Fe doped TiO₂. *Chemical Engineering and Processing: Process Intensification*, 99, 10-18.
152. Hoffman, D. L., Novak, T. P., & Chatterjee, P. (1995). Commercial scenarios for the web: opportunities and challenges. *Journal of computer-mediated communication*, 1(3), JCMC136.
153. Serpone, N. (2006). Is the band gap of pristine TiO₂ narrowed by anion-and cation-doping of titanium dioxide in second-generation photocatalysts?. *The Journal of Physical Chemistry B*, 110(48), 24287-24293.
154. Saravanan, R., Gracia, F., & Stephen, A. (2017). Basic principles, mechanism, and challenges of photocatalysis. *Nanocomposites for visible light-induced photocatalysis*, 19-40.
155. Ajmal, A., Majeed, I., Malik, R. N., Idriss, H., & Nadeem, M. A. (2014). Principles and mechanisms of photocatalytic dye degradation on TiO₂ based photocatalysts: a comparative overview. *Rsc Advances*, 4(70), 37003-37026.
156. Malato, S., Fernández-Ibáñez, P., Maldonado, M. I., Blanco, J., & Gernjak, W. (2009). Decontamination and disinfection of water by solar photocatalysis: recent overview and trends. *Catalysis today*, 147(1), 1-59.
157. Bradley, B. R., Daigger, G. T., Rubin, R., & Tchobanoglous, G. (2002). Evaluation of onsite wastewater treatment technologies using sustainable development criteria. *Clean Technologies and Environmental Policy*, 4, 87-99.
158. Pattabathula, V., & Richardson, J. (2016). Introduction to ammonia production. *Chem. Eng. Prog*, 112(9), 69-75.
159. Schrauzer, G. N., & Guth, T. D. (2002). Photolysis of water and photoreduction of nitrogen on titanium dioxide. *Journal of the American chemical society*, 99(22), 7189-7193.

160. Wang, J., Lin, S., Tian, N., Ma, T., Zhang, Y., & Huang, H. (2021). Nanostructured metal sulfides: classification, modification strategy, and solar-driven CO₂ reduction application. *Advanced Functional Materials*, 31(9), 2008008.
161. Pouretedal, H. R., Norozi, A., Keshavarz, M. H., & Semnani, A. (2009). Nanoparticles of zinc sulfide doped with manganese, nickel, and copper as a nanophotocatalyst in the degradation of organic dyes. *Journal of hazardous materials*, 162(2-3), 674-681.
162. He, H. Y., Huang, J. F., Cao, L. Y., & Wu, J. P. (2010). Photodegradation of methyl orange aqueous solution on MnWO₄ powder under different light sources and initial pH. *Desalination*, 252(1-3), 66-70.
163. Karunakaran, C., & Dhanalakshmi, R. (2008). Semiconductor-catalyzed degradation of phenols with sunlight. *Solar energy materials and solar cells*, 92(11), 1315-1321.
164. Venkatachalam, N., Palanichamy, M., Arabindoo, B., & Murugesan, V. (2007). Enhanced photocatalytic degradation of 4-chlorophenol by Zr⁴⁺ doped nano TiO₂. *Journal of Molecular Catalysis. A, Chemical*, 1(266), 158-165.
165. Sun, H., Bai, Y., Jin, W., & Xu, N. (2008). Visible-light-driven TiO₂ catalysts doped with low-concentration nitrogen species. *Solar Energy Materials and Solar Cells*, 92(1), 76-83.
166. Wang, H., Zhang, L., Chen, Z., Hu, J., Li, S., Wang, Z., ... & Wang, X. (2014). Semiconductor heterojunction photocatalysts: design, construction, and photocatalytic performances. *Chemical Society Reviews*, 43(15), 5234-5244.
167. Maruska, H. P., & Ghosh, A. K. (1978). Photocatalytic decomposition of water at semiconductor electrodes. *Solar Energy*, 20(6), 443-458.
168. Meng, Y., Huang, X., Wu, Y., Wang, X., & Qian, Y. (2002). Kinetic study and modeling on photocatalytic degradation of para-chlorobenzoate at different light intensities. *Environmental Pollution*, 117(2), 307-313.
169. Wang, L., Zhao, J., Liu, H., & Huang, J. (2018). Design, modification, and application of semiconductor photocatalysts. *Journal of the Taiwan Institute of Chemical Engineers*, 93, 590-602.
170. Swift, E. (2019). A durable semiconductor photocatalyst. *Science*, 365(6451), 320-321.

171. Vaya, D., & Surolia, P. K. (2020). Semiconductor based photocatalytic degradation of pesticides: An overview. *Environmental technology & innovation*, 20, 101128.
172. Navidpour, A. H., Abbasi, S., Li, D., Mojiri, A., & Zhou, J. L. (2023). Investigation of advanced oxidation process in the presence of TiO₂ semiconductor as photocatalyst: property, principle, kinetic analysis, and photocatalytic activity. *Catalysts*, 13(2), 232.
173. Sudhaik, A., Raizada, P., Rangabhashiyam, S., Singh, A., Nguyen, V. H., Van Le, Q., ... & Singh, P. (2022). Copper sulfides based photocatalysts for degradation of environmental pollution hazards: A review on the recent catalyst design concepts and future perspectives. *Surfaces and Interfaces*, 33, 102182.
174. Liu, X., Li, J., & Yao, W. (2020). CdS@ MoS₂ hetero-structured nanocomposites are highly effective photo-catalysts for organic dye degradation. *ACS omega*, 5(42), 27463-27469.
175. Ullah, S., Khan, A., & Ali, M. (2023). MoS₂-based catalysts for sustainable photocatalysis applications: A review. *Frontiers in Chemistry*, 11, 694.
176. Tran, D. T., Nguyen, V. D., & Le, A. T. (2024). Enhanced photocatalytic performance of MoS₂-CdS composite for environmental remediation. *Scientific Reports*, 14, 13456.
177. Li, Q., Li, X., Wageh, S., Al-Ghamdi, A. A., & Yu, J. (2015). CdS/graphene nanocomposite photocatalysts. *Advanced Energy Materials*, 5(14), 1500010.
178. Zhao, D., & Yang, C. F. (2016). Recent advances in the TiO₂/CdS nanocomposite used for photocatalytic hydrogen production and quantum-dot-sensitized solar cells. *Renewable and sustainable energy reviews*, 54, 1048-1059.
179. Meng, Y., Hong, Y., Huang, C., & Shi, W. (2017). Fabrication of novel Z-scheme InVO₄/CdS heterojunctions with efficiently enhanced visible light photocatalytic activity. *CrystEngComm*, 19(6), 982-993.
180. Mishra, S. R., Gadore, V., & Ahmaruzzaman, M. (2023). Development of high-performance bi-functional novel CdSnS₂ atom clusters for adsorption of rose Bengal and AOP-assisted degradation of methylene blue. *Environmental Science: Water Research & Technology*, 9(2), 586-602.
181. Gadore, V., Mishra, S. R., & Ahmaruzzaman, M. (2023). One-pot synthesis of CdS/CeO₂ heterojunction nanocomposite with tunable bandgap for the enhanced advanced oxidation process. *Scientific Reports*, 13(1), 7708.

182. Gadore, V., & Ahmaruzzaman, M. (2021). Fly ash–based nanocomposites: A potential material for effective photocatalytic degradation/elimination of emerging organic pollutants from aqueous stream. *Environmental Science and Pollution Research*, 28(34), 46910-46933.
183. Zhang, J., Wageh, S., Al-Ghamdi, A., & Yu, J. (2016). New understanding on the different photocatalytic activity of wurtzite and zinc-blende CdS. *Applied Catalysis B: Environmental*, 192, 101-107.
184. Dadigala, R., Bandi, R., Alle, M., Gangapuram, B. R., Guttena, V., & Kim, J. C. (2021). In-situ fabrication of novel flower like MoS₂/CoTiO₃ nanorod heterostructures for the recyclable degradation of ciprofloxacin and bisphenol A under sunlight. *Chemosphere*, 281, 130822.
185. Ahamad, T., Naushad, M., Alzahrani, Y., & Alshehri, S. M. (2020). Photocatalytic degradation of bisphenol-A with g-C₃N₄/MoS₂-PANI nanocomposite: kinetics, main active species, intermediates and pathways. *Journal of Molecular Liquids*, 311, 113339.
186. Zhou, Y., Lu, F., Fang, T., Gu, D., Feng, X., Song, T., & Liu, W. (2022). A brief review on metal halide perovskite photocatalysts: History, applications and prospects. *Journal of Alloys and Compounds*, 911, 165062.
187. Zhang, Q., Deng, X., Tan, C., Zhou, Y., Chen, X., Bai, X., ... & Lin, H. (2020). Gamma-phase CsPbBr₃ perovskite nanocrystals/polymethyl methacrylate electrospun nanofibrous membranes with superior photo-catalytic property. *The Journal of Chemical Physics*, 153(2).
188. Jing, J., Cao, C., Ma, S., Li, Z., Qu, G., Xie, B., ... & Zhao, Y. (2021). Enhanced defect oxygen of LaFeO₃/GO hybrids in promoting persulfate activation for selective and efficient elimination of bisphenol A in food wastewater. *Chemical Engineering Journal*, 407, 126890.
189. Johar, M. A., Afzal, R. A., Alazba, A. A., & Manzoor, U. (2015). Photocatalysis and bandgap engineering using ZnO nanocomposites. *Advances in Materials Science and Engineering*, 2015(1), 934587.
190. Patil, G. E., Kajale, D. D., Shinde, S. D., Wagh, V. G., Gaikwad, V. B., & Jain, G. H. (2013). Synthesis of Cu-doped SnO₂ thin films by spray pyrolysis for gas sensor application. *Advancement in Sensing Technology: New Developments and Practical Applications*, 299-311.

191. Rehman, S., Ullah, R., Butt, A., & Gohar, N. D. (2009). Strategies of making TiO₂ and ZnO visible light active. *Journal of hazardous materials*, 170(2-3), 560-569.
192. Guo, Y., Qiu, X., Dong, H., & Zhou, X. (2015). Trends in non-metal doping of the SrTiO₃ surface: A hybrid density functional study. *Physical Chemistry Chemical Physics*, 17(33), 21611-21621.
193. Yan, H., Wang, X., Yao, M., & Yao, X. (2013). Band structure design of semiconductors for enhanced photocatalytic activity: The case of TiO₂. *Progress in Natural Science: Materials International*, 23(4), 402-407.
194. Yu, J., Yang, Y., Fan, R., Li, L., & Li, X. (2014). Rapid Electron Injection in Nitrogen-and Fluorine-Doped Flower-Like Anatase TiO₂ with {001} Dominated Facets and Dye-Sensitized Solar Cells with a 52% Increase in Photocurrent. *The Journal of Physical Chemistry C*, 118(17), 8795-8802.
195. Bhosale, R., Pujari, S., Muley, G., Pagare, B., & Gambhire, A. (2013). Visible-light-activated nanocomposite photocatalyst of Cr₂O₃/SnO₂. *Journal of Nanostructure in Chemistry*, 3, 1-7.
196. Ramasamy, E., & Lee, J. (2010). Ordered mesoporous SnO₂- based photoanodes for high-performance dye-sensitized solar cells. *The Journal of Physical Chemistry C*, 114(50), 22032-22037.
197. Borse, P. H., Kim, J. Y., Lee, J. S., Lim, K. T., Jeong, E. D., Bae, J. S., ... & Kim, H. G. (2012). Ti-dopant-enhanced photocatalytic activity of a CaFe₂O₄/MgFe₂O₄ bulk heterojunction under visible-light irradiation. *Journal of the Korean Physical Society*, 61, 73-79.
198. Wang, F., Di Valentin, C., & Pacchioni, G. (2012). Doping of WO₃ for photocatalytic water splitting: hints from density functional theory. *The Journal of Physical Chemistry C*, 116(16), 8901-8909.
199. Long, R., Dai, Y., Meng, G., & Huang, B. (2009). Energetic and electronic properties of X-(Si, Ge, Sn, Pb) doped TiO₂ from first-principles. *Physical Chemistry Chemical Physics*, 11(37), 8165-8172.
200. Yaghoubi, H., Li, Z., Chen, Y., Ngo, H. T., Bhethanabotla, V. R., Joseph, B., ... & Takshi, A. (2015). Toward a visible light-driven photocatalyst: the effect of midgap-states-induced energy gap of undoped TiO₂ nanoparticles. *Acs Catalysis*, 5(1), 327-335.

201. Kolahalam, L. A., Viswanath, I. K., Diwakar, B. S., Govindh, B., Reddy, V., & Murthy, Y. L. N. (2019). Review on nanomaterials: Synthesis and applications. *Materials Today: Proceedings*, 18, 2182-2190.
202. Bokov, D., Turki Jalil, A., Chupradit, S., Suksatan, W., Javed Ansari, M., Shewael, I. H., ... & Kianfar, E. (2021). Nanomaterial by sol-gel method: synthesis and application. *Advances in materials science and engineering*, 2021(1), 5102014.
203. Medina-Ramírez, I., Hernández-Ramírez, A., & Maya-Trevino, M. L. (2015). Synthesis methods for photocatalytic materials. *Photocatalytic Semiconductors: Synthesis, Characterization, and Environmental Applications*, 69-102.
204. Jing, L., Zhou, W., Tian, G., & Fu, H. (2013). Surface tuning for oxide-based nanomaterials as efficient photocatalysts. *Chemical Society Reviews*, 42(24), 9509-9549.
205. Liu, Z., Li, Z., Zhong, H., Zeng, G., Liang, Y., Chen, M., ... & Shao, B. (2017). Recent advances in the environmental applications of biosurfactant saponins: a review. *Journal of environmental chemical engineering*, 5(6), 6030-6038.
206. Akerdi, A. G., Es'haghzade, Z., Bahrami, S. H., & Arami, M. (2017). Comparative Study of GO and Reduced GO Coated Graphite Electrodes for Decolorization of Acidic and Basic Dyes from Aqueous Solutions through Heterogeneous.
207. Byrne, C., Subramanian, G., & Pillai, S. C. (2018). Recent advances in photocatalysis for environmental applications. *Journal of environmental chemical engineering*, 6(3), 3531-3555.
208. Huang, X., Guo, Q., Yan, B., Liu, H., Chen, K., Wei, S., ... & Wang, L. (2021). Study on photocatalytic degradation of phenol by BiOI/Bi₂WO₆ layered heterojunction synthesized by hydrothermal method. *Journal of Molecular Liquids*, 322, 114965.
209. Zhang, Y., Selvaraj, R., Sillanpää, M., Kim, Y., & Tai, C. W. (2014). The influence of operating parameters on heterogeneous photocatalytic mineralization of phenol over BiPO₄. *Chemical Engineering Journal*, 245, 117-123.
210. Herrmann, E., Hernández-Lloreda, M. V., Call, J., Hare, B., & Tomasello, M. (2010). The structure of individual differences in the cognitive abilities of children and chimpanzees. *Psychological Science*, 21(1), 102-110.
211. Silva, C. G., Sampaio, M. J., Carabineiro, S. A., Oliveira, J. W., Baptista, D. L., Bacsá, R., ... & Faria, J. L. (2014). Developing highly active photocatalysts: gold-loaded ZnO for solar phenol oxidation. *Journal of catalysis*, 316, 182-190.

212. Al-Sabahi, J., Bora, T., Al-Abri, M., & Dutta, J. (2016). Controlled defects of zinc oxide nanorods for efficient visible light photocatalytic degradation of phenol. *Materials*, 9(4), 238.
213. Sima, J., & Hasal, P. (2013). Photocatalytic degradation of textile dyes in a TiO₂/UV system. *Chemical Engineering Transactions*, 32, 79-84.
214. Hickman, R., Walker, E., & Chowdhury, S. (2018). TiO₂-PDMS composite sponge for adsorption and solar mediated photodegradation of dye pollutants. *Journal of water process engineering*, 24, 74-82.
215. Khataee, A. R., & Kasiri, M. B. (2010). Photocatalytic degradation of organic dyes in the presence of nanostructured titanium dioxide: Influence of the chemical structure of dyes. *Journal of Molecular Catalysis A: Chemical*, 328(1-2), 8-26.
216. Touati, A., Hammedi, T., Najjar, W., Ksibi, Z., & Sayadi, S. (2016). Photocatalytic degradation of textile wastewater in presence of hydrogen peroxide: Effect of cerium doping titania. *Journal of Industrial and Engineering Chemistry*, 35, 36-44.
217. Jorfi, S., Mirali, S., Mostoufi, A., & Ahmadi, M. (2018). Visible light photocatalytic degradation of azo dye and a real textile wastewater using Mn, Mo, La/TiO₂/AC nanocomposite. *Chemical and biochemical engineering quarterly*, 32(2), 215-227.
218. Amornpitoksuk, P., & Suwanboon, S. (2016). Photocatalytic degradation of dyes by AgBr/Ag₃PO₄ and the ecotoxicities of their degraded products. *Chinese Journal of Catalysis*, 37(5), 711-719.
219. Vaya, D., & Surolia, P. K. (2020). Semiconductor based photocatalytic degradation of pesticides: An overview. *Environmental technology & innovation*, 20, 101128.
220. Truc, N. T. T., Duc, D. S., Van Thuan, D., Al Tahtamouni, T., Pham, T. D., Hanh, N. T., ... & Le Chi, N. T. P. (2019). The advanced photocatalytic degradation of atrazine by direct Z-scheme Cu doped ZnO/g-C₃N₄. *Applied Surface Science*, 489, 875-882.
221. Ahamad, T., & Alshehri, S. M. (2022). Fabrication of Ag@ SrTiO₃/g-C₃N₄ heterojunctions for H₂ production and the degradation of pesticides under visible light. *Separation and Purification Technology*, 297, 121431.
222. Sheikhpour, H., Saljooqi, A., Shamspur, T., & Mostafavi, A. (2021). Co-Al Layered double hydroxides decorated with CoFe₂O₄ nanoparticles and g-C₃N₄

- nanosheets for efficient photocatalytic pesticide degradation. *Environmental Technology & Innovation*, 23, 101649.
223. Yadav, S., Kumar, N., Kumari, V., Mittal, A., & Sharma, S. (2019). Photocatalytic degradation of Triclopyr, a persistent pesticide by ZnO/SnO₂ nanocomposites. *Materials Today: Proceedings*, 19, 642-645.
 224. Teixeira, S., Gurke, R., Eckert, H., Kühn, K., Fauler, J., & Cuniberti, G. (2016). Photocatalytic degradation of pharmaceuticals present in conventional treated wastewater by nanoparticle suspensions. *Journal of Environmental Chemical Engineering*, 4(1), 287-292.
 225. Deng, F., Zhao, L., Luo, X., Luo, S., & Dionysiou, D. D. (2018). Highly efficient visible-light photocatalytic performance of Ag/AgIn₅S₈ for degradation of tetracycline hydrochloride and treatment of real pharmaceutical industry wastewater. *Chemical engineering journal*, 333, 423-433.
 226. Talwar, S., Sangal, V. K., & Verma, A. (2018). Feasibility of using combined TiO₂ photocatalysis and RBC process for the treatment of real pharmaceutical wastewater. *Journal of Photochemistry and Photobiology A: Chemistry*, 353, 263-270.
 227. Lofrano, G., Libralato, G., Casaburi, A., Siciliano, A., Iannece, P., Guida, M., ... & Carotenuto, M. (2018). Municipal wastewater spiramycin removal by conventional treatments and heterogeneous photocatalysis. *Science of the total environment*, 624, 461-469.
 228. Wajahat, R., Yasar, A., Khan, A. M., Tabinda, A. B., & Bhatti, S. G. (2019). Ozonation and photo-driven oxidation of ciprofloxacin in pharmaceutical wastewater: degradation kinetics and energy requirements. *Pol. J. Environ. Stud*, 28(3), 1933.
 229. Lofrano, G., Libralato, G., Casaburi, A., Siciliano, A., Iannece, P., Guida, M., ... & Carotenuto, M. (2018). Municipal wastewater spiramycin removal by conventional treatments and heterogeneous photocatalysis. *Science of the total environment*, 624, 461-469.
 230. Emam, E. A., & Aboul-Gheit, N. A. K. (2014). Photocatalytic degradation of oil-emulsion in water/seawater using titanium dioxide. *Energy Sources, Part A: Recovery, Utilization, and Environmental Effects*, 36(10), 1123-1133.
 231. Kaneco, S., Katsumata, H., Suzuki, T., & Ohta, K. (2006). Titanium dioxide mediated photocatalytic degradation of dibutyl phthalate in aqueous solution—kinetics, mineralization and reaction mechanism. *Chemical Engineering Journal*, 125(1), 59-66.

232. Hsu, Y. Y., Hsiung, T. L., Wang, H. P., Fukushima, Y., Wei, Y. L., & Chang, J. E. (2008). Photocatalytic degradation of spill oils on TiO₂ nanotube thin films. *Marine pollution bulletin*, 57(6-12), 873-876.
233. Shivaraju, H. P., Muzakkira, N., & Shahmoradi, B. (2016). Photocatalytic treatment of oil and grease spills in wastewater using coated N-doped TiO₂ polyscales under sunlight as an alternative driving energy. *International journal of environmental science and technology*, 13, 2293-2302.
234. Nasrollahzadeh, M., Sajjadi, M., Iravani, S., & Varma, R. S. (2021). Starch, cellulose, pectin, gum, alginate, chitin, and chitosan-derived (nano) materials for sustainable water treatment: A review. *Carbohydrate polymers*, 251, 116986.
235. Schwarzenbach, R. P., Escher, B. I., Fenner, K., Hofstetter, T. B., Johnson, C. A., Von Gunten, U., & Wehrli, B. (2006). The challenge of micropollutants in aquatic systems. *Science*, 313(5790), 1072-1077.
236. Huang, Y., Li, J., Chen, X., & Wang, X. (2014). Applications of conjugated polymer-based composites in wastewater purification. *Rsc Advances*, 4(107), 62160-62178.
237. Al Sharabati, M., & Sabouni, R. (2020). Selective removal of dual dyes from aqueous solutions using a metal organic framework (MIL-53 (Al)). *Polyhedron*, 190, 114762.
238. Abhinaya, M., Parthiban, R., Kumar, P. S., & Vo, D. V. N. (2021). A review on cleaner strategies for the extraction of chitosan and its application in toxic pollutant removal. *Environmental Research*, 196, 110996.
239. Van Der Meer, T. P., Chung, M. K., Van Faassen, M., Makris, K. C., Van Beek, A. P., Kema, I. P., ... & Patel, C. J. (2021). Temporal exposure and consistency of endocrine-disrupting chemicals in a longitudinal study of individuals with impaired fasting glucose. *Environmental research*, 197, 110901.
240. Al Sharabati, M., Abokwiek, R., Al-Othman, A., Tawalbeh, M., Karaman, C., Orooji, Y., & Karimi, F. (2021). Biodegradable polymers and their nano-composites for the removal of endocrine-disrupting chemicals (EDCs) from wastewater: A review. *Environmental Research*, 202, 111694.
241. Repousi, V., Petala, A., Frontistis, Z., Antonopoulou, M., Konstantinou, I., Kondarides, D. I., & Mantzavinos, D. (2017). Photocatalytic degradation of bisphenol A over Rh/TiO₂ suspensions in different water matrices. *Catalysis Today*, 284, 59-66.

242. Naraginti, S., Li, Y., Wu, Y., Zhang, C., & Upreti, A. R. (2016). Mechanistic study of visible light driven photocatalytic degradation of EDC 17 α -ethinyl estradiol and azo dye Acid Black-52: phytotoxicity assessment of intermediates. *RSC advances*, 6(90), 87246-87257.
243. Tang, Y., Yin, X., Mu, M., Jiang, Y., Li, X., Zhang, H., & Ouyang, T. (2020). Anatase TiO₂@ MIL-101 (Cr) nanocomposite for photocatalytic degradation of bisphenol A. *Colloids and Surfaces A: Physicochemical and Engineering Aspects*, 596, 124745.
244. Denicourt-Nowicki, A., Péliesson, C. H., Soutrel, I., Favier, L., & Roucoux, A. (2021). Remediation of diethyl phthalate in aqueous effluents with tio₂-supported rh₀ nanoparticles as multicatalytic materials. *Catalysts*, 11(10), 1166.
245. Li, J., Wang, R., Cox, P., Gao, Y., Walter, F., Wagg, J., ... & Narayanan, D. (2020). Ionized and atomic interstellar medium in the z= 6.003 quasar SDSS J2310+1855. *The Astrophysical Journal*, 900(2), 131.
246. Alikarami, M., Soltani, R. D. C., & Khataee, A. (2019). An innovative combination of electrochemical and photocatalytic processes for decontamination of bisphenol A endocrine disruptor from aquatic phase: Insight into mechanism, enhancers and bio-toxicity assay. *Separation and Purification Technology*, 220, 42-51.
247. Ponnaiah, S. K., Prakash, P., Arumuganathan, T., & Jeyaprabha, B. (2019). Effectual light-harvesting and electron-hole separation for enhanced photocatalytic decontamination of endocrine disruptor using Cu₂O/BiOI nanocomposite. *Journal of Photochemistry and Photobiology A: Chemistry*, 380, 111860.
248. Wang, G., Dai, J., Luo, Q., & Deng, N. (2021). Photocatalytic degradation of bisphenol A by TiO₂@ aspartic acid- β -cyclodextrin@ reduced graphene oxide. *Separation and Purification Technology*, 254, 117574.
249. Perumal, K., Shanavas, S., Ahamad, T., Karthigeyan, A., & Murugakoothan, P. (2023). Construction of Ag₂CO₃/BiOBr/CdS ternary composite photocatalyst with improved visible-light photocatalytic activity on tetracycline molecule degradation. *Journal of Environmental Sciences*, 125, 47-60.
250. Khammar, S., Bahramifar, N., & Younesi, H. (2020). Preparation and surface engineering of CM- β -CD functionalized Fe₃O₄@ TiO₂ nanoparticles for photocatalytic degradation of polychlorinated biphenyls (PCBs) from transformer oil. *Journal of hazardous materials*, 394, 122422.

251. Liu, Y., Sun, N., Hu, J., Li, S., & Qin, G. (2018). Photocatalytic degradation properties of α -Fe₂O₃ nanoparticles for dibutyl phthalate in aqueous solution system. *Royal Society open science*, 5(4), 172196.
252. Zulfiqar, M., Samsudin, M. F. R., & Sufian, S. (2019). Modelling and optimization of photocatalytic degradation of phenol via TiO₂ nanoparticles: An insight into response surface methodology and artificial neural network. *Journal of Photochemistry and Photobiology A: Chemistry*, 384, 112039.
253. Amiri, F., Dehghani, M., Amiri, Z., Yousefinejad, S., & Azhdarpoor, A. (2021). Photocatalytic degradation of 2, 4-dichlorophenoxyacetic acid from aqueous solutions by Ag₃PO₄/TiO₂ nanoparticles under visible light: kinetic and thermodynamic studies. *Water Science and Technology*, 83(12), 3110-3122.
254. Wang, H., Zhou, Y., Wang, J., Li, A., & Corvini, P. F. X. (2022). BiOBr/Bi₄O₅Br₂/PDI constructed for visible-light degradation of endocrine disrupting chemicals: synergistic effects of bi-heterojunction and oxygen evolution. *Chemical Engineering Journal*, 433, 133622.
255. Görmez, Ö., Yakar, E., Gözmen, B., Kayan, B., & Khataee, A. (2022). CoFe₂O₄ nanoparticles decorated onto graphene oxide and graphitic carbon nitride layers as a separable catalyst for ultrasound-assisted photocatalytic degradation of Bisphenol-A. *Chemosphere*, 288, 132663.
256. Ahmadpour, N., Sayadi, M. H., Sobhani, S., & Hajiani, M. (2020). Photocatalytic degradation of model pharmaceutical pollutant by novel magnetic TiO₂@ ZnFe₂O₄/Pd nanocomposite with enhanced photocatalytic activity and stability under solar light irradiation. *Journal of environmental management*, 271, 110964.
257. Al-Hajji, L. A., Ismail, A. A., Alseidi, M., Almutawa, F., Ahmad, S., & Bumajdad, A. (2020). Green approach and ease synthesis of C/N-codoped TiO₂ nanocrystals for photodegradation of endocrine. *Journal of Nanoparticle Research*, 22, 1-14.
258. Ahmed, A., Usman, M., Yu, B., Gao, F., Shen, Y., & Cong, H. (2021). Heterogeneous activation of peroxymonosulfate using superparamagnetic β -CD-CoFe₂O₄ catalyst for the removal of endocrine-disrupting bisphenol A: performance and degradation mechanism. *Separation and Purification Technology*, 279, 119752.

259. Yasir, M., Masar, M., Sopik, T., Ali, H., Urbanek, M., Antos, J., ... & Kuritka, I. (2022). ZnO nanowires and nanorods based ZnO/WO₃/Pt heterojunction for efficient photocatalytic degradation of estriol (E3) hormone. *Materials Letters*, 319, 132291.
260. Choudhary, S., Rani, M., & Shanker, U. (2022). Green biosynthesized N-doped Bi₂O₃@ SnO₂ nanocomposite for efficient remediation of endocrine disrupting pesticides. *Environmental Nanotechnology, Monitoring & Management*, 18, 100746.
261. Zhang, Y., Yu, H., Li, S., Wang, L., Huang, F., Guan, R., ... & Sun, J. (2021). Rapidly degradation of di-(2-ethylhexyl) phthalate by Z-scheme Bi₂O₃/TiO₂@ reduced graphene oxide driven by simulated solar radiation. *Chemosphere*, 272, 129631.
262. Pi, X., Zhang, S., Wang, L., Li, H., Hei, Y., Zheng, Z., ... & Luo, L. (2021). BiVO₄ photo-catalyst with controllable wettability and its improved visible light catalytic activity for degradation of 17 α -Ethinylestradiol. *Journal of the Taiwan Institute of Chemical Engineers*, 127, 140-150.
263. Ali, H., Yasir, M., Masar, M., Suly, P., Sopik, T., Zubair, M., ... & Kuritka, I. (2024). Titanium dioxide and halloysite loaded polylactic acid-based membrane continuous flow photoreactor for 17 α -ethinylestradiol (EE2) hormone degradation: Optimization, kinetics, mechanism, and reusability study. *Catalysis Today*, 432, 114602.
264. Orona-Návar, C., Park, Y., Srivastava, V., Hernández, N., Mahlkecht, J., Sillanpää, M., & Ornelas-Soto, N. (2021). Gd³⁺ doped BiVO₄ and visible light-emitting diodes (LED) for photocatalytic decomposition of bisphenol A, bisphenol S and bisphenol AF in water. *Journal of Environmental Chemical Engineering*, 9(5), 105842.
265. Hossain, N., Mobarak, M. H., Mimona, M. A., Islam, M. A., Hossain, A., Zohura, F. T., & Chowdhury, M. A. (2023). Advances and significances of nanoparticles in semiconductor applications—A review. *Results in Engineering*, 19, 101347.
266. Venkatesh, R., Selvakumar, S., Dhasneem, S., & Kannan, L. V. (2024). Semiconductor Devices: An Overview. *Futuristic Trends in Electrical Engineering Volume 3 Book, 1*, 11-37.
267. Agladze, G. R., Tsursumia, G. S., Jung, B. I., Kim, J. S., & Gorelishvili, G. (2007). Comparative study of hydrogen peroxide electro-generation on gas-diffusion

- electrodes in undivided and membrane cells. *Journal of Applied Electrochemistry*, 37, 375-383.
268. An, T., Yang, H., Li, G., Song, W., Cooper, W. J., & Nie, X. (2010). Kinetics and mechanism of advanced oxidation processes (AOPs) in degradation of ciprofloxacin in water. *Applied Catalysis B: Environmental*, 94(3-4), 288-294.
 269. Barros, W. R., Borges, M. P., Reis, R. M., Rocha, R. S., Bertazzoli, R., & Lanza, M. R. (2014). Degradation of dipyrone by the electro-Fenton process in an electrochemical flow reactor with a modified gas diffusion electrode. *Journal of the Brazilian Chemical Society*, 25, 1673-1680.
 270. Nosuhi, M., & Nezamzadeh-Ejhi, A. (2017). Comprehensive study on the electrocatalytic effect of copper-doped nano-clinoptilolite towards amoxicillin at the modified carbon paste electrode-solution interface. *Journal of colloid and interface science*, 497, 66-72.
 271. Fazaeli, R., Aliyan, H., Nezamzadeh-Ejhi, A., & Richeson, D. (2024). Investigation of the synergistic photocatalytic activity of a ternary ZrTiO₄/TiO₂/Mn₃O₄ (ZTM) nanocomposite in a typical water treatment process. *Surfaces and Interfaces*, 52, 104877.
 272. Brillas, E., Bastida, R. M., Llosa, E., & Casado, J. (1995). Electrochemical destruction of aniline and 4-chloroaniline for wastewater treatment using a carbon-PTFE O₂-fed cathode. *Journal of the Electrochemical Society*, 142(6), 1733.
 273. Martínez-Huitle, C. A., & Brillas, E. (2009). Decontamination of wastewaters containing synthetic organic dyes by electrochemical methods: a general review. *Applied Catalysis B: Environmental*, 87(3-4), 105-145.
 274. Pérez, T., Sirés, I., Brillas, E., & Nava, J. L. (2017). Solar photoelectro-Fenton flow plant modeling for the degradation of the antibiotic erythromycin in sulfate medium. *Electrochimica Acta*, 228, 45-56.
 275. Cotillas, S., Lacasa, E., Herraiz, M., Sáez, C., Cañizares, P., & Rodrigo, M. A. (2019). The role of the anode material in selective penicillin G oxidation in urine. *ChemElectroChem*, 6(5), 1376-1384.
 276. Cotillas, S., Lacasa, E., Sáez, C., Cañizares, P., & Rodrigo, M. A. (2018). Removal of pharmaceuticals from the urine of polymedicated patients: A first approach. *Chemical Engineering Journal*, 331, 606-614.
 277. Shanmugaraj, K., Campos, C. H., Mangalaraja, R. V., Nandhini, K., Aepuru, R., Torres, C. C., ... & Vo, D. V. N. (2023). Gold nanoparticle-decorated earth-

abundant clay nanotubes as catalyst for the degradation of phenothiazine dyes and reduction of 4-(4-nitrophenyl) morpholine. *Environmental Science and Pollution Research*, 30(60), 124447-124458

278. Chankhanittha, T., & Nanan, S. (2021). Visible-light-driven photocatalytic degradation of ofloxacin (OFL) antibiotic and Rhodamine B (RhB) dye by solvothermally grown ZnO/Bi₂MoO₆ heterojunction. *Journal of Colloid and Interface Science*, 582, 412-427.
279. Cheng, J., Shen, Y., Chen, K., Wang, X., Guo, Y., Zhou, X., & Bai, R. (2018). Flower-like Bi₂WO₆/ZnO composite with excellent photocatalytic capability under visible light irradiation. *Chinese Journal of Catalysis*, 39(4), 810-820.
280. Huang, D., Li, J., Zeng, G., Xue, W., Chen, S., Li, Z., ... & Cheng, M. (2019). Facile construction of hierarchical flower-like Z-scheme AgBr/Bi₂WO₆ photocatalysts for effective removal of tetracycline: Degradation pathways and mechanism. *Chemical Engineering Journal*, 375, 121991.
281. Derikvandi, H., & Nezamzadeh-Ejhieh, A. (2017). Increased photocatalytic activity of NiO and ZnO in photodegradation of a model drug aqueous solution: effect of coupling, supporting, particles size and calcination temperature. *Journal of hazardous materials*, 321, 629-638.
282. Yousefi, A., & Nezamzadeh-Ejhieh, A. (2021). Preparation and characterization of SnO₂-BiVO₄-CuO catalyst and kinetics of phenazopyridine photodegradation. *Iran. J. Catal.*, 11(3), 247-259.
283. Rezaei, M., Nezamzadeh-Ejhieh, A., & Massah, A. R. (2024). A Comprehensive Review on the Boosted Effects of Anion Vacancy in the Heterogeneous Photocatalytic Degradation, Part II: Focus on Oxygen Vacancy. *ACS omega*, 9(6), 6093-6127.
284. Rezaei, M., Nezamzadeh-Ejhieh, A., & Massah, A. R. (2024). A comprehensive review on the boosted effects of anion vacancy in the heterogeneous photocatalytic degradation, part I: Focus on sulfur, nitrogen, carbon, and halogen vacancies. *Ecotoxicology and Environmental Safety*, 269, 115927.
285. Rezaei, M., Nezamzadeh-Ejhieh, A., & Massah, A. R. (2024). A Comprehensive Review on the Boosted Effects of Anion Vacancy in the Photocatalytic Solar Water Splitting: Focus on Sulfur Vacancy. *Energy & Fuels*, 38(9), 7637-7664.

286. Mirsalari, S. A., & Nezamzadeh-Ejhieh, A. (2021). CdS–Ag₃PO₄ nano-catalyst: A brief characterization and kinetic study towards methylene blue photodegradation. *Materials Science in Semiconductor Processing*, 122, 105455.
287. Chankhanittha, T., Yenjai, C., & Nanan, S. (2022). Utilization of formononetin and pinocembrin from the stem extract of *Dalbergia parviflora* as capping agents for the preparation of ZnO photocatalysts for degradation of RR141 azo dye and ofloxacin antibiotic. *Catalysis Today*, 384, 279-293.
288. Kaur, A., Gupta, G., Ibhaddon, A. O., Salunke, D. B., Sinha, A. S. K., & Kansal, S. K. (2018). A Facile synthesis of silver modified ZnO nanoplates for efficient removal of ofloxacin drug in aqueous phase under solar irradiation. *Journal of Environmental Chemical Engineering*, 6(3), 3621-3630.
289. Patidar, R., & Srivastava, V. C. (2021). Mechanistic and kinetic insights of synergistic mineralization of ofloxacin using a sono-photo hybrid process. *Chemical Engineering Journal*, 403, 125736.
290. Senasu, T., & Nanan, S. (2017). Photocatalytic performance of CdS nanomaterials for photodegradation of organic azo dyes under artificial visible light and natural solar light irradiation. *Journal of Materials Science: Materials in Electronics*, 28, 17421-17441.
291. Senasu, T., Hemavibool, K., & Nanan, S. (2018). Hydrothermally grown CdS nanoparticles for photodegradation of anionic azo dyes under UV-visible light irradiation. *RSC advances*, 8(40), 22592-22605.
292. Senasu, T., Chankhanittha, T., Hemavibool, K., & Nanan, S. (2021). Visible-light-responsive photocatalyst based on ZnO/CdS nanocomposite for photodegradation of reactive red azo dye and ofloxacin antibiotic. *Materials Science in Semiconductor Processing*, 123, 105558.
293. Nezamzadeh-Ejhieh, A., & Banan, Z. (2014). Photodegradation of dimethyldisulfide by heterogeneous catalysis using nanoCdS and nanoCdO embedded on the zeolite A synthesized from waste porcelain. *Desalination and Water Treatment*, 52(16-18), 3328-3337.
294. Nezamzadeh-Ejhieh, A., & Banan, Z. (2011). A comparison between the efficiency of CdS nanoparticles/zeolite A and CdO/zeolite A as catalysts in photodecolorization of crystal violet. *Desalination*, 279(1-3), 146-151.

295. Chen, Q., De Marco, N., Yang, Y. M., Song, T. B., Chen, C. C., Zhao, H., ... & Yang, Y. (2015). Under the spotlight: The organic–inorganic hybrid halide perovskite for optoelectronic applications. *Nano Today*, 10(3), 355-396.
296. Ye, T., Pan, L., Yang, Y., Liang, Q., Lu, Y., Sui, M., ... & Wang, X. (2020). Synthesis of highly-oriented black CsPbI₃ microstructures for high-performance solar cells. *Chemistry of Materials*, 32(7), 3235-3244.
297. Tie, S., Zhao, W., Huang, W., Xin, D., Zhang, M., Yang, Z., ... & Zhang, W. H. (2020). Efficient X-ray attenuation lead-free AgBi₂I₇ halide rudorffite alternative for sensitive and stable X-ray detection. *The Journal of Physical Chemistry Letters*, 11(19), 7939-7945.
298. Turkevych, I., Kazaoui, S., Ito, E., Urano, T., Yamada, K., Tomiyasu, H., ... & Aramaki, S. (2017). Photovoltaic rudorffites: lead-free silver bismuth halides alternative to hybrid lead halide perovskites. *ChemSusChem*, 10(19), 3754-3759.
299. Park, B. W., Philippe, B., Zhang, X., Rensmo, H., Boschloo, G., & Johansson, E. M. (2015). Bismuth Based Hybrid Perovskites A₃Bi₂I₉ (A: Methylammonium or Cesium) for Solar Cell Application. *Advanced Materials* (Deerfield Beach, Fla.), 27(43), 6806-6813.
300. Khan, Z. R., Zulfequar, M., & Khan, M. S. (2011). Chemical synthesis of CdS nanoparticles and their optical and dielectric studies. *Journal of materials science*, 46(16), 5412-5416.
301. Ramos Corona, A., Rodríguez López, J., Rangel Segura, R., Martínez Garcia, M. M., Flores, E., Rodríguez Gattorno, G., & Alvarado Gil, J. J. (2024). Microwave-Assisted Synthesis of CdS-MOF MIL-101 (Fe) Composite: Characterization and Photocatalytic Performance. *Inorganic Chemistry*, 63(42), 19536-19552.
302. Ding, Y., Wang, C., Bandaru, S., Pei, L., Zheng, R., Ng, Y. H., ... & Su, B. L. (2024). Cs₃Bi₂Br₉ nanoparticles decorated C₃N₄ nanotubes composite photocatalyst for highly selective oxidation of benzylic alcohol. *Journal of Colloid and Interface Science*.
303. Kumar, S., & Sharma, J. K. (2016). Stable phase CdS nanoparticles for optoelectronics: a study on surface morphology, structural and optical characterization. *Materials Science-Poland*, 34(2), 368-373.
304. Senobari, S., & Nezamzadeh-Ejehieh, A. (2018). A pn junction NiO-CdS nanoparticles with enhanced photocatalytic activity: a response surface methodology study. *Journal of Molecular Liquids*, 257, 173-183.

305. Wang, S., Yu, J., Zhao, P., Guo, S., & Han, S. (2021). One-step synthesis of water-soluble CdS quantum dots for silver-ion detection. *ACS omega*, 6(10), 7139-7146.
306. Tailor, N. K., Maity, P., & Satapathi, S. (2021). Observation of Negative Photoconductivity in Lead-Free Cs₃Bi₂Br₉ Perovskite Single Crystal. *Acs Photonics*, 8(8), 2473-2480.
307. Hemmatpour, P., Nezamzadeh-Ejhieh, A., & Ershadi, A. (2022). A brief study on the Eriochrome Black T photodegradation kinetic by CdS/BiVO₄ coupled catalyst. *Materials Research Bulletin*, 151, 111830.
308. Azimi, S., & Nezamzadeh-Ejhieh, A. (2015). Enhanced activity of clinoptilolite-supported hybridized PbS–CdS semiconductors for the photocatalytic degradation of a mixture of tetracycline and cephalexin aqueous solution. *Journal of Molecular Catalysis A: Chemical*, 408, 152-160.
309. Tamiji, T., & Nezamzadeh-Ejhieh, A. (2019). Study of kinetics aspects of the electrocatalytic oxidation of benzyl alcohol in aqueous solution on AgBr modified carbon paste electrode. *Materials Chemistry and Physics*, 237, 121813.
310. Zhao, Y., Zuo, Y., He, G., Chen, Q., Meng, Q., & Chen, H. (2021). Synthesis of graphene-based CdS@ CuS core-shell nanorods by cation-exchange for efficient degradation of ciprofloxacin. *Journal of Alloys and Compounds*, 869, 159305.
311. Farsi, M., & Nezamzadeh-Ejhieh, A. (2022). A Z-scheme Cobalt (II) oxide-silver tungstate nano photocatalyst: experimental design and mechanism study for the degradation of methylene blue. *Surfaces and Interfaces*, 32, 102148.
312. Omrani, N., & Nezamzadeh-Ejhieh, A. (2020). Focus on scavengers' effects and GC-MASS analysis of photodegradation intermediates of sulfasalazine by Cu₂O/CdS nanocomposite. *Separation and Purification Technology*, 235, 116228.
313. Mehrabanpour, N., Nezamzadeh-Ejhieh, A., Ghattavi, S., & Ershadi, A. (2023). A magnetically separable clinoptilolite supported CdS-PbS photocatalyst: Characterization and photocatalytic activity toward cefotaxime. *Applied Surface Science*, 614, 156252.
314. Ghattavi, S., & Nezamzadeh-Ejhieh, A. (2019). A brief study on the boosted photocatalytic activity of AgI/WO₃/ZnO in the degradation of Methylene Blue under visible light irradiation. *Desalination and Water Treatment*, 166, 92-104.
315. Ghattavi, S., & Nezamzadeh-Ejhieh, A. (2020). A visible light driven AgBr/g-C₃N₄ photocatalyst composite in methyl orange photodegradation: focus on

- photoluminescence, mole ratio, synthesis method of g-C₃N₄ and scavengers. *Composites Part B: Engineering*, 183, 107712.
316. Rani, M., Keshu, & Shanker, U. (2023). Efficient visible light photocatalytic organic colorants elimination performance induced by biosynthesized titanium dioxide coupled cadmium sulfide nanostructures. *International Journal of Environmental Science and Technology*, 20(5), 5491-5508.
 317. Rao, M. D., & Pennathur, G. Green synthesis and characterization of cadmium sulphide nanoparticles from *Chlamydomonas reinhardtii* and their application as photocatalysts. *Materials Research Bulletin*. 85 (2017) 64-73.
 318. Sankhla, A., Sharma, R., Yadav, R. S., Kashyap, D., Kothari, S. L., & Kachhwaha, S. (2016). Biosynthesis and characterization of cadmium sulfide nanoparticles—an emphasis of zeta potential behavior due to capping. *Materials Chemistry and Physics*, 170, 44-51.
 319. Nezamzadeh-Ejhieh, A., & Salimi, Z. (2011). Solar photocatalytic degradation of o-phenylenediamine by heterogeneous CuO/X zeolite catalyst. *Desalination*, 280(1-3), 281-287.
 320. Ejhieh, A. N., & Khorsandi, M. (2010). Photodecolorization of Eriochrome Black T using NiS–P zeolite as a heterogeneous catalyst. *Journal of Hazardous Materials*, 176(1-3), 629-637.
 321. Tabasum, S., Rani, S., Sharma, A., Dhupar, N., Singh, P. P., Bagri, U., & Kumar, D. (2023). Efficient Photocatalytic Degradation of Chlorpyrifos Pesticide from Aquatic Agricultural Waste Using g-C₃N₄ Decorated Graphene Oxide/V₂O₅ Nanocomposite. *Topics in Catalysis*, 1-12.
 322. Sun, X., Liu, G., Li, R., Li, L., Dai, J., & Yang, H. (2024). Experimental and theoretical revealing of piezo-photocatalyst Bi₂O₂CO₃ for degradation of ciprofloxacin in water. *Environmental Science and Pollution Research*, 31(5), 7194-7213.
 323. Gupta, B., Gupta, A. K., Tiwary, C. S., & Ghosal, P. S. (2021). A multivariate modeling and experimental realization of photocatalytic system of engineered S–C₃N₄/ZnO hybrid for ciprofloxacin removal: Influencing factors and degradation pathways. *Environmental research*, 196, 110390.

324. Amiri, M., & Nezamzadeh-Ejhieh, A. (2015). Improvement of the photocatalytic activity of cupric oxide by deposition onto a natural clinoptilolite substrate. *Materials Science in Semiconductor Processing*, 31, 501-508.
325. Sharma, A., & Lee, B. K. (2016). Rapid photo-degradation of 2-chlorophenol under visible light irradiation using cobalt oxide-loaded TiO₂/reduced graphene oxide nanocomposite from aqueous media. *Journal of environmental management*, 165, 1-10.
326. Arabpour, N., & Nezamzadeh-Ejhieh, A. (2016). Photodegradation of cotrimaxazole by clinoptilolite-supported nickel oxide. *Process Safety and Environmental Protection*, 102, 431-440.
327. Khodami, Z., & Nezamzadeh-Ejhieh, A. (2015). Investigation of photocatalytic effect of ZnO–SnO₂/nano clinoptilolite system in the photodegradation of aqueous mixture of 4-methylbenzoic acid/2-chloro-5-nitrobenzoic acid. *Journal of Molecular Catalysis A: Chemical*, 409, 59-68.
328. Meky, A. I., Hassaan, M. A., El-Nemr, M. A., Fetouh, H. A., Ismail, A. M., & El Nemr, A. (2025). Kinetics, central composite design and artificial neural network modelling of ciprofloxacin antibiotic photodegradation using fabricated cobalt-doped zinc oxide nanoparticles. *Scientific Reports*, 15(1), 1610.
329. Nezamzadeh-Ejhieh, A., & Banan, Z. (2012). Kinetic investigation of photocatalytic degradation of dimethyldisulfide by zeolite A containing nano CdS. *Iranian Journal of Catalysis*, 2(2).
330. Salesi, S., & Nezamzadeh-Ejhieh, A. (2022). Boosted photocatalytic effect of binary AgI/Ag₂WO₄ nanocatalyst: characterization and kinetics study towards ceftriaxone photodegradation. *Environmental Science and Pollution Research*, 29(60), 90191-90206.
331. Narenuch, T., Senasu, T., Chankhanittha, T., & Nanan, S. (2021). Solvothermal synthesis of CTAB capped and SDS capped BiOCl photocatalysts for degradation of rhodamine B (RhB) dye and fluoroquinolone antibiotics. *Journal of Solid State Chemistry*, 294, 121824.
332. Mohapatra, L., & Parida, K. M. (2012). Zn–Cr layered double hydroxide: visible light responsive photocatalyst for photocatalytic degradation of organic pollutants. *Separation and purification technology*, 91, 73-80.
333. Mohapatra, L., & Parida, K. M. Zn–Cr layered double hydroxide: visible light responsive photocatalyst for photocatalytic degradation of organic pollutants. *Separation and purification technology*. 91 (2012) 73-80.

334. Wen, X. J., Niu, C. G., Zhang, L., Liang, C., Guo, H., & Zeng, G. M. (2018). Photocatalytic degradation of ciprofloxacin by a novel Z-scheme CeO₂-Ag/AgBr photocatalyst: influencing factors, possible degradation pathways, and mechanism insight. *Journal of catalysis*, 358, 141-154.
335. El-Kemary, M., El-Shamy, H., & El-Mehasseb, I. (2010). Photocatalytic degradation of ciprofloxacin drug in water using ZnO nanoparticles. *Journal of Luminescence*, 130(12), 2327-2331.
336. Sarkhosh, M., Sadani, M., Abtahi, M., Mohseni, S. M., Sheikhmohammadi, A., Azarpira, H., ... & Bay, A. (2019). Enhancing photo-degradation of ciprofloxacin using simultaneous usage of eaq⁻ and OH over UV/ZnO/I-process: Efficiency, kinetics, pathways, and mechanisms. *Journal of hazardous materials*, 377, 418-426.
337. Aghdasi, S., & Shokri, M. (2016). Photocatalytic degradation of ciprofloxacin in the presence of synthesized ZnO nanocatalyst: The effect of operational parameters. *Iranian Journal of Catalysis*, 6(5), 481-487.
338. Kumar, A., Kumar, A., Sharma, G., Ala'a, H., Naushad, M., Ghfar, A. A., ... & Stadler, F. J. (2018). Biochar-templated g-C₃N₄/Bi₂O₂CO₃/CoFe₂O₄ nano-assembly for visible and solar assisted photo-degradation of paraquat, nitrophenol reduction and CO₂ conversion. *Chemical Engineering Journal*, 339, 393-410.
339. Gaurav Sharma, G. S., Anuj Kumar, A. K., Mu Naushad, M. N., Amit Kumar, A. K., Al-Muhtaseb, A. H., Pooja Dhiman, P. D., ... & Khan, M. R. (2018). Photoremediation of toxic dye from aqueous environment using monometallic and bimetallic quantum dots-based nanocomposites.
340. Diao, Z. H., Lin, Z. Y., Chen, X. Z., Yan, L., Dong, F. X., Qian, W., ... & Chu, W. (2020). Ultrasound-assisted heterogeneous activation of peroxymonosulphate by natural pyrite for 2, 4-dichlorophenol degradation in water: Synergistic effects, pathway and mechanism. *Chemical Engineering Journal*, 389, 123771.
341. Olaniran, A. O., & Igbinsola, E. O. (2011). Chlorophenols and other related derivatives of environmental concern: properties, distribution, and microbial degradation processes. *Chemosphere*, 83(10), 1297-1306.
342. Alkaram, U. F., Mukhlis, A. A., & Al-Dujaili, A. H. (2009). The removal of phenol from aqueous solutions by adsorption using surfactant-modified bentonite and kaolinite. *Journal of Hazardous Materials*, 169(1-3), 324-332.

343. Yin, L., Dai, Y., Niu, J., Bao, Y., & Shen, Z. (2012). Rapid dechlorination of chlorophenols in aqueous solution by [Ni| Cu] microcell. *Journal of hazardous materials*, 209, 414-420.
344. Della-Flora, A., Wilde, M. L., Thue, P. S., Lima, D., Lima, E. C., & Sirtori, C. (2020). Combination of solar photo-Fenton and adsorption process for removal of the anticancer drug Flutamide and its transformation products from hospital wastewater. *Journal of hazardous materials*, 396, 122699.
345. Dong, W., Jin, Y., Zhou, K., Sun, S. P., Li, Y., & Chen, X. D. (2019). Efficient degradation of pharmaceutical micropollutants in water and wastewater by FeIII-NTA-catalyzed neutral photo-Fenton process. *Science of the Total Environment*, 688, 513-520.
346. Han, X., Liu, S., Huo, X., Cheng, F., Zhang, M., & Guo, M. (2020). Facile and large-scale fabrication of (Mg, Ni)(Fe, Al) $2O_4$ heterogeneous photo-Fenton-like catalyst from saprolite laterite ore for effective removal of organic contaminants. *Journal of hazardous materials*, 392, 122295.
347. Al Kausor, M., & Chakraborty, D. (2021). Graphene oxide-based semiconductor photocatalysts for degradation of organic dye in waste water: A review on fabrication, performance enhancement, and challenges. *Inorganic Chemistry Communications*, 129, 108630.
348. Liou, M. J., Lu, M. C., & Chen, J. N. (2004). Oxidation of TNT by the photo-Fenton process. *Chemosphere*, 57(9), 1107-1114.
349. Li, Y., Cai, C., Sun, B., & Chen, J. (2017). Novel electronic properties of 2D MoS_2/TiO_2 van der Waals heterostructure. *Semiconductor Science and Technology*, 32(10), 105011.
350. Xu, X., Liu, W., Kim, Y., & Cho, J. (2014). Nanostructured transition metal sulfides for lithium-ion batteries: progress and challenges. *Nano Today*, 9(5), 604-630.
351. Gupta, V. K., Pathania, D., Asif, M., & Sharma, G. (2014). Liquid phase synthesis of pectin-cadmium sulfide nanocomposite and its photocatalytic and antibacterial activity. *Journal of Molecular Liquids*, 196, 107-112.
352. Ayodhya, D., & Veerabhadram, G. (2018). Highly efficient sunlight-driven photocatalytic degradation of organic pollutants and fluorescence detection of Hg^{2+} using multifunctional GO- Bi_2S_3 nanostructures. *Journal of Photochemistry and Photobiology A: Chemistry*, 356, 545-555.

353. Seo, B., & Joo, S. H. (2017). Recent advances in unveiling active sites in molybdenum sulfide-based electrocatalysts for the hydrogen evolution reaction. *Nano Convergence*, 4, 1-11.
354. Sharma, G., Gupta, V. K., Agarwal, S., Bhogal, S., Naushad, M., Kumar, A., & Stadler, F. J. (2018). Fabrication and characterization of trimetallic nano-photocatalyst for the remediation of ampicillin antibiotic. *Journal of molecular liquids*, 260, 342-350.
355. Shahi, S. K., Kaur, N., Sandhu, S., Shahi, J. S., & Singh, V. (2017). Influences of a new templating agent on the synthesis of coral-like TiO₂ nanoparticles and their photocatalytic activity. *Journal of Science: Advanced Materials and Devices*, 2(3), 347-353.
356. Chandrasekar, L. B., Chandramohan, R., Vijayalakshmi, R., & Chandrasekaran, S. (2015). Preparation and characterization of Mn-doped ZnS nanoparticles. *International Nano Letters*, 5, 71-75.
357. Ayodhya, D., & Veerabhadram, G. (2016). Green synthesis, characterization, photocatalytic, fluorescence and antimicrobial activities of *Cochlospermum gossypium* capped Ag₂S nanoparticles. *Journal of Photochemistry and Photobiology B: Biology*, 157, 57-69.
358. Zhang, Z., Ji, R., Sun, Q., He, J., Chen, D., Li, N., ... & Lu, J. (2023). *Applied Catalysis B: Environmental*, 324, 122276.
359. Lai, C., Zhang, M., Li, B., Huang, D., Zeng, G., Qin, L., ... & Chen, L. (2019). Fabrication of CuS/BiVO₄ (0 4 0) binary heterojunction photocatalysts with enhanced photocatalytic activity for Ciprofloxacin degradation and mechanism insight. *Chemical Engineering Journal*, 358, 891-902.
360. Ayodhya, D., & Veerabhadram, G. (2019). Facile fabrication, characterization and efficient photocatalytic activity of surfactant free ZnS, CdS and CuS nanoparticles. *Journal of Science: Advanced Materials and Devices*, 4(3), 381-391.
361. Patil, M., Jang, H., Han, S. H., Gattu, K. P., Tonpe, D. A., Kutwade, V. V., & Sharma, R. (2023). Electrochemical performance of low-cost PANI-anchored CuS electrode for lithium-ion batteries. *Applied Physics A*, 129(2), 142.
362. An, Y., Li, X. F., Zhang, Y. J., Tao, F. J., Zuo, M. C., Dong, L. H., & Yin, Y. S. (2015). Fabrication and application of a new-type photothermal conversion nano composite coating. *Journal of Nanoscience and Nanotechnology*, 15(4), 3151-3156.

363. Riyaz, S., Parveen, A., & Azam, A. (2016). Microstructural and optical properties of CuS nanoparticles prepared by sol–gel route. *Perspectives in Science*, 8, 632-635.
364. Nafees, M., Ali, S., Rasheed, K., & Idrees, S. (2012). The novel and economical way to synthesize CuS nanomaterial of different morphologies by aqueous medium employing microwaves irradiation. *Applied Nanoscience*, 2, 157-162.
365. Ba-Abbad, M. M., Takriff, M. S., & Mohammad, A. W. (2016). Enhancement of 2-chlorophenol photocatalytic degradation in the presence Co²⁺-doped ZnO nanoparticles under direct solar radiation. *Research on Chemical Intermediates*, 42, 5219-5236.
366. Dustgeer, M. R., Asma, S. T., Jilani, A., Raza, K., Hussain, S. Z., Shakoor, M. B., ... & Darwesh, R. (2021). Synthesis and characterization of a novel single-phase sputtered Cu₂O thin films: Structural, antibacterial activity and photocatalytic degradation of methylene blue. *Inorganic Chemistry Communications*, 128, 108606.
367. Nasseh, N., Arghavan, F. S., Daglioglu, N., & Asadi, A. (2021). Fabrication of novel magnetic CuS/Fe₃O₄/GO nanocomposite for organic pollutant degradation under visible light irradiation. *Environmental Science and Pollution Research*, 28, 19222-19233.
368. Pandit, M. A., Billakanti, S., & Muralidharan, K. (2020). A simplistic approach for the synthesis of CuS-CdS heterostructure: A novel photo catalyst for oxidative dye degradation. *Journal of Environmental Chemical Engineering*, 8(2), 103542.
369. Singh, V., Sharma, A. K., Tripathi, D. N., & Sanghi, R. (2009). Poly (methylmethacrylate) grafted chitosan: An efficient adsorbent for anionic azo dyes. *Journal of hazardous materials*, 161(2-3), 955-966.
370. Borthakur, P., Boruah, P. K., Das, P., & Das, M. R. (2021). CuS nanoparticles decorated MoS₂ sheets as an efficient nanozyme for selective detection and photocatalytic degradation of hydroquinone in water. *New Journal of Chemistry*, 45(19), 8714-8727.
371. Lai, C., Zhang, M., Li, B., Huang, D., Zeng, G., Qin, L., ... & Chen, L. (2019). Fabrication of CuS/BiVO₄ (0 4 0) binary heterojunction photocatalysts with enhanced photocatalytic activity for Ciprofloxacin degradation and mechanism insight. *Chemical Engineering Journal*, 358, 891-902.

372. Turchi, C. S., & Ollis, D. F. (1990). Photocatalytic degradation of organic water contaminants: mechanisms involving hydroxyl radical attack. *Journal of catalysis*, 122(1), 178-192.
373. Saranya, M., Ramachandran, R., Samuel, E. J. J., Jeong, S. K., & Grace, A. N. (2015). Enhanced visible light photocatalytic reduction of organic pollutant and electrochemical properties of CuS catalyst. *Powder Technology*, 279, 209-220.
374. Ajibade, P. A., & Oluwalana, A. E. (2021). Enhanced photocatalytic degradation of ternary dyes by copper sulfide nanoparticles. *Nanomaterials*, 11(8), 2000.
375. Siadatnasab, F., Farhadi, S., & Khataee, A. (2018). Sonocatalytic performance of magnetically separable CuS/CoFe₂O₄ nanohybrid for efficient degradation of organic dyes. *Ultrasonics sonochemistry*, 44, 359-367.
376. Michael, I.; Rizzo, L.; Mc Ardell, C. S.; Manaia, C. M.; Merlin, C.; Schwartz, T.; Dagot, C.; Fatta-Kassinos, D. Urban wastewater treatment plants as hotspots for the release of antibiotics in the environment: A review. *Water Res.* 2013, 47, 957–995.
377. Hou, W.; Yang, J.; Xu, H.; Li, D.; Zou, Z.; Xia, D. Syntheses of Nymphaea-like BiOCl with oxygen vacancies for effective removal of tetracycline hydrochloride. *CrystEngComm* 2020, 22, 3956–3964.
378. Massima Mouele, E. S.; Tijani, J. O.; Badmus, K. O.; Pereao, O.; Babajide, O.; Zhang, C.; Shao, T.; Sosnin, E.; Tarasenko, V.; Fatoba, O. O.; Laatikainen, K.; Petrik, L. F. Removal of Pharmaceutical Residues from Water and Wastewater Using Dielectric Barrier Discharge Methods-A Review. *Int. J. Environ. Res. Public Health* 2021, 18, 1683.
379. Dao, Y. H., Tran, H. N., Tran-Lam, T. T., Pham, T. Q., & Le, G. T. (2018). Degradation of paracetamol by an UV/chlorine advanced oxidation process: Influencing factors, factorial design, and intermediates identification. *International Journal of Environmental Research and Public Health*, 15(12), 2637.
380. Wang, F.; Feng, Y.; Chen, P.; Wang, Y.; Su, Y.; Zhang, Q.; Zeng, Y.; Xie, Z.; Liu, H.; Liu, Y.; Lv, W.; Liu, G. Photocatalytic degradation of fluoroquinolone antibiotics using ordered mesoporous g-C₃N₄ under simulated sunlight irradiation: kinetics, mechanism, and antibacterial activity elimination. *Appl. Catal., B* 2018, 227, 114–122.
381. Sharma, S.; Bhattacharya, A. Drinking water contamination and treatment techniques. *Appl. Water Sci.* 2017, 7, 1043–1067.

382. Boczkaj, G.; Fernandes, A. Wastewater treatment by means of advanced oxidation processes at basic pH conditions: A review. *Chem. Eng. J.* 2017, 320, 608–633.
383. Serpone, N.; Emeline, A. V. Semiconductor Photocatalysis - Past, Present, and Future Outlook. *J. Phys. Chem. Lett.* 2012, 3, 673–677.
384. Wang, A.; Chen, Y.; Zheng, Z.; Wang, H.; Li, X.; Yang, Z.; Qiu, R.; Yan, K. In situ N-doped carbon-coated mulberry-like cobalt manganese oxide boosting for visible light driving photocatalytic degradation of pharmaceutical pollutants. *Chem. Eng. J.* 2021, 411, 128497.
385. Bhembe, Y. A., Lukhele, L. P., Hlekelele, L., Ray, S. S., Sharma, A., Vo, D. V. N., & Dlamini, L. N. (2020). Photocatalytic degradation of nevirapine with a heterostructure of few-layer black phosphorus coupled with niobium (V) oxide nanoflowers (FL-BP@ Nb₂O₅). *Chemosphere*, 261, 128159.
386. Crabb, D.W., Im, G.Y., Szabo, G., Mellinger, J.L. and Lucey, M.R., 2020. Diagnosis and treatment of alcohol-associated liver diseases: 2019 practice guidance from the American Association for the Study of Liver Diseases. *Hepatology*, 71(1), pp.306-333.
387. Gloria, D. C. S., Brito, C. H. V., Mendonça, T. A. P., Brazil, T. R., Domingues, R. A., Vieira, N. C. S., ... & Gonçalves, M. (2023). Preparation of TiO₂/activated carbon nanomaterials with enhanced photocatalytic activity in paracetamol degradation. *Materials Chemistry and Physics*, 305, 127947.
388. Garrido-Cardenas, J. A., Esteban-García, B., Agüera, A., Sánchez-Pérez, J. A., & Manzano-Agugliaro, F. (2020). Wastewater treatment by advanced oxidation process and their worldwide research trends. *International Journal of Environmental Research and Public Health*, 17(1), 170.
389. Pant, B., Park, M., & Park, S. J. (2019). MoS₂/CdS/TiO₂ ternary composite incorporated into carbon nanofibers for the removal of organic pollutants from water. *Inorganic Chemistry Communications*, 102, 113-119.
390. Singh, V., Lee, J.K., Seshadri, M., Bhat, A.A., Watanabe, S. and Rao, T.G., 2024. Photoluminescence and EPR spectroscopic studies on narrowband ultraviolet-B (NB-UVB) emitting trivalent gadolinium-doped CaAl₄O₇ material for phototherapy lamps. *Ceramics International*, 50(3), pp.4632-4639.

391. Bharti, D. B., Bharati, A. V., & Wankhade, A. V. (2018). Synthesis, characterization and optical property investigation of CdS nanoparticles. *Luminescence*, 33(8), 1445-1449.
392. Hussain, A., & Tayyab, M. (2020). Effect of Cu concentration and dopant site on the band gap of MoS₂: A DFT study. *Computational Condensed Matter*, 24, e00494.
393. Wang, W.; Zhao, W.; Huang, H.; Chen, R.; Shi, H. A 2D/2D Sscheme photo-Fenton catalyst based on ultrathin Bi₂MoO₆ and Fe₂O₃ hexagonal nanosheets for efficient tetracycline degradation. *Catal. Sci. Technol.* 2021, 11, 2948–2956.
394. Cao, H.L., Cai, F.Y., Yu, K., Zhang, Y.Q., Lü, J. and Cao, R., 2019. Photocatalytic degradation of tetracycline antibiotics over CdS/nitrogen-doped carbon composites derived from in situ carbonization of metal–organic frameworks. *ACS Sustainable Chemistry & Engineering*, 7(12), pp.10847-10854.
395. Yu, Z., Li, F., and Xiang, Q., 2023. Carbon dot-based nanocomposites for heterogeneous photocatalysis. *Journal of Materials Science & Technology*.
396. Gupta, J., Singhal, P., & Rattan, S. S. (2022, February). Microwave Assisted Synthesis of Molybdenum Disulfide/Tungsten Trioxide/Reduced Graphene Oxide (MoS₂/WO₃/RGO) Nanocomposites for Organic Vapor Sensing. In *IOP Conference Series: Materials Science and Engineering* (Vol. 1225, No. 1, p. 012001). IOP Publishing.
397. Dey, P. C., Sarkar, S., & Das, R. (2020). X-ray diffraction study of the elastic properties of jagged spherical CdS nanocrystals. *Materials Science-Poland*, 38(2), 271-278.
398. Liu, S., Zhang, X., Shao, H., Xu, J., Chen, F. and Feng, Y., 2012. Preparation of MoS₂ nanofibers by electrospinning. *Materials Letters*, 73, pp.223-225.
399. Martin, T.P. and Schaber, H., 1982. Matrix isolated II-VI molecules: Sulfides of Mg, Ca, Sr, Zn, and Cd. *SpectrochimicaActa Part A: Molecular Spectroscopy*, 38(6), pp.655-660.
400. Raja, P. B., Munusamy, K. R., Perumal, V., & Ibrahim, M. N. M. (2022). Characterization of nanomaterial used in nanobioremediation. In *Nano-bioremediation: fundamentals and applications* (pp. 57-83). Elsevier.
401. Liu, X., Ruan, Z., Zhang, L., Li, Y., Jiang, Y., Fan, J., Xu, X., Du, Y., Yuan, Y. and Lin, K., 2021. Porous cauliflower-like molybdenum disulfide/cadmium sulfide hybrid micro/nano structure: Enhanced visible light absorption ability and photocatalytic activity. *Journal of Colloid and Interface Science*, 590, pp.352-364.

402. Wamsley, M., Zou, S., & Zhang, D. (2023). Advancing Evidence-Based Data Interpretation in UV–Vis and Fluorescence Analysis for Nanomaterials: An Analytical Chemistry Perspective. *Analytical Chemistry*, 95(48), 17426-17437.
403. Ebnonnasir, A., Narayanan, B., Kodambaka, S. and Ciobanu, C.V., 2014. Tunable MoS₂ bandgap in MoS₂-graphene heterostructures. *Applied Physics Letters*, 105(3).
404. Zhang, Q., Cheng, S., Xia, H., Zhang, L., Zhou, J., Li, C., ... & Jiang, X. (2019). Paracetamol degradation performance and mechanisms using microwave-assisted heat-activated persulfate in solutions. *Water, Air, & Soil Pollution*, 230(12), 271.
405. Sharma, A., & Lee, B. K. (2016). Structure and activity of TiO₂/FeO co-doped carbon spheres for adsorptive-photocatalytic performance of complete toluene removal from the aquatic environment. *Applied Catalysis A: General*, 523, 272-282.
406. Lozano-Morales, S. A., Morales, G., López Zavala, M. Á., Arce-Sarria, A., & Machuca-Martínez, F. (2019). Photocatalytic treatment of paracetamol using TiO₂ nanotubes: Effect of pH. *Processes*, 7(6), 319.
407. Chijioke-Okere, M. O., Hir, Z. A. M., Ogukwe, C. E., Njoku, P. C., Abdullah, A. H., & Oguzie, E. E. (2021). TiO₂/Polyethersulphone films for photocatalytic degradation of acetaminophen in aqueous solution. *Journal of Molecular Liquids*, 338, 116692.
408. Chekira, N., Sabbaa, N., Benhabilesb, O., Tassalitb, D., & Sahraouia, N. (2022). Optimizing operating parameters using experimental design in photocatalytic degradation of a model pollutant, paracetamol, by TiO₂. *Desalination and water treatment*, 279, 115-123.
409. Rani, S., Tabasum, S., Sharma, A., Singh, P., Singh, P. P., Reehl, P., ... & Singh, H. (2023). Effects of Cu substitution on photocatalytic performance of ZnO nanorods synthesised via hydrothermal route for the degradation of chlorobenzene. *International Journal of Environmental Analytical Chemistry*, 1-13.
410. Parveen, I., Rose, M., Phillips, H. C., Flower, S. E., Woodman, T. J., Garty, C. A., & Threadgill, M. D. (2023). Two-step synthesis of paracetamol (acetaminophen), a practical illustration of carbonyl reactivity for Year-One biosciences students. *Journal of Chemical Education*, 100(10), 3955-3959.
411. Sharma, A., & Lee, B. K. (2016). Rapid photo-degradation of 2-chlorophenol under visible light irradiation using cobalt oxide-loaded TiO₂/reduced graphene oxide

- nanocomposite from aqueous media. *Journal of Environmental Management*, 165, 1-10.
412. Aggelopoulos, C. A., Meropoulis, S., Hatzisymeon, M., Lada, Z. G., & Rassias, G. (2020). Degradation of antibiotic enrofloxacin in water by gas-liquid nsp-DBD plasma: Parametric analysis, effect of H₂O₂ and CaO₂ additives, and exploration of degradation mechanisms. *Chemical Engineering Journal*, 398, 125622.
 413. Tabasum, S., Sharma, A., Rani, S., Chaudhary, S., Malik, A. Q., Kumar, D., & Deshpande, T. (2023). Prolific fabrication of lanthanum oxide with Graphitic carbon/graphene oxide for enhancing photocatalytic degradation of carbofuran from aqueous solution. *Rasayan Journal of Chemistry*, 16(2).
 414. Yun, W. C., Lin, K. Y. A., Tong, W. C., Lin, Y. F., & Du, Y. (2019). Enhanced degradation of paracetamol in water using sulfate radical-based advanced oxidation processes catalyzed by 3-dimensional Co₃O₄ nanoflower. *Chemical Engineering Journal*, 373, 1329-1337.
 415. Noorisepehr, M., Ghadirinejad, K., Kakavandi, B., Esfahani, A. R., & Asadi, A. (2019). Photo-assisted catalytic degradation of acetaminophen using peroxymonosulfate decomposed by magnetic carbon heterojunction catalyst. *Chemosphere*, 232, 140-151.
 416. Puri, S., Thakur, I., Verma, A., & Barman, S. (2021). Degradation of pharmaceutical drug paracetamol via UV irradiation using Fe-TiO₂ composite photocatalyst: statistical analysis and parametric optimization. *Environmental science and pollution research*, 28, 47327-47341.
 417. Schwarzenbach, R.P., Escher, B.I., Fenner, K., Hofstetter, T.B., Johnson, C.A., von Gunten, U. and Wehrli, B., 2006. The challenge of micropollutants in aquatic systems. *Science*, 313, 1072.
 418. Boxall, A.B., Rudd, M.A., Brooks, B.W., Caldwell, D.J., Choi, K., Hickmann, S., Innes, E., Ostapyk, K., Staveley, J.P., Verslycke, T. and Ankley, G.T., 2012. Pharmaceuticals and personal care products in the environment: what are the big questions? *Environmental Health Perspectives*, 120, 1221.
 419. Kezzim, A., Boudjemaa, A., Belhadi, A. and Trari, M., 2017. Photo-catalytic degradation of ibuprofen over the new semiconducting catalyst α -(Cu, Fe)2O3 prepared by the hydrothermal route. *Research on Chemical Intermediates*, 43, 3727.
 420. Garg, A., Basu, S., Shetti, N.P., and Reddy, K.R., 2021. 2D materials and their heterostructured photocatalysts: Synthesis, properties, functionalization, and

- applications in environmental remediation. *Journal of Environmental Chemical Engineering*, 9, 106408.
421. Langenhoff, A., Inderfurth, N., Veuskens, T., Schraa, G., Blokland, M., Kujawa-Roeleveld, K. and Rijnaarts, H., 2013. Microbial removal of the pharmaceutical compounds ibuprofen and diclofenac from wastewater. *BioMed Research International*, 2013, 325806.
 422. Mao, S., Liu, C., Xia, M., Wang, F., and Ju, X., 2021. Construction of a Z-scheme 1D/2D FeV₃O₈/gC₃N₄ composite for ibuprofen degradation: mechanism insight, theoretical calculation, and degradation pathway. *Catalysis Science & Technology*, 11, 3466.
 423. Jagannathan Madhavan, J.M., Grieser, F., and Muthupandian Ashokkumar, M.A., 2010. Combined advanced oxidation processes for the synergistic degradation of ibuprofen in aqueous environments. 178, 202
 424. Mearaj, T., Farooq, A., Hafiz, A.K., Bi, W., and Bhat, A.A., 2024. Enhanced photodetection performance of WSe₂/V₂O₅ nanocomposite on flexible substrate: synergistic advantages and improved efficiency. *ACS Applied Materials & Interfaces*, 16, 57277.
 425. Sheikh, Z.A., Kim, H., Vikraman, D., Aftab, S., Bhat, A.A., Hussain, I., Batoo, K.M., Kim, H.S., Jung, J., Hussain, S., and Kim, D.K., 2024. Improved charge storage kinetics using metal carbide integrated NiO hybrid composite electrodes for supercapacitors. *Journal of Energy Storage*, 100, 113605.
 426. Chackrabarti, S., Mearaj, T., Siddiqui, A., Zargar, R.A., Bhat, A.A., Siddiqui, N.A., Khan, A., and Shkir, M., 2024. Thermally induced Modulation of optoelectronic characteristics in (ZrO₂)_{0.8} doped (CuO)_{0.2} screen-printed thick films: An Innovative approach to enhanced materials. *Optical Materials*, 156, 115934.
 427. Upadhyay, S., Bhat, B.A., Tomar, R. and Bhat, A.A., 2024. Development and performance of a PANI@NiMnO₃ nanocomposite for enhanced supercapacitors and photocatalytic applications. *ACS Applied Bio Materials*, 7, 7256.
 428. Buscema, M., Barkelid, M., Zwiller, V., van der Zant, H.S., Steele, G.A. and Castellanos-Gomez, A., 2013. Large and tunable photothermoelectric effect in single-layer MoS₂. *Nano Letters*, 13, 358.
 429. Lau, T.H., Lu, X., Kulhavy, J., Wu, S., Lu, L., Wu, T.S., Kato, R., Foord, J.S., Soo, Y.L., Suenaga, K. and Tsang, S.C.E., 2018. Transition metal atom doping of the

- basal plane of MoS₂ monolayer nanosheets for electrochemical hydrogen evolution. *Chemical Science*, 9, 4769.
430. Zhang, J.R., Zhao, Y.Q., Chen, L., Yin, S.F., and Cai, M.Q., 2019. Density functional theory calculation on facet-dependent photocatalytic activity of MoS₂/CdS heterostructures. *Applied Surface Science*, 469, 27.
 431. Zhang, P., Wang, Z., Liu, L., Klausen, L.H., Wang, Y., Mi, J., and Dong, M., 2019. Modulation the electronic property of 2D monolayer MoS₂ by an amino acid. *Applied Materials Today*, 14, 151.
 432. Taghilou, S., Nakhjirgan, P., Esrafil, A., Dehghanifard, E., Kermani, M., Kakavandi, B., and Pelalak, R., 2024. Performance, progress, and mechanism of g-C₃N₄-based photocatalysts in the degradation of pesticides: A systematic review. *Chemosphere*, 368, 143667.
 433. Bahadoran, A., Dolatimehr, A., Fayazi, D., Rafiee, M., Kakavandi, B., Hosseini, S.R. and Galluzzi, M., 2024. Highly efficient treatment of pharmaceutical contaminants: A comprehensive study on the performance and mechanism of sustainable yolk-in-double-shelled CuCo₂S₄@ Bi-doped TiO₂ photocatalyst. *Journal of Water Process Engineering*, 68, 106247.
 434. Bashardoust, P., Giannakis, S., Dehghanifard, E., Kakavandi, B., and Dewil, R., 2024. Treatment of pharmaceutical wastewater by a sequential KMnO₄/CoFe₂O₄-mediated catalytic ozonation process. *Chemical Engineering Journal*, 490, 151350.
 435. Kakavandi, B., Ahmadi, M., Bedia, J., Hashamfirooz, M., Naderi, A., Oskoei, V., Yousefian, H., Kalantary, R.R., Pelalak, R., and Dewil, R., 2024. Metronidazole degradation mechanism by sono-photo-Fenton processes using a spinel ferrite cobalt on activated carbon catalyst. *Chemosphere*, 358, 142102.
 436. Singh, V., Bhat, A.A., Kadam, A.R., Saravanakumar, S., Tripathi, P.K., Dhoble, S.J., and Joo, J.B., 2024. Optimal doping of Ho³⁺ in CaTiO₃ perovskite for enhanced photoluminescence and sustainable green emission. *Journal of Electronic Materials*, 53, 6384.
 437. Zai, H., Zhu, C., Xie, H., Zhao, Y., Shi, C., Chen, Z., Ke, X., Sui, M., Chen, C., Hu, J., and Zhang, Q., 2017. Congeneric incorporation of CsPbBr₃ nanocrystals in a hybrid perovskite heterojunction for photovoltaic efficiency enhancement. *ACS Energy Letters*, 3, 30.
 438. Singh, V., Bhat, A.A. and Jamil, M., 2024. Enhanced Green Luminescence of La₉.33Si₆O₂₆:Tb³⁺ Phosphors. *Journal of Electronic Materials*, 53, 7946.
 439. Bhat, A.A., Zaman, M.B., Malik, J.H., Malik, K.A., Assadullah, I. and Tomar, R., 2021. Facile way of making hydrothermally synthesized crystalline SrSnO₃

- perovskite nanorods suitable for blue LEDs and spintronic applications. *ACS Omega*, 6, 16356.
440. Musiienko, A., Cizek, J., Elhadidy, H., Praus, P., Higgins, K., Dryzhakov, B., Kanak, A., Sureau, F., Pipek, J., Belas, E., and Betusiak, M., 2021. Origin of defects and positron annihilation in hybrid and all-inorganic perovskites. *Chemistry of Materials*, 34, 297.
 441. Ding, X., Ren, Y., Wu, Y., Xu, Y., Zhu, J., Tasawar, H., Ahmed, A., Li, Z., Huang, Y. and Dai, S., 2017. Sequential deposition method for fabricating carbon-based fully-inorganic perovskite solar cells. *Science China Materials*, 61, 73.
 442. Bresolin, B. M., Sgarbossa, P., Bahnemann, D. W., & Sillanpää, M. 2020. Cs₃Bi₂I₉/g-C₃N₄ as a new binary photocatalyst for efficient visible-light photocatalytic processes. *Separation and Purification Technology*, 251, 117320.
 443. Sathiyar, S., Ahmad, H., Chong, W.Y., Lee, S.H. and Sivabalan, S., 2015. Evolution of the Polarizing Effect of MoS₂. *IEEE Photonics Journal*, 7, 1.
 444. Lee, J.K., Bhat, A.A., Nande, A., Watanabe, S., Rao, T.G., and Singh, V., 2024. Optimized Mn⁴⁺ doped Sr₉Y₂W₄O₂₄ perovskite for enhanced far-red-emitting luminescent material. *Ceramics International*, 50, 32978.
 445. Baghdadi, Y., Temerov, F., Cui, J., Daboczi, M., Rattner, E., Sena, M.S., Itskou, I., and Eslava, S., 2023. Cs₃Bi₂Br₉/g-C₃N₄ Direct Z-Scheme Heterojunction for Enhanced Photocatalytic Reduction of CO₂ to CO. *Chemistry of Materials*, 35, 8607.
 446. Malik, K.A., Malik, J.H., Bhat, A.A., Assadullah, I., and Tomar, R., 2021. Trap-assisted visible light luminescent properties of hydrothermally grown Gd-doped ZnO nanostructures. *Vacuum*, 183, 109832.
 447. Lv, J.R., Guo, R.T., Zhu, H.W., Shi, X.D., Liu, M.Y., and Pan, W.G., 2024. Recent Advances in Metal Halide Perovskites for CO₂ Photocatalytic Reduction: An Overview and Future Prospects. *Small*, 2408921.
 448. Jing, L., Xie, M., Xu, Y., Tong, C., Du, X., Zhao, H., Zhong, N., Li, H., and Hu, J., 2024. Advanced oxidation via the synergy of C-defective/C–O band modified ultrathin porous g-C₃N₄ and PMS for efficient photothermal degradation of bisphenol pollutants and lignin derivatives. *Green Energy & Environment*, 9, 1159.
 449. Muhammad Tanveer, M.T., Guyer, G.T., and Ghulam Abbas, G.A., 2019. Photocatalytic degradation of ibuprofen in water using TiO₂ and ZnO under artificial UV and solar irradiation. 91, 822.
 450. Oad, N., Chandra, P., Mohammad, A., Tripathi, B. and Yoon, T., 2023. MoS₂-based hetero-nanostructures for photocatalytic, photoelectrocatalytic, and piezocatalytic remediation of hazardous pharmaceuticals. *Journal of Environmental Chemical Engineering*, 11, 109604.

451. Cai, J., Niu, B., Xie, Q., Lu, N., Huang, S., Zhao, G., and Zhao, J., 2022. Accurate removal of toxic organic pollutants from complex water matrices. *Environmental Science & Technology*, 56, 2917.
452. Fauzi, A.A., Jalil, A.A., Mohamed, M., Triwahyono, S., Jusoh, N.W.C., Rahman, A.F.A., Aziz, F.F.A., Hassan, N.S., Khusnun, N.F., and Tanaka, H., 2018. Altering fiber density of cockscomb-like fibrous silica–titania catalysts for enhanced photodegradation of ibuprofen. *Journal of Environmental Management*, 227, 34.



Wet Chemical Co-precipitation Route of CuS Nanoparticles: Synthesis and Characteristics Studies Towards Photo-Degradation of 2-Chlorophenol

Saima Jan¹ · Jyoti Varma¹ · Ajit Sharma¹ · Malik Aalim² · Meenakshi Choudhary¹ · Bindu Mangla³

Accepted: 27 December 2024

© The Author(s), under exclusive licence to Springer Science+Business Media, LLC, part of Springer Nature 2025

Abstract

CuS nanoparticles (NPs) were synthesized by wet chemical co-precipitation and Solgel method and used to promote photocatalytic degradation of 2-Chlorophenol (2-CP) from aqueous media. The Tauc plot and diffused reflectance spectroscopy (DRS-UV) was studied to determine the 2.1 eV band gap of CuS NPs. The high degree of crystallinity was observed by X-ray diffraction (XRD) analysis. The exothermic nature of CuS NPs was pragmatic at 380°C using thermal gravimetric analysis (TGA) technique. The photo-catalytic activity of CuS NPs towards 2-CPdegradation was influenced with visible light intensity from 20 to 100 W. The strong photocatalytic elimination of 2-CP from an aqueous solution was caused by the increased charge transmission.

Keywords Wet chemical process · Solgel process · CuS · 2-CP · Photocatalysis · Degradation · Regeneration

1 Introduction

Recent years have seen the growth of process industries that employ a lot of pollutants, such as herbicides, pesticides, dyes and nitrophenols, as a result of population growth and human settlement expansion [1]. One of the main concerns is the existence of extremely harmful and poisonous contaminants in the water and wastewater that the chemical industries discharge [2]. Due to the extreme toxicity, bio-accumulation and persistence, chlorophenol compounds (CPCs), which are used more and more in agriculture, manufacturing, and medical treatment, are being released into

the environment in greater quantities. This has an adverse effect on both humans' health and environment [3]. Additionally, CPs shows toxicity towards the development and metabolism of microorganisms. Trace chlorophenol do not effectively remove these substances from drinking water or other water sources, and it is important to consider the threat to water quality safety associated with microbial leakage [4]. Instead of the decomposition of pollutants and full mineralization, which might easily result in secondary pollution, physical adsorption can only, realize the quick transfer and physical concentration of chlorine phenol contaminants [5, 6]. The principal approach for reducing CP contaminants is the conventional chemical reduction-oxidation process; however, this method has expensive operation costs and rigorous criteria for the reaction equipment. Additionally, this process frequently results in by-products and is difficult to mineralize completely. Eliminating contaminants from water is a difficult problem [7]. Recently Suman et al. demonstrate that ZnO and La-doped ZnO photocatalyst were used to study the degradation of 2-chlorophenol (2-CP) at the ideal pH, irradiation duration, and catalytic dose. It's interesting to note that at an optimal pH of 2, ZnO and La-doped ZnO showed maximum degradation efficiency of 75.85% and 83.92%, respectively, with a catalytic dose of 10 mg and an irradiation period of 2 h [8].

✉ Ajit Sharma
 ajitsharma2003@gmail.com

✉ Bindu Mangla
 bindumangla@gmail.com

¹ Department of Chemistry, School of Chemical Engineering and Physical Sciences, Lovely Professional University, Phagwara, Punjab 144411, India

² Department of Physics, National institute of technology Srinagar, Srinagar, Jammu and Kashmir 190006, India

³ Department of Chemistry, J.C. Bose University of Science and Technology YMCA, Faridabad 121006, India



Enhanced photocatalytic ciprofloxacin degradation in industrial aquatic waste using CdS/Cs₃Bi₂Br₉ nanocomposite synthesized by microwave energy

Saima Jan^a, Ajit Sharma^{a,b,*}, Amar Srivastava^c, Van-Duong Dao^d, Rashmi Sanghi^e

^a Department of Chemistry, School of Chemical Engineering and Physical Sciences, Lovely Professional University, Phagwara, Punjab 144411, India

^b Centre for Nanoscience and Nano Biotechnology, School of Chemical Engineering and Physical Sciences, Lovely Professional University, Phagwara, Punjab 144411, India

^c Department of Physics, School of Engineering, Dayananda Sagar University, Bangalore, Karnataka 562112, India

^d Faculty of Biotechnology, Chemistry and Environmental Engineering, Phenikaa University, Hanoi 10000, Viet Nam

^e Amity School of Chemical Sciences, Amity University Punjab, IT City Mohali 140006, India

ARTICLE INFO

Keywords:

CdS
Cs₃Bi₂Br₉
Ciprofloxacin
Microwave
Nanocomposite
Photo-degradation

ABSTRACT

For degradation of ciprofloxacin the as-prepared material was synthesized by microwave process. This study shows how to synthesize a hybrid heterojunction between Cs₃Bi₂Br₉ and CdS at various ratios. SEM-EDX pictures were used to assess morphological investigations and the composition of the dopants, demonstrating the existence of CdS in Cs₃Bi₂Br₉ nanostructured hybrid. Powder XRD was used to confirm the crystalline structures of CdS, Cs₃Bi₂Br₉ and CdS/Cs₃Bi₂Br₉ nanocomposites with crystalline size of 16.8 nm, 11.7 nm and 7.02 nm respectively. The bandgap energies for CdS, Cs₃Bi₂Br₉ and CdS/Cs₃Bi₂Br₉ is 3.4 eV, 3.5 eV and 3 eV respectively. The as-prepared material CdS, Cs₃Bi₂Br₉ and CdS/Cs₃Bi₂Br₉ photocatalysts were used to study the degradation of ciprofloxacin (CIP) at the irradiation time, ideal pH, H₂O₂ conc. catalytic dosage and effect of temperature. Unsurprisingly, at an ideal pH of 8, CdS, Cs₃Bi₂Br₉ and 5 %CdS/Cs₃Bi₂Br₉ demonstrated maximum degradation efficiency of 80 %, 65.5 % and 98.4 % respectively as compared to Solgel method based CdS which is 60 %, with a catalytic dosage of 10 mg and an irradiation period of three hours.

1. Introduction

The escalating presence of persistent pharmaceutically active compounds in aquatic ecosystems is primarily attributed to the widespread use of antibiotics and the limitations of conventional water treatment processes [1]. Fluoroquinolones (FQs), one of the most commonly utilized antibiotic classes, have been frequently detected in environmental samples [2]. Notably, FQs exhibit remarkable stability, resulting in over 70 % of the compound being excreted unchanged or as active metabolites, highlighting their potential for environmental persistence [3].

The β -lactam group is one of the most often used antibiotics to treat infectious infections in both humans and animals. The β -lactam antibiotic family, which includes amoxicillin (AMX), has antibacterial activity against both Gram-positive and Gram-negative bacteria. AMX inhibits the production of peptidoglycans, which are the primary component of the bacterial cell wall, and has a higher rate of absorption

in living organisms than other β -lactam antibiotics. Owing to its extensive use, it continues to be used in biological fluids and animal feed, which results in certain negative effects on humans. Antibiotic-associated colitis, rashes, nausea, and vomiting are some of its adverse effects. Therefore, it's critical to find its remnant in biological fluids and food manufacturing [4]. Metoclopramide (MCP), a well-known derivative of 4-aminobenzoic acid and substituted benzamide, is a dopamine antagonist that has antiemetic and analgesic properties, particularly for various gastroenterological issues. In addition to treating gastroparesis and gastroesophageal reflux, it also decreases migraine attacks and labor pain, serves as a local anesthetic and relieves hiccup symptoms, stops postoperative nausea and vomiting, stops chemotherapy-induced vomiting, and promotes gastric emptying. About 80 % of an oral dose of MCP (as an unaltered molecule and its conjugates) is excreted in the urine within 24 h, and it is well absorbed and rapidly excreted in humans with a short half-life of a few hours. Less than 2 % of MCP is excreted in the

* Corresponding author at: Department of Chemistry, School of Chemical Engineering and Physical Sciences, Lovely Professional University, Phagwara, Punjab 144411, India.

E-mail address: ajitsharma2003@gmail.com (A. Sharma).

<https://doi.org/10.1016/j.molliq.2025.127450>

Received 20 November 2024; Received in revised form 9 March 2025; Accepted 22 March 2025

Available online 23 March 2025

0167-7322/© 2025 Elsevier B.V. All rights are reserved, including those for text and data mining, AI training, and similar technologies.

Efficient Photocatalytic Degradation of Ibuprofen from Aquatic Waste Using a Microwave Synthesized $\text{MoS}_2@\text{Cs}_3\text{Bi}_2\text{Br}_9$ Nanocomposite

Saima Jan, Ajit Sharma,* Owais Hassan Wani, Shah Jahan Ul Islam, Shahid Ahmad Shah, Wengang Bi,* and Aadil Ahmad Bhat*

Cite This: <https://doi.org/10.1021/acs.langmuir.5c00882>

Read Online

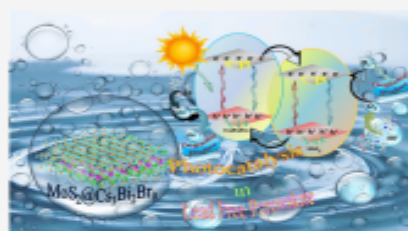
ACCESS |

Metrics & More

Article Recommendations

Supporting Information

ABSTRACT: The persistent presence of pharmaceutical contaminants such as ibuprofen (IBF) in aquatic ecosystems poses significant environmental and health risks, as conventional wastewater treatments often fail to eliminate these recalcitrant compounds. Herein, a novel $\text{MoS}_2@\text{Cs}_3\text{Bi}_2\text{Br}_9$ heterojunction photocatalyst was synthesized via sol-gel and microwave methods to address this challenge. Comprehensive characterization (XRD, FTIR, SEM, EDX, and UV-vis) confirmed the structure of composite and optical properties, revealing a reduced bandgap of 3.04 eV (vs pristine $\text{Cs}_3\text{Bi}_2\text{Br}_9$) due to a type II heterojunction with staggered band alignment. This configuration enabled efficient charge separation, as photogenerated electrons migrated from the conduction band (CB) of $\text{Cs}_3\text{Bi}_2\text{Br}_9$ to MoS_2 (~ 0.3 eV), while holes transferred inversely, suppressing recombination and enhancing the redox activity. Under optimized conditions (20 mg/L IBF, pH 6.0, visible light, 0.1% H_2O_2), the 5% $\text{MoS}_2@\text{Cs}_3\text{Bi}_2\text{Br}_9$ composite achieved 96.77% degradation efficiency within 3 h, outperforming individual catalysts (61% for MoS_2 -sol-gel, 76% for MoS_2 -microwave, and 69% for $\text{Cs}_3\text{Bi}_2\text{Br}_9$). The staggered energy bands of the heterojunction facilitate electron transfer from $\text{Cs}_3\text{Bi}_2\text{Br}_9$ to MoS_2 and hole migration in the reverse direction, suppressing recombination and amplifying hydroxyl radical ($\bullet\text{OH}$) generation. Low-dose H_2O_2 (0.1%) acted as an electron scavenger to boost $\bullet\text{OH}$ production, while excess H_2O_2 (1%) promoted recombination, reducing the efficiency. The composite exhibited exceptional reusability, retaining >90% activity over five cycles via H_2O_2 -assisted regeneration. This work underscores the potential of $\text{MoS}_2@\text{Cs}_3\text{Bi}_2\text{Br}_9$ as a sustainable, high-performance photocatalyst for degrading pharmaceutical pollutants, offering a viable strategy to mitigate emerging contaminants in water systems.



INTRODUCTION

The contamination of freshwater systems globally by a vast array of industrial and natural compounds has emerged as a significant environmental issue. Pharmaceuticals and personal care products, in particular, are among the most alarming emerging pollutants and have been frequently detected in natural water sources in recent years.^{1,2} Ibuprofen (IBF), a widely utilized nonsteroidal anti-inflammatory drug, is produced in several thousand tons annually due to its effective antipyretic and analgesic properties. Despite its relatively low toxicity, IBF demonstrates both nonphotodegradability and nonbiodegradability, leading to its accumulation in aquatic environments and biological organisms.^{3,4} This persistence poses potential risks to human health and ecological systems. Conventional wastewater treatment methods are insufficient in completely eliminating IBF and can sometimes result in the formation of more hazardous intermediate byproducts. Therefore, it is crucial to develop effective and environmentally friendly technologies for the removal of the IBF from contaminated water. The IBF, known for its endocrine-

disrupting and potential carcinogenic properties, poses serious threats to both human and environmental health. Chronic exposure to IBF concentrations exceeding 1 $\mu\text{g/L}$ in water bodies has been linked to disruption in aquatic organisms, antibiotic resistance in microbial communities, and potential risks to human health through contaminated drinking water sources.⁵ Conventional wastewater treatment has been able to remove nearly 95% of ibuprofen, but it has severe side effects, including the creation of hydroxyl-IBF and carboxy-IBF, which are sometimes much more harmful than IBF.

Photocatalysis has emerged as a promising advanced oxidation process (AOP) that is characterized by high

Received: February 20, 2025

Revised: May 1, 2025

Accepted: May 1, 2025



Photocatalytic and Structural Activity of V_2O_5 Immobilized ZnS Nanocomposite for Bacterial Detoxification Under Visible Light Irradiation

Jyoti Varma¹ · Saima Jan¹ · Ayushi Chaudhary² · Ajit Sharma¹ · Prachi Saxena¹ · Himani Badoni² · Devendra Kumar³ · Meenakshi Choudhary¹ · Ujwal D. Patil⁴ · Nem Singh⁵

Accepted: 9 September 2024

© The Author(s), under exclusive licence to Springer Science+Business Media, LLC, part of Springer Nature 2024

Abstract

Zinc sulphide (ZnS) along with different transition metals has been used for various optoelectronic, photocatalytic and antimicrobial activities. In the present report, zinc sulphide (ZnS) and ZnS/ V_2O_5 nanocomposites have been prepared using the chemical co-precipitation (CcP) and microwave (MW) method and their comparison was done. The presence of functional groups was assessed using the Fourier Transform Infrared Spectroscopy along with elemental detection using Energy Dispersive X-ray. The structural properties were studied with the help of referral X-ray diffraction (XRD) indicating the major planes of the synthesized nanoparticles and their structural nature. Immobilization of the dopant significantly reduced the bandgap energy of ZnS from 3.5 eV to 2.78 eV. SEM analysis revealed the sheet-like arrangement of the doped nanoparticles. Antibacterial studies on the disease-causing bacterial species such as *Escherichia coli*, *Bacillus subtilis*, *Staphylococcus aureus*, *Enterococcus faecalis* and *Salmonella typhi* showed positive responses on using pure ZnS NPs and ZnS/ V_2O_5 nanocomposites synthesized by co-precipitation and microwave methods. It was observed that the microwave synthesized nanoparticles and nanocomposites exhibited higher antibacterial activity with the maximum shown by ZnS/ V_2O_5 (1%).

Keywords Nanocomposite · Antibacterial activity · Zinc sulphide · Reactive oxygen species · Chemical co-precipitation · Microwave

✉ Ajit Sharma
ajitsharma2003@gmail.com

✉ Ujwal D. Patil
udpatil@nmu.ac.in

✉ Nem Singh
nsl.nsm@gmail.com

¹ Department of Chemistry, School of Chemical Engineering and Physical Sciences, Lovely Professional University, Phagwara, Punjab 144411, India

² School of Applied and Life sciences, Uttarakhand University, Arcadia Grant, Prem Nagar, Chandan Wari, Dehradun, Uttarakhand 248007, India

³ Department of Microbiology, Chaudhary Charan Singh University Meerut, Meerut, UP 250004, India

⁴ University Institute of Chemical Technology Kavayitri Bahinabai Chaudhari North Maharashtra University Jalgaon, Jalgaon 425001, India

⁵ Department of Chemistry, Korea University, Seoul, South Korea

1 Introduction

Bacterial infections have been a major concern in health-care, irrespective of advancements in science and technology. The accidental discovery of penicillin in 1928 opened the door to the possibility of reducing the adverse effects of bacterial infections, especially the mortality rates. Ever since there have been major developments in the types and diversities of antibiotics and their courses.

Every year, 100,000 tons of antibiotics are produced to combat bacterial infections. With the overuse of so many antibiotics, the emergence of multiple-drug resistance by bacteria has posed a serious threat [1]. Parallely, the chronic use of topical antibacterials and antiseptics to prevent and treat skin infections has brought the challenges of increasing rates of bacterial resistance due to their indiscriminate usage [2]. Human hands serve as a channel for the exchange of microorganisms between the body and the surrounding

Conferences Attend





दिनांक/Dated:26/03/2025

LOVELY PROFESSIONAL UNIVERSITY, LOVELY
PROFESSIONAL UNIVERSITY, JALANDHAR, DELHI-GT
ROAD, PHAGWARA PUNJAB-144411
INDIAN

LITERARY/ DRAMATIC WORK

PHOTOCATALYTIC DEGRADATION OF ENDOCRINE DISRUPTING CHEMICALS BY SEMICONDUCTOR-BASED PEROVSKITE MATERIALS

ENGLISH

SAIMA JAN, LOVELY PROFESSIONAL UNIVERSITY,
JALANDHAR, DELHI-GT ROAD, PHAGWARA PUNJAB-
144411
INDIAN

DR. AJIT KUMAR SHARMA, LOVELY PROFESSIONAL
UNIVERSITY, JALANDHAR, DELHI-GT ROAD, PHAGWARA
PUNJAB-144411
INDIAN

UNPUBLISHED

NA

LOVELY PROFESSIONAL UNIVERSITY, LOVELY
PROFESSIONAL UNIVERSITY, JALANDHAR, DELHI-GT
ROAD, PHASE-2, MUKHERNAGAR, JALANDHAR-150133

INDIAN

అధ్యక్షులు, భారత ప్రభుత్వము, రోగిని
అధ్యక్షులు, భారత ప్రభుత్వము, రోగిని

10

०२३०८१७६०२३, बौद्धिक संपदा **अज्ञान और भय**

சொத்து அலுவலகம், இந்திய அரசு, Registrar of Copyrights

9 19

1998, 1999, 2000, 2001, 2002, 2003, 2004, 2005, 2006, 2007, 2008, 2009, 2010, 2011, 2012, 2013, 2014, 2015, 2016, 2017, 2018, 2019, 2020, 2021, 2022, 2023, 2024, 2025, 2026, 2027, 2028, 2029, 2030, 2031, 2032, 2033, 2034, 2035, 2036, 2037, 2038, 2039, 2040, 2041, 2042, 2043, 2044, 2045, 2046, 2047, 2048, 2049, 2050, 2051, 2052, 2053, 2054, 2055, 2056, 2057, 2058, 2059, 2060, 2061, 2062, 2063, 2064, 2065, 2066, 2067, 2068, 2069, 2070, 2071, 2072, 2073, 2074, 2075, 2076, 2077, 2078, 2079, 2080, 2081, 2082, 2083, 2084, 2085, 2086, 2087, 2088, 2089, 2090, 2091, 2092, 2093, 2094, 2095, 2096, 2097, 2098, 2099, 2100, 2101, 2102, 2103, 2104, 2105, 2106, 2107, 2108, 2109, 2110, 2111, 2112, 2113, 2114, 2115, 2116, 2117, 2118, 2119, 2120, 2121, 2122, 2123, 2124, 2125, 2126, 2127, 2128, 2129, 2130, 2131, 2132, 2133, 2134, 2135, 2136, 2137, 2138, 2139, 2140, 2141, 2142, 2143, 2144, 2145, 2146, 2147, 2148, 2149, 2150, 2151, 2152, 2153, 2154, 2155, 2156, 2157, 2158, 2159, 2160, 2161, 2162, 2163, 2164, 2165, 2166, 2167, 2168, 2169, 2170, 2171, 2172, 2173, 2174, 2175, 2176, 2177, 2178, 2179, 2180, 2181, 2182, 2183, 2184, 2185, 2186, 2187, 2188, 2189, 2190, 2191, 2192, 2193, 2194, 2195, 2196, 2197, 2198, 2199, 2200, 2201, 2202, 2203, 2204, 2205, 2206, 2207, 2208, 2209, 2210, 2211, 2212, 2213, 2214, 2215, 2216, 2217, 2218, 2219, 2220, 2221, 2222, 2223, 2224, 2225, 2226, 2227, 2228, 2229, 2230, 2231, 2232, 2233, 2234, 2235, 2236, 2237, 2238, 2239, 2240, 2241, 2242, 2243, 2244, 2245, 2246, 2247, 2248, 2249, 2250, 2251, 2252, 2253, 2254, 2255, 2256, 2257, 2258, 2259, 2260, 2261, 2262, 2263, 2264, 2265, 2266, 2267, 2268, 2269, 2270, 2271, 2272, 2273, 2274, 2275, 2276, 2277, 2278, 2279, 2280, 2281, 2282, 2283, 2284, 2285, 2286, 2287, 2288, 2289, 2290, 2291, 2292, 2293, 2294, 2295, 2296, 2297, 2298, 2299, 2300, 2301, 2302, 2303, 2304, 2305, 2306, 2307, 2308, 2309, 2310, 2311, 2312, 2313, 2314, 2315, 2316, 2317, 2318, 2319, 2320, 2321, 2322, 2323, 2324, 2325, 2326, 2327, 2328, 2329, 2330, 2331, 2332, 2333, 2334, 2335, 2336, 2337, 2338, 2339, 2340, 2341, 2342, 2343, 2344, 2345, 2346, 2347, 2348, 2349, 2350, 2351, 2352, 2353, 2354, 2355, 2356, 2357, 2358, 2359, 2360, 2361, 2362, 2363, 2364, 2365, 2366, 2367, 2368, 2369, 2370, 2371, 2372, 2373, 2374, 2375, 2376, 2377, 2378, 2379, 2380, 2381, 2382, 2383, 2384, 2385, 2386, 2387, 2388, 2389, 2390, 2391, 2392, 2393, 2394, 2395, 2396, 2397, 2398, 2399, 2400, 2401, 2402, 2403, 2404, 2405, 2406, 2407, 2408, 2409, 2410, 2411, 2412, 2413, 2414, 2415, 2416, 2417, 2418, 2419, 2420, 2421, 2422, 2423, 2424, 2425, 2426, 2427, 2428, 2429, 2430, 2431, 2432, 2433, 2434, 2435, 2436, 2437, 2438, 2439, 2440, 2441, 2442, 2443, 2444, 2445, 2446, 2447, 2448, 2449, 2450, 2451, 2452, 2453, 2454, 2455, 2456, 2457, 2458, 2459, 2460, 2461, 2462, 2463, 2464, 2465, 2466, 2467, 2468, 2469, 2470, 2471, 2472, 2473, 2474, 2475, 2476, 2477, 2478, 2479, 2480, 2481, 2482, 2483, 2484, 2485, 2486, 2487, 2488, 2489, 2490, 2491, 2492, 2493, 2494, 2495, 2496, 2497, 2498, 2499, 2500, 2501, 2502, 2503, 2504, 2505, 2506, 2507, 2508, 2509, 2510, 2511, 2512, 2513, 2514, 2515, 2516, 2517, 2518, 2519, 2520, 2521, 2522, 2523, 2524, 2525, 2526, 2527, 2528, 2529, 2530, 2531, 2532, 2533, 2534, 2535, 2536, 2537, 2538, 2539, 2540, 2541, 2542, 2543, 2544, 2545, 2546, 2547, 2548, 2549, 2550, 2551, 2552, 2553, 2554, 2555, 2556, 2557, 2558, 2559, 2560, 2561, 2562, 2563, 2564, 2565, 2566, 2567, 2568, 2569, 2570, 2571, 2572, 2573, 2574, 2575, 2576, 2577, 2578, 2579, 2580, 2581, 2582, 2583, 2584, 2585, 2586, 2587, 2588, 2589, 2590, 2591, 2592, 2593, 2594, 2595, 2596, 2597, 2598, 2599, 2600, 2601, 2602, 2603, 2604, 2605, 2606, 2607, 2608, 2609, 2610, 2611, 2612, 2613, 2614, 2615, 2616, 2617, 2618, 2619, 2620, 2621, 2622, 2623, 2624, 2625, 2626, 2627, 2628, 2629, 2630, 2631, 2632, 2633, 2634, 2635, 2636, 2637, 2638, 2639, 2640, 2641, 2642, 2643, 2644, 2645, 2646, 2647, 2648, 2649, 2650, 2651, 2652, 2653, 2654, 2655, 2656, 2657, 2658, 2659, 2660, 2661, 2662, 2663, 2664, 2665, 2666, 2667, 2668, 2669, 2670, 2671, 2672, 2673, 2674, 2675, 2676, 2677, 2678, 2679, 26

Manuscript under Consideration

1. Visible Light Responsive Photocatalytic Degradation of Paracetamol using MoS₂/CdS Nanocomposites from Pharmaceutical Aquatic Waste Streams; in Industrial & Engineering Chemistry Research (Manuscript ID: ie-2025-00759w)